

## **ABSTRACT**

RINGLEY, CHAD J. Numerical Modeling Studies of Multiple Aviation Turbulence Forecasting Problems in the Troposphere and Stratosphere. (Under the direction of Profs. Yuh-Lang Lin and Michael Kaplan).

This thesis is composed of papers derived from two separate projects designed to investigate important aspects and problems in turbulence evolution and forecasting in aviation meteorology. The first paper explores the validation of an updated numerical model configuration performed for the design of a comprehensive low-level wind climatology for boundary layer turbulence in conjunction with the National Aeronautics and Space Administration (NASA) Terminal Area Productivity Program (TAP). The second paper investigates turbulence generation and evolution with explicit turbulence diagnostics with both convective and orographic forcing in the upper troposphere and lower stratosphere in conjunction with the United States Air Force Research Laboratory.

In the first paper, a new version of the Terminal Area PBL Prediction System (TAPPS-2) model is tested to simulate low-level winds, turbulent kinetic energy (TKE) and eddy dissipation rate (EDR) profiles in order to develop a statistically-based wake vortex forecasting tool for air-traffic controllers. A series of TAPPS-2 simulations are validated against tower observations from the Aircraft Vortex Observing and Sampling System (AVOSS) at the Dallas-Fort Worth International Airport from the 17-20 September 1997 intense observing periods (IOPs). The TAPPS-2 system simulated the evolution of turbulence with respect to diurnal forcing and the ubiquitous diurnally-forced low-level jet during the validation period. The TAPPS-2 system also showed significant sensitivity to vertical resolution, model

initialization time, and the formulation of the characteristic length scale of large eddies, and recommendations for the design of the low-level wind climatology are presented.

In the second paper, the stratospheric version of the Non-Hydrostatic Mesoscale Atmospheric Simulation System (NHMASS) model is used to simulate and evaluate the development, maintenance, and evolution of turbulence in the upper troposphere and lower stratosphere where convective and terrain-induced aviation turbulence pose a significant threat to high-altitude flying aircraft operated by the United States Air Force. Using both a convective case (12 December 2002) and mountain wave case (9 December 1992), the NHMASS model's 1.5 order PBL-based TKE scheme is compared against an explicit spatial and temporal Reynolds' averaging technique used to derived explicit turbulence diagnostics. The Reynolds'-averaging based TKE calculations, derived from explicit momentum and heat fluxes, reveals a much more detailed potential turbulence evolution as compared with the PBL-based TKE flux parameterizations. Explicit grid turbulence diagnostics are able to resolve small-amplitude gravity waves in the lower and middle stratosphere in the convective case when the mean wind shear and model TKE is low in the convective case and a shift in hydraulic jump within the PBL which is coincident with wave breaking in the lower stratosphere. The explicit grid based diagnostics are to be used in future automatic grid nesting algorithms at very fine horizontal grid spacing.

# **Numerical Modeling Studies of Multiple Aviation Turbulence Forecasting Problems in the Troposphere and Stratosphere**

by

**Chad J. Ringley**

A thesis submitted to the Graduate Faculty of  
North Carolina State University  
In partial fulfillment of the  
Requirements for the Degree of  
Master of Science

**MARINE, EARTH, AND ATMOSPHERIC SCIENCES**

Raleigh, NC

2006

**APPROVED BY:**

---

Dr. Yuh-Lang Lin  
Co-Chair of Advisory Committee

---

Dr. Michael Kaplan

---

Dr. Sethu Raman

## BIOGRAPHY

Chad J. Ringley was born on September 1<sup>st</sup>, 1981 in Abingdon, Virginia. In the fall of 1999, Chad graduated from Ervinton High School in Nora, Virginia. After spending two years at The University of Virginia's College at Wise, he transferred to the University of Oklahoma in the fall of 2001. During this time at Oklahoma, he became a professional storm chaser and spotter and participated in the Joint-Urban 2003 field project campaign in Oklahoma City, Oklahoma. He graduated with a Bachelor's of Science in Meteorology from The University of Oklahoma in August of 2004. Shortly thereafter, he enrolled in the Masters' of Science program in Atmospheric Sciences at North Carolina State University under the direction of Dr. Michael Kaplan and Dr. Yuh-Lang Lin in the Mesoscale Modeling and Dynamics Laboratory. He will officially graduate in December 2006.

## ACKNOWLEDGEMENTS

I would like to thank my committee members Dr. Michael Kaplan, Dr. Yuh-Lang Lin, and Dr. Sethu Raman for their patience, input, guidance, and encouragement. I would also like to thank NC State faculty members Dr. Gary Lackmann and Dr. S. Pal Ayra for providing helpful suggestions and analysis.

Since my thesis is composed of two different projects, I would like to thank members of the individual project teams, specifically, Dr. David W. Hamilton and Dr. Fred Proctor of NASA Langley and Dr. Doug Hahn of the AFRL. I owe large debts of gratitude to Mesolab members Paul Suffern and Dave Vollmer for their invaluable input and data for the Air Force Project, and Zach Brown for his outstanding computing contributions to the NASA project. I would like to also thank Heather Reeves, Chenjie (Christine) Huang, Michael Kiefer, Morgan Silverman, Barrett Smith, Chris Hill, and Emily Lunde for their support, input, and laughs along the way. I would also like to thank Forecasting Lab members Kelly Mahoney, Kevin Hill, Nicole Haglund and former member Dr. Michael Brennan for answering questions and providing assistance over the years.

I would like to give very special thanks to my mother Kathy, my father Ronnie, my brother Chris, my nephew Jaden and my other wonderful family members for their love and support over the years. I'd also like to thank my Aunt Rose, who helped turn my fear of weather into a lifelong fascination. Lastly, I'd like to thank my best friend and girlfriend Jessica Sanders for providing love and support and helping me make it through the research and writing process.

# TABLE OF CONTENTS

	Page
LIST OF TABLES.....	vi
LIST OF FIGURES .....	vii
<b>Chapter 1 Introduction .....</b>	<b>1</b>
<b>Chapter 2 Evaluation of Boundary-Layer Turbulence Profiles for the Development of a Statistically-Based Wake Vortex Forecasting Algorithm.....</b>	<b>4</b>
<b>1. Introduction.....</b>	<b>4</b>
<b>2. Motivation and Methodology.....</b>	<b>9</b>
2.1 TAPPS-2 Model Configuration.....	9
2.2: Post-Processing and Validation Techniques .....	11
<b>3. Dallas-Fort Worth International Airport Validation Simulations.....</b>	<b>16</b>
3.1: Introduction and Synoptic-Scale Flow.....	16
3.2 TAPPS-2 Validation Simulations (17-19 September 1997) .....	21
3.2.1: Analysis Introduction.....	21
3.2.2: Model TKE and EDR Point Validation: 00 UTC Simulations .....	23
3.2.3: Model TKE and EDR Point Validation: 12 UTC Simulations .....	29
3.2.4: TAPPS-2 Multi-Variable Sounding Analysis.....	34
3.2.5: TAPPS-2 Crosswind Velocity Sensitivity Test.....	47
<b>4. Eddy Dissipation Rate Sensitivity: DFW Validation Simulations .....</b>	<b>52</b>
4.1: Introduction.....	52
4.2: Sensitivity Experiment Design.....	54
4.3: EDR Formulation Sensitivity Results .....	56
<b>5. Conclusions .....</b>	<b>65</b>
<b>6. Acknowledgements.....</b>	<b>75</b>
<b>7. References .....</b>	<b>77</b>
<b>Chapter 3 Investigations of Numerically-Simulated Turbulence Diagnostics in the Upper Troposphere and Lower Stratosphere.....</b>	<b>163</b>
<b>1. Introduction.....</b>	<b>163</b>
<b>2. Observational Overview of Case Studies .....</b>	<b>171</b>
2.1: 12 December 2002 Convective Case .....	171

2.2 9 December 1992 Mountain Wave Case.....	177
<b>3. Experimental Design and Methodology .....</b>	<b>180</b>
3.1: Numerical Model Configuration.....	180
3.2: The TKE Budget and Explicit Calculations .....	183
<b>4. 12 December 2002 Convective Case Study Results .....</b>	<b>190</b>
4.1 NH-MASS Coarse Grid (MASS18C, MASS6C) Summary .....	190
4.2: Deep Moist Convection within the MASS2C Simulation.....	195
4.3: Fine-Grid Individual Convective Cell Evolution .....	198
4.3.1: MASS667C Simulation Results: Texas and Louisiana Convective Cells....	198
4.3.2: MASS222C Simulation Results: Texas Convective Cells .....	202
4.4 Model-Derived Turbulence Characteristics in the Stratosphere .....	204
4.5: Explicit Grid-Based Turbulence Experiments .....	210
4.5.1: Introduction .....	210
4.5.2: Temporal Reynolds' Averaging Results .....	212
4.5.3: Spatial Reynolds' Averaging Results: Flux Contributions .....	214
4.5.3: Spatial Reynolds' Averaging Results: MASS667C Investigation .....	219
4.5.3.1: MASS667C Explicitly Calculated Horizontal Advection Terms .....	220
4.5.3.2: Explicitly Calculated Production Terms.....	223
4.5.3.3: Turbulent Transport and Pressure Perturbation Contributions .....	232
<b>5. 9 December 1992 Mountain Wave Case Results .....</b>	<b>234</b>
5.1 9 December 1992 NH-MASS Simulation Introduction .....	234
5.2 9 December 1992 MASS2M/MASS667M Explicit Turbulence Diagnostics.....	236
5.3 9 December 1992 MASS222M Explicit Turbulence Diagnostics .....	243
<b>6. Conclusions .....</b>	<b>247</b>
<b>7. Acknowledgements.....</b>	<b>253</b>
<b>8. References .....</b>	<b>254</b>

## LIST OF TABLES

	Page
<b>Chapter 2. Evaluation of Boundary Layer Turbulence Profiles for the Development of a Statistically-Based Wake Vortex Forecasting Algorithm</b>	
Table 1: Comparisons of TAPPS-1 and TAPPS-2 model configurations. Dashes are used to represent the absence of a “super-fine” 1-kilometer grid mesh in TAPPS 1. TAPPS-1 details from Kaplan et al. (2000).....	79
Table 2a: Basic validation statistics for the 00 UTC simulations from 17-20 September 1997, generated using the SAS Statistics program. TKE units are $m^2s^{-2}$ and EDR units are $m^2s^{-3}$ .....	80
Table 2b: As with Table 2a, but for the 12 UTC Simulations.....	80
Table 3: Summary of observed variables as a function of model simulation for the NASA validation simulations. The black bars indicate the simulation time period in which the statistics are valid.....	81
Table 4: Comparisons of model sigma distributions between the 60-level version used in TAPPS-1 and the 36km grid mesh in TAPPS-2 and the new 90-level version used in the 6 and 1 km grid mesh in TAPPS-2. Note that model layer 1, by definition, is $\sigma = \tilde{1}$ .....	82
Table 5: Characteristic Length Scale statistics showing the base 4-day time average, the adjusted moving average (with values less than the nighttime mean set to the nighttime mean), and the resultant Gaussian redistribution of the characteristic length scale.....	83

## LIST OF FIGURES

### Chapter 2. Evaluation of Boundary Layer Turbulence Profiles for the Development of a Statistically-Based Wake Vortex Forecasting Algorithm

Figure 1: 17 NHMASS 36 km simulation four panel plot of 250 hPa (left panel) and 500 hPa (right panel) winds and geopotential height at (a), (b) 12 UTC 17 September 1997 and (c), (d) 12 UTC 18 September 1997. ....	85
Figure 2: As with Fig. 1, but for 850 hPa winds and geopotential height at (a) 06 UTC (b) 12 UTC 17 September 1997 and (c) 06 UTC and (d) 12 UTC 18 September 1997. ....	86
Figure 3: As with Fig. 2, but for 850 hPa (a) 00 UTC , (b) 06 UTC 19 September 1997 and (c) 09 UTC, (d) 12 UTC 19 September 1997. ....	87
Figure 4: NHMASS 36 km four panel plot of 850 hPa of heights and winds valid (a) 0700 UTC; (b) 0730 UTC; (c) 0800 UTC; (d) 0830 UTC 18 September 1997. ....	88
Figure 5: NHMASS 36 km four panel plot of 850 hPa of heights and winds valid (a) 0700 UTC; (b) 0730 UTC; (c) 0800 UTC; (d) 0830 UTC 19 September 1997. ....	89
Figure 6: 17 NHMASS 36 km from 00-00 UTC 17-18 September 1997 (17_36_00) time series plot of 5/15 and 40 m TKE vs. time from the model simulation and AVOSS tower data.....	90
Figure 7: As with Fig. 7, but for 00-00 UTC 18-19 September 1997. ....	91
Figure 8: As with Fig. 7, but for 00-00 UTC 18-19 September 1997. ....	92
Figure 9: Histogram plots of TKE values from 00 UTC NHMASS simulations using (a) Observations; and (b) 36 km grid resolution from point statistics taken at the DFW runway over the three-four day validation period. ....	93
Figure 10: 17 NHMASS 6 km from 00-00 UTC 17-18 September 1997 (17_36_00) time series plot of 5/15 and 40 m TKE vs. time from the model simulation and AVOSS tower data.....	94
Figure 11: As with Fig. 10, but for 00-00 UTC 18-19 September 1997. ....	95
Figure 12: As with Fig. 11, but for 00-00 UTC 19-20 September 1997. ....	96

Figure 13: As with Fig. 9, but for (a) Observations, (b) 6 km grids and (c) 1 km grids.....97

Figure 14: 17 NHMASS 1 km from 00-00 UTC 17-18 September 1997 (17\_36\_00) time series plot of 5/15 and 40 m TKE vs. time from the model simulation and AVOSS tower data.....98

Figure 15: As with Fig. 14, but for 00-00 UTC 18-19 September 1997.....99

Figure 16: As with Fig. 15, but for 00-00 UTC 18-19 September 1997.....100

Figure 17: Sensitivity to initialization structure comparing the 30-min “spin” runs against observations (AVOSS) and from continuously integrated 6 and 1 km runs valid from 17\_06\_00 from 12 UTC-18 UTC 17 September 1997.....101

Figure 18: 17 NHMASS 36 km from 00-00 UTC 17-18 September 1997 (17\_36\_00) time series plot of 5/15 and 40 m eddy dissipation rate (EDR, log scale) vs. time from the model simulation and AVOSS tower data.....102

Figure 19: As with Fig. 18, but for 00-00 UTC 18-19 September 1997.....103

Figure 20: As with Fig. 19, but for 00-00 UTC 18-19 September 1997.....104

Figure 21: 17 NHMASS 6 km from 00-00 UTC 17-18 September 1997 (17\_6\_00) time series plot of 5/15 and 40 m eddy dissipation rate (EDR, log scale) vs. time from the model simulation and AVOSS tower data.....105

Figure 22: As with Fig. 21, but for 00-00 UTC 18-19 September 1997.....106

Figure 23: As with Fig. 22, but for 00-00 UTC 19-20 September 1997.....107

Figure 24: As with Fig. 20, but for 1-km (17\_01\_00) valid 00-00 UTC 17-18 September 1997.....108

Figure 25: 17 NHMASS 36 km from 12-12 UTC 17-18 September 1997 (17\_36\_00) time series plot of 5/15 and 40 m TKE vs. time from the model simulation and AVOSS tower data.....109

Figure 26: As with Fig. 25, but for 00-00 UTC 18-19 September 1997.....110

Figure 27: As with Fig. 26, but for 00-00 UTC 18-19 September 1997.....111

Figure 28: 17 NHMASS 6 km from 12-12 UTC 17-18 September 1997 (17\_36\_00) time series plot of 5/15 and 40 m TKE vs. time from the model simulation and AVOSS tower data.....112

Figure 29: As with Fig. 28, but for 12-12 UTC 18-19 September 1997. ....	113
Figure 30: As with Fig. 29, but for 12-12 UTC 19-20 September 1997. ....	114
Figure 31: 17 NHMASS 1 km from 12-12 UTC 18-19 September 1997 (18_36_00) time series plot of 5/15 and 40 m TKE vs. time from the model simulation and AVOSS tower data. ....	115
Figure 32: NHMASS 36 km from 12-12 UTC 17-18 September 1997 (17_36_12) time series plot of 5/15 and 40 m eddy dissipation rate (EDR, log scale) vs. time from the model simulation and AVOSS tower data. ....	116
Figure 33: As with Fig. 32, but for 00-00 UTC 18-19 September 1997. ....	117
Figure 34: As with Fig. 33, but for 00-00 UTC 18-19 September 1997. ....	118
Figure 35: 17 NHMASS 6 km from 12-12 UTC 17-18 September 1997 (17_06_12) time series plot of 5/15 and 40 m eddy dissipation rate (EDR, log scale) vs. time from the model simulation and AVOSS tower data. ....	119
Figure 36: As with Fig. 35, but for 00-00 UTC 18-19 September 1997. ....	120
Figure 37: As with Fig. 36, but for 00-00 UTC 19-20 September 1997. ....	121
Figure 38: Temperature sounding evolution from 17_36_00 valid 12-21 UTC 17 September 1997 plotted at 3-hr intervals. ....	122
Figure 39: Crosswind (u) wind sounding evolution from 18_36_00 valid 00-12 UTC 18 September 1997 plotted at 3-hr intervals. In addition, observations from the FWD radar are plotted at 00 and 03 UTC (color match). ....	123
Figure 40: Headwind (v) wind sounding evolution from 18_36_00 valid 00-12 UTC 18 September 1997 plotted at 3-hr intervals. In addition, observations from the FWD radar are plotted at 00 and 03 UTC (color match). ....	124
Figure 41: Temperature sounding evolution from 18_36_00 valid 00-12 UTC 18 September 1997 plotted at 3-hr intervals. ....	125
Figure 42: TKE sounding evolution from 18_36_00 valid 00-12 UTC 18 September 1997 plotted at 3-hr intervals from the surface to 500 m, near the height of the DLLJ. ....	126
Figure 43: EDR sounding evolution from 18_36_00 valid 00-12 UTC 18 September 1997 plotted at 3-hr intervals from the surface to 500 m, near the height of the DLLJ. ....	127

Figure 44: Headwind (v) wind sounding evolution from 17_06_00 valid 00-12 UTC 17 September 1997 plotted at 3-hr intervals.....	128
Figure 45: Temperature sounding evolution from 17_06_00 valid 00-12 UTC 17 September 1997 plotted at 3-hr intervals. ....	129
Figure 46: TKE sounding evolution from 17_06_00 valid 00-12 UTC 17 September 1997 plotted at 3-hr intervals. ....	130
Figure 47: EDR sounding evolution from 17_06_00 valid 00-12 UTC 17 September 1997 plotted at 3-hr intervals. ....	131
Figure 48: Vertical sounding evolution of vertical velocity (w) from 18_36_00 valid 12-00 UTC 18 September 1997 plotted at 3-hr intervals.....	132
Figure 49: Crosswind (u) wind sounding evolution from 17_36_12 valid 00-12 UTC 18 September 1997 plotted at 3-hr intervals. In addition, observations from the FWD radar are plotted at 00 and 03 UTC (color match). ....	133
Figure 50: Crosswind (u) wind sounding evolution from 18_06_00 valid 00-12 UTC 18 September 1997 plotted at 3-hr intervals.....	134
Figure 51: Crosswind (u) wind sounding evolution from 18_06_00 valid 00-12 UTC 18 September 1997 plotted at 3-hr intervals, with a color coordinated comparison to the PLNO soundings taken near the time plotted in the model simulations (lighter colors). ....	135
Figure 52: Crosswind (u) wind sounding evolution from 17_06_12 valid 00-12 UTC 18 September 1997 plotted at 3-hr intervals, with a color coordinated comparison to the PLNO soundings taken near the time plotted in the model simulations (lighter colors). ....	136
Figure 53: Temperature sounding evolution from 17_06_12 valid 00-12 UTC 18 September 1997 plotted at 3-hr intervals. ....	137
Figure 54: Temperature sounding evolution from 18_36_12 valid 00-12 UTC 19 September 1997 plotted at 3-hr intervals. ....	138
Figure 55: Crosswind (u) wind sounding evolution from 18_36_12 valid 00-12 UTC 19 September 1997 plotted at 3-hr intervals.....	139
Figure 56: Temperature sounding evolution from 18_06_12 valid 00-12 UTC 19 September 1997 plotted at 3-hr intervals. The temperature profile from 08 UTC at PLNO is also included.....	140

Figure 57: Crosswind (u) wind sounding evolution from 18_36_12 valid 00-12 UTC 19 September 1997 plotted at 3-hr intervals.....	141
Figure 58: Crosswind (u) wind sounding evolution from 18_06_12 valid 00-12 UTC 18 September 1997 plotted at 3-hr intervals, with a color coordinated comparison to the PLNO soundings taken near the time plotted in the model simulations (lighter colors). .....	142
Figure 59: Temperature sounding evolution from 19_36_00 valid 00-12 UTC 19 September 1997 plotted at 3-hr intervals. ....	143
Figure 60: As with Fig. 59, but for 19_06_00. ....	144
Figure 61: Crosswind (u) wind sounding evolution from 19_36_00 valid 00-12 UTC 19 September 1997 plotted at 3-hr intervals.....	145
Figure 62: As with Fig. 61, but for 19_06_00. ....	146
Figure 63: TKE sounding evolution from 18_06_12 valid 00-12 UTC 17 September 1997 plotted at 3-hr intervals. Note the secondary increase of TKE above 1.5 km at 09 UTC in association with a secondary cross-wind maximum at 1.5 km. ....	147
Figure 64: 18_36_12_CTRL (a) and 18_36_12_TST (b) 3-hr nocturnal inversion evolution from 00-12 UTC 19 September 1997. Note that while both profiles have similar curves between 00-03 UTC, the 90-level 18_36_12_TST simulation develops a stronger inversion faster than the CTRL. ....	148
Figure 65: 18_36_12_CTRL (a) and 18_36_12_TST (b) 3-hr headwind velocity soundings from 00-12 UTC 19 September 1997. ....	149
Figure 66: 18_36_12_CTRL (a) and 18_36_12_TST (b) 3-hr crosswind velocity soundings from 00-12 UTC 19 September 1997. ....	150
Figure 67: 850 hPa temperature (color fill) and winds from 17_36_12 and 18_06_00 valid 06 UTC 18 September 1997 across the Southern Plains. Note that the temperature gradient northwest of DFW is oriented east to west, particularly in 18_06_00.....	151
Figure 68: As with Fig. 67, but for (a) 08 UTC 19 September from 18_06_12 and (b) 08 UTC 20 September 1997 from 19_06_12. Note the shift in temperature gradient at 850 h-Pa to a more north to south orientation, coincident with the veering LLJ. ....	152

Figure 69: Derived characteristic mixing length  $\Lambda$  at 40 meters from AVOSS tower observations (light blue curve) and (a) 36 km 00 UTC simulations and (b) 36 km 12 UTC simulations, valid 17-21 September 1997..... 153

Figure 70: Derived characteristic mixing length  $\Lambda$  at 40 meters from AVOSS tower observations (light blue curve) and (a) 6 km 00 UTC simulations and (b) 6 km 12 UTC simulations, valid 17-21 September 1997..... 154

Figure 71: Derived characteristic mixing length  $\Lambda$  soundings from 18\_06\_12 for (a) 12-00 UTC and (b) 00-12 UTC 19 September 1997..... 155

Figure 72: Gaussian cumulative distribution function showing the characteristic mixing length  $\Lambda$  used to produce GAUSS EDR values. .... 156

Figure 73: EDR sensitivity time-series plots for 17\_36\_12 valid 00-12 18 September for the observed values (blue circles), NOWVIV (pink squares), MASS (yellow triangles), and GAUSS (black circles)..... 157

Figure 74: EDR sensitivity time-series plots for 18\_36\_12 valid 00-12 19 September for the observed values (blue circles), NOWVIV (pink squares), MASS (yellow triangles), and GAUSS (black circles)..... 158

Figure 75: EDR sensitivity time-series plots for 19\_36\_12 valid 00-12 20 September for the observed values (blue circles), NOWVIV (pink squares), MASS (yellow triangles), and GAUSS (black circles)..... 159

Figure 76: EDR sensitivity time-series plots for 17\_06\_12 valid 00-12 18 September for the observed values (blue circles), NOWVIV (pink squares), MASS (yellow triangles), and GAUSS (black circles)..... 160

Figure 77: EDR sensitivity time-series plots for 18\_06\_12 valid 00-12 19 September for the observed values (blue circles), NOWVIV (pink squares), MASS (yellow triangles), and GAUSS (black circles)..... 161

Figure 78: EDR sensitivity time-series plots for 19\_06\_12 valid 00-12 20 September for the observed values (blue circles), NOWVIV (pink squares), MASS (yellow triangles), and GAUSS (black circles)..... 162

### **Chapter 3. Investigations of Numerically-Simulated Turbulence Diagnostics in the Upper Troposphere and Lower Stratosphere**

Figure 1: NARR Reanalysis valid 1200 UTC 12 December 2002: 300 h-Pa wind (m/s), isotachs (colored) and height (m). State outlines in dark red, with the region of interest in far Southeast Texas and Southwest Louisiana..... 259

Figure 2: Plymouth State Weather Center archived standard surface data plot valid 1200 UTC 12 December 2002 in the Southern Plains. The strong stable layer north of the warm front is noted along the Texas Coast..... 260

Figure 3: Google Earth composite plot of GPS microbarogram maximum 6-hr pressure falls associated with the large amplitude gravity wave 1200-1900 UTC 12-13 December 2002. Times marked with a \* indicated observations ending on 13 December 2002. .... 261

Figure 4: Four-panel plot of GPS microbarogram traces of pressure vs. time following gravity wave features valid 12 UTC-12 UTC 12-14 December 2002 from (a) Houston (HOU), TX; (b) Ledbetter (LED), TX; (c) Palestine (PAL), TX; and (d) Lafayette (LAF), LA..... 262

Figure 5: NOAA NWS Level-III Base Reflectivity radar data from Houston, TX valid (a) 1603 UTC (b) 1703 UTC 12 December 2002..... 263

Figure 6: Four-panel plot of NOAA NWS Level-II Base Reflectivity from Lake Charles, LA (LCH) valid at (a) 2201 UTC; (b) 2220 UTC; (c) 2242 UTC; (d) 2302 UTC, showing the erosion of precipitation north and south of the warm front behind the primary squall line. .... 264

Figure 7: NOAA NWS Level-II Tilt-2 Spectrum Width (velocity variance) from Lake Charles, LA (LCH) radar valid (a) 2151 UTC; (b) 2201 UTC 12 December 2002. The gravity wave signal is south of the warm frontal boundary and northwest of the radar location..... 265

Figure 8: Four-panel plot of NOAA FSL Profiler data from 12-13 December 2002 from (a) vertical wind profile from PAL; (b) horizontal velocity variance from PAL; (c) as with (a), but for LED; (d) as with (b), but for LED. Time positioned from right to left..... 266

Figure 9: AMSU satellite data plots of virtual potential temperature fluctuations valid ~13 UTC 12 December 2002 for (a) Channel 9 (~90 hPa) and (b) Channel 10 (~60 hPa)..... 267

Figure 10: As with Fig. 9, but for ~20 UTC in (a) Channel 9 (~90 hPa) and (b) Channel 10 (~60 hPa)..... 268

Figure 11: Adapted from Clark et al. (2000), a cross-section through the accident location (indicated by the time and star) of pilot reports of turbulence, lidar position, and lidar-indicated flow reversal region, tropopause and surface topography from 9 December 1992 (Vollmer et al. (2006))...... 269

Figure 12: NWS routine radiosondes from (a) Denver, CO (DEN) and (b) Grand Junction, CO (GJT) valid 12 UTC 9 December 1992. Note the pronounced warming in the lower stratosphere in both soundings. Data courtesy of sounding archives at The University of Wyoming. .... 270

Figure 13: Range-Height Indicator (RHI) plot of radial velocity from NOAA ERL/ETL lidar at Table Mountain Colorado, valid 16 UTC 9 December 1992. Note the reversal of flow within the lower stratosphere ~10 km east and ~10 km above the lidar. Adapted from Ralph et al. (1997). .... 271

Figure 14: NHMASS fine resolution simulations for 9 December 1992 case, shown in the following order: 2 km is the outer portion (white), followed by 667 m (green hatch), 222 m (green), 71 m (bright green). From Ringley et al. (2005). 272

Figure 15: MASS18C 300-hPa winds (barbs), isotachs (color fill), and heights (contoured) valid (a) 0000 UTC; (b) 1200 UTC; (c) 1900 UTC 12 December 2002 and (d) 0000 UTC 13 December 2002. .... 273

Figure 16: MASS6C accumulated precipitation (mm) valid (a) 1330 UTC; (b) 1430 UTC; (c) 1530 UTC; (d) 1630 UTC, showing the development of individual convective cells in the Texas Hill Country prior to the development of a strong linear convective system. .... 274

Figure 17: MASS6C 300 hPa winds (barbs), isotachs (color fill) and heights (white contours) valid (a) 1330 UTC; (b) 1430 UTC; (c) 1530 UTC; (d) 1630 UTC, showing the development of a significant upstream wind maxima over Northern Texas and Southern Oklahoma. .... 275

Figure 18: MASS6C cross-sections of isotachs (color fill) and isentropes (white contours) valid (a) 1400 UTC; (b) 1500 UTC; (c) 1600 UTC; (d) 1700 UTC, illustrating the impact of convective bursts within MASS6C on the stratosphere. .... 276

Figure 19: MASS6C NCSU1 turbulence index (color fill) at 90 hPa valid (a) 1800 UTC; (b) 1900 UTC; (c) 2000 UTC; (d) 2100 UTC, showing the region of enhanced NCSU1 in far southeast Texas responsible for triggering the 2-km autonest. .... 277

Figure 20: MASS2C composite plots of model-derived TKE (left panel) and model-derived reflectivity (right panel) and wind at 250-m MMSL valid (a) 2100 UTC; (b) 2130 UTC; (c) 2200 UTC; (d) 2230 UTC 12 December 2002. .... 278

Figure 21: As with Fig. 20, but for 10-km MMSL valid (a) 2245 UTC; (b) 2300 UTC; (c) 2315 UTC; (d) 2330 UTC 12 December 2002. .... 279

Figure 22: MASS2C composite plots of divergence (left panel) and mixing ratio (right panel) and wind at 10 km MMSL valid (a) 2245 UTC; (b) 2300 UTC; (c) 2315 UTC; (d) 2330 UTC 12 December 2002. .... 280

Figure 23: As with Fig. 21, but valid (a) 2345 UTC; (b) 0000 UTC; (c) 0015 UTC; (d) 0030 UTC 12-13 December 2002. .... 281

Figure 24: As with Fig. 22, but valid (a) 2345 UTC; (b) 0000 UTC; (c) 0015 UTC; (d) 0030 UTC 12-13 December 2002. .... 282

Figure 25: MASS667C composite plots of model-derived TKE (left panel) and model-derived reflectivity (right panel) and wind at 250-m MMSL valid (a) 2206 UTC; (b) 2209 UTC; (c) 2212 UTC; (d) 2215 UTC 12 December 2002. .... 283

Figure 26: As with Fig. 25, but for 8km MMSL valid (a) 2206 UTC; (b) 2209 UTC; (c) 2212 UTC; (d) 2215 UTC 12 December 2002. .... 284

Figure 27: As with Fig. 26, but valid (a) 2233 UTC; (b) 2239 UTC; (c) 2245 UTC; (d) 2251 UTC 12 December 2002. .... 285

Figure 28: Model TKE and reflectivity at (a) 2245 and (b) 2303 UTC 12 December, and grid accumulated precipitation at (c) 2245 UTC; (d) 2303 UTC 12 December 2002. .... 286

Figure 29: As with Fig. 27, but valid (a) 2321 UTC; (b) 2330 UTC; (c) 2339 UTC; (d) 2348 UTC 12 December 2002. .... 287

Figure 30: MASS222C composite plots of model-derived TKE (left panel) and model-derived reflectivity (right panel) and wind at 250-m MMSL valid (a) 2218 UTC; (b) 2220 UTC; (c) 2222 UTC; (d) 2224 UTC 12 December 2002. .... 288

Figure 31: As with Fig. 30, but for 8km MMSL valid (a) 2218 UTC; (b) 2220 UTC; (c) 2222 UTC; (d) 2224 UTC 12 December 2002. .... 289

Figure 32: As with Fig. 31, but for 8km MMSL valid (a) 2243 UTC; (b) 2245 UTC; (c) 2247 UTC; (d) 2249 UTC 12 December 2002. .... 290

Figure 33: MASS667C MMSL crosssections of model derive TKE (color fill) and virtual potential temperature (green contours) from 250m-20km at (a) 2212 UTC; (b) 2227 UTC; (c) 2239 UTC; (d) 2248 UTC 12 December 2002. .... 291

Figure 34: MASS667C four-panel plot (color fill) of scaled model-parameterized u-momentum (top left), v-momentum (top right), heat (bottom left) and TKE (bottom right) flux at 8 km valid (a) 2212 UTC; (b) 2300 UTC 12 December 2002. 292

Figure 35: As with Fig. 34, but for 14 kilometers valid (a) 2212 UTC; (b) 2300 UTC 12 December 2002. .... 293

Figure 36: MASS667C NCSU1 turbulence index (left panel ) and divergence (right panel) valid (a) 2212 UTC; (b) 2227 UTC; NCSU2 turbulence index (left panel) and divergence (right panel) valid (c) 2212 UTC; (d) 2239 UTC 12 December 2002. .... 294

Figure 37: MASS667C NCSU1 turbulence index (left panel ) and divergence (right panel) valid (a) 2248 UTC; (b) 2254 UTC; (c) 2300 UTC; (d) 2306 UTC 12 December 2002. .... 295

Figure 38: MASS667C 30-hPa winds (barbs), isotachs (color fill) and heights (black contours) associated with each deep convective burst valid (a) 2230 UTC; (b) 2334 UTC 12 December 2002. .... 296

Figure 39: MASS667C temporally-averaged u-wind velocity (color fill), and virtual potential temperature (green contours) from 250n-22 km valid (a) 2227 UTC; (b) 2257 UTC; (c) 2327 UTC; (d) 2357 UTC 12 December 2002. .... 297

Figure 40: MASS667C temporally-derived u-wind velocity perturbations (color fill), and virtual potential temperature (green contours) from 250n-22 km valid (a) 2227 UTC; (b) 2230 UTC; (c) 2327 UTC; (d) 2330 UTC 12 December 2002. Note the dramatic shift in flux contribution because of a shift in the temporal average. .... 298

Figure 41: MASS667C two-panel plots of model parameterized u-momentum flux (left panel) and spatially-derived explicit u-momentum flux valid (right panel) valid (a) 2242 UTC; (b) 2248 UTC; (c) 2254 UTC; (d) 2300 UTC 12 December 2002. .... 299

Figure 42: MASS667C two-panel plots of model parameterized u-momentum flux (left panel) and spatially-derived explicit u-momentum flux valid (right panel) valid 2257 UTC 12 December 2002 at (a) 10km; (b) 12km; (c) 14km; (d) 16km MMSL. .... 300

Figure 43: As with Fig. 42, but for 14 km valid (a) 2227 UTC; (b) 2230 UTC 12 December 2002. .... 301

Figure 44: MASS222C four-panel plot (color fill) of scaled model-parameterized u-momentum (top left), v-momentum (top right), heat (bottom left) and TKE

(bottom right) flux at 8 km valid (a) 2241 UTC; (b) 2244 UTC 12 December 2002.  
..... 302

Figure 45: MASS667C explicit grid-based turbulence diagnostics valid 2239 UTC  
12 December 2002 for Term 1: U-Advection at (a) 8km; (b) 12km; and for Term  
2: V-Advection, for (c) 8km; (d) 12km MMSL. .... 303

Figure 46: MASS667C cross-section through Orange County, TX convection of  
Term 1- U-Mechanical Shear (color fill), wind (barbs) and virtual potential  
temperature (contoured) valid (a) 2233 UTC; (b) 2236 UTC; (c) 2239 UTC; (d)  
2242 UTC 12 December 2002. .... 304

Figure 47: As with Fig. 46, but for Term 2: V-Advection, valid (a) 2233 UTC; (b)  
2236 UTC; (c) 2239 UTC; (d) 2242 UTC 12 December 2002. .... 305

Figure 48: As with Fig. 47, but for Term 3: W-Advection, valid (a) 2233 UTC; (b)  
2236 UTC; (c) 2239 UTC; (d) 2242 UTC 12 December 2002. .... 306

Figure 49: MASS667C explicit grid-based turbulence diagnostics valid 2239 UTC  
12 December 2002 for Term 4: Buoyancy Production at 8 km for (a) 2236 UTC;  
(b) 2239 UTC; (c) 2242 UTC; (d) 2245 UTC 12 December 2002..... 307

Figure 50: MASS667C explicit grid-based turbulence diagnostics for Term 5: U-  
Mechanical Shear (color fill) and u-wind shear (solid positive, dash negative  
contours) for 8 km at (a) 2239; (b) 2245 UTC; and 12 km at (c) 2239 UTC; (d)  
2245 UTC 12 December 2002. .... 308

Figure 51: As with Fig. 50, but for Term 5-2: V-Mechanical Shear and v-wind  
shear for (a) 2239 UTC; (b) 2245 UTC at 8 km and (c) 2239 UTC; (d) 2245 UTC  
12 December 2002 at 12 km..... 309

Figure 52: MASS667C cross-section through Orange County, TX convection of  
Term 4- Buoyancy (color fill), wind (barbs) and virtual potential temperature  
(contoured) valid (a) 2233 UTC; (b) 2236 UTC; (c) 2239 UTC; (d) 2242 UTC 12  
December 2002. .... 310

Figure 53: As with Fig. 52, but for Term 5- U-Mechanical Shear, valid (a) 2233  
UTC; (b) 2236 UTC; (c) 2239 UTC; (d) 2242 UTC 12 December 2002. .... 311

Figure 54: As with Fig. 53, but for Term 5-2 V-Mechanical Shear, valid (a) 2233  
UTC; (b) 2236 UTC; (c) 2239 UTC; (d) 2242 UTC 12 December 2002. .... 312

Figure 55: MASS667C Term 5 U-Mechanical Shear at 12 km valid (a) 2303 UTC;  
(b) 2315 UTC; and Term 5-2 V-Mechanical at 12km valid (c) 2303 UTC; (d) 2315  
UTC 12 December 2002. .... 313

Figure 56: MASS667C cross-section through Beauregard Parish, LA convection of Term 4- Buoyancy (color fill), wind (barbs) and virtual potential temperature (contoured) valid (a) 2324 UTC; (b) 2330 UTC; (c) 2336 UTC; (d) 2342 UTC 12 December 2002. ....314

Figure 57: As with Fig. 56, but for V-Mechanical Shear, valid (a) 2324 UTC; (b) 2330 UTC; (c) 2336 UTC; (d) 2342 UTC 12 December 2002. ....315

Figure 58: MASS667CBuoyancy Production at 14 km valid (a) 2336 UTC; (b) 2342 UTC; and for V-Mechanical Shear Production (contour filled) and v-wind shear (contoured) at 14 km valid (c) 2336 UTC; (d) 2342 UTC 12 December 2002. ....316

Figure 59: MASS667C Buoyancy Production at 18 km valid (a) 2339 UTC; (b) 2351 UTC; and for U-Mechanical Shear Production (color fill) and wind shear (countoured) at 18 km valid (c) 2339 UTC; (d) 2351 UTC 12 December 2002. 317

Figure 60: MASS667C Term 6: Turbulent Transport at 8 km valid (a) 2339 UTC; (b) 2351 UTC; and for Term 7: Pressure Perturbations at 8 km valid (c) 2339 UTC; (d) 2351 UTC 12 December 2002. ....318

Figure 61: MASS2M 10 km model-derived TKE (left panel) and divergence (right panel) valid (a) 1445 UTC; (b) 1454 UTC; (c) 1503 UTC; (d) 1512 UTC 9 December 1992. ....319

Figure 62: As with Fig. 61, but for 14 km valid (a) 1445 UTC; (b) 1454 UTC; (c) 1503 UTC; (d) 1512 UTC 9 December 1992. ....320

Figure 63: MASS667M model-parameterized u-momentum flux (left panel) versus explicit u-momentum flux (right panel) at 11.5 km valid (a) 1445 UTC; (b) 1454 UTC; (c) 1503 UTC; (d) 1512 UTC 9 December 1992. ....321

Figure 64: As with Fig. 63, but for v-momentum flux at 11.5 km valid (a) 1445 UTC; (b) 1454 UTC; (c) 1503 UTC; (d) 1512 UTC 9 December 1992. ....322

Figure 65: As with Fig. 63, but for v-momentum flux at 11.5 km valid (a) 1445 UTC; (b) 1454 UTC; (c) 1503 UTC; (d) 1512 UTC 9 December 1992. ....323

Figure 66: Physical map of the state of Colorado with county boundaries, highlighting the region of interest in the 9 December 1992 mountain wave study. Image courtesy geology.com. ....324

Figure 67: MASS667M explicit grid based turbulence diagnostics for Term 1: U-Advection at 9.75 km valid (a) 1445 UTC; (b) 1515 UTC; and for Term 2: V-Advection at 9.75 km valid (c) 1445 UTC; (d) 1515 UTC 9 December 1992....325

Figure 68: MASS667M explicit grid based turbulence diagnostics for Term 4: Buoyancy Production at 9.75 km valid (a) 1445 UTC; (b) 1500 UTC;..... 326

Figure 69: As with Fig. 68, but for Term 5: U-Mechanical Shear Production at 9.75 km valid (a) 1445 UTC; (b) 1500 UTC; ..... 327

Figure 70: As with Fig. 69, but for Term 5-2: V-Mechanical Shear Production at 9.75 km valid (a) 1445 UTC; (b) 1500 UTC; ..... 328

Figure 71: As with Fig. 70, but for Term 4: Buoyancy Production at 14 km valid (a) 1445 UTC; (b) 1500 UTC; ..... 329

Figure 72: MASS667M cross-Section through transient features in the Palmer Divide of Term 4: Buoyancy Production valid (a) 1451 UTC; (b) 1457 UTC; (c) 1503 UTC; (d) 1509 UTC 9 December 1992. Note the wave propagating through the unstable layer between 13.5-15.5 km. .... 330

Figure 73: MASS222M Cross-Section through the accident location of Term 1: U-Advection (color fill) and virtual potential temperature (contoured) valid (a) 1458 UTC; (b) 1500 UTC; (c) 1502 UTC; (d) 1504 UTC 9 December 1992. .... 331

Figure 74: As with Fig. 73, but for Term 4: Buoyancy production valid (a) 1505 UTC; (b) 1510 UTC; (c) 1515 UTC; (d) 1520 UTC 9 December 1992. .... 332

Figure 75: As with Fig. 74, but for Term 5: U-Mechanical shear production valid (a) 1505 UTC; (b) 1510 UTC; (c) 1515 UTC; (d) 1520 UTC 9 December 1992. .... 333

Figure 76: As with Fig. 75, but for Term 5-2: V-Mechanical shear production valid (a) 1505 UTC; (b) 1510 UTC; (c) 1515 UTC; (d) 1520 UTC 9 December 1992. .... 334

Figure 77: MASS222M cross-section of vertical velocity (W, color fill) with positive (negative) in warm (cool) colors and isentropes (contoured) valid (a) 1455 UTC; (b) 1500 UTC; (c) 1505 UTC; (d) 1510 UTC 9 December 1992. .... 335

Figure 78: MASS667M cross-section of TKE (color fill) and isentropes (contoured) valid (a) 1455 UTC; (b) 1500 UTC; (c) 1505 UTC; (d) 1510 UTC 9 December 1992. .... 336

## 1. Introduction

This thesis is composed of papers derived from two separate projects designed to investigate important aspects and problems in turbulence evolution and forecasting in aviation meteorology. The first paper explores the validation of a new modeling system for use in developing a low-level wind climatology for the boundary layer turbulence forecasting in conjunction with the National Aeronautics and Space Administration (NASA) Terminal Area Productivity Program (TAP). The second paper investigates the turbulence generation and evolution as a function of forcing in the upper troposphere and lower stratosphere in conjunction with the United States Air Force Research Laboratory.

In the first paper, a new version of the Terminal Area PBL Prediction System (TAPPS) model is implemented to simulate low-level winds, turbulent kinetic energy (TKE) and eddy dissipation rate (EDR) profiles on a quasi-climatological scale in order to develop a statistically-based wake vortex forecasting tool for air-traffic controllers. A series of TAPPS simulations are validated against tower observations from the Aircraft Vortex Observing and Sampling System (AVOSS) at the Dallas-Fort Worth International Airport from the 17-20 September 1997 intense observing periods (IOPs). Various model sensitivity tests, including horizontal grid resolution, sigma layer distributions, and model initialization times are performed over the 4 day period. Evaluation of various turbulence diagnostics in the vertical are presented, and results of model sensitivity tests to the formation of diurnally-forced low-level jets are shown. The sensitivity to model vertical resolution is significant, and suggested that the smooth increasing 90-level sigma distribution allow for the detection of fine-

scale potentially hazardous turbulence features, such as crosswind shear layers well displaced above the nocturnal boundary layer. The simulated turbulence profiles, overall, performed well in both the nighttime stable and daytime convective planetary boundary layers (PBL) and showed promising distributions for different turbulence forcing regimes. Comparisons of different EDR formulations, performed by varying the characteristic mixing length of large eddies, is also compared with the observations and original model output. Analysis of large eddy mixing length revealed that the observed mixing length was much higher than original model calculations, and that adjusting the daily profile of characteristic mixing length using a Gaussian distribution improves EDR prediction during quiescent conditions where buoyancy is the dominant production term. In the nocturnal boundary layer,

In the second paper, the stratospheric version of the Non-Hydrostatic Mesoscale Atmospheric Simulation System (NHMASS) model is used to simulate and evaluate the development, maintenance, and evolution of turbulence in the upper troposphere and lower stratosphere where convective and terrain-induced aviation turbulence pose a significant threat to high-altitude flying aircraft operated by the United States Air Force. The first aviation turbulence case is from a large-amplitude deep tropospheric gravity wave and associated deep convection on 12 December 2002 in Southeast Texas and Western Louisiana. Comparisons to synoptic and mesoscale surface and radar observations and satellite-derived upper-air turbulence measurements reveal that the NHMASS simulations displaced the large-amplitude gravity wave, convection, and associated upper-air turbulence farther to the north than in the observations. The NHMASS model's 1.5 order PBL-

based TKE scheme is compared against an explicit spatial and temporal Reynolds' averaging technique. The Reynolds'-averaging based TKE calculations, derived from explicit momentum and heat fluxes, reveals a much more detailed turbulence evolution as compared with the PBL-based TKE flux parameterizations which can be used as part of an automatic grid nesting algorithm for high resolution case studies. Explicit TKE budget calculations suggest that: (1) TKE advection contributions are non-negligible; (2) buoyancy and mechanical shear are the most dominant source terms; and (3) outflow-generated gravity waves can induce aircraft-threatening turbulence at altitudes as high as 20 kilometers. The explicit grid-based turbulence diagnostics were able to identify low wavelength signals of gravity waves generated by the convective overshooting tops in layers where the model TKE, due to the presence of small mean wind shear, show very little signal. The second aviation turbulence case generation case is the infamous 9 December 1992 Boulder, Colorado downslope wind storm and associated aviation accident. Comparison of the model to the parameterized fluxes and attendant turbulence evolution is similar to the explicit scheme with higher order detail. The explicit TKE budget diagnosis showed that the buoyancy and mechanical shear terms were the same order of magnitude, and resolved the transitioning mountain wave and hydraulic jump from the boundary layer through the lower stratosphere. The explicit spatial averaging technique will be implemented in high resolution runs as an automatic grid-nesting parameter to aid the model in detecting areas of turbulence generation in the stratosphere.

## **2. Evaluation of Boundary-Layer Turbulence Profiles for the Development of a Statistically-Based Wake Vortex Forecasting Algorithm**

### **1. Introduction**

The evolution of turbulence profiles and wake vortices near airport runways pose a significant problem for pilots and air-traffic control (ATC) responsible for regulating airport activity. Presently, ATCs use specific aircraft guidelines such as airplane weight and flight speed to set spacing during instrument meteorological conditions (IMC) in order to avoid wake vortices between arriving and departing aircraft. The process of spatial distribution is, at present time, independent of weather conditions for instrument approaches. During visual meteorological conditions (VMC), the pilot accepts responsibility for spacing behind aircraft based off of visual observation of conditions and wake relevance, but most often follow closer than the recommendation that would be provided by ATC. Studies such as Proctor (1998) have shown that wake vortices can be transported into and dissipated within flight corridors depending on atmospheric turbulence profiles, and suggest important atmospheric profile implications for wake vortex behavior and associated low-level winds profiles. Identifying atmospheric conditions, which promote the dissipation of wake vortices, could allow ATCs to safely decrease spacing, which would have a profound impact on airline production. The need to increase aircraft capacity is

especially important to airlines that face increasing demand and recover from financial setbacks as a result of the 11 September 2001 terror attacks.

In order to provide ATCs with forecasting tools that incorporate boundary layer turbulence evolution into capacity decisions, a meso- $\beta$  scale (i.e., 20 to 200 km scale) numerical weather prediction model capable of short and medium range forecasting has been developed under the direction of the National Aeronautics and Space Administration (NASA)'s Terminal Area Productivity (TAP) program. Through this program, a state-of-the-art operational forecasting system, called the Aircraft Vortex Spacing System (AVOSS) has been developed to incorporate wake vortex observations, wake vortex transport and decay algorithms, and both observed and numerically simulated weather conditions to safely increase airport capacity by decreasing aircraft spacing beyond the IMC flight rules. The AVOSS system has been detailed in previous studies such as Hinton (1995, 1996), Perry et al. (1997), Hinton et al. (1999) and Kaplan et al. (2000).

To provide more detailed information on atmospheric conditions relevant to wake vortex transport and decay than present observations, a regional-to-meso- $\beta$ -scale numerical weather prediction system called the Terminal Area PBL Prediction System (TAPPS) has been incorporated into the AVOSS development. TAPPS produces forecast analyses and soundings of temperature, wind (both headwind and crosswind), turbulent kinetic energy (TKE), and eddy dissipation rate (EDR) in order to aid AVOSS in anticipating spatial distribution changes due to evolving weather conditions.

In a previous study, Kaplan et al. (2000) (hereafter, K00) detailed the development of the TAPPS-1 system, which was used to simulate the NASA-Langley wake-vortex observational field study that took place at Dallas-Fort Worth International Airport on 15-20 September 1997. The focus of the research was to introduce the TAPPS system and the system's ability to model the ubiquitous diurnal low-level jet (LLJ) phenomena often observed during the overnight in the Central United States. The low-level jet, defined as a fast moving stream of air situated near the surface, is a significant weather feature in the Great Plains of the United States (Lin 2007). Though a low-level jet can be forced by various different mechanisms (such as warm conveyor belts and synoptic scale forcing), the low-level jets in this study are associated with topographic features and the transitioning convective to nocturnal boundary layer.

The diurnally-forced LLJ (hereafter, DLLJ), have been studied for over 60 years with several different formation mechanisms. The forcing mechanism identified by K00 in the original 15-20 September 1997 time frame was the inertial oscillation mechanism, first proposed by Blackadar (1957). As the boundary layer transitions from a convective state during the daytime to the nocturnal state, the end of turbulent mixing within the boundary layer and the cooling surface layer allows the surface layer to decouple from the residual layer above. The effects of friction are dramatically reduced near the top of the surface inversion and within the residual layer. Thus, the ageostrophic wind undergoes an inertial oscillation which generates a nocturnal low-level jet controlled by the diurnal cycle, with a maximum wind occurring ~9 hours after sunset in the

idealized framework (Lin 2007). Another formation mechanism, proposed by Blecker and Andre (1951) and Holton (1967), uses the thermal wind relationship to illustrate how baroclinicity generated by differences in topography can reverse the thermal wind during the early nighttime hours and aid in the development of a southerly LLJ in the lee of the Rocky Mountains. Though both formation mechanisms are likely at play in the 15-20 September 1997 observations, the TAPPS-1 system accurately represented the location, strength, and shear structure of the diurnal LLJ that was observed from asynoptic observations taken from the field study at various rawinsonde sites in and around the Dallas-Fort Worth metroplex. The enhanced strong shear profiles produced by the diurnal LLJ produced TKE maxima that were roughly aligned with the cross-runway ( $u$ ) wind speed, and EDR maxima near the surface on the order of  $2 - 5 \times 10^{-3} \text{ m}^2\text{s}^{-3}$ . EDR comparisons from the TAPPS-1 simulations indicated slight overestimation, forced primarily by mechanical shear generation, in the early morning hours and underestimation during the afternoon, forced primarily by buoyancy production. In addition to the aforementioned research on diurnal LLJs, the TAPPS-1 system produced datasets for the AVOSS program at various domestic airport locations such as Los Angeles International Airport (LAX), Boston's Logan International Airport (BOS), and San Francisco International Airport (SFO), in anticipation of the development of the next generation of TAPPS.

The purpose of this paper is to introduce the development of the next version of the TAPPS system (known as TAPPS-2) and introduce results from validation simulations using the AVOSS dataset described in K00. In order to

develop and test a new version of the TAPPS modeling system, evaluation of the same important turbulence-generating phenomena during the AVOSS deployment at Dallas-Fort Worth International Airport on 15-20 September 1997. The primary feature identified in K00, the diurnally-forced low level jet (DLLJ) across the Central United States, is examined using altered model design and configurations. The utility of finer resolution numerical simulations, both in the horizontal and vertical are explored using the new TAPPS-2 system. In addition, various sensitivity tests to model configuration and numerical formulation, such as eddy dissipation rate, are performed to improve the TAPPS-2 forecasting system. Information gained from the new TAPPS-2 validation and subsequent sensitivity tests is then used to set the framework for the development of a series of quasi-climatological low-level wind and turbulence simulations at St. Louis-Lambert International Airport. The paper is organized as follows: Section 2 details the motivation and methodology in developing TAPPS-2 and the low-level wind climatology; Section 3 presents results and error analysis from validation simulations performed using AVOSS data at Dallas-Fort Worth International Airport with emphasis on the sensitivity of TAPPS-2 to model configuration and design related to the forecasting of the DLLJ ; Section 4 presents results from an eddy-dissipation rate formulation sensitivity test, and Section 5 summarizes the results and conclusions of the validation and subsequent recommendations for the low-level wind climatology at St. Louis-Lambert International Airport.

## **2. Motivation and Methodology**

### *2.1 TAPPS-2 Model Configuration*

The TAPPS system is based off of the Mesoscale Atmospheric Simulation System (MASS), which is a regional-to-mesoscale numerical weather prediction model. As described in full detail in K00, the TAPPS-1 system was based off of MASS version 5.10 and was run in a hydrostatic mode. The model used a one-way-nesting algorithm, as described in Davies (1976), with horizontal grids of 60x60x56 at a 36 and 12 kilometer horizontal resolution. The sigma-level distribution provided by TAPPS-1 included 10 model layers below 100 meters with vertical grid stretching above the PBL. The 36-kilometer grid mesh was integrated continuously for 24 h from two initial start times of 0000 and 1200 UTC while the 12-kilometer grid mesh was run for 21 h from interpolated conditions derived at 1500 and 0300 UTC.

In order to provide more accurate simulations of PBL evolution possible through advancements in computing power, the TAPPS-2 system underwent a series of modifications intended to improve the quality of the simulations. First, a new non-hydrostatic core version of the MASS model (version 6.4.3) is used as the centerpiece of TAPPS-2. The inclusion of a non-hydrostatic core is intended to provide a more realistic representation of boundary layer processes, especially when buoyant processes and free convection dominate. Secondly, the horizontal and vertical grid structure was expanded and an additional domain is added. For the coarse domain (36 kilometers), the grid is expanded to 100x100 points, and the vertical structure held constant with 60- $\sigma$  levels, which is the same vertical

structure detailed in K00. In TAPPS-2, the “inner” or second domain is changed to have a 6-kilometer resolution with a 100x100 horizontal grid mesh. A third domain, denoted as the “fine” resolution domain, is tested using a horizontal grid resolution of 1-kilometer, with a 50x50 horizontal grid centered directly over the airport of interest. Thirdly, a new 90  $\sigma$ -level structure is implemented with increased vertical resolution in the lowest 3 kilometers, a 30  $\sigma$ -level increase over the previous vertical structures in TAPPS-1, for the 6 and 1-kilometer domains. The switch to a non-hydrostatic core and increase in horizontal and vertical resolution in the new TAPPS-2 system is hypothesized to provide a more realistic representation of the features responsible for near surface aviation turbulence. The finer resolution is anticipated to increase the predictability and detection of fine scale feature that could pose a threat to aviation, such as shear in the 0-2 kilometer layer. As will be demonstrated in Sections 3 and 4, the change in horizontal and vertical (sigma structure) resolution in the newest version of TAPPS can significantly alter the forecasting of turbulent features in the boundary layer.

The 36-kilometer (coarse) grid mesh is initialized using the Eta-211 model grid data for both the validation and climatology simulations with boundary condition updates every six hours. The 6-kilometer mesh ingests data at hourly increments from the coarse grid mesh, while the 1-kilometer mesh ingests data at 15-minute increments from the second grid mesh. The two outer grid meshes (36 and 6 km), use the Kain-Fritsch (Kain and Fritsch 1990) cumulus parameterization scheme, Lin et al. (1983) microphysics, and the super-fine 1-

kilometer grid mesh employ an explicit cumulus parameterization scheme. All grid meshes employ an elaborate TKE PBL scheme detailed by Therry and Lacarrere (1983). The adjustments to the model configuration from the TAPPS-1 system are summarized in Table 1.

## *2.2: Post-Processing and Validation Techniques*

For both the validation simulations presented in Section 3, and the low-level wind climatology described in Section 5, two independent one-way nested runs are performed at 00 and 12 UTC on the days in question. Each grid mesh (36,6,1 kilometers) are integrated over a full twenty-four period for the validation simulations, and was changed slightly for the climatology simulations based off of the validation results discussed in Section 3. The two initialization times are performed in order to capture all busy traffic times and use the overlapping forecasts to test the sensitivity of the model as a function of the PBL regime and to the initialization time. In addition, during the previous NASA wake-vortex project using TAPPS-1, results suggested that the 12 UTC initialization time performed better overall than the 00 UTC runs, and this is explored in the validation runs.

The model data is post-processed using a cubic-splining algorithm that generates model-derived fields at 5-meter vertical resolution from the surface to 2- kilometers at a particular grid point within the model simulations. For the validation case studies selected for DFW and discussed in Section 3, values of  $u$  and  $v$  wind velocities, TKE and EDR are examined at heights of 5, 15, and 40 meters above ground level (AGL) from the model centered over the airport

runway. From the documentation provided in the AVOSS data sets, the values of turbulent kinetic energy (TKE) used for the validation is derived from three-dimensional sonic anemometers at the northern site of the airport. The variances are calculated from the wind field sampled at 10-Hz frequency and averaged over a 5, 15, and 30 minute time period. For the purposes of the project, the average TKE from the 15 minute averages is used over the validation period. From the north site tower data, the eddy dissipation rate is also derived from the 3-D sonic anemometer tower data using spectral analysis. The power spectrum of each component of the wind is computed and smoothed in frequency by a rectangular frequency window whose width varies logarithmically with increasing frequency, such that:

$$S(U_*) = \frac{N}{S_{RATE}} \left| FFT(U_*') \right|_{2\pi}^2 \quad (2.2.1)$$

where  $S_{RATE}$  is 10 Hz,  $N$  is the number of observations, and  $U_*$  and  $U_*'$  are the average and perturbations of the three wind components ( $*$  = 1,2,3 for (u,v,w) wind components). Using Kolmogorov's (1941) inertial subrange hypothesis, the inertial subrange of each power spectrum is determined automatically by examining a log-log relationship between the power spectrum  $S$  and the wavenumber:

$$K = 2\pi \frac{f}{U_*} \quad (2.2.2)$$

Using (2.1) and (2.2), the EDR from the AVOSS tower data set is calculated such that:

$$\varepsilon_{AVOSS} = [S(U_*) \left( \frac{K^{5/3}}{C} \right)]^{3/2}$$

$$C = 0.52, \text{ for } * = 1 \text{ (} u \text{-component)} \quad (2.2.3)$$

$$C = 0.69\bar{3} \text{ for } * = 2, 3 \text{ (} v, w \text{-component)}$$

The derived TKE and EDR fields are then compared to tower observations taken in 15-minute intervals as part of the AVOSS observing system at DFW, which can be directly compared to the cubically-splined output. Previous studies such as Hinton (1995, 1996), Perry et al. (1997), Hinton et al. (1999) have detailed the observations taken using the AVOSS system. Statistical analysis of the modeled and observed data within the validation simulations (Section 3) and sensitivity to EDR formulation (Section 4) is also explored. In addition, soundings of important turbulent related quantities, such as temperature, wind, TKE and EDR, are generated from the splined model output and explored in detail within the validation simulations presented in Section 3.

A crucial element of the TAPPS-2 system is to produce realistic turbulence forecasts near the surface that would be implemented within a statistical forecasting framework for wake vortices. Thus, the model turbulence calculation is the centerpiece of the TAPPS-2 evaluation. The TKE and EDR are calculated in TAPPS-2 following the Therry and Lacarrere (1983) 1.5-order TKE algorithm.

The TKE tendency equation, given from Stull (1988) as:

$$\frac{\partial \bar{e}}{\partial t} = -\bar{u} \frac{\partial \bar{e}}{\partial x} - \bar{v} \frac{\partial \bar{e}}{\partial y} - \bar{w} \frac{\partial \bar{e}}{\partial z} + \frac{g}{\theta_v} \overline{(w'\theta_v')} - \overline{(u'w')} \frac{\partial \bar{u}}{\partial z} - \overline{(v'w')} \frac{\partial \bar{v}}{\partial z} - \frac{\partial}{\partial z} \overline{(w'e)} - \frac{1}{\rho} \frac{\partial}{\partial z} \overline{(w'p')} - \varepsilon \quad (2.2.4)$$

In the model TKE scheme described in Therry and Lacarrere (1983), the advection of TKE is set to zero, and the pressure perturbation and turbulent transport terms are combined and parameterized as a function PBL regime. The

second moment turbulent fluxes are parameterized following recommendations by Yamada and Mellor (1975). The EDR, which is the last term in the TKE tendency equation, is parameterized and calculated using:

$$\varepsilon = \frac{\bar{e}^{-3/2}}{8l_e} \quad (2.2.5)$$

where  $\bar{e}$  is the average TKE, and  $l_e$  is the dissipation length scale, which is an elaborate function of PBL regime and flux parameterizations. The expression  $8l_e$  make up the characteristic length scale (CLS) within the 1.5-order TKE closure scheme (e.g., Stull 1988, Ayra 2001). From (2.2.4), the TKE tendency equation can be simplified for neutral conditions often present beneath the nocturnal inversion within the boundary layer. Assuming horizontally homogeneous flow near the aircraft runway, negligible TKE profile contributions from the pressure correlation and turbulent transport terms, no significant change in the TKE locally, and a dominant east-west (crosswind,  $u$ ) wind component, Eq. (2.2.4) can be expressed in terms of the eddy dissipation rate, such that:

$$\varepsilon \approx -\overline{(u'w')} \frac{\partial \bar{u}}{\partial z} \quad (2.2.6)$$

Using the definition of friction velocity and surface layer wind shear, where:

$$u_*^2 = \overline{u'w'}, \frac{\partial \bar{u}}{\partial z} \approx \frac{u_*}{kz} \quad (2.2.7)$$

Eq. (2.2.6) can be re-written as:

$$\varepsilon \approx \frac{u_*^3}{kz} \quad (2.2.8)$$

In the relatively quiescent boundary layer flow regimes noted in the sonic anemometer data at the north site tower beneath the nocturnal inversion, a

friction velocities of the scale  $u_* = 0.1-1$  m/s at a 40 m AGL would yield eddy dissipation rate values on the order of  $\varepsilon = 10^{-2}-10^{-4}$   $\text{m}^2\text{s}^{-3}$ . The majority of the EDR values derived from the tower data using the AVOSS system fell between  $10^{-2}-10^{-3}$   $\text{m}^2\text{s}^{-3}$  over the validation period within the nocturnal boundary layer, and rarely exceeded  $10^{-2}$   $\text{m}^2\text{s}^{-3}$  within the convective boundary layer. While commercial aviation flights are not as frequent during the nighttime, increased aviation traffic from couriers such as Federal Express and UPS make aviation forecasting during the overnight hours a significant problem for air-traffic controllers, especially since the guidelines for spacing vary depending on the weights of the aircraft.

The evaluation of the observed EDR to the model EDR is of paramount importance for the validation simulations. As discussed in Stull (1988), the choice of the CLS is rather arbitrary and has been chosen as a function of observational evidence in previous studies. From Therry and Lacarrere (1983), the CLS is not set to a constant value, but rather, is calculated using an elaborate function where  $l_e$  is a function of the height above ground level, the depth of the PBL, and the local stability. The function for the CLS was derived from a 3<sup>rd</sup>-order direct numerical simulation of the boundary layer and is intended to be used in all relevant PBL structures. As noted in K00, however, the TAPPS-1 EDR values exhibited a biased over-estimation of the dissipation at levels relevant to wake vortices. For the TAPPS-2 simulations, several different EDR calculation algorithms are tested against the observations in order to determine if alternate calculations of EDR might be useful to improve the representation of turbulence

dissipation. The EDR is derived from sensitivity tests where (1) the dissipation length scale is calculated using the Therry and Lacarrere (1983) function; (2) the dissipation length scale is held constant (e.g., Frech and Hozäpfel 2006), (3) the dissipation length scale is derived from empirical observations and normalized using a Gaussian distribution. The results of the EDR sensitivity are explored in further detail in Section 4.

### **3. Dallas-Fort Worth International Airport Validation Simulations**

#### *3.1: Introduction and Synoptic-Scale Flow*

Using the TAPPS-2 model configuration described in Section 2, a series of model simulations were performed for the Dallas-Fort Worth International Airport in order to test the turbulence diagnostics produced by the system against tower observations from the AVOSS system. The AVOSS experiment included a field-study at the DFW airport in order to test the TAPPS-1 system presented and used in K00. The days chosen for validation were part of the field experiment, and include the time period from 00 UTC 17 September 1997 through 00 UTC 21 September 1997. To test the TAPPS-2 system in different types of turbulence generation environments, an additional validation day (27 September 1997) was also performed. For the purposes of the analysis included in this manuscript, only the 17-20 September 1997 validation periods is considered.

The analysis of the TAPPS-2 modeling system over the validation days are performed to determine the utility of the higher vertical and horizontal resolution employed in the new configuration. Specifically, it is hypothesized that the higher resolution in the vertical and horizontal are anticipated to better

represent the small-scale features, such as subtle differences in wind velocity, which could prove critical to the aviation forecasting and attendant aircraft spacing. The improvement is expected to be manifested in both the center-grid point validation (Section 3.2) and the sounding analysis (Section 3.4) for observed turbulence variables such as TKE and EDR. The structure of wind profiles are also expected to greatly improve due to the new TAPPS-2 system. In particular, evaluation of the structure of mechanically-shear generated turbulence within the DLLJ structures during the validation is the focus of the sounding analysis presented in Section 3.2.4.

The synoptic scale flow across the Southern Plains was rather quiescent during the 17-18 September 1997 period. The Southern Plains was dominated by a strong upper level anticyclone centered over northern Mexico and far Southwest Texas with a strong shortwave trough ejecting across the Northern Plains (e.g. 250 hPa in Fig. 1). The 250-500 hPa flow between 17-18 September was primarily northerly to northwesterly across Northern Texas, influenced primarily by the northeastern quadrant of the upper-level high pressure system. The flow was rather weak, averaging between 20-30 knots at upper levels and surface winds at or below 10 knots. The synoptic scale flow above the airport was at the very edge of the stronger belt of westerlies associated with the shortwave trough ejecting over the Northern Plains. Nevertheless, a very weak diurnal low-level jet signal is present on 17-18 September beneath the upper level ridge (e.g. Fig. 2). The synoptic scale subsidence contributed to warmer than average surface temperatures and strong mixing within the PBL during 17-

18 September 1997. Therefore, the strongest contributor to the turbulence profile during the daytime across the DFW airport is expected to be buoyancy forces. The strong surface heating would lead to a strong diurnal signal in turbulence profiles, and as detailed in K00, the TAPPS-1 system accurately produced strong diurnally-driven low-level jet (DLLJ) signals. The strong DLLJ signals were responsible for mechanically-shear generated turbulence within the PBL during stable conditions, and these LLJ structures were the focus of K00 and are explored in this research using TAPPS-2.

During the daytime hours on 18 September 1997, a vigorous long wave trough approaches the Pacific Northwest, and is visible entering the western boundary of many of the validation simulations as early as 1200 UTC 18 September 1997 (e.g. Fig. 2). The long-wave trough quickly progresses eastward across the Intermountain West and begins to impact the synoptic scale forcing across Northern Texas by 0000 UTC 19 September 1997 (e.g. Fig. 3). The strong-upper level ridge centered over Northern Mexico begins to elongate and weaken slightly, and by 0600 UTC 19 September 1997, the 250-500hPa flow across Southern Oklahoma and Western North Texas increases and backs to a more westerly-dominated component. However, the robust diurnal low-level jet signal (DLLJ) that is present across West Texas and Western Oklahoma during the overnight hours of 19 September 1997 remained, controlled primarily by the diurnal cycle, as the strong upper-level ridging blocks any synoptic scale disturbances from altering the boundary layer profiles near DFW. As discussed in Kaplan et al. (2006), the difference in maximum diurnal low-level jet intensity and

subsequent orientation of the pressure gradient force vector across Oklahoma and Western North Texas is quite substantial between 18 and 19 September 1997. The low-level jet signal on 18 September is weaker than the other validation days with maximum 850-hPa flow around 30 knots between 0700-0900 UTC 18 September across Central Oklahoma (e.g. Fig. 4). Thus, the east-west pressure-gradient force is weak across Northern Texas, and from K00, would suggest lower overall nocturnal shear-generated turbulence near the DFW airport. The 850-hPa diurnal low-level jet peaks in intensity across Northern and Northwest Oklahoma and the Texas Panhandle with model-simulated low-level jet wind fields approaching 60 knots with a southwesterly component between 0700-0900 UTC 19 September 1997 (e.g. Fig. 5). The 850-hPa wind field across Northern Texas veers substantially from southerly to southwesterly during the 12-hour simulated period (00-12 UTC 19 September) with a substantial east-to-west gradient in height, leading to a strong horizontally-oriented pressure gradient force vector.

The polar jet streak associated with the Pacific Northwest trough propagates across the Northern Plains on 20-21 September 1997 and moved a surface-cold front across the Central Plains. The cold front moves into Northwest Oklahoma and the Northern Texas Panhandle during the afternoon by 0000 UTC 20 September. The front propagates slowly southward, reaching Oklahoma City by 1200 UTC 20 September and northerly winds are reported as the edge of the front eclipses the DFW airport at 0000 UTC 21 September. The temperature gradient across the front is rather strong, with temperatures between 15-20C in

the Texas Panhandle, while readings near the boundary exceed 30C. However, the strong ridging across Northern Texas prevents the synoptic scale front from crossing the airport during the validation times presented in this section, allowing for comparison between different simulation times during the 17-19 September 1997 period.

Each of the case study days (17 September, 18 September, 19 September, 20 September) has separate validation treatment due to (1) changes in horizontal and vertical resolution and (2) changes in model physics (e.g., convective parameterization). Therefore, nomenclature identifying the different model simulations is needed to assess the quality of the TAPPS-2 simulations. In particular, the possibility of sensitivity to grid resolution or model physics could play an important role in determining the proper configuration of TAPPS-2 for the low-level wind climatology. The model simulations that pertain strictly to validation are addressed with a “run tag” corresponding to the day when the model integration was started (such as 17, 18, etc.), a horizontal model grid resolution (such as 36, etc.), and a start time (such as 00, etc.). For the purposes of model validation, a total of 30 validation simulations were conducted via the one-way grid nesting technique. In the subsequent sections, results from various validation simulations are presented with emphasis on (1) the comparison of model versus observed TKE and EDR near the surface (below 100 m in the convective or stable boundary layer); (2) the model evolution of TKE, EDR, and wind profiles as a function of the diurnal cycle and expected values; (3)

soundings of wind, temperature, and turbulence diagnostics in the boundary layer.

### *3.2 TAPPS-2 Validation Simulations (17-19 September 1997)*

#### *3.2.1: Analysis Introduction*

Using the TAPPS-2 model configuration discussed in Section 2, a series of one-way nested simulations were conducted for the 17-19 September 1997 time period centered on Dallas-Fort Worth International Airport. As discussed in Section 3.1, the synoptic scale flow on these days remained quiescent, dominated by an upper level ridge over central Mexico. Because significant consistency is present in the 24 hour runs for the 17, 18, 19 September 1997, with overall mean 500-hPa geopotential height errors less than 20 m, the discussion of synoptic scale results is deferred and not presented in this manuscript.

Since the aim of the project is to produce reliable forecasts of turbulent kinetic energy and eddy dissipation rate at levels near the surface where wake vortices are important, the validation of the model TKE, EDR, and winds are the focus of the validation for Dallas Fort Worth International Airport (DFW). Since the runway at DFW is aligned north-to-south, the  $u$  ( $v$ ) wind component is hereafter referred to the head-wind (crosswind) velocity component. As discussed in K00, vortex drift in the near surface to 500 m layer contains the approach and takeoff corridors for aircraft at DFW and the vortex drift within this layer is controlled by the magnitude of the crosswind velocity component. Therefore, evaluating the structure of the crosswind velocity is of paramount

importance for the aviation forecasting problem at DFW. Using the TAPPS-2 modeling system and cubic-splining algorithm discussed in Section 2, a series of validation simulations were analyzed with regards to the headwind and crosswind velocity, temperature, TKE, and EDR. The variables are validated using the AVOSS data set at heights near the surface and through soundings with respect to height above ground level (AGL). The AVOSS tower data is available at heights of 5 and 40 m AGL. The NHMASS TKE PBL scheme generally sets the surface layer TKE to a constant value of  $1 \times 10^{-2} \text{ m}^2 \text{ s}^{-2}$  at the start of model integration. As discussed in Section 2, the upgrade of TAPPS-1 to TAPPS-2 included a 60-sigma level increase in the fine grid (6 and 1) kilometer simulations. In order to provide a smooth sigma distribution while increasing the number of sigma levels, the sigma-level structure in direct proximity to the model surface (i.e., < 20 m) incurred the loss of one sigma level. However, the number of sigma levels below 2 km doubled from the TAPPS-1 to TAPPS-2 configuration. The coarse grid simulation (i.e., 36 km) kept the same model sigma structure as the TAPPS-1 configuration prescribed in K00. The model-surface layer, however, usually corresponded to a height of 8-13 m, a few meters below the AVOSS tower data independent of sigma-level distribution. Due to the number of sigma levels capable of being approximated near the surface, and the fact that the lowest model layer rarely corresponded to a height of 5 m AGL, the model fields are validated at 15 meters instead of 5 meters. The 40 m data, however, is in a range of 4-6 sigma levels that is sufficient for splining against the AVOSS tower data. Evaluation of the sounding structure and notes on sensitivity

to model sigma structure in the dependent variables is discussed in Section 3.2.4.

### *3.2.2: Model TKE and EDR Point Validation (17-19 September 1997 00 UTC)*

The model TKE and EDR are compared against the AVOSS tower data (described in Section 2.2) for the 17 September 1997 time frame from 00-00 UTC 17-18 September and 12-12 UTC 17-18 September for all model horizontal resolutions. The cubic splining algorithm creates 5-m vertical resolution soundings at the center of the grid, closest to where the runway would be at DFW. Examining the coarsest grid simulation (36 km) and first initialization time (00 UTC) first, the TKE trace from the 17\_36\_00, 18\_36\_00, and 19\_36\_00 (e.g. Fig. 6-8) indicate that both the (5/15) and 40 m TKE in the 36 km simulations, on average, underestimate the TKE during the overnight hours within the nocturnal boundary layer. The first six hours of 17\_36\_00 closely matches the observations, but then averages  $0.25\text{-}0.50\text{ m}^2\text{s}^{-2}$  below the observations through 12 UTC for both the near surface (5/15 m) and 40 m heights. The  $0.50\text{ m}^2\text{s}^{-2}$  underestimation of the observed TKE is also shown in the 18\_36\_00 (e.g. Fig. 7) and 19\_36\_00 (e.g. Fig. 8) in the nocturnal boundary layer. At sunrise, the 36 km TKE simulations remain  $0.50\text{ m}^2\text{s}^{-2}$  below the observations as the depth of the boundary layer grows through mixing. The TKE traces closely mimic the slope of TKE increase with time through the maximum values in TKE, which average approximately  $2.00\text{-}2.50\text{ m}^2\text{s}^{-2}$  around 18-19 UTC. The 17\_36\_00 TKE curve drops off faster than the other two days, with several hours of TKE at (5/15) and 40 m above  $1\text{ m}^2\text{s}^{-2}$  during the duration of daytime hours. The AVOSS tower data

peaks about 1 h later around 20 UTC all three days with the 40 m TKE approaching  $3 \text{ m}^2\text{s}^{-2}$  on 17 and 18 September. After 20 UTC, the model and observations are once again very close through the end of the simulation, with the 36 km simulations actually exceeding the observations between 21-00 UTC during all three simulation days. The overall shape of the model TKE curve appears much smoother than that of the observations, which could be attributed to the coarser horizontal grid spacing. The TKE curves in the 36 km simulations, however, provide surprisingly good point validation statistics and appear to handle the diurnal cycle of TKE.

Because of the inconsistencies present in the representation of the near surface elements that contribute to turbulence between the models and real observations, such as the presence of aircraft, buildings, and other structures, the 40 m height was chosen for further statistical analysis. Histogram plots (e.g. Fig. 9 for 36 km, Fig. 13 for 6 and 1 km) of the observed versus the model TKE for all three days (17-19 September) for the 00 UTC 36 km simulations indicate that roughly 75% of the observed TKE values fell between 0-0.9  $\text{m}^2\text{s}^{-2}$  in the observations, with 40% falling between 0.3-0.9  $\text{m}^2\text{s}^{-2}$ . The 36 km simulations, however, had approximately 60% of the 40 m TKE below 0.45  $\text{m}^2\text{s}^{-2}$ . Both the modeled and observed TKE values had TKE values greater than 2  $\text{m}^2\text{s}^{-2}$  less than 15% of the time, indicating that the model very rarely over-estimated the TKE during the convective boundary layer. As shown in the time-series plots, the statistical results indicate that the bulk of the overall error in the 40 m TKE is manifested during the nocturnal boundary layer, between 00-12 UTC.

The one-way nesting technique described in Section 2 is used to initialize the suite of 6 km simulations ((17/18/19)\_06\_00), with TKE time series plots shown in Figures 10-12, respectively. The time series traces reveal that the 6 km TKE is much lower than the observations and the 36 km simulations, particularly near the ground where the (5/15)m TKE rarely exceeds  $0.25 \text{ m}^2\text{s}^{-2}$ . The 40m TKE on 17\_06\_00 (e.g. Fig. 10) is noticeably lower than the observations, but improves with the 18\_06\_00 (e.g. Fig. 11) and 19\_06\_00 (e.g. Fig. 12) simulations. The 6 km simulations have average errors on the order of  $-1-2 \text{ m}^2\text{s}^{-2}$  throughout the entire simulation period, with higher errors noted at the height of the convective boundary layer. The maximum value of TKE in the 6 km simulations occurs closer to the observed maximums (i.e., 20-21 UTC) than the 36 km simulations, but with  $1-2 \text{ m}^2\text{s}^{-2}$  underestimations. Following the maximum in TKE, as with the 36 km simulation, the 6 km simulation overall error decreases, with the 40 m height closely following the observations. The results indicate that there is significant sensitivity to both the change in horizontal grid resolution from 36 to 6 km and in the sigma-level structure, which is explored in the sounding analysis in Section 3.2.4.

Despite the overall shift of the TKE profile at 40 m downward in the 6 km simulations, it does not significantly alter the distribution of TKE values, as indicated in the histogram plots shown in Figure 13. The TKE in the 6 km simulation is between  $0-0.6 \text{ m}^2\text{s}^{-2}$  at a much higher percentage than the observed 40 m TKE, indicating that the model TKE is, on average, much lower than the observations. The TKE is lower than  $1.5 \text{ m}^2\text{s}^{-2}$  approximately 93% of the

simulation periods, comparable to TKE lower than  $1.6 \text{ m}^2\text{s}^{-2}$  90% of the time in the observations. Thus, as was the case with the 36 km simulations and is shown in the time series plots, the 6 km TKE provides a good estimation of the growth of the convective boundary layer and diurnal cycle evolution, with the majority of the error coming from the nocturnal boundary layer (i.e., 00-12 UTC).

The one-way nesting algorithm is once again employed to produce a very-fine 1-km simulation of the validation days ((17/18/19)\_01\_00). The time series plots shown in Figures 14-16 indicate that the 1 km simulations experience a peculiar noise effect every 4<sup>th</sup> model output time, and the TKE trace is strikingly similar to the 6 km simulations shown in Figures 10-12. The peculiar dip in both the (5/15) m and 40 m TKE in the 1 km simulations is due to the way the original 1-km simulations were initialized. From the original TAPPS-1 configuration, the 1-km simulations were comprised of a series of 24 1-hr runs initialized from the hourly output using the 6 km simulations. The configuration from TAPPS-1 was designed to cut down on overall simulation time by utilizing shorter model integration periods. However, the effect of model “spin-up” is apparent in the time-series plots, which show the effect of adjusting the TKE profile downward in the observations every 4<sup>th</sup> output time when the 24 simulations are compiled together. To test the utility of the original TAPPS-1 configuration, a series of 24-hr continuous 1 km runs were performed and subsequently compared to the 1-km configuration for the 17 September 1997 00 UTC simulation (e.g. Fig. 17). The 1-km continuous simulations did require quite a bit more computing time, but eliminated the model-“spin-up” issue, as shown in comparison plots in Fig. 17.

Furthermore, comparison of the continuous 1-km and continuous 6-km TKE traces suggest that despite the decrease in horizontal grid spacing, the TKE profiles do not change significantly. Investigation of basic statistics between the 6 and 1 km simulations, shown in Table 2, indicate that including the similar time series traces, the 6 and 1 km simulations have similar means, minimums, maximums, and standard deviations. On average, the 1 km simulations have lower, but not appreciably lower, TKE traces than their 6 km counterparts. Since there is a noticeable and significant error noted in the original TAPPS-1 configuration of 24 separate 1-hr 1-km runs, a continuous 1-km simulation is necessary. However, because the 6 and 1 km 00 UTC simulations appear similar, the practicality of having a 1-km simulation for the purposes of comprehensive low-level wind climatologies is brought into question. Analysis of sounding structures between the 90-sigma level 6 and 1 km simulations are investigated in Section 3.4.3.

As noted in Section 2, the model-derived eddy dissipation rate (EDR) has a different proportionality to the model TKE depending on the magnitude of the turbulence, because the magnitude of the TKE is raised to the three-halves power. The model EDR, however, is inversely proportional to the characteristic dissipation length scale. Examination of the EDR plots from the 36 km simulations (e.g. Fig. 18-20) indicates that the near surface (5/15 m) TKE is substantially overestimating the eddy dissipation rate. The (5/15) m EDR remains on a  $10^{-2} \text{ m}^2\text{s}^{-3}$  scale during the nocturnal boundary layer times (00-12 UTC) while the observations indicate EDR on the order of  $10^{-3} \text{ m}^2\text{s}^{-3}$  near the surface.

The over-estimation in EDR near the surface approaches the  $10^{-1} \text{ m}^2\text{s}^{-3}$  scale as the convective boundary layer develops during the daytime hours (12-00 UTC), while the observations on the three days remain between  $10^{-2} \text{ m}^2\text{s}^{-3}$  and  $10^{-3} \text{ m}^2\text{s}^{-3}$ . Thus, the 36 km EDR tends to overestimate the near surface dissipation rate by one to one-and-a-half orders of magnitude for the validation days. The 40 m EDR, on the other hand, matches the observations much better during the nighttime hours and can actually provide an underestimation of EDR during the daylight hours (e.g. Fig. 18-20). The dramatic difference in eddy dissipation rate from (5-15) m to 40 m within the 36 km simulations suggest a dramatic shift in eddy dissipation rate in the vertical, examined further in the sounding structures discussed in Section 3.2.4.

The (5/15) m EDR in the 6 km simulations at (5/15) m have lower overall mean errors than the 36 km simulations, as noted in Fig. 21-23. However, this result can be misleading. From theory, such as Stull (1988), the eddy dissipation rate is fundamentally tied to the turbulent kinetic energy, and thus, the higher (lower) the TKE, the higher (lower) the EDR. Despite a non-linear relationship between TKE and EDR, this constraint is manifested by fluctuations in the dissipation length scale within the calculation. Thus, the better validation of EDR at the (5/15) m height in the 6 km simulations is attributed to the overall lower TKE values aforementioned. Though improved horizontal and vertical grid spacing may play some role in adjusting the validation, the main factor in the better 40 m validation is attributed to overall lower TKE values. Despite good validation of the 40 m TKE in the 6 km simulations, the EDR traces average

close to  $10^{-2} \text{ m}^2\text{s}^{-3}$ , around one order of magnitude higher than the EDR traces in the observations. The 6-km EDR appears to follow the same pattern between 15 and 40 m, while a substantial difference between 15 and 40 m is noted in the 36 km simulations. As noted in the TKE traces, the results of the EDR validation suggest that there is significant sensitivity to both the horizontal and vertical resolution in the TAPPS-2 simulations. Investigations of the other variable in the EDR formulation, the dissipation length scale, are discussed in Section 4. The traces of 1-km EDR, shown from the 17\_00\_01 simulation in Fig. 24, show the exact same pattern noted in the TKE fields. The EDR is lower, but not appreciably lower, than the 6-km EDR traces for all of the validation days.

### *3.2.3: Model TKE and EDR Point Validation: 12 UTC Simulations*

Research completed by K00 and Kaplan et al. (2005) suggests that the TAPPS-1 simulations, when initialized at 12 UTC, seem to provide better overall validation results than the 00 UTC simulations. Thus, another series of runs configured the same as the 00 UTC runs discussed in Section 3.2.2, are performed with the initialization time set to 12 UTC on the day in question. Therefore, there is a 12-hr overlap into the next day, ending with the 12 UTC 19 September (19\_XX\_12) simulation ending on 12 UTC 20 September, where “XX” is the horizontal resolution of the model.

The TKE time series plots for the 36 km simulations are shown in Figures 25-27 for 17\_36\_12, 18\_36\_12, and 19\_36\_12. On 17 September, the 17\_36\_12 simulation does a remarkable job simulating the TKE trace compared to the observations, including accurately forecasting the time of maximum TKE at

~2000 UTC. The model TKE in 17\_36\_12 actually exceeds the observed values for the majority of the duration of the convective boundary layer, indicating that TAPPS-2 may be overestimating the effect of mixing. The observed TKE trace drops off at a significant rate from the maximum value at 2000 UTC and reaches a local minimum of  $0.50 \text{ m}^2\text{s}^{-2}$  around 0000 UTC. The model TKE trace, however, drops off at a slower rate and reaches a local minimum of  $0.25 \text{ m}^2\text{s}^{-2}$  around 0100 UTC. From 0100-0700 UTC, the TAPPS-2 TKE in 17\_36\_12 remains around  $0.25 \text{ m}^2\text{s}^{-2}$  lower than the observations, and begins to increase to  $0.75 \text{ m}^2\text{s}^{-2}$  at 0900 UTC. During this period, the observations continue to indicate a downward trend in (5/15) 40 m TKE, reaching a simulation minimum around  $0.25 \text{ m}^2\text{s}^{-2}$  at 0900 UTC. The 17\_36\_12 then begins decreasing back to the observed value of  $0.50 \text{ m}^2\text{s}^{-2}$  by 1200 UTC 18 September. As will be investigated in Section 3.2.4, the impact of the diurnally-driven low-level jet has a significant impact on the TKE structure within the nocturnal boundary layer and forces the oscillation in TKE values between 06-12 UTC 18 September as shown in the time series plots.

A very similar diurnal pattern is noted in the time series plots for 18\_36\_12 (e.g. Fig. 26), with the daytime TKE values reaching a maximum value at 2000 UTC. The TKE profile at both (5/15) and 40 m begins dropping off at a slower rate in 18\_36\_12 than in the observations. The observed TKE begins rising around 0200 UTC from a local minimum value of near  $0.10 \text{ m}^2\text{s}^{-2}$  at 0100 UTC. By 0400 UTC, the observed TKE at both (5/15) and 40 m exceeds  $1.00 \text{ m}^2\text{s}^{-2}$ . The 18\_36\_12 simulation also begins rising from a local minimum of  $0.25 \text{ m}^2\text{s}^{-2}$

to a nocturnal maximum of over  $1.00 \text{ m}^2\text{s}^{-2}$  around 0600 UTC. From their respective nocturnal maxima, both the model and observations decrease the (5/15) and 40 m TKE to around  $0.50 \text{ m}^2\text{s}^{-2}$  at 1200 UTC. The modeled and observed patterns in TKE, variation during the overnight period is again attributed to the formation of a significant diurnal low-level jet, as shown in K00 and further detailed in Section 3.2.4.

Unlike the previous two 36-km simulations, 19\_36\_12 over-estimates the (5/15) m and 40 m TKE throughout the duration of the convective boundary layer. Though the TKE profile initializes much lower than the observations, the 19\_36\_12 near-surface TKE rapidly increase to over  $2.50 \text{ m}^2\text{s}^{-2}$  by 1800 UTC,  $0.50 \text{ m}^2\text{s}^{-2}$  higher than the observations. The 19\_36\_12 15 m TKE continues climbing to  $> 3.25 \text{ m}^2\text{s}^{-2}$  by 2000 UTC, while the 40 m TKE remains around  $2.50 \text{ m}^2\text{s}^{-2}$ . From 2300-0200 19-20 September 1997, the 19\_36\_12 TKE trace rapidly descends to a minimum value in TKE around  $0.20 \text{ m}^2\text{s}^{-2}$ , much lower than the observations. The observed TKE again begins climbing above  $1 \text{ m}^2\text{s}^{-2}$  at 0400 UTC as the nocturnal low-level jet forms and then decreases back to near  $0.25 \text{ m}^2\text{s}^{-2}$  by 0600 UTC, remaining constant throughout the remainder of the simulation. Unlike the other two 36 km simulations, the 19\_36\_12 shows only a small increase in (5/15) and 40 m TKE between 0400-0600 UTC in response to the low-level jet.

Overall, the 36 km 12 UTC DFW simulations validate better than their 00 UTC counterparts in the convective portion of the boundary layer and display more signal during the nocturnal boundary layer. The evolution of the convective

boundary layer, which was well simulated in a 12-hr forecast range by the 00 UTC simulations, are even closer to the observed TKE values in the 12 UTC simulations. The better 12 UTC validation during the day suggests that TAPPS-2 may handle the convective boundary layer formation and attendant turbulence profiles due to (1) in shorter forecast times and better initial conditions from the 12 UTC radiosondes. The 12 UTC simulations appear to have more TKE oscillations in near-surface turbulence forced by the diurnal low-level jet (DLLJ) than their 00 UTC counterparts, as discussed in K00. Traces of TKE from the 36 km 00 UTC simulations showed little variability during the nocturnal boundary layer, while the 12 UTC simulations show a response to the formation of a diurnal low-level jet feature consistent with the observations over the Southern Great Plains. The impact of the low-level jets on the turbulence structure is discussed in length in Section 3.2.4.

As noted in the 00 UTC simulations, there were significant differences in the TKE profiles between the 60-level 36 km simulations and 90-level 6-km simulations. The TKE traces from the three validation days are shown in Figures 28-30 for (17/18/19)\_06\_12 simulations. As was the case with the 00 UTC simulations, the near surface (5/15) m TKE trace shifts significantly downward, while the 40 m TKE trace remains just slightly below the 36 km forecast. The 40 m TKE in the (17/18)\_06\_12 occurs slightly after the observed maximum from the AVOSS tower data. The TKE trace in the 19\_06\_12 simulation is much smaller than its 36 km outer grid mesh, with the 40 m TKE trace having lower overall error and reaching a maximum value around the same time as the

observations. The diurnal low-level jet signal in the 6 km simulations are consistent with the 36 km grid mesh with the TKE trace shifted slightly downward at 40 m and significantly downward at (5/15) m. The low-level jet signal is strongest in the 18\_06\_12 simulation closely matching the time evolution in the 36 km grid mesh. The 19\_06\_12 simulation shows a stronger low-level jet signal than its 36 km counterpart, closely matching the time evolution indicated in the AVOSS tower observations. Overall, the 6 km TKE traces using a 12 UTC initialization time have lower overall error at the 40 m validation height than the 00 UTC simulations, consistent with the results in the 36 km coarser grid mesh.

The 1-km simulation traces of TKE are, as shown in the 00 UTC simulation sets, not appreciably different than the 6-km grids. The TKE trends for the three validation days at a 1-km grid resolution, however, appear to have a slower response to the building of the convective boundary layer at times than the 6-km grids, as noted for 18\_01\_12 (e.g. Fig. 31). Combination plots of the TKE trace from the 6 and 1-km grid meshes confirms a slight downward shift in the TKE trace, but the shift is not as substantial as the difference between the 36 and 6 km grids.

Analysis of the traces in EDR during the daytime from the 12 UTC 36 km, 6 km, and 1 km simulations reveal remarkably consistent patterns that were noted in the 00 UTC of the same horizontal grid resolution. The (5/15) m EDR is substantially higher than the observed near-surface values, while the 40 m EDR is within a half-order of magnitude of the observations for all three validation days during the convective boundary layer structure (e.g. Fig. 32-34 for 36 km, Fig. 35-

37 for 6 km). The difference in nocturnal boundary layer evolution in EDR is also noted, with the eddy dissipation rates rising in conjunction with the rises in TKE noted during the formation of the nocturnal low-level jet (e.g. Fig. 25-27). The EDR values during the nocturnal boundary layer structure actually approach, and in some cases, exceed EDR values forecasted during the daytime despite lower values of TKE (e.g. for 18\_06\_12, Fig. 36). The shift in maximum EDR to the nocturnal boundary layer was not found in the 00 UTC simulations, with the maximum EDR values occurring during the daytime hours coincident with the maximum in TKE. The results suggest that the 12 UTC simulations are resolving the nocturnal low-level jet more accurately than the 00 UTC simulations and adjusting the near-surface EDR values accordingly, and this hypothesis is further examined in Section 3.2.4.

#### *3.2.4: TAPPS-2 Multi-Variable Sounding Analysis*

As part of the suite of products generated by the TAPPS-2 forecasting system, a cubic splining algorithm, as discussed in Section 2, is used to generate soundings of many crucial turbulent-diagnostic variables within the planetary boundary layer. As such, soundings of temperature, head-wind and crosswind velocity components, turbulent kinetic energy, and eddy dissipation rate are produced at a 5-m vertical resolution from the lowest model layer (generally between 6-11 meters) to a height of 2000 m for all horizontal grid resolution and initialization times within the validation simulation suite. The analysis of sounding structure between the various simulation configuration will allow for a more complete understanding of the model evolution which contributed to the

validation statistics discussed in Sections 3.2.2 and 3.2.3, as well as a better understanding to the changes made between the TAPPS-1 and TAPPS-2 simulation systems.

The first series of sounding analysis involves the cross-runway ( $u$ ) and headwind ( $v$ ) wind velocity components. As illustrated in K00 using the TAPPS-1 modeling system (at 36 and 12 km horizontal resolutions), the TAPPS-1 validation simulations over the 17-19 September 1997 time frame accurately simulated the mesoscale structure and evolution of the diurnally-driven low-level jet over North Texas. The strong upper-level anticyclone, as discussed in Section 3.1, produced synoptic scale subsidence, clear skies, and the development of strongly buoyantly-driven convective boundary layers between 17-19 September 1997. As illustrated in K00, the quiescent upper level flow pattern, which contained very weak synoptic scale boundary layer wind flow during the afternoon hours, set up prime conditions for the formation of a stable-layer inversion shortly after sunset as the boundary layer transits from convective to nocturnal mode. The strength of the inversion is controlled by differences in the diurnal range in temperature. As shown in idealized studies by McNider and Pielke (1981), the formation of a mesoscale low-level jet phenomena occurred just above the level of a nocturnally-induced temperature inversion and subsequent veering of the boundary layer flow from south-southeasterly to south-southwesterly as the night progressed. The strength of the inversion, in turn, directly impacted the magnitude of the simulated mesoscale low-level jet forced exclusively by the diurnal cycle. The TAPPS-1 modeling system accurately

simulated this process, and in order to test the utility of an altered TAPPS-2 modeling system for use in comprehensive low-level wind climatologies, the formation, structure, and evolution of cross-runway and headwind velocity profiles in both the convective and nocturnal boundary layer are performed.

The evaluation of the sounding evolution in the validation simulations has three specific aims. First, the ability of the TAPPS-2 modeling system to produce realistic forecast profiles of boundary layer evolution under different forcing mechanisms is evaluated against special rawinsondes taken during the intense observational period at DFW between 17-19 September 1997. In conjunction with the first aim, the second goal of the sounding comparison is to determine what the impact of improving the horizontal and vertical resolution in the model has on forecasting important aviation turbulence hazards, such as cross-wind velocity and associated TKE and EDR profiles. In particular, assessments of differences between the different horizontal and vertical configurations are provided. Lastly, the comparison of the 00 and 12 UTC initialization times is evaluated in order to determine which initialization time provides the best quality aviation forecast to the relevant turbulence features.

As discussed previously, the diurnally-driven low-level jet (hereafter, DLLJ) is the key forcing mechanism for turbulence within the nocturnal boundary layer and the biggest threat to aviation interests at DFW during the 17-19 September 1997 period. The sounding comparisons in this section are geared toward evaluation of the DLLJ formation, evolution, and representation in the array of validation simulations. A reference table of relevant DLLJ statistics from

the 12 relevant validation simulations is provided in Table 3. Due to similarities noted in previous sections between the 6 and 1 km validation simulations, the 1 km statistics are not provided in Table 3. The validation simulations on the 36 and 6 kilometer grid mesh were integrated for 24 hours from their respective initialization times (i.e., 00 and 12 UTC). Thus, the 00 and 12 UTC simulations included a 12 hour overlap in model coverage over the three day continuous validation period. For model evaluation within the nocturnal boundary layer, the overlap included the present days 00 UTC simulation and the previous days 12 UTC simulation, which would include information in a 12-hour window directly corresponding to output from the present day 00 UTC simulation. Therefore, an inter-comparison between the 00 and 12 UTC simulations is possible for several nocturnal boundary layer periods in the validation.

Vertical soundings of temperature (e.g. Fig. 38) between 12-00 UTC on 17-18 September in the 17\_36\_00 simulation indicates that a 13 K increase in surface temperature after the nocturnal inversion at 500 m mixes out, giving way to a nearly dry-adiabatic lapse rate. Immediately following sunset, vertical soundings of cross-wind (e.g. Fig. 39) from 18\_36\_00 velocity indicate the near-surface wind backs to an easterly component in the lowest 200 m of the boundary layer, reaching a negative maximum of  $3 \text{ ms}^{-1}$  at 165 m at 0300 UTC. Using the radar-derived winds from the Dallas-Fort Worth radar site (FWD), the backing of the surface flow is also shown, and indicates that the model has under-estimated the backing in the first three hours after sunset. The backing near-surface nocturnal boundary layer flow is in response to the horizontal

pressure gradient induced by both synoptic and terrain differences, as noted with observations and simulations in the TAPPS-1 system (e.g. K00). The cross-wind velocity component then veers significantly with height and the near-surface cross-wind velocity veers with time as the DLLJ develops. The headwind (e.g. Fig. 40) velocity soundings indicate that the DLLJ quickly is apparent by 0300 UTC, reaching a maximum value of  $16 \text{ ms}^{-1}$  at 0600 UTC at a height of 325 m (e.g. Fig. 40). Examination of the nighttime evolution in temperature (e.g. Fig. 41) shows a pronounced nocturnal inversion which strengthens with time to a maximum value at 11 UTC. The cross-wind velocity component continues increasing in response to the temperature inversion throughout the overnight hours, reaching a maximum value of  $10 \text{ ms}^{-1}$  at 1200 UTC 18 September around 400 m (e.g. Fig. 39). The crosswind and headwind velocity components appear out of phase, with the crosswind velocity reaching a maximum value 3-6 hr after the headwind velocity maxima, consistent with the observations and simulations in K00. The height of the DLLJ in the headwind velocity component does not vary much with height and only varies slightly in the crosswind component. Evaluation of direct turbulence diagnostics, such as turbulent kinetic energy (TKE) and eddy dissipation rate (EDR) in sounding format from 18\_36\_00 indicate that the surface layer TKE and EDR reach a maximum value at 25 m at the same time as the headwind velocity component, as shown in Table 3 and Figures 42 and 43. The TKE and EDR profiles in the nocturnal boundary layer go to zero below the level of the DLLJ, with the slope in EDR change more drastic than the TKE profile. Therefore, the turbulence profiles are restrained below the

level of the DLLJ and below the level of the maximum shear, which would impact planes departing and arriving at the airport.

The 17\_06\_00 simulation shows similar crosswind, headwind, and turbulence profiles and patterns and evolution when compared to the 36 km simulation with only a few exceptions. The main difference between the two simulations is that the height of the DLLJ in the headwind velocity component increases around 100 m between 06-12 UTC (e.g. Fig. 44), and the crosswind velocity maxima is about 90 m higher than in the 36 km grid. The 36 km grid showed very little change in DLLJ height, despite an upward displacement in temperature inversion height with time. The temperature profiles from 17\_06\_00 are similar to 17\_36\_00, but show more complex structure, especially later in the model integration (e.g. Fig. 45). The results suggest that the increase in horizontal and vertical resolution may indeed impact the evolution of the DLLJ and subsequent turbulence in the nocturnal boundary layer. The maximum value of TKE and EDR in the 6-kilometer grids is 20 m higher than the 36-kilometer grids. Closer examination of the TKE and EDR soundings (e.g. Fig. 46-47) reveal that the TKE and EDR profiles in the 36-kilometer grids increase abruptly from the near surface (5/15 m) to a maximum value near 20 m, where the 6-kilometer grids increase at a slower rate to a maximum value near 40 m. The differences in TKE and EDR soundings between the two grid meshes are directly attributable to a change in sigma level distribution shown in Table 4 and discussed in Section 2. The loss of one sigma level near the ground in the 6 kilometer grid meshes due to smoothing of the sigma distribution primarily forces lower near-surface (i.e.

5/15 m) validation, discussed in Section 3.2.3, and shifts the TKE and EDR curves slightly upward near the ground when compared to the 36 km grids. The same pattern in TKE and EDR is noted in the remainder of the validation simulations, and the soundings are revisited as part of the characteristic mixing length sensitivity shown in Section 4.

The 17\_(36/06)\_12 and 18\_(36/06)\_00 simulations have 12-hr periods which overlap during a nocturnal boundary layer and DLLJ period, namely, the simulation period between 00-12 UTC 18 September. As shown in Table 3, the crosswind velocity maximum is located, on average, between 350-500 m with a range of DLLJ values between 10-13  $\text{ms}^{-1}$  at 11-12 UTC. The headwind velocity maximum ranges from 16-18  $\text{ms}^{-1}$  within the 350-500 m layer at 09 UTC, with only the 18\_36\_00 simulation having a DLLJ maximum at a different time. All four simulations show that the height of the DLLJ varies between 50-200 m throughout the entirety of the simulation period in both the 36 and 6 km grid meshes. In general, upward (downward) displacement of the crosswind DLLJ height occurs prior (after) the headwind velocity maximum is reached. Daytime soundings of vertical velocity from all four simulation sets (e.g. Fig. 48) indicate synoptic scale-subsidence, on the order of  $10^{-2} \text{ms}^{-1}$ , occurs over the airport and generally increase with time during the day. At night, vertical velocity profiles in the majority of the simulations during the 00-12 UTC 18 September period reveal rising motion on the order of  $10^{-2}$ - $10^{-3} \text{ms}^{-1}$  above and below the height of the DLLJ. As shown in Table 3, maximum values of TKE and EDR corresponds to

the maximum value of headwind velocity component, and the turbulence profiles were restricted below the DLLJ level in all of the simulation sets.

Using the closest proximity sounding taken during the overnight hours on 18 September from Plano (PLNO), Texas, observed crosswind and headwind velocity components are compared to the modeled wind components. The headwind velocity component profiles are very similar for all four simulations, with the strongest headwind velocities within the DLLJ found in the 17\_36\_00 simulation. A distinct difference in crosswind component profiles as a function of grid configuration, namely, the 36 and 6 km grid meshes, is noted for the 00-12 UTC 18 September 1997 period. Crosswind velocity profiles from 17\_36\_12 and 18\_36\_00 indicate that the crosswind velocity reaches a maximum value at the DLLJ height and then smoothly backs in direction and decreases in magnitude with height to 2 kilometers (e.g. Fig. 39 and 49). The same profile is noted in 18\_06\_00 (e.g. Fig. 50), with the crosswind smoothly decreasing toward zero and then returning to an easterly component above 1 km. Using the asynoptic balloon observations from the closest sounding location to the center of grid, the Plano, Texas (PLNO) soundings are plotted against the 18\_06\_00 crosswind soundings (e.g. Fig. 51). The sounding from Plano indicates that the crosswind velocity does not necessarily smoothly decrease with height late in the period, particularly in the 08-12 UTC 18 September near 1.5 km. The presence of secondary u-wind maxima is more apparent in the 17\_06\_12 simulation, where a secondary maximum in crosswind velocity occurs at 1.5 km (e.g. Fig. 52), well above the DLLJ maximum at 400-500 m. The crosswind DLLJ signal within the

nocturnal boundary layer in 17\_06\_12 is  $2 \text{ ms}^{-1}$  stronger than observations at 9 UTC and  $\sim 4 \text{ ms}^{-1}$  stronger than observations at 12 UTC. Similarly, the secondary wind maximum at 1.5 km is  $4\text{-}6 \text{ ms}^{-1}$  higher than the observations. The model crosswind velocity profiles closely match the observations in terms of vertical distribution and timing, suggesting that the TAPPS-2 simulation is accurately simulating the wind structure and overestimating the strength of the jets. In addition, the surface wind within the lower 500 m of the boundary layer in 17\_06\_12 shows that the near surface boundary layer flow is more easterly for a longer duration of time than the other three simulations, suggesting differences in the horizontal pressure gradient across Northern Texas. The temperature soundings from 17\_06\_12 (e.g. Fig. 53) indicate that the lapse rates between 00-03 UTC are steeper than the other three simulations (e.g., 17\_36\_12 and 18(36/06)\_00) from the surface to 1 km. In contrast, the temperature profile is warmer in 17\_06\_12 between 06-11 UTC and not nearly as dry adiabatic as the other three simulations, suggesting that the thermal character of the 1-2 kilometer layer is most likely providing the majority of the crosswind profile differences. Thus, differences in the temperature profiles above the nocturnal boundary layer apparently induce a secondary wind maximum above the DLLJ at 1.5 km on 18 September, and the 17\_06\_12 was the only TAPPS-2 simulation to capture the secondary crosswind maximum. The presence of a secondary crosswind maximum within 17\_06\_12 and the observations imply the presence of a secondary shear layer within the free atmosphere displaced by almost 1 km from the DLLJ, which would provide another source of danger for approaching or

departing aircraft aside from the turbulence within the nocturnal boundary layer. A further analysis, including a sensitivity test focused on the development of a secondary cross-wind maxima, is presented in Section 3.2.5.

The second period of model overlap occurs during the 00-12 UTC 19 September time frame from the 18\_(36/06)\_12 and 19\_(36/06)\_00 TAPPS-2 simulations. The comparison of the DLLJ within the headwind velocity component reveal maximum headwind velocity ranging from 17 (20)  $\text{ms}^{-1}$  in the 18\_36\_(06)\_12 simulations to 17  $\text{ms}^{-1}$  in the 19\_(36/06)\_00 simulations. The DLLJ heights varied a bit from simulation to simulation, but were confined to the 400-500 m layer. Observations from the PLNO soundings indicate that the maximum value of the DLLJ in the simulation period was 17  $\text{ms}^{-1}$  at a height 550 m at 08 UTC 19 September, similar to the simulated DLLJ within TAPPS-2. The higher values of headwind velocity in the 18\_(36/06)\_12 simulations lead to TKE maximum in the 25-40 m layer almost twice that of the 19\_(36/06)\_00 simulations, as noted in Table 3. The TKE and EDR were highest in the 18\_36\_12 simulation, consistent with the highest value of headwind velocity among the four simulations.

The maximum value of cross-wind velocity varied more between the simulations, with crosswind velocity maximum near 8.5  $\text{ms}^{-1}$  in the 18\_(36/06)\_12 simulations and near 10  $\text{ms}^{-1}$  in the 19\_(36/06)\_00 simulations. Vertical soundings of temperature from 18\_36\_12 (e.g. Fig. 54) indicate that the nocturnal inversion is present in the 400-500 layer between 00-12 UTC with the surface temperature cooling 9 K between 00-12 UTC. The vertical profile of

crosswind velocity in 18\_36\_12 (e.g. Fig. 55) shows that the crosswind velocity minimum occurs at 03 UTC, after which, the near surface flow veers to a more westerly direction. Above the DLLJ, the crosswind velocity decreases rapidly below zero with height, indicating an easterly component to the wind velocity above the nocturnal boundary layer. The soundings within 18\_06\_12, however, reveal a much different thermodynamic and attendant kinematic profile than the 36 km grid. The vertical profile of temperature in 18\_06\_12 shows only 4 K of cooling at the surface between 00-12 UTC 19 September and more complex temperature structures, including the presence of a few isothermal layers, above the nocturnal inversion within the 1-2 kilometer layer (e.g. Fig. 56). The more complex temperature structure was noted within the 17\_06\_12 simulations, with the development of a secondary wind maximum at the 1.5 km level consistent with observations from the PLNO soundings. As such, the presence of a secondary wind maximum is shown in the 18\_06\_12 simulation above the nocturnal inversion, developing sharply in the 03-09 UTC 19 September time frame (e.g. Fig. 57). As with 17\_06\_12, the near surface boundary layer flow acquires a stronger easterly component of flow between 03-06 UTC before veering more westerly as the night progresses, suggesting substantial differences in horizontal pressure gradients between the 36 and 6 kilometer simulations. The crosswind velocity profile at 06 UTC is very complex, with  $-4 \text{ ms}^{-1}$  crosswind flow near the surface (i.e.,  $< 250 \text{ m}$ ) changing to nearly  $10 \text{ ms}^{-1}$  at 1400 m. Observations from PLNO, shown with 18\_06\_12 in Figure 58, indicate that the dramatic shift in crosswind velocity was present at 02 UTC 19

September, with near surface crosswind velocities near  $-10 \text{ ms}^{-1}$  to  $2 \text{ ms}^{-1}$  at 1400 m. In addition, the 09/12 UTC crosswind velocity profile has very low error throughout the depth of the boundary layer when compared to the 08/11 UTC PLNO observations, capturing both the DLLJ signal near 500 m with a  $\sim 2 \text{ ms}^{-1}$  under-prediction. The 08 and 11 UTC PLNO soundings also indicate the presence of a secondary wind maximum in the 1400-1600 m layer, which the 18\_06\_12 simulation captures but under-predicts at 09 and 11 UTC, respectively. However, these secondary wind maxima were not present in the 36-kilometer simulation, suggesting that the increased horizontal and vertical resolution is indeed aiding in moving the model simulation closer to the actual observations. The presence of secondary wind maxima is noticeably absent in the 6 kilometer simulations covering the 00-12 UTC 19 September 1997 in the 00 UTC simulations. Examination of the headwind velocity profile shows that the 19\_06\_00 DLLJ height is  $\sim 100 \text{ m}$  higher than 19\_36\_00. Similar magnitudes and evolution of crosswind velocity are noted throughout the entire duration of the model integration. Vertical soundings of temperature between 19\_36\_00 and 19\_06\_00 (e.g. Fig. 59 and 60) reveal a larger nocturnal temperature range in the 19\_06\_00 simulation and similar nocturnal inversion formation. Above the nocturnal boundary layer, the temperature profiles between the 36 and 6 km grids are very similar and contain no isothermal or inversion layers above the nocturnal boundary layer. The vertical soundings of crosswind velocity (e.g. Fig. 61 and 62) show that both the 19\_36\_00 and 19\_06\_00 simulations have smooth transitions in crosswind velocity from the DLLJ maximum at 400 m into

the free atmosphere. In the 18\_06\_12 simulation, the presence of a secondary wind maximum appears related, at least within the point sounding validation, to a more complex temperature structure within the 1-2 kilometer layer, similar to the observations from PLNO soundings.

The sounding analysis unambiguously shows the development of a secondary maximum in the crosswind (u) component within several of the validation simulations and is consistent with observations taken from the PLNO soundings. Further investigation of the raw data taken from the soundings suggests that the headwind velocity component decreases, and thus, the overall magnitude of the total wind does not increase. The profile adjustments, as noted previously, are likely not tied to local changes in any patterns within the DLLJ since the maximum occurs within the free atmosphere well displaced from the developing nocturnal inversion. The secondary crosswind maximum is best described as a secondary shear layer and not a “jet” phenomena. However, since the u-wind represents the cross-wind component at DFW, an increase in u-wind velocity over a certain depth would suggest that a secondary area of increase turbulence generation via mechanical shear is present. The TAPPS-2 simulation actually identifies the hazard, as shown in Figure 63, where a secondary increase in TKE forced by mechanical shear generation in the u-wind direction is noted in the 1.5-2 km layer at 09 UTC. The secondary crosswind maximum and resultant secondary shear layer could pose a significant threat to unaware approaching or departing aircraft, and is studied further in the preceding section.

### *3.2.5: TAPPS-2 Crosswind Velocity Sensitivity Test*

As noted previously, the development of an observed secondary crosswind maximum was present in the 6 km 12 UTC DFW simulations and not the 6 km 00 UTC simulations or either set of 36 km simulations on both 17 September and 18 September 1997. Using the closest proximity sounding from Plano, Texas (PLNO), evidence of a secondary crosswind maximum is present at the 1.5 km level for both of the validation days. Since the vertical distribution of model sigma layers change at in the TAPPS-2 modeling system when one goes from 36 to 6 km, changes in both the horizontal and vertical resolution occur. Therefore, separation or any direct diagnosis of the impact of increasing the vertical or horizontal resolution on a simulated feature is not possible from the original validation simulations. In order to investigate the impact of increasing the resolution from the outer 36-kilometer grid to the 6-kilometer grid and attendant 30-sigma level increase, a sensitivity test is performed. The 12 UTC 18 September validation simulation, covering the nocturnal boundary layer period from 00-12 UTC 19 September is chosen to run a 36-kilometer 90-sigma level run, focusing on the development of a secondary wind maximum at the 1.5 km level. In addition to model configuration sensitivity, explanations and analysis of the factors responsible for a possible secondary crosswind maximum are also explored.

The sensitivity test for the 00-12 19 September 1997 period allows for a direct comparison between the 60-level 18\_36\_12 (control, hereafter, CTRL) simulation and the 90-level test simulation, labeled 18\_36\_12\_TST. Though

some differences are noted, for the most part, the evaluation of daytime soundings of temperature, wind, and TKE/EDR between the CTRL and TST simulations is quite minimal; suggesting the increase in vertical resolution may not have a big role in changing the boundary layer in quiescent and primarily convective conditions. However, a significant change in the nocturnal boundary layer is noted, starting with the temperature inversion evolution in Figure 64. The CTRL simulation develops a nocturnal inversion only 1 K in strength between 400 and 500 meters at 11 UTC, with the first signs of an inversion not readily apparent until 09 UTC. At 06 UTC, the inversion development is seen in the form of a near isothermal layer between 400-500 m. In the TST simulation, the nocturnal inversion has already developed by 06 UTC in the 100-200 m layer, and by 09-11 UTC, the inversion is much stronger and 3-4 K warmer at 500 m than the CTRL. The results indicate that the 30-sigma level increase in the TST simulation leads to stronger nocturnal inversions that develop faster than their 60-level counterparts. The trend was shown in the 6-kilometer temperature soundings shown earlier in the sounding analysis.

The headwind velocity component comparison (e.g. Fig. 65) reveals changes in the magnitude and structure of the DLLJ also occurred when the sigma levels were changed. In the CTRL, the DLLJ reaches a maximum intensity of  $\sim 20 \text{ ms}^{-1}$  at 0600 UTC. In the TST simulation, the DLLJ reaches maximum intensity of only  $\sim 17 \text{ ms}^{-1}$  three hours later at 0900 UTC. In addition, finer scale structure is noted in the DLLJ wind profiles in the TST simulation when compared to the CTRL. Therefore, subtle changes in the nocturnal temperature evolution,

as noted in Figure 64, would have an impact on the strength and structure of the DLLJ. One possible explanation for the delayed timing and smaller magnitude of the DLLJ in the headwind velocity component in TST is an increase in mixing around the inversion height due to the higher vertical resolution. In any event, as noted in the temperature profiles, a much different solution is obtained when the 90-vertical level sigma structure is used.

The crosswind component soundings, shown in Figure 66, reveal that a secondary crosswind maximum in the 1.5-km layer is not generated in the TST simulation, as was the case in the 6 km simulation. However, the crosswind velocity profile in TST does not smoothly decrease with height as it does in the CTRL simulation, with the u-wind velocity remaining constant with height between 1-1.75 km. The CTRL simulation has u-wind velocity values  $\sim 1.5 \text{ ms}^{-1}$  at 1.5 kilometers between 09-11 UTC, while the TST simulation has u-wind velocity values near  $1 \text{ ms}^{-1}$  between 09-11 UTC at 1.5 kilometers. Therefore, while increasing the vertical resolution did not develop an intense secondary wind maximum, the TST simulation did have a much different solution to the crosswind velocity above the nocturnal inversion, indicating that the increase in vertical resolution does play a significant role in the wind profiles. However, the increase in horizontal resolution must also play a role in developing the secondary shear layer, and illustrates the utility of the higher resolution simulations in TAPPS-2.

As noted in Fig. 66, while the u-wind velocity changes sign, the overall magnitude of the wind does not increase between TST and CTRL. Therefore, the

overall direction of the wind must change in the 1-2 kilometer layer between the two simulations. As discussed previously, since the total magnitude of the wind does not change, the feature diagnosed in the 6 km 12 UTC simulations and observations is not a jet, and therefore, cannot be forced by any low-level jet formation mechanism. In addition, since no convection occurs in the simulation and the region of interest is far displaced from steep topography, diabatic effects (e.g. Lackmann 2002) or orographic effects (Wexler 1961) can contribute to the DLLJ from the different proposed low-level jet formation mechanisms (Lin 2007). The change in u-wind sign indicates that since the mean flow direction is southerly within the DLLJ in the Southern Plains, the u-wind velocity must veer in the 1-2 kilometer layer from a southerly direction to a more westerly direction. The veering of the DLLJ was discussed in K00, and is common in strong low-level jet patterns across the Southern Plains. Since the upper-level ridging present over North Texas during the period prevents any synoptic scale forcing from affecting the region, large scale forcing can be eliminated as a possible cause of a wind direction change. Using the geostrophic wind relationship, the magnitude of the u-wind component can be changed by fluctuations in the geopotential height field, such that:

$$u_g = -\frac{1}{\rho f} \frac{\partial \Phi}{\partial y} \propto \frac{\partial T}{\partial y} \quad (3.2.5.1)$$

where  $\Phi = gz$ , the geopotential height. Thus, a change in the north-south orientation of the geopotential height could affect the magnitude of the u-wind component. Investigations of the 850-mb height and wind field north of the DFW metroplex show that simulations in which no secondary shear layer develops has

a much weaker 850-mb height gradient and subsequently, a weaker 850-mb temperature gradient (i.e. Fig. 67). However, the 6 km 12 UTC simulations in which a secondary crosswind maximum does develop has a 850-hPa height and temperature gradient that shifts from a east-to-westerly orientation to a more north-to-south orientation (i.e. Fig. 68). The change in orientation occurs within the first 1-3 hr after sunset, where significant warming in the 850-hPa layer occurs over the Texas Panhandle and Western North Texas. Shortly thereafter, the 850 h-Pa flow veers to the southwest, and would thus increase the magnitude of the crosswind velocity in a sounding format. Therefore, one possible mechanism which could be responsible for increasing the crosswind velocity in the 1-2 km layer over DFW and the development of a secondary shear layer would be the veering of the DLLJ in the free atmosphere above the nocturnal inversion in response to changing temperature and height patterns north of the airport. The more complex temperature patterns noted in the sounding analysis over DFW in which the secondary shear layer developed could be tied to the warming in the 850 hPa layer noted in the temperature and height analysis. The warming is attributed to the advection of the residual layer from the veering DLLJ origination in the higher terrain over West Texas. Since the crosswind shear layer did not develop in simulations where the 850 hPa flow does not veer to the southwest, the warming due to the advection of the residual layer would not be aligned as favorably, and thus, the 850-hPa height gradient would not change orientation as it does in simulations where the veering occurs. The results suggest that while the inertial oscillation mechanism (Blackadar

1957) may be forcing the DLLJ primarily, baroclinic effects (Bleck and Andre 1951, Holton 1967) may play a role in altering the direction of the crosswind component via adjustments in the temperature and height structure north of the airport.

#### **4. Eddy Dissipation Rate Sensitivity: DFW Validation Simulations**

##### *4.1: Introduction*

As shown in Section 3.2.3 and 3.2.4, the profiles of turbulent kinetic energy (TKE) and eddy dissipation rate (EDR) were validated in point format using AVOSS tower data from Dallas-Fort Worth International Airport (DFW) during an IOP from 17-20 September 1997. The results from Section 3.2.3 suggested that the 36 and 6 km grids estimated the profiles of TKE generated from convective and nocturnal boundary layers differently across the 3-4 day period. The 36 km TKE from the 12 UTC simulations tended to validate better against the AVOSS tower observations at 40 m than the 00 UTC simulations. The 6 km TKE time series from the 12 UTC simulations tended to under-estimate the value of TKE dramatically near the surface (i.e., 5/15 m) and slightly at 40 meters. Investigations of the vertical profile of TKE presented in Section 3.2.4 illustrated that the TKE profile was shifted, on average, around 15-20 m upward in the 6 km grid simulations due to a change in sigma level distribution in employing the new TAPPS-2 system. However, the profile of TKE throughout the depth of the boundary layer was relatively consistent between the 36 and 6 km simulations in both the 00 and 12 UTC simulation sets regardless of boundary layer regime. The TKE reached a maximum value at 20 (40) meters in the 36 (6)

kilometer grids, then remained relatively constant with height during the convective boundary layer and decreased rapidly to zero at the height of the DLLJ in the nocturnal boundary layer. Though the 6 km grids had lower overall TKE than the AVOSS tower observations, the evolution of TKE throughout the simulation period closely mimicked the observations.

The validation of the eddy dissipation rate (EDR) in the 36 and 6 km grids revealed that the 36 km grids tended to dramatically over-estimate EDR by one to two orders of magnitude near the surface (i.e., 5/15 m) and had relatively good validation at 40 m. The 6 km grids had EDR traces that matched the evolution within the tower observations, but were shifted one half to one full order of magnitude higher than the observations. Evaluation of the sounding structures in Section 3.2.4 revealed that the EDR profiles showed only slight variation across the 36 and 6 km grid meshes, reaching a maximum value coincident with the maximum in TKE at 20 (40) meters in the 36 (6) kilometer simulations. The EDR profile then became constant with height to the level of the DLLJ in the nocturnal boundary layer and decreased rapidly to below  $10^{-3} \text{ m}^2\text{s}^{-3}$  above 100 meters. The TKE profiles, on the other hand, showed more variation and higher values above 100 meters, bringing into question the rapid decrease of EDR above 100 meters. The crosswind validation presented in Section 3.2.4 also revealed that the 6 km simulations may have benefited from having additional horizontal and vertical resolution and resolved secondary wind maxima in the crosswind component, particularly in the 12 UTC 6 km simulations. The secondary wind maxima would

provide a secondary shear layer and source of potential danger for aircraft in addition to the DLLJ generated just above the nocturnal boundary layer.

#### 4.2: Sensitivity Experiment Design

From Section 2, the model EDR generated from the TAPPS-2 PBL scheme is represented by:

$$\varepsilon = \frac{e^{-3/2}}{\Lambda}, \Lambda \equiv \frac{1}{8l_e} \quad (4.1.1)$$

where  $l_e$  is the dissipation length scale and  $e$  is the model averaged TKE profile at the given model sigma level. The dissipation length scale is a complicated function of model stability, shear, and PBL height as derived from a 3<sup>rd</sup>-order closure simulation from Therry and Lacarrere (1983). The formulation in Eq. 4.1.1 is used in the 1.5-order TKE-based PBL scheme in the NHMASS model, the core of the TAPPS-2 simulation system. The problem of closure in the planetary boundary layer has been discussed by authors such as Stull (1988) and Ayra (2001), as the parameterization of the characteristic length scale  $\Lambda$  is rather arbitrary and is a source of error in most 1.5-order closure TKE schemes. While the formulation from Therry and Lacarrere (1983) is rather elegant and advanced, other authors have made use of different characteristic length scales. In particular, Frech and Hozapfel (2006) used a constant value of characteristic length scales for simulations of wake-vortex operations in Germany. Variations in the characteristic length scale, as shown in Eq. 4.1.1, would have a significant impact on the EDR profiles within the TAPPS-2 simulations.

Since the model eddy dissipation rate is a function of only two dependent variables (TKE and the dissipation length scale  $l_e$ ), investigations of alternate

formulations of EDR are possible by varying the characteristic length scale  $\Lambda$ . From the point validation presented in Section 3.2.3 and the sounding analysis in Section 3.2.4, the model profiles of TKE appear to capture atmospheric trends and responses to turbulence reasonably well when compared to the AVOSS tower data, especially at a 40 m validation height. Thus, if we take the model-derived TKE to be representative of the true nature of the turbulence profiles observed at DFW, varying the other dependent variable in the EDR formulation, the characteristic length scale, would provide a sensitivity test for the EDR formulation. Different forms of EDR formulation may improve on the current TAPPS-2 EDR algorithm and provide additional data to aid a statistically-based forecasting database for use by air-traffic-controllers (ATC).

The sensitivity test for the EDR formulation is based off varying the characteristic length scale  $\Lambda$  in three different manners. First, the model-derived EDR, labeled as “MASS” in vertical soundings and time series plots in this section, is based off the variant dissipation length scale hypothesis in the original model scheme from Therry and Lacarrere (1983). The other two formulations of EDR derive information from the AVOSS tower data presented in point validation form in Section 3.2.3. Since the observed TKE and EDR at 40 meters is available at all of the validation times, an observed estimated characteristic length scale  $\Lambda$  (or, after scaling, dissipation length scale  $l_e$ ) can be calculated. Using the design of Frech and Hozapfel (2006), a secondary formulation of EDR may be derived by setting the characteristic length scale to a constant value derived from the observations. Since this formulation algorithm is based off of Frech and

Hozapfel's (2006) work on the NOWVIV wake vortex forecasting system, the second EDR formulation is labeled "NOWVIV" in the succeeding analysis. The third version of EDR is based off of curve fitting technique derived from the estimate observed characteristic length scale. All three versions of EDR are then compared to the original formulation of EDR from the AVOSS tower data.

#### *4.3: EDR Formulation Sensitivity Results*

Using the tower data at 40 m from the AVOSS data set, an estimation of the characteristic length scale  $\Lambda$  is derived from the observed TKE and EDR and subsequently compared to the estimate the characteristic length scale from the TAPPS-2 TKE PBL scheme for the 17-19 September 1997. Since the NHMASS model calculates the dissipation length scale, which is a scaled factor of the characteristic length scale, plots of the eddy dissipation length  $l_e$  as a function of TAPPS-2 horizontal and vertical grid spacing (i.e., 36km, 6km), are show in Figures 69-70. The observed characteristic length scale when calculated at the 40 m level appears to remain nearly constant in the nocturnal boundary layer, with an average characteristic length scale of 336 meters between 00-12 UTC during the validation period. The characteristic length scale during the day, however, grows as the convective boundary layer grows, in a pattern reminiscent of a Gaussian curve, reaching maximum values of over 2000 meters between 19000-2100 UTC. The length scale then rapidly decreases back to a more constant value that rarely drops below 300 meters between 00-12 UTC within the nocturnal boundary layer. The modeled characteristic length scale, on the other hand, is much lower than the observations across all grid resolutions and

initialization times at the 40 m height. The 36 km grid meshes tend to over-estimate the characteristic length scale at 40 m during the mid afternoon hours (i.e., 17-21 UTC) and under-estimate the characteristic length scale at night with errors, on average, over 200 meters between 00-12 UTC for the validation days. In the 6-kilometer simulations (e.g. Fig. 70) the characteristic length scale is again much lower than the observations during both the day and night, with average mean errors at the height in the convective boundary layer and within the nocturnal boundary layer approaching 200 meters. However, the TAPPS-2 characteristic mixing length profiles do suggest an increase, albeit rather weak, in response to the building of the convective boundary layer, consistent with the strong diurnal signal in the observations. The mixing lengths stay much lower than that observed from the AVOSS tower data at DFW across all different model configurations at the 40 m validation height. Vertical soundings of the characteristic mixing length  $\Lambda$  taken from the 12 UTC 6 km simulations on 18 September (e.g. Fig. 71) show that the TAPPS-2 characteristic length scale increases with height and time as the convective boundary grows. The length scale increases at a very steep slope from the surface to 200 m, then increases at a slower rate to the estimate top of the boundary layer, where the mixing length reaches its maximum value, between 1200-1600 meters during the late afternoon hours. Above the top of the convective boundary layer, the characteristic mixing length decreases rapidly with height and approaches 1-3 meters up to the 2 kilometer vertical level. During the nighttime hours, the characteristic length scale reaches a maximum value of 200 meters below the

level of the DLLJ, between 200-300 m AGL. The length scale then decreases below 50 m throughout the remainder of the sounding. A notable exception to this profile occurs above 1.5 km, where the mixing length increases to over 300 m at 09 UTC in response to elevated TKE (e.g. Fig. 63) and the presence of secondary crosswind maxima and crosswind shear layer discussed in Section 3.2.4-3.2.5. In general, the time series and sounding plots of the observed and modeled estimated characteristic mixing length suggest that the modeled version of  $\Lambda$  is systematically lower than the observed characteristic length scale at 40 meters and may remain lower than the observed values throughout the depth of the boundary layer across all of the TAPPS-2 simulations in the validation period. Further validation of the mixing length scale in the vertical direction is not performed because the model TKE and EDR observed at the airport was done exclusively for the near surface (i.e., 5-40 m) layer.

Using the observed values of estimated characteristic length scale from the AVOSS tower data at 40 m, the third approach to the EDR formulation is constructed. First, the characteristic length scales at the 40 m level are averaged as a function of time during the 17-20 September 1997 periods. From these time-based averages, statistics of the observed characteristic length scale (e.g. Table 5), are generated with emphasis on the mean and standard deviation of characteristic length scale with respect boundary layer mode (i.e., convective and nocturnal). The different daytime means, standard deviations, and maximum values are to construct a quasi-normal distribution of characteristic length scale to re-estimate EDR using the observed mixing length scales. As noted in the

observations, the nighttime characteristic length scale remained roughly constant, and therefore, the characteristic length scale during the nocturnal boundary layer is set to a constant value of  $\Lambda = 400$  meters. The hourly mean characteristic length scales, however, appear to be best approximated using a normal distribution. To smooth the time-averaged characteristic length scales, one-hourly moving mean values at each 15 minute observation are performed. Using the hourly means as the base state data point, the cumulative distribution function (c.d.f) for this quasi-normal distribution is:

$$\Lambda_{GAUSS} = \frac{A}{\sqrt{2\pi}\sigma_{DAY}} \exp\left(-\frac{(\Lambda_* - \overline{\Lambda_{DAY}})^2}{2\sigma_{DAY}^2}\right) \quad (4.2.1)$$

where  $\sigma_{DAY}$  is the standard deviation of the averaged length scale between 13-00 UTC,  $\overline{\Lambda_{DAY}}$  is the mean averaged length scale between 13-00 UTC,  $\Lambda_*$  is the moving hourly-averages of the characteristic length scale, and A is the adjustment amplitude, defined as:

$$A = \Lambda_{MAX} - \overline{\Lambda_{NIGHT}} \quad (4.2.2)$$

The effect of the adjustment amplitude on the c.d.f requires that the characteristic length scale remains constant at the nighttime average and never drops below this value. At 1300 UTC, the characteristic length scale increases in a Gaussian bell-curve fashion to a maximum value at 1900 UTC and then decreases back to the average nighttime value by 0000 UTC. The profile of the Gaussian-averaged characteristic length scale for daytime hours at DFW is shown in Figure 72.

Using the three introduced variations of characteristic length scale, composite time series plots of the three EDR formulations and the AVOSS tower

data at 40 meters is shown for the 17-19 September 1997 12 UTC simulations in Figures 73-75. At 36 kilometers, the original TAPPS-2 EDR, labeled “MASS”, slightly under-estimates the EDR during the daytime hours and slightly over-estimates the EDR during the nighttime hours for 17\_36\_12 (e.g. Fig. 73) and 18\_36\_12 (e.g. Fig. 74). From 00-06 UTC, the MASS EDR closely matches the observations, then deviates to a one-half order of magnitude over-estimate by the end of the simulation. The “NOWVIV” EDR, using a constant value of  $\Lambda = 400$  m, significantly overestimates the EDR during the time hours but performs well during the nighttime hours in 17\_36\_12 (e.g. Fig. 73) and 18\_36\_12 (e.g. Fig. 74). From the observations, the averaged derived nighttime characteristic length scale remained between 300-400 m, and then grew substantially to over 2000 m at the height of the convective boundary layer. Thus, the significant over-estimation in EDR is expected since the characteristic mixing length is inversely proportional to the EDR. The “GAUSS” EDR, using the aforementioned smoothed Gaussian distribution during the daytime hours, provides a very good estimate of the 40 m EDR during the convective boundary layer as compared to the other two formulations. The average error of the GAUSS EDR in 17\_36\_12 and 18\_36\_12 during the daytime hours rarely exceed  $5 \times 10^{-3} \text{ m}^2\text{s}^{-3}$ . The EDR profile in the observations remained relatively constant at 40 m during the daytime hours, remaining between  $1-2 \times 10^{-3} \text{ m}^2\text{s}^{-3}$  throughout the majority of the three day period. The 36 km MASS EDR profile varied more than the observations responding in part to the diurnal cycle. The GAUSS EDR, on the other hand, is able to maintain a constant value of EDR throughout the daytime

hours as the characteristic mixing length profile responds to the diurnal cycle. The results from the daytime hours suggest that the GAUSS EDR's adjustment of the characteristic mixing length provides a quasi-constant value of 40 m EDR that better captures the EDR time series in the tower observations. At nighttime, however, the application of a constant mixing length in the GAUSS EDR (and, consequently, the NOWVIV EDR) tends to under-estimate the EDR in 17\_36\_12 between 00-06 UTC 18 September and overestimates the EDR between 06-12 UTC. For 18\_36\_12, however, the MASS EDR consistently over-estimates the 40 m EDR while the NOWVIV and GAUSS EDR closely resemble the observed AVOSS tower data. The results suggest that the application of the GAUSS EDR in the 36 km 12 UTC simulations did improve the validation of 40 m EDR during the daytime, and may improve the validation of EDR in the nocturnal boundary layer as well, though some exceptions are noted (i.e., Fig. 73 of 17\_36\_12 00-06 UTC).

In 19\_36\_12, the GAUSS EDR has very low errors during the daytime hours, while the MASS and NOWVIV EDR provide a one-order-of-magnitude over-estimation of the dissipation rate. As noted in the rawinsondes from the NASA launch location at FWD (e.g. Fig. 75) they suggest that the boundary layer flow beneath the nocturnal inversion between 00-06 UTC 20 September was much weaker and the TKE and EDR much lower than previous validation days. The observed EDR begins dropping off significantly from  $1 \times 10^{-3} \text{m}^2 \text{s}^{-3}$  prior to 22 UTC to  $1 \times 10^{-4} \text{m}^2 \text{s}^{-3}$  after 00 20 September UTC. All three EDR formulations resolve this one-order-of-magnitude drop in EDR, reaching a minimum value 1-2

hr after the observed EDR at 02 UTC. The sensitivity plots of EDR formulation in 19\_36\_12 (e.g. Fig. 75) that after 02 UTC, the MASS EDR drops only to a minimum of  $1 \times 10^{-3} \text{m}^2 \text{s}^{-3}$  and remains constant between 02-07 UTC. The observed EDR begins rising during the overnight hours back to a value of  $1 \times 10^{-3} \text{m}^2 \text{s}^{-3}$  during the 02-07 UTC period. The GAUSS and NOWVIV EDRs, however, remains much lower than the observed EDR and MASS EDR at  $1 \times 10^{-4} \text{m}^2 \text{s}^{-3}$  and continually drops through the overnight period to  $1 \times 10^{-5} \text{m}^2 \text{s}^{-3}$  by the end of the simulation. Examination of the estimated mixing length values from the observations (MASS formulation) suggest very low mixing lengths between 100-200 (30-70) meters, quite smaller than the constant value of 400 meters in the GAUSS and NOWVIV formulations. The results suggest that the constant value of characteristic mixing length is vulnerable to under-estimation of EDR in weakly turbulent nocturnal boundary layers when the characteristic mixing length is low, such as 19\_36\_12, and may require a downward adjustment as a function as the TKE approaches zero.

In the 6 km simulations, the EDR formulation sensitivity for 17\_06\_12 (e.g. Fig. 76), 18\_06\_12 (e.g. Fig. 77), and 19\_06\_12 (e.g. Fig. 78) illustrate the differences between the 36 and 6 km simulations. In the 36 km grid mesh, the MASS EDR varied more during the simulation period, while the observations indicate that, with the exception of a few periods, the EDR remained relatively constant. In the 6 km grid meshes, the MASS EDR remains more constant than in the 36 km grid meshes. The discrepancies between the 36 and 6 km EDR profiles are discussed in Section 2 and Section 3.2.4, where differences in

sigma-level distribution are responsible for a shift in the overall TKE and EDR profiles upward in the 90-sigma level 6 km runs. In the 36 km grid meshes, the maximum value of TKE and EDR was near 20 m, while the maximum value of EDR from the 6 km grid meshes, as discussed in Section 3.2.4, occur near the validation height of 40 m. Thus, the shift in the EDR profile upward by the sigma level distribution change is the most likely explanation for the difference in the profiles.

Examination of the EDR time series plots for the 6 km grid meshes in Figures 76-78 reveal that the MASS EDR maintains a relatively constant value near  $10^{-2}\text{m}^2\text{s}^{-3}$  throughout all three validation days, an order of magnitude higher than the observations. Meanwhile, the GAUSS EDR again provides an excellent estimation of the observed 40 m EDR during the daytime hours and tends to under-estimate EDR between 00-06 UTC in (17/18)\_06\_12 while overestimating the EDR in 19\_06\_12. The NOWVIV EDR also overestimates the EDR during the daytime hours and closely follows the GAUSS EDR during the nighttime hours. The EDR on 19\_06\_12 does not fall off as dramatically as the 36 km grid meshes and validates better than the MASS EDR, which maintains a nearly constant value at  $10^{-2}\text{m}^2\text{s}^{-3}$ . As shown in the 36 km grid meshes, the GAUSS EDR provides closer estimations of 40 m EDR than the MASS or NOWVIV EDR during the daytime hours. At night, the GAUSS EDR provides relatively good representation at night, though some exceptions exist, particularly between 00-06 UTC during the validation period. In the 6 km grid mesh, because the MASS EDR is consistently one-order-of-magnitude higher than the observations, the

GAUSS EDR provides a much better EDR estimate near the surface for both the convective and nocturnal boundary layer than the MASS EDR. Therefore, based on the validation simulations, the GAUSS EDR provides the best estimate for near surface EDR and should be used when the 6 km grid meshes are used in a statistical based forecasting system at the airport, particularly during the daytime hours.

The model (observed) characteristic length scale has been approximated from the TKE and EDR values from the model (tower data) with a few sources of error. The characteristic mixing length used for comparison has been engineered numerically from the TKE and EDR profiles at 40 meters and may not represent the exact numerical value calculated within the TKE PBL scheme. The estimated observed characteristic mixing length may also incur errors from noise within the TKE and EDR profiles near the airport, generated by variations in roughness length, obstacles, or other important near-surface variables. The modeled TKE and EDR profiles were generated using a cubic splining algorithm that interpolated the values to 5 meter resolution below two kilometers, and as such, some minor errors in truncation and extrapolation may be present. The eddy dissipation length scale  $l_e$  has not been analyzed in terms of the different variables within the Therry and Lacarrere formulation, such as stability and boundary layer depth. Therefore, a complete analysis of the model characteristic length scale in which we examine the dependency of the EDR on these parameters is planned in future work.

## 5. Conclusions

The latest version of the TAPPS modeling system, known as TAPPS-2, is developed and tested for the 17-19 September 1997 period at Dallas-Fort Worth International Airport. The purpose of the validation simulations was to test different model configurations in order to obtain the most accurate simulation of turbulence related features possible in an environment where visual flight conditions exist and turbulence may be present at and near the runway flight corridors. The TAPPS-2 system is being developed in order to create a comprehensive low-level wind climatology for St. Louis-Lambert International Airport which can be used for a statistically-based forecasting algorithm which may aid air-traffic controllers in determining hazards that could be present during visual flight conditions.

The TAPPS-2 system is based on the non-hydrostatic version of the Mesoscale Atmospheric Simulation System (MASS), and underwent a series of model configuration changes from the previous hydrostatic TAPPS-1 version. Using a 36-6-1 kilometer one-way nesting algorithm, a series of validation simulations were performed for the 17-19 September 1997 time frame centered on the runway location at Dallas-Fort Worth International Airport. The model was initialized at two different initialization times, 00 UTC and 12 UTC on the day in question, creating periods of 12-hr model overlap between the two initialization times. The overlapping periods were the focus of both single-point validation analyses from tower data taken using the AVOSS observational system at the airport, and allowed for intra-model comparisons between the different

configurations. In addition to the change in horizontal resolution and model start time, a change in the model vertical resolution from 60 sigma levels to 90 sigma levels was implemented for the fine resolution (i.e., 6 and 1 kilometer) simulations. The 90-sigma level distribution included over 40 sigma levels below the 2 kilometer layer, a significant increase in resolution from the 60-level versions used in the 36 km grid mesh and the TAPPS-1 system.

Single point validation of time-series plots of TKE and EDR taken at 5/15 meters and 40 meters AGL from the various model simulations and the AVOSS tower data suggested that the 36 kilometer grid mesh had lower overall TKE error than the 6 or 1 kilometer grid mesh. The EDR on the 36-kilometer grid mesh near the surface was an order of magnitude or more higher than the observations, while the 40 m EDR closer matched the observations. The EDR in the 6 and 1 kilometer grid meshes displayed similar trends to the observed data but with a one-order-of magnitude shift in the values. The better validation at the coarse 36-km grid resolution is attributed to the difference in model-sigma level distribution; the 36-kilometer grid benefited from an additional sigma layer not present in the smoother 90-level distribution. The 6-kilometer grid mesh had low overall TKE error at the 40-meter height, but was significantly lower than observations near the ground due to the loss of the sigma level due to smoothing. The 1-kilometer grid mesh, using the same vertical distribution as the 6-kilometer, had very similar TKE and EDR time series plots and validation statistics, and thus, no additional information regarding the validation period was gained by increasing the horizontal resolution. The results suggest that the

generation of turbulence statistics from different model configurations has a strong dependency on the initial model vertical resolution due to the interpolation process needed to obtain the high-resolution 5-m data. In addition, the continuously integrated 1-kilometer simulations were able to correct an anomalously low TKE/EDR value present in the original TAPPS-1 configuration during the re-initialization process (i.e., every 4<sup>th</sup> time step), where the 1-kilometer grid mesh is comprised of a series of shorter simulations. Since the continuously-integrated 1-kilometer simulations provided no additional information to the TKE and EDR profiles near the airport, the use of an additional 1-kilometer grid mesh, using a 90-sigma level distribution, may not provide any additional information for the low-level wind climatology. The result is significant, since the omission of the 1-kilometer grid mesh will greatly reduce the integration time for the low-level wind climatology and also reduce the amount of storage space necessary for the climatological data generated. The point validation suggested that the overall error in TKE and EDR was lower in the 12 UTC simulations than the 00 UTC simulations, particularly during the daytime hours. The 40 m TKE and EDR seemed to under-estimate the turbulence at night and over-estimate the turbulence during the daytime hours regardless of horizontal or vertical resolution. The result is somewhat trivial, because one would expect that the closer the model integration time is to the observed time periods, the smaller the error since model errors grows with time. However, investigation of the nighttime validation of TKE and EDR suggests that the 12 UTC simulations also perform better at night since the 00 UTC simulations have much lower overall

profiles in the nocturnal boundary layer than the 12 UTC simulations. This result is attributed to a model-spin up issue within the 00 UTC simulations and potential errors in the initialization which are manifested in the model's development of a nocturnal boundary layer.

From the full sounding analysis of the validation periods presented in Section 3.2.4, several key discoveries are noted. The point validation presented in Section 3.2.3 suggested that the 36 km simulations performed better in AVOSS tower data TKE and EDR validation than the 6 and 1 km simulations near the surface (i.e., 5 and 15 meters) and slightly better at 40 m. Analysis of the vertical soundings of TKE and EDR within the near-surface convective and nocturnal boundary layer revealed that the difference in TKE and EDR profiles between the 36 and 6 km simulations are directly attributable to a shift in sigma level distribution near the ground, as discussed in Section 2. The loss of sigma levels near the ground acts to shift both the maximum TKE and EDR upward within the boundary layer by an average of 15-20 m, while the average profile of TKE and EDR in both the convective and nocturnal boundary layer showed very little difference otherwise. Therefore, the results from the point validation suggest that while higher TKE and EDR is present in the 36 km simulations, the overall turbulence profile is not appreciably different from the 6 km grid mesh. In the nocturnal boundary layer, the TKE and EDR maxima are constrained to lie below the level of the DLLJ, with the maximum values corresponding to the maximum headwind velocity component. The TKE and EDR profiles decrease abruptly from their maximum values at 20 (40) m in the 36 (6) km simulations to near zero at

the height of the DLLJ. During the convective boundary layer, however, the TKE and EDR decrease slower with height during the early afternoon hours and are nearly constant to 2 km at the height of the convective mixed layer.

Analysis of vertical profiles of both headwind ( $u$ ), crosswind ( $v$ ), and vertical motion ( $w$ ) wind profiles in the nocturnal boundary layer are evaluated with respect to the development of a diurnally-driven low level jet in the 17-20 September 1997 time period. The profiles of vertical motion indicated that synoptic scale subsidence was prevalent during the daytime hours during the simulation periods, and rising motion was prevalent during the overnight periods, especially at the 6 km horizontal grid resolution. The vertical velocity profiles are consistent with the results shown in K00, indicating that the synoptic-scale subsidence beneath the upper-level ridge allowed strong diurnal cycles and buoyantly-driven convective boundary layers while impeding the progression of any large-scale features through the airport during the simulation period. The TAPPS-2 validation simulations accurately simulated the development of DLLJ signals within all of the validation simulations during the period. The magnitude of the DLLJ was generally within  $2\text{-}4\text{ ms}^{-1}$  of the observed soundings from the IOP at DFW and from the previous TAPPS-1 simulations conducted in K00. The height of the DLLJ also corresponded well to the observations and results of previous studies, such as Whiteman et al. (1997) and K00, suggesting that the diurnally-driven low-level jet reaches a maximum value between 400-500 m AGL in the Southern Great Plains. Due to the 24 hr model integration bracketing the 00 and 12 UTC simulations, the maximum in the TAPPS-2 modeled DLLJ often

occurred between 06-09 UTC in the headwind velocity component and 11-12 UTC in the crosswind velocity component. The maximum crosswind velocity component in the TAPPS-1 simulations shown in K00 indicated that the average time of the DLLJ during the 15-20 September 1997 simulation came at 14 UTC, a few hours after the results shown for TAPPS-2. However, model spin-up and initial conditions in the 12 UTC simulations may retard the DLLJ from increasing in intensity from the initial time, and the 00 UTC simulations end before the 14 UTC time period can be reached. Thus, the discrepancy in modeled DLLJ timing is attributed to the TAPPS-2 configuration itself, not the actual simulated wind profiles.

As shown in Table 3, the magnitude of the DLLJ in the headwind and crosswind velocities showed remarkable consistency across different grid resolutions and simulation start times. However, several key differences between the evolution of the wind profiles were noted. The 36 km simulations, ran with 30 less sigma levels, had smoother velocity profiles in general than their higher vertical resolution 6-km grid mesh counterparts. In addition, the height of the DLLJ, controlled by subtle changes in the nocturnal inversion, varied more in the 6 km simulations with time than the 36 km grids. These results indicate that the 30-sigma level increase and factor of 6 increase in horizontal resolution plays an instrumental role in the evolution of the DLLJ within the TAPPS-2 modeling system. The 6-km simulations tended to keep the near-surface low-level flow with a more easterly component, which, as shown in K00, is directly attributable in the Southern Great Plains nocturnal boundary layer to the variation in horizontal

pressure gradient force. Series of balloon observations from PLNO indicate that the increased easterly low-level flow in the first six hours of nocturnal boundary layer evolution was observed during several of the validation periods. In addition, the 6 km 12 UTC simulations developed secondary maxima in crosswind velocity, which was shown in the PLNO soundings in the free atmosphere between 1-2 kilometers, while the 6 km 00 UTC and 36 km simulations did not. The development of the secondary crosswind maxima corresponds to the presence of more complex temperature distributions within the 1-2 km layer that were not present in the smoothly decreasing temperature profiles in the 00 UTC 6 km simulations and 36 km simulations. The secondary maximum in crosswind velocity is a very important feature within the nocturnal aviation wind profile due to the presence of an otherwise unresolved shear layer that would introduce yet another source of potential turbulence for both ascending and descending aircraft perpendicular to the aircraft within the approach and descent corridors. The potential generation of turbulence from the existence of this shear layer is seen in the simulations in which it developed, as the TKE and EDR increased in the .5 kilometer layer above the crosswind maximum. A sensitivity test was performed for the 00-12 UTC 19 September time period using a 90-level 36-kilometer simulation. The results of the sensitivity test revealed that the 90-level version (TST): (a) developed a stronger nocturnal inversion faster; (b) kept the low-level flow backed to a more easterly direction longer; (c) kept the crosswind velocity positive in the 1-2 kilometer layer; when compared to the 60-level (CTRL) version. While no secondary crosswind maximum developed, the change in

crosswind velocity in the 1-2 kilometer layer between CTRL and TST suggest that the vertical resolution change is at least partially responsible for the capturing of the secondary crosswind maximum in the observations while sensitivity to horizontal resolution and initialization time may also be factors. The results illustrate that the use of overlapping initialization times and finer resolution horizontal and vertical grid configurations can improve the forecasting of aviation related turbulence hazards for use in the low-level wind climatology.

Since the crosswind maximum and attendant shear layer is displaced 1-kilometer from the DLLJ height shown in the observations and simulations, the shear layer is most likely not attributable to any DLLJ formation mechanism. In addition, investigations of the wind data suggested that while the u-wind component increased, the total magnitude of the wind did not, suggesting that the crosswind shear layer is not a secondary jet, but rather, attributed to a wind directional change. Analysis of the horizontal distribution of geopotential height and temperature in the 1-2 kilometer layer across the Southern Plains revealed that simulations where the crosswind shear layer developed underwent a change in horizontal geopotential height gradients from a more east-to-west orientation near 00 UTC to a more north-south orientation north of the airport several hours later. The 850-hPa flow veered to a more southwesterly direction near and north of the airport, which would act to increase the u-wind component while not changing the total magnitude of the wind. The change in height gradient and veering of the flow coincided with warming in the 850-hPa analysis north of the airport as the flow veered. Thus, the advection of the residual layer from the

higher terrain of Texas and New Mexico could cause this warming and change the orientation of height gradients and wind direction across North Texas. The simulations where the shear layer did not develop maintained a north-south orientation in height and the 850 hPa flow remained more southerly. Therefore, the residual layer over the higher terrain would not be able to advect into Northern Texas and the height and wind gradients would not change as they did in the simulations in which the secondary shear layer developed.

As noted in the point validation in Section 3, the EDR time series evolution in the 36 and 6 kilometer simulations often were shifted an order of magnitude higher at times from the observations. The MASS model algorithm for estimating EDR uses an elaborate formulation for estimating the characteristic length scale  $\Lambda$  based off of a third-order closure simulation by Therry and Lacarrere (1983). Evaluation of derived characteristic length scale values from the AVOSS tower data and TAPPS-2 simulations revealed that the  $\Lambda$  derived from the AVOSS tower data was much higher than the original TAPPS-2 simulations. The observed  $\Lambda$  had a bell-shape structure mimicking the development of the convective boundary layer, and remained nearly constant at night. Though TAPPS-2 was able to somewhat replicate the patterns shown in the observations, the overall value of the characteristic length scale near the ground was much lower than the observations.

To test different EDR calculations in the validation simulations, sensitivity tests to the characteristic length scale were performed and compared to the observations using three different formulations for  $\Lambda$ . The three different

formulations tested used a constant value, the original MASS model formulation, and an Gaussian-based estimation derived from hourly averages of  $\Lambda$  derived from the AVOSS tower observations. The GAUSS EDR, as expected, vastly improved the EDR validation during the daytime hours for both the 36 and 6 kilometer grid meshes over the MASS and NOWVIV formulations. At nighttime, the validation was not as clear, with the GAUSS EDR (using a constant  $\Lambda$ ) performing better at times and the MASS EDR performing better at times. The MASS EDR benefits from extra complexity introduced by shear and stability, while the GAUSS EDR remains constant. The results suggested that the use of a constant value of  $\Lambda$  during the nocturnal boundary layer may not provide the most desirable results all of the time, and  $\Lambda$  may need to be adjusted in the formulation as a function of another turbulence diagnostic (such as TKE) in the convective boundary layer. The 6-kilometer grid mesh, whose EDR validation was consistently an order of magnitude higher than the observations, greatly benefited from the GAUSS formulation throughout the entire validation period. The GAUSS EDR can be a significant utility in the low-level wind climatology statistical analysis for St. Louis Lambert International Airport, and should be calculated by deriving  $\Lambda$  from observations of TKE and EDR near the runway. The GAUSS EDR would be most beneficial in the 6-kilometer grid meshes where the EDR appears to be consistently shifted one order of magnitude higher than observed values, which could be attributable to the loss of a sigma layer in the smoother 90-level vertical distribution.

The results presented in this manuscript provide a series of recommendations for the low-level wind climatology that is being performed for St. Louis-Lambert International Airport during the July-December 2004 time frame. The grid configurations only need a 36 and 6 kilometer resolution, since no additional information is gained by nesting to 1 kilometer. Secondly, the use of two initialization times (i.e., 00 UTC and 12 UTC) is recommended since useful information can be extracted from both sets of simulations, and the 12-hr overlap would provide the ability to compare model simulations when examining specific cases. The development of important turbulence features in the 1-3 kilometer layer appear to be best resolved by the 90-level 6-kilometer simulations and should be noted when evaluating features such as low-level jets. In addition to the model-derived EDR from the model, a secondary formulation of EDR using a Gaussian-based characteristic length scale model derived from observations may provide better validation statistics, particularly during the daytime hours. However, in the nocturnal boundary layer, the original TAPPS-2 EDR may provide better estimations when the TKE is higher, and thus, the GAUSS EDR should be used with caution particularly in complex atmospheric conditions.

## **6. Acknowledgements**

This research is supported by the NASA Airspace Systems/Airportal Program under the direction of Dr. Fred H. Proctor and David W. Hamilton. The author wishes to acknowledge project team partner Mr. Zachary Brown for his outstanding contributions to the project. The author wishes to thank the following individuals for their contributions to this specific project: Committee members Dr.

Michael Kaplan (University of Nevada), Dr. Yuh-Lang Lin (North Carolina State University), Dr. Sethu Raman (North Carolina State University), and Dr. Gary Lackmann (North Carolina State University). Special thanks are in order for Dr. S. Pal Ayra (North Carolina State University), Ken Waight (MESO, Inc.), and Paul Suffern (North Carolina State University) for helpful comments and suggestions and various computing issues.

## 7. References

- Ayra, S. P., 2001: *Introduction to Micrometeorology*. Kuwler Academic Press, 307 pp.
- Blackadar, A. K. 1957: Boundary layer and maxima and their significance for the growth of nocturnal inversions. *Bull. Amer. Meteor. Soc.*, **38**, 283-290.
- Blecker, W., and M. J. Andre 1951: On the diurnal variation of precipitation, particularly over central U.S.A., and its relation to large-scale orographic circulation systems. *Quart. J. Roy. Meteor. Soc.*, **77**, 260-271.
- Holton, J. R., 1967: The diurnal boundary layer oscillation above sloping terrain. *Tellus*, **19**, 199-205.
- Hinton, D. A. 1995: Aircraft Vortex Spacing System (AVOSS) Conceptual Design. NASA Tech. Memo. 110184, 32 pp. [Available from NASA Langley Research Center, Hampton, VA 23681].
- , 1996: An aircraft vortex spacing system (AVOSS) for dynamical wake vortex spacing criteria. Preprints, *AGARD CP-584*, Paper 23, Advisory Group for Aerospace Research and Development, 11 pp.
- Davies, H. C., 1976: A lateral boundary formulation for multilevel prediction models. *Quart. J. Roy. Meteor. Soc.*, **102**, 405–418.
- Frech, M. and F. Holzäpfel. 2006: Skill of an aircraft wake-vortex transport and decay model using weather prediction and observations. Preprints, *12<sup>th</sup> Conference on Aviation Range and Aerospace Meteorology*. Atlanta, GA, Amer. Meteor. Soc., 10 pp.
- Kaplan, M. L. and Y.-L. Lin, J.J. Charney, K. D. Pfeiffer, D.B. Ensley, D. S. DeCroix and R. P. Weglarz. 2000: A Terminal Area PBL Prediction System at Dallas–Fort Worth and Its Application in Simulating Diurnal PBL Jets. *Bull. Amer. Meteor. Soc.*, **81**, pp. 2179–2204.
- ,----- Y.-L. Lin, C.J. Ringley, Z.G. Brown, P. S. Suffern, M.T. Kiefer, and A. Hoggarth 2006: Wake vortex simulations from a Terminal Area PBL Prediction System (TAPPS). Preprints, *44<sup>th</sup> Aerospace Sciences Meeting and Exhibit*. Reno, NV, AIAA paper 06-1074. American Institute of Aeronautics and Astronautics, 26 pp.
- Kain, J.S., and J. M. Fritsch, 1990: A one-dimensional entraining/detraining plume model. *J. Atmos. Sci.*, **47**, 2784-2802.

- Kolmogorov, A.N., 1941: Energy dissipation in locally isotropic turbulence. *Doklady AN SSSR*, **32**, No. 1, 19-21.
- Lackmann, G. M. 2002: Potential vorticity redistribution, the low-level jet, and moisture transport in extratropical cyclones. *Mon. Wea. Rev.*, **130**, 59–74.
- Lin, Y. L., R. D. Farley, and H.D. Orville, 1983: Bulk parameterization of the snow field in a cloud model. *J. Climate Appl. Meteor.*, **22**, 1065-1092.
- , 2007: *Mesoscale Dynamics*. Cambridge University Press (In Press), TBD pp.
- McNider, R.T., and R.A. Peilke, 1981: Diurnal boundary-layer development over sloping terrain. *J. Atmos. Sci.*, **38**, 2198-2212.
- Perry, R. P., D. A. Hamilton, and R. A. Stuever, 1997: NASA wake vortex research for aircraft spacing. Preprints, *35<sup>th</sup> Aerospace Sciences Meeting and Exhibit*, Reno, NV, AIAA Paper 98-0589, American Institute of Aeronautics and Astronautics, 9 pp.
- Proctor, F. H., 1998: The NASA-Langley wake vortex modeling effort in support of an operational aircraft spacing system. Preprints, *36<sup>th</sup> Aerospace Sciences Meeting and Exhibit*, Reno, NV, AIAA Paper 98-0589, American Institute of Aeronautics and Astronautics, 19 pp.
- Stull, Roland B., 1988: *An Introduction to Boundary Layer Meteorology*. Kluwer Academic Press: 639 pp.
- Therry, G., and P. Lacarrere, 1983: Improving the eddy kinetic energy model for the planetary boundary layer. *Bound.-Layer Meteor.*, **25**, 63–88.
- Wexler, H., 1961: A boundary layer interpretation of the low-level jets. *Tellus*, **13**, 368-378.
- Whiteman, C.D., X. Bian, S. Zhong, 1997: Low-level jet climatologies from enhanced rawinsonde observations at a site in the Southern Great Plains. *J. Appl. Meteor.*, **36**, 1363-1376.
- Yamada, Tetsuji and George Mellor. 1975: A Simulation of the Wangara Atmospheric Boundary Layer Data. *J. Atmos. Sci.*, **32**, 2309–2329.

Table 1: Comparisons of TAPPS-1 and TAPPS-2 model configurations. Dashes are used to represent the absence of a “super-fine” 1-kilometer grid mesh in TAPPS 1. TAPPS-1 details from Kaplan et al. (2000).

<b>Model System</b>	<b>MASS Version</b>	<b>Horiz. Resolutions (km)</b>	<b>Vertical Levels (<math>\sigma</math>)</b>	<b>Horizontal Grid Structures</b>	<b>Run Durations (h)</b>	<b>Temporal Output (h)</b>
<i>TAPPS-1</i>	Hydro. 5.4	36,12,-	60,56,-	60x60, 60x60, -	24,21,-	1,0.25,-
<i>TAPPS-2</i>	Non-Hydro. 6.4.3	36,6,1	60,90,90	100x100, 100x100, 50x50	24,24,24	1,0.25,.0.25

Table 2a: Basic validation statistics for the 00 UTC simulations from 17-20 September 1997, generated using the SAS Statistics program. TKE units are  $m^2s^{-2}$  and EDR units are  $m^2s^{-3}$ .

Simulation/Dataset	Mean	Std. Dev.	Variance	Maximum	Minimum	Median
TKE_OBS	0.915201	0.678908	0.460916	6.4323	0.0433	0.78715
EDR_OBS	0.00165	0.00087	7.58E-07	0.003943	6.46E-05	0.001599
TKE_36KM	0.829354	0.717797	0.515233	3.58617	0	0.445049
EDR_36KM	0.002456	0.00351	1.23E-05	0.038083	0	0.002054
TKE_6KM	0.766997	0.59997	0.359964	4.36153	0.0001	0.561692
EDR_6KM	0.012978	0.00751	5.64E-05	0.028212	0.0001	0.011212
TKE_1KM	0.687061	0.514637	0.264851	2.31711	0	0.505098
EDR_1KM	0.014127	0.006994	4.89E-05	0.03757	0	0.014305

Table 2b: As with Table 2a, but for the 12 UTC Simulations.

Simulation/Dataset	Mean	Std. Dev.	Variance	Maximum	Minimum	Median
TKE_OBS	1.025858	0.705876	0.498261	6.4323	0.0433	0.91125
EDR_OBS	0.001891	0.00127	1.61E-06	0.009545	6.46E-05	0.001674
TKE_36KM	1.124757	0.948178	0.899041	4.30761	0.001847	0.885969
EDR_36KM	0.005991	0.009768	9.54E-05	0.068067	0	0.002325
TKE_6KM	1.04292	0.741943	0.55048	4.94741	0.0001	0.810236
EDR_6KM	0.019371	0.009889	9.78E-05	0.051958	0.001782	0.018108
TKE_1KM	0.819185	0.502352	0.252358	2.31584	0	0.636179
EDR_1KM	0.021543	0.014668	0.000215	0.077486	0	0.017946

Table 3: Summary of observed variables as a function of model simulation for the NASA validation simulations. The black bars indicate the simulation time period in which the statistics are valid.

<u>Simulation</u>	<u>U<sub>max</sub> (m/s)</u>	<u>V<sub>max</sub> (m/s)</u>	<u>e<sub>max</sub> (m<sup>2</sup>s<sup>-2</sup>)</u>	<u>ε<sub>max</sub> (m<sup>2</sup>s<sup>-3</sup>)</u>	<u>MAX LLJ VARY</u> (m)
17_36_00	10 @ 420 m 11 UTC	16 @ 325 m 6 UTC	0.5 @ 25 6 UTC	2 x 10 <sup>-2</sup> @ 25 6 UTC	~0 m
17_06_00	8.5 @ 495 m 12 UTC	16 @ 365 m 6 UTC	0.5 @ 40 6 UTC	2 x 10 <sup>-2</sup> @ 40 6 UTC	100 m from 6-12 UTC
<b>00-12 UTC 17 SEPTEMBER</b>					
17_36_12	13 @ 430 m 11 UTC	18 @ 400 m 9 UTC	0.9 @ 20 9 UTC	4 x 10 <sup>-2</sup> @ 20 9 UTC	~250 m from 3-9 UTC
17_06_12	11 @ 485 m 12 UTC	16 @ 540 m 9 UTC	0.6 @ 50 9 UTC	4 x 10 <sup>-2</sup> @ 40 9 UTC	~200 m from 3-9 UTC
18_36_00	10 @ 410 m 11 UTC	16 @ 330 m 6 UTC	0.5 @ 20 6 UTC	1.6 x 10 <sup>-2</sup> @ 20 6 UTC	~80 m 6-12 UTC
18_06_00	11 @ 575 m 12 UTC	16 @ 460 m 9 UTC	0.53 @ 45 9 UTC	2 x 10 <sup>-2</sup> @ 35 9 UTC	~200 m from 3-9 UTC
<b>00-12 UTC 18 SEPTEMBER</b>					
18_36_12	8.75 @ 530 m 11 UTC	20 @ 435 m 6 UTC	1.25 @ 25 6 UTC	6 x 10 <sup>-2</sup> @ 20 6 UTC	~ 0 m
18_06_12	8.6 @ 1400 m 6 UTC	17 @ 485 m 9 UTC	1.17 @ 40 6 UTC	2 x 10 <sup>-2</sup> @ 20 9 UTC	~180 m up (3-9 UTC), then 90 m down (11 UTC)
19_36_00	10.5 @ 430 m 11 UTC	17.3 @ 380 m 6 UTC	0.5 @ 30 6 UTC	2 x 10 <sup>-2</sup> @ 20 6 UTC	~ 0 m
19_06_00	9.6 @ 515 m 11 UTC	17 @ 435 m 6 UTC	0.62 @ 45 6 UTC	2 x 10 <sup>-2</sup> @ 45 6 UTC	< 50 m
19_36_12	8.20 @ 310 m 11 UTC	16.5 @ 280 m 6 UTC	0.5 @ 25 6 UTC	1.65 x 10 <sup>-2</sup> @ 20 6 UTC	~ 0 m
19_06_12 Two maxima	7/7 @ 410/1260 m 6/11 UTC	15 @ 420 m 9 UTC	0.43 @ 45 9 UTC	2 x 10 <sup>-2</sup> @ 20 9 UTC	Two maxima with upward/downward mixing behavior

Table 4: Comparisons of model sigma distributions between the 60-level version used in TAPPS-1 and the 36km grid mesh in TAPPS-2 and the new 90-level version used in the 6 and 1 km grid mesh in TAPPS-2. Note that model layer 1, by definition, is  $\sigma=1$ .

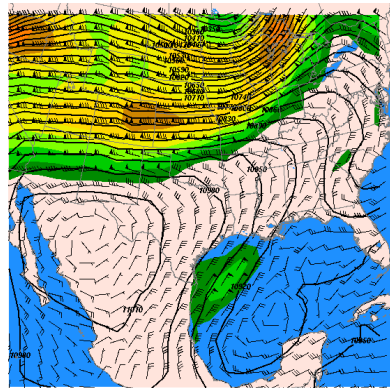
<u><math>\sigma</math>-level</u>	<u><math>\sigma_{60}</math></u>	<u><math>\sigma_{90}</math></u>	<u><math>\sim Z_{60}</math></u>	<u><math>\sim Z_{90}</math></u>	<u><math>\delta\sigma_1</math></u>	<u><math>\delta\sigma_2</math></u>
26	0.8654	0.9021	1131	818	0.0170	0.057
25	0.8788	0.9076	1012	771	0.0155	0.056
24	0.8911	0.9130	906	725	0.0141	0.054
23	0.9022	0.9182	810	681	0.0128	0.053
22	0.9124	0.9232	723	638	0.0117	0.051
21	0.9216	0.9280	644	596	0.0106	0.050
20	0.9300	0.9328	573	556	0.0097	0.048
19	0.9376	0.9374	509	518	0.0088	0.047
18	0.9446	0.9419	451	480	0.0080	0.046
17	0.9509	0.9463	399	444	0.0073	0.044
16	0.9567	0.9505	351	408	0.0066	0.043
15	0.9619	0.9546	308	374	0.0060	0.042
14	0.9667	0.9586	269	341	0.0055	0.041
13	0.9710	0.9625	234	309	0.0050	0.039
12	0.9749	0.9663	202	278	0.0045	0.038
11	0.9785	0.9699	172	248	0.0041	0.037
10	0.9818	0.9735	146	219	0.0038	0.036
9	0.9847	0.9770	122	190	0.0034	0.035
8	0.9875	0.9804	100	163	0.0031	0.034
7	0.9899	0.9836	80	137	0.0028	0.033
6	0.9922	0.9868	62	112	0.0026	0.032
5	0.9942	0.9899	45	87	0.0023	0.031
4	0.9961	0.9929	30	62	0.0019	0.030
3	0.9977	0.9958	17	39	0.0018	0.030
2	0.9922	0.9986	5	16	0.0016	0.029

Table 5: Characteristic Length Scale statistics showing the base 4-day time average, the adjusted moving average (with values less than the nighttime mean set to the nighttime mean), and the resultant Gaussian redistribution.

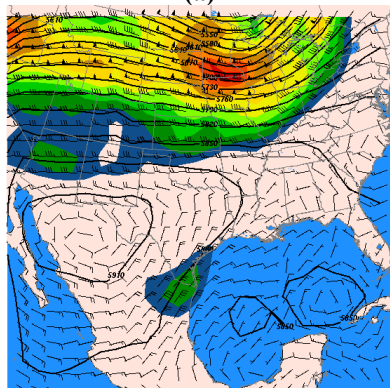
Time (UTC)	$\Delta$ -4 Day Mean	Adjusted Moving $\Delta$ Average	Adjusted Gaussian $\Delta$
0000	339.8742	336.5092	336.5092
0015	313.8736	336.5092	336.5092
0030	392.9659	336.5092	336.5092
0045	346.5292	336.5092	336.5092
0100	322.7357	336.5092	336.5092
0115	289.3674	336.5092	336.5092
0130	606.9137	336.5092	336.5092
0145	372.2666	336.5092	336.5092
0200	303.6979	336.5092	336.5092
0215	319.3685	336.5092	336.5092
0230	340.4717	336.5092	336.5092
0245	294.2554	336.5092	336.5092
0300	281.1931	336.5092	336.5092
0315	361.3437	336.5092	336.5092
0330	267.693	336.5092	336.5092
0345	351.2868	336.5092	336.5092
0400	300.7894	336.5092	336.5092
0415	440.6431	336.5092	336.5092
0430	379.2686	336.5092	336.5092
0445	516.936	336.5092	336.5092
0500	319.6767	336.5092	336.5092
0515	342.9333	336.5092	336.5092
0530	347.6629	336.5092	336.5092
0545	333.2415	336.5092	336.5092
0600	336.3418	336.5092	336.5092
0615	367.0435	336.5092	336.5092
0630	341.8679	336.5092	336.5092
0645	415.7208	336.5092	336.5092
0700	292.6209	336.5092	336.5092
0715	349.6484	336.5092	336.5092
0730	374.6185	336.5092	336.5092
0745	292.1805	336.5092	336.5092
0800	373.3701	336.5092	336.5092
0815	320.2029	336.5092	336.5092
0830	288.7103	336.5092	336.5092
0845	277.9497	336.5092	336.5092
0900	236.6115	336.5092	336.5092
0915	279.6173	336.5092	336.5092
0930	272.3314	336.5092	336.5092
0945	263.7208	336.5092	336.5092
1000	321.7276	336.5092	336.5092
1015	245.7673	336.5092	336.5092
1030	322.995	336.5092	336.5092
1045	292.049	336.5092	336.5092
1100	401.0484	336.5092	336.5092
1115	412.9211	336.5092	336.5092

Table 5 (continued).

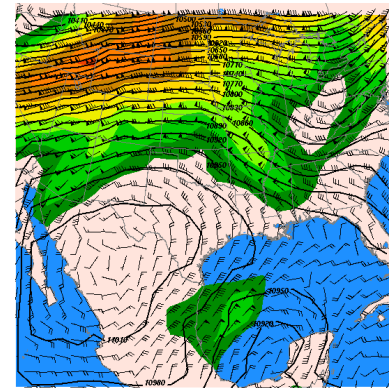
<b>1130</b>	370.8725	336.5092	336.5092
<b>1145</b>	345.4146	336.5092	336.5092
<b>1200</b>	362.928	336.5092	336.5092
<b>1215</b>	271.5594	336.5092	336.5092
<b>1230</b>	285.5429	336.5092	336.5092
<b>1245</b>	298.1061	336.5092	336.5092
<b>1300</b>	344.7656	402.3655353	336.5092
<b>1315</b>	333.9271	428.0144753	336.5092
<b>1330</b>	502.5963	478.439028	336.5092
<b>1345</b>	428.1731	510.4424126	336.5092
<b>1400</b>	447.3614	565.1463564	338.4851
<b>1415</b>	535.6254	602.3755673	388.2854
<b>1430</b>	630.6098	654.5212803	464.6279
<b>1445</b>	646.9888	668.4543297	486.2481
<b>1500</b>	596.2782	726.7640119	581.7111
<b>1515</b>	744.2082	750.6730958	622.9072
<b>1530</b>	686.342	758.569099	636.7378
<b>1545</b>	880.2276	790.189514	693.1028
<b>1600</b>	691.9146	801.4665044	713.5365
<b>1615</b>	775.7922	864.9448855	830.7859
<b>1630</b>	812.8237	864.5343111	830.0194
<b>1645</b>	925.3355	940.3745081	971.6283
<b>1700</b>	945.8281	1000.082248	1080.775
<b>1715</b>	774.1499	969.497071	1025.323
<b>1730</b>	1116.184	1026.168202	1127.056
<b>1745</b>	1164.167	1035.372186	1143.121
<b>1800</b>	823.4874	1019.290064	1114.956
<b>1815</b>	1000.834	1073.292368	1207.628
<b>1830</b>	1153	1073.464085	1207.914
<b>1845</b>	1099.838	1060.471718	1186.14
<b>1900</b>	1039.497	1217.907576	1421.775
<b>1915</b>	1001.521	1482.708707	1658.027
<b>1930</b>	1101.031	1515.249151	1674.383
<b>1945</b>	1729.581	1555.35191	1691.536
<b>2000</b>	2098.701	1498.930853	1666.469
<b>2015</b>	1131.683	1368.692126	1580.568
<b>2030</b>	1261.442	1394.355547	1600.973
<b>2045</b>	1503.897	1307.811004	1524.627
<b>2100</b>	1577.746	1216.613417	1420.117
<b>2115</b>	1234.337	1020.355584	1116.836
<b>2130</b>	915.2638	968.9115963	1024.251
<b>2145</b>	1139.107	932.2992243	956.6281
<b>2200</b>	792.7149	806.0602453	721.9034
<b>2215</b>	1028.561	794.1937771	700.3405
<b>2230</b>	768.8143	683.9248534	510.8178
<b>2245</b>	634.151	622.1427709	416.3473
<b>2300</b>	745.249	545.4764901	336.5092
<b>2315</b>	587.4851	581.8938612	360.3863
<b>2330</b>	521.686	528.7585733	336.5092
<b>2345</b>	327.4858	531.1160952	336.5092



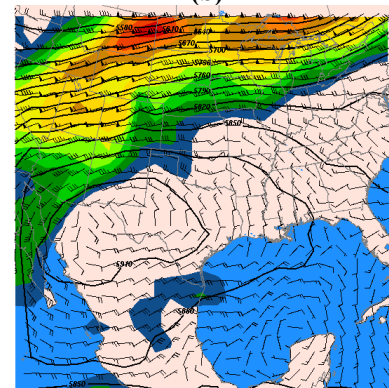
(a)



(c)

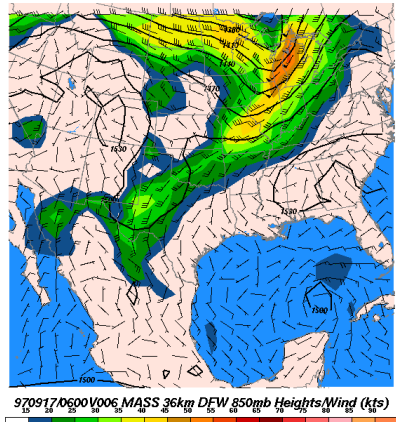


(b)

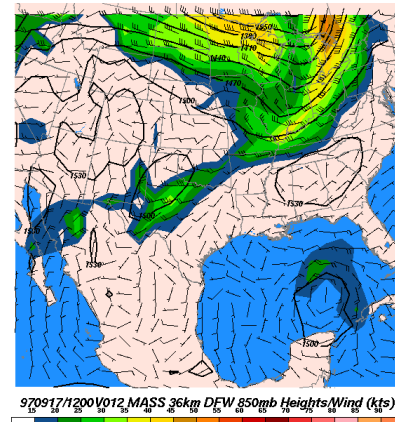


(d)

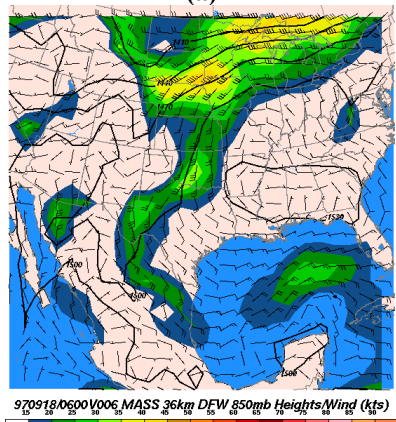
Figure 1: 17 NHMASS 36 km simulation four panel plot of 250 hPa (left panel) and 500 hPa (right panel) winds and geopotential height at (a), (b) 12 UTC 17 September 1997 and (c), (d) 12 UTC 18 September 1997.



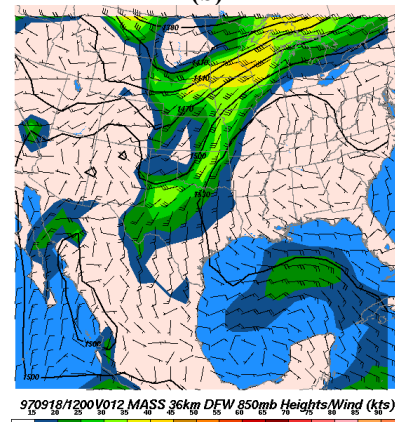
(a)



(b)

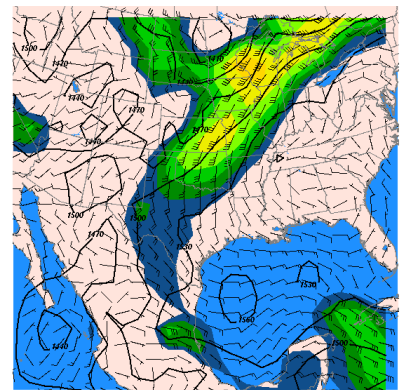


(c)



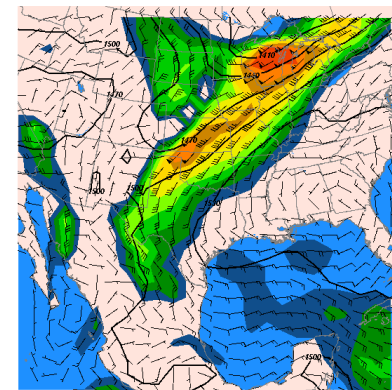
(d)

Figure 2: As with Fig. 1, but for 850 hPa winds and geopotential height at (a) 06 UTC (b) 12 UTC 17 September 1997 and (c) 06 UTC and (d) 12 UTC 18 September 1997.



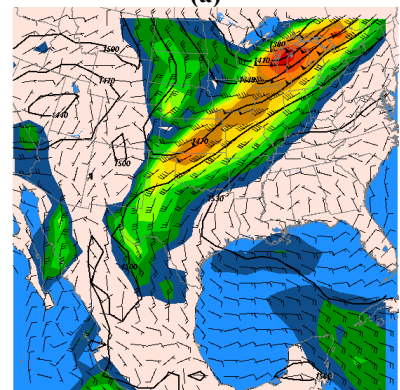
970919/0015V00015 MASS 36km DFW 850mb Heights/Wind (kts)

(a)



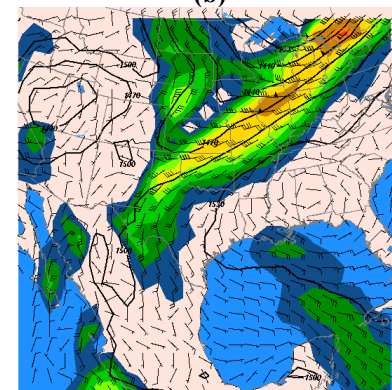
970919/0600V006 MASS 36km DFW 850mb Heights/Wind (kts)

(b)



970919/0900V009 MASS 36km DFW 850mb Heights/Wind (kts)

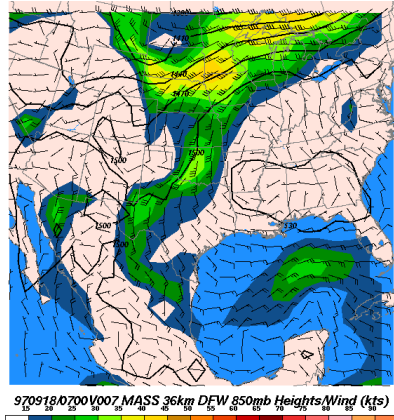
(c)



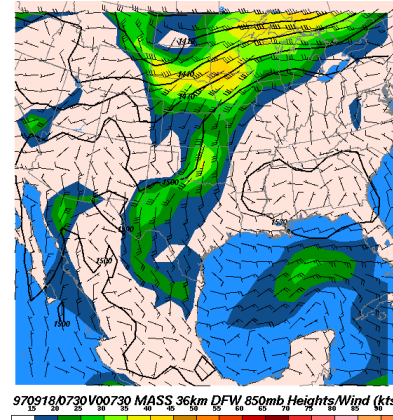
970919/1200V012 MASS 36km DFW 850mb Heights/Wind (kts)

(d)

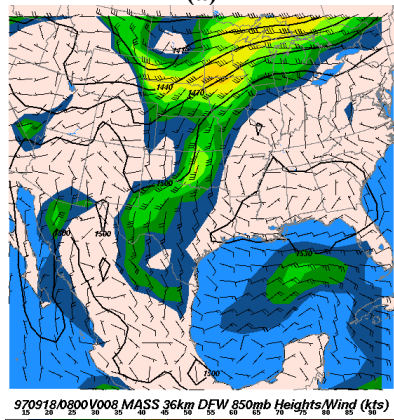
Figure 3: As with Fig. 2, but for 850 hPa (a) 00 UTC , (b) 06 UTC 19 September 1997 and (c) 09 UTC, (d) 12 UTC 19 September 1997.



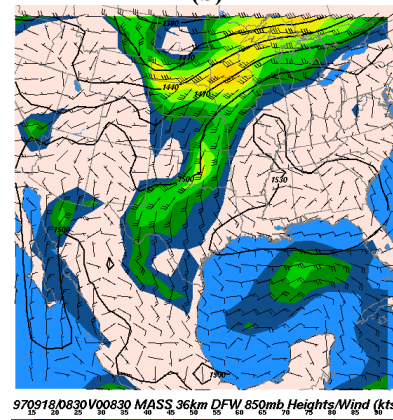
(a)



(b)

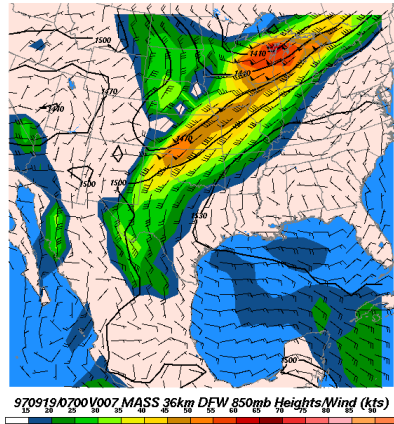


(c)

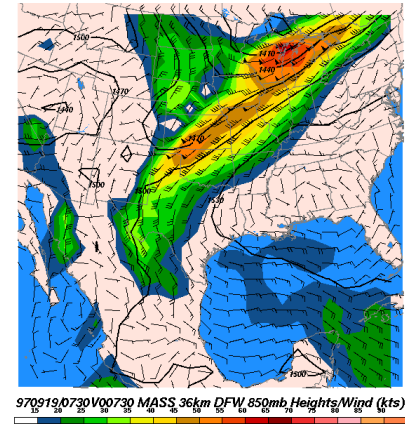


(d)

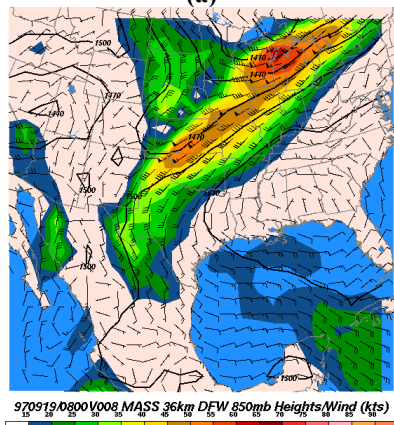
Figure 4: NHMASS 36 km four panel plot of 850 hPa of heights and winds valid (a) 0700 UTC; (b) 0730 UTC; (c) 0800 UTC; (d) 0830 UTC 18 September 1997.



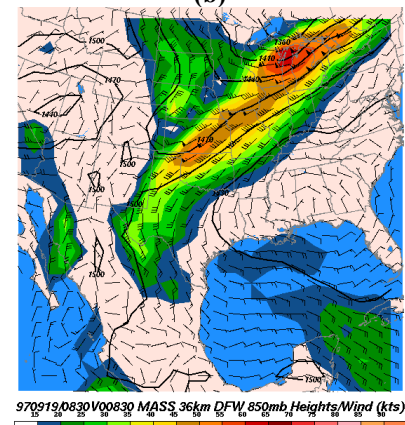
(a)



(b)



(c)



(d)

Figure 5: NHMASS 36 km four panel plot of 850 hPa of heights and winds valid (a) 0700 UTC; (b) 0730 UTC; (c) 0800 UTC; (d) 0830 UTC 19 September 1997.

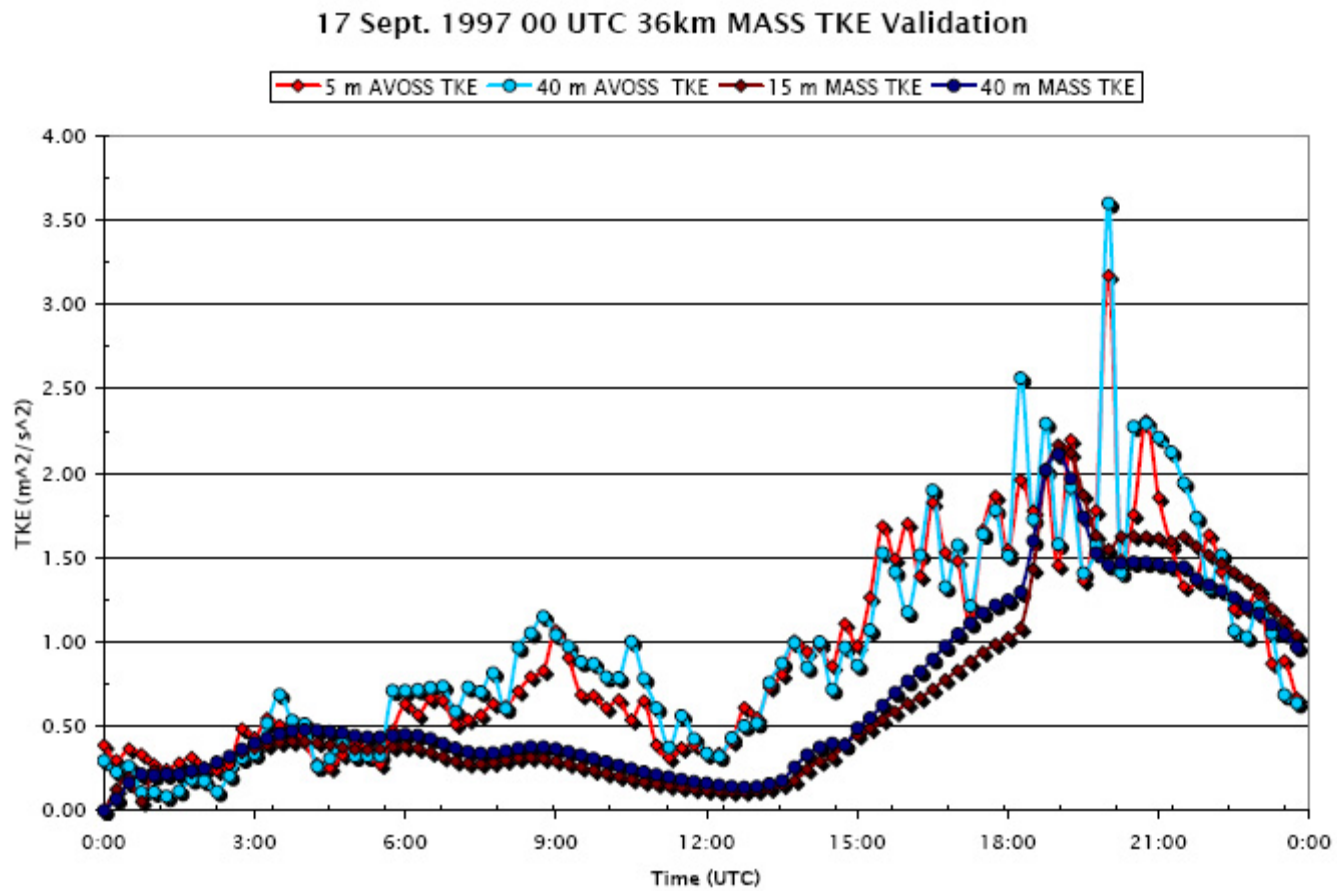


Figure 6: 17 NHMASS 36 km from 00-00 UTC 17-18 September 1997 (17\_36\_00) time series plot of 5/15 and 40 m TKE vs. time from the model simulation and AVOSS tower data.

### 18 Sept. 1997 00 UTC 36km MASS TKE Validation

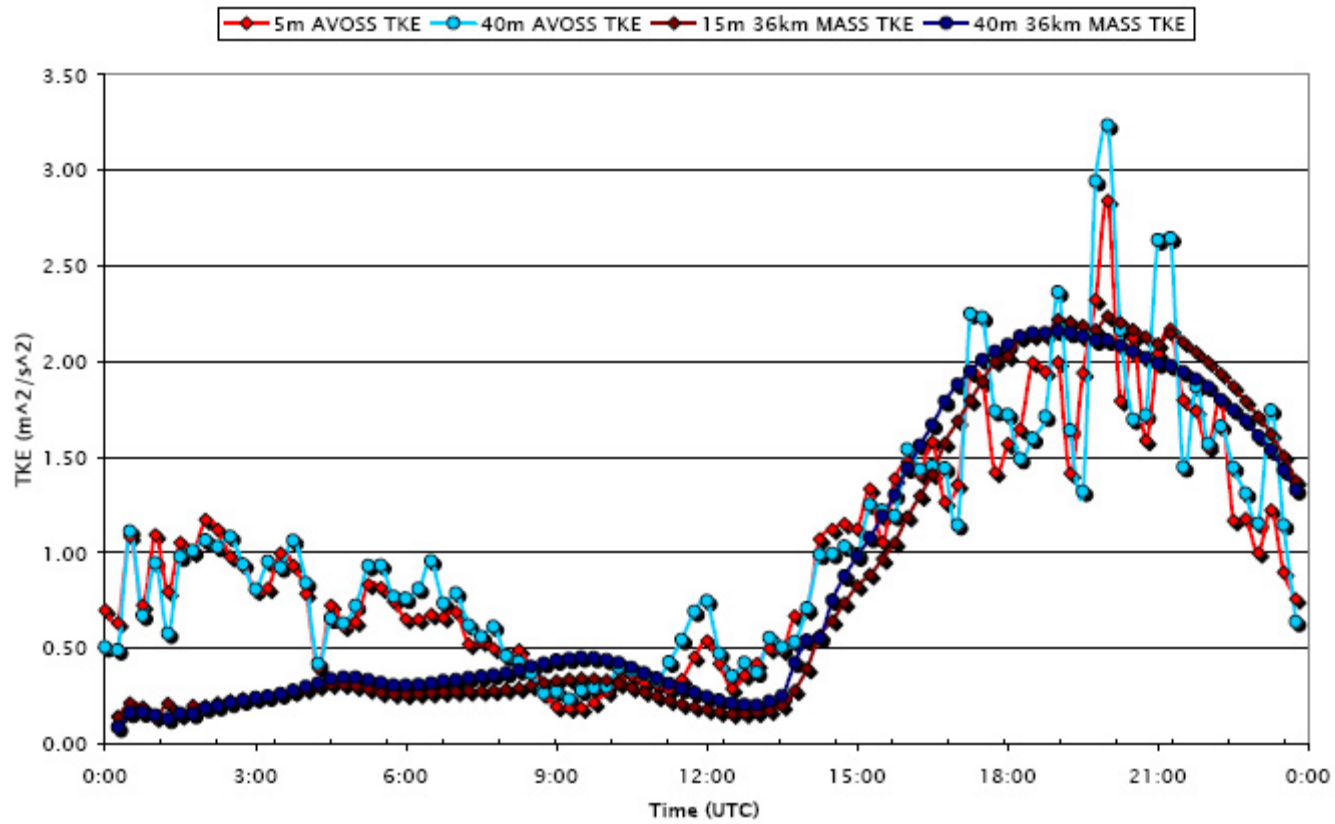


Figure 7: As with Fig. 7, but for 00-00 UTC 18-19 September 1997.

19 Sept. 1997 00 UTC 36km MASS TKE Validation

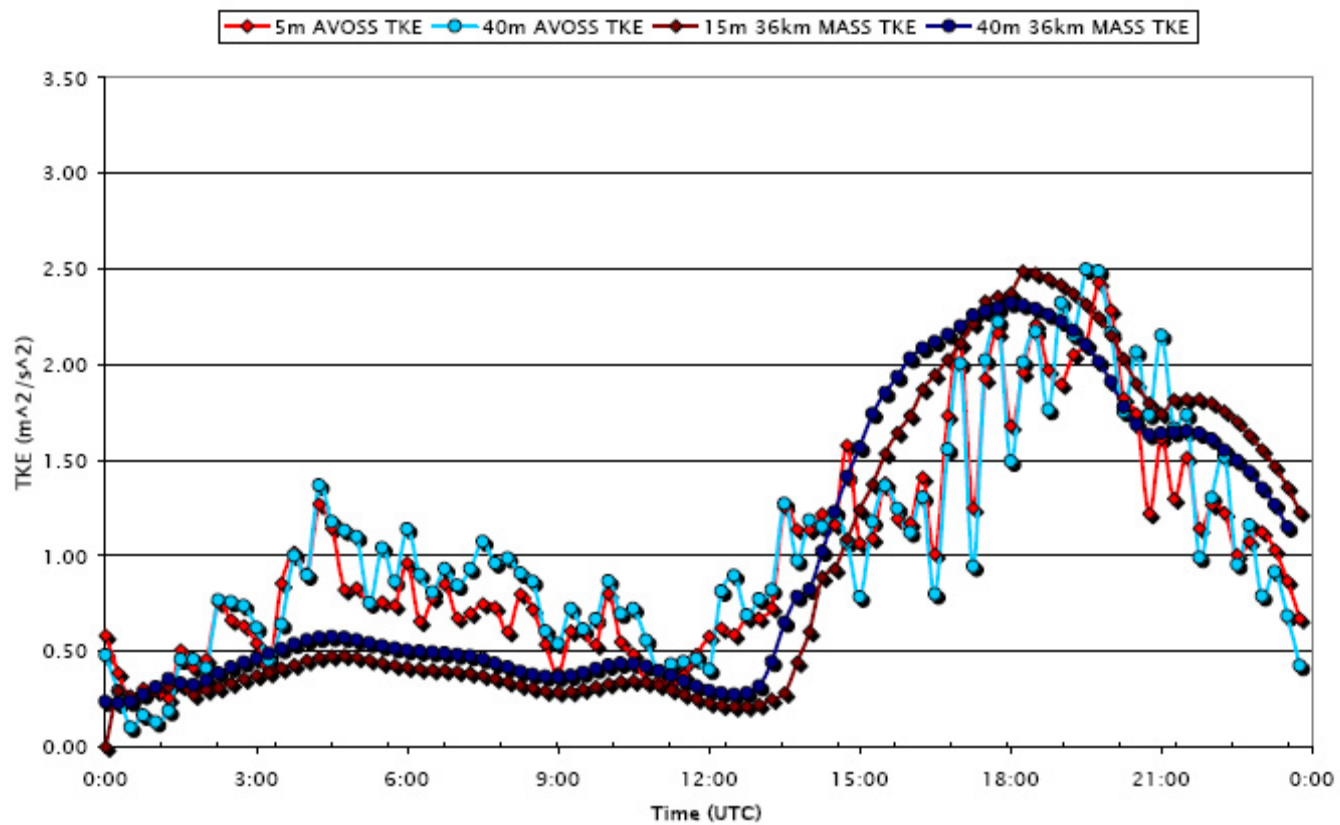
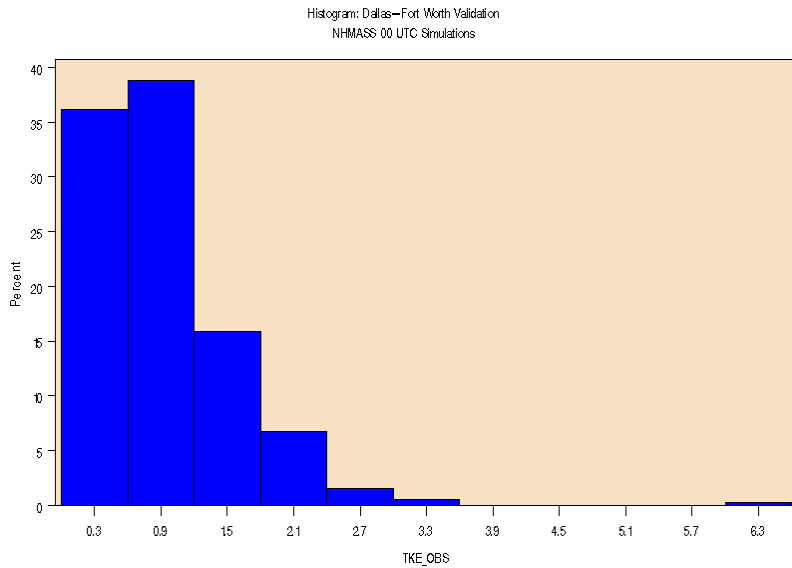
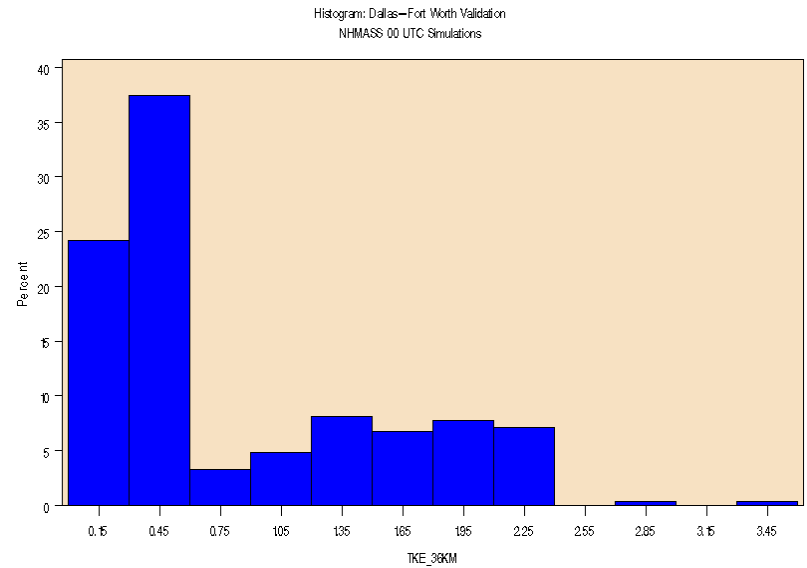


Figure 8: As with Fig. 7, but for 00-00 UTC 18-19 September 1997.



(a)



(b)

**Figure 9: Histogram plots of TKE values from 00 UTC NHMASS simulations using (a) Observations; and (b) 36 km grid resolution from point statistics taken at the DFW runway over the three-four day validation period.**

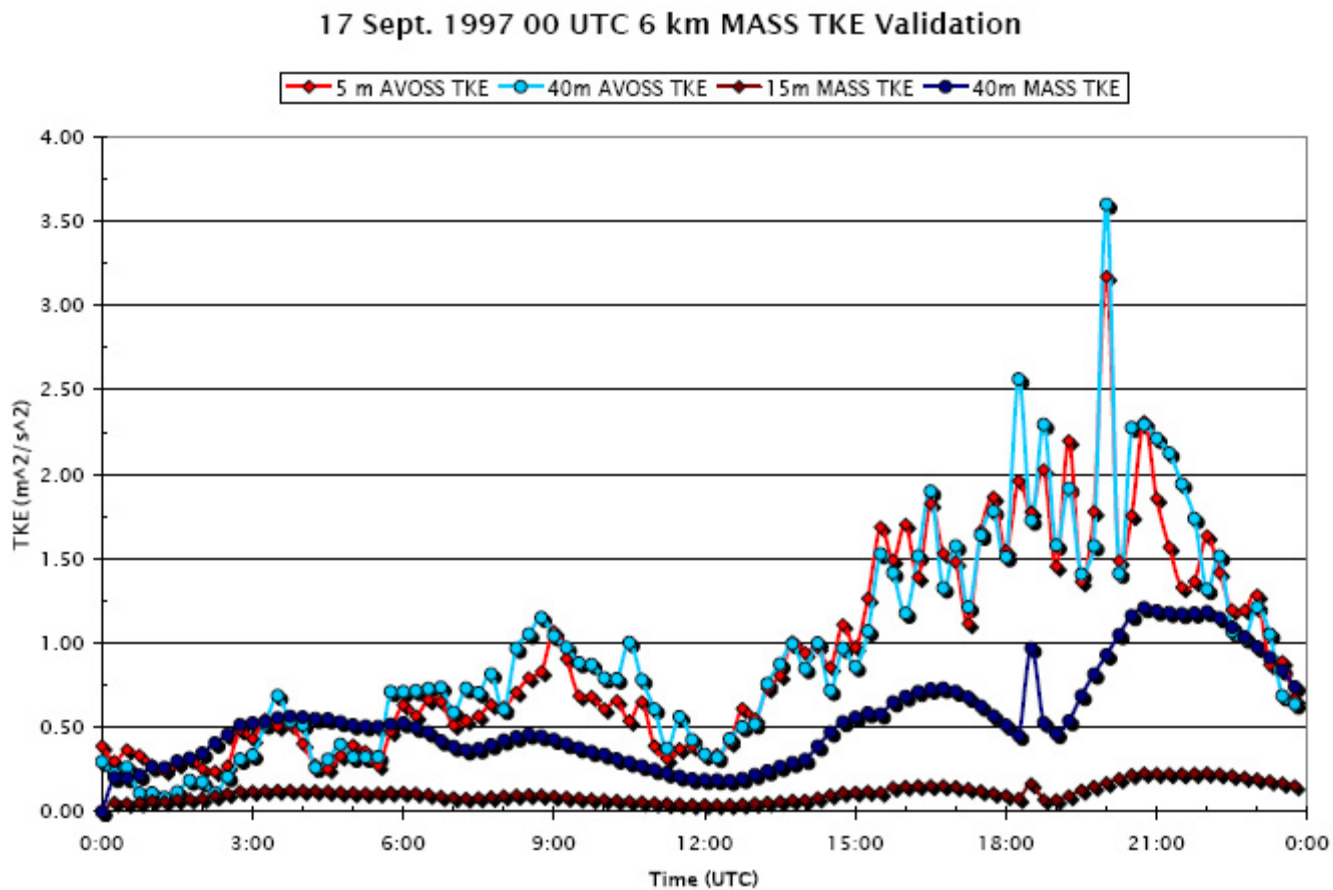


Figure 10: 17 NHMASS 6 km from 00-00 UTC 17-18 September 1997 (17\_36\_00) time series plot of 5/15 and 40 m TKE vs. time from the model simulation and AVOSS tower data.

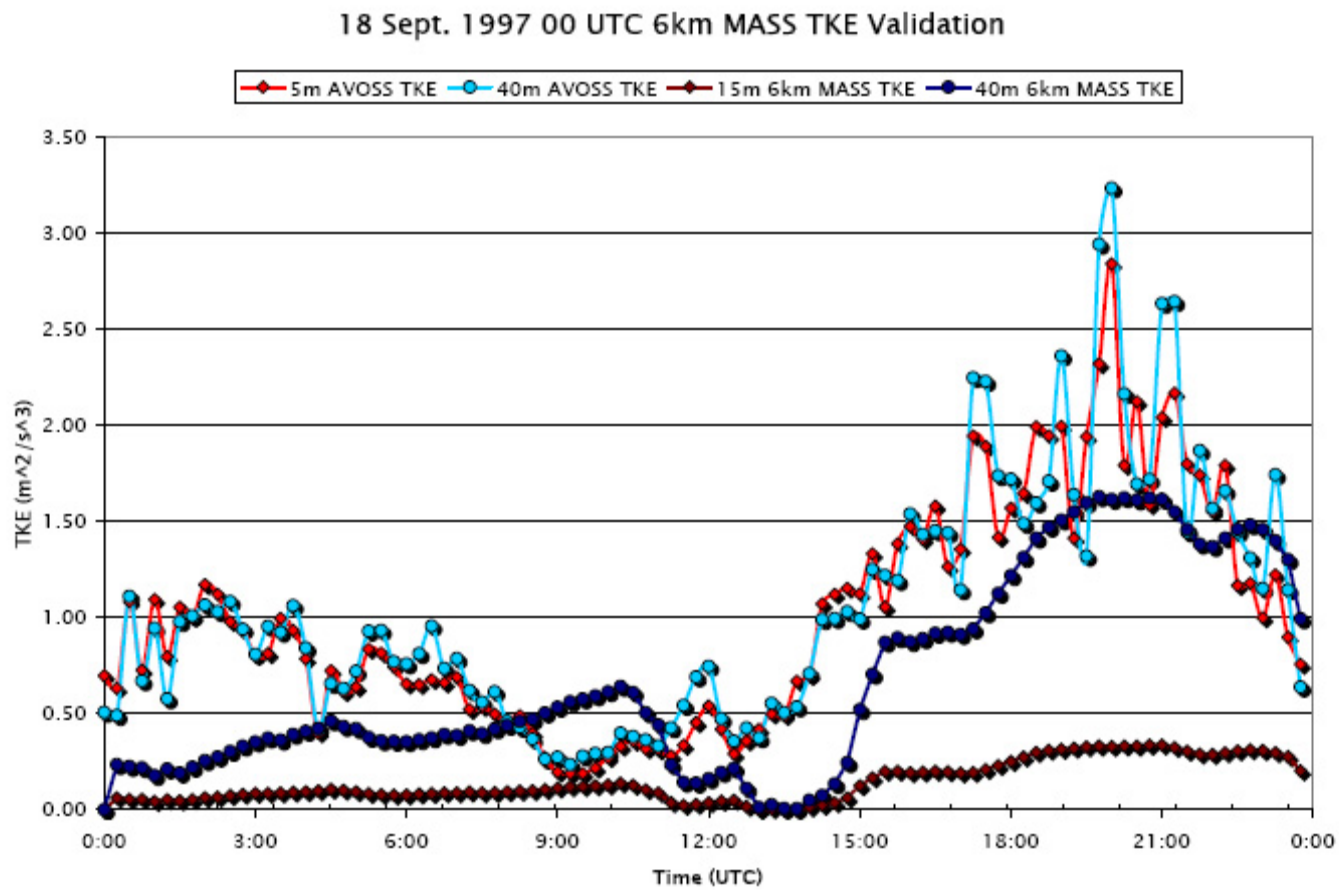


Figure 11: As with Fig. 10, but for 00-00 UTC 18-19 September 1997.

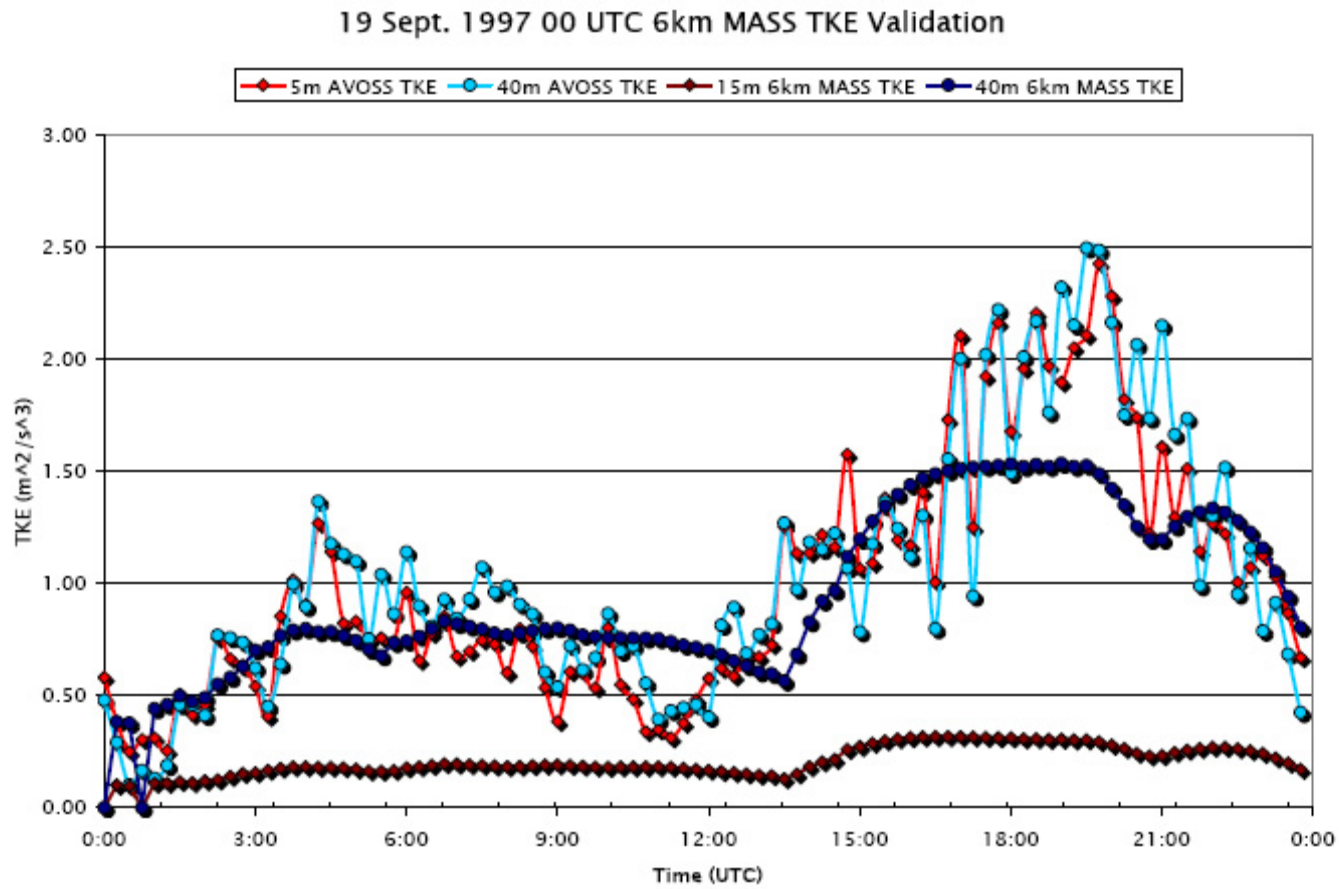
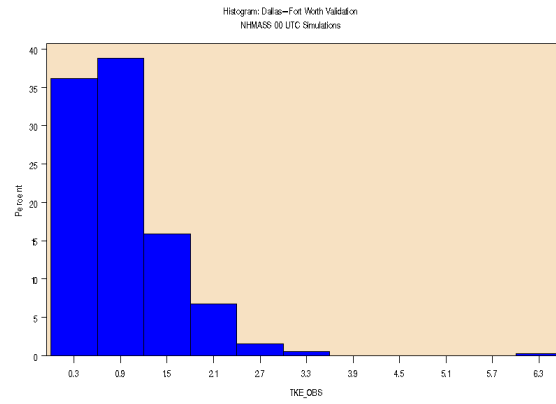
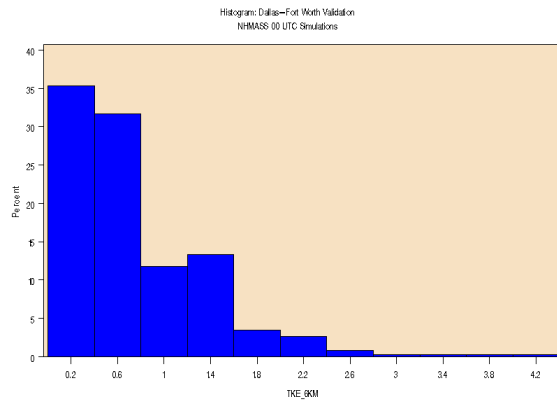


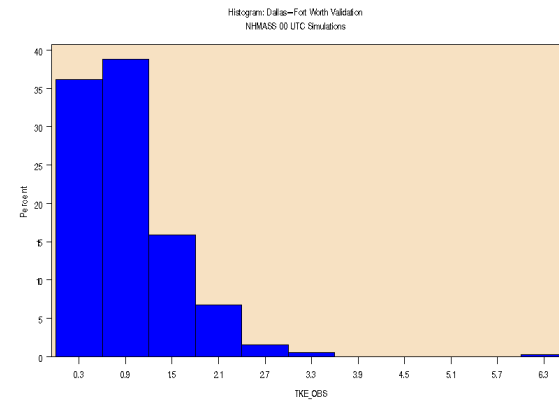
Figure 12: As with Fig. 11, but for 00-00 UTC 19-20 September 1997.



(a)



(b)



(c)

Figure 13: As with Fig. 9, but for (a) Observations, (b) 6 km grids and (c) 1 km grids.

### 17 Sept. 1997 00 UTC 1 km MASS TKE Validation

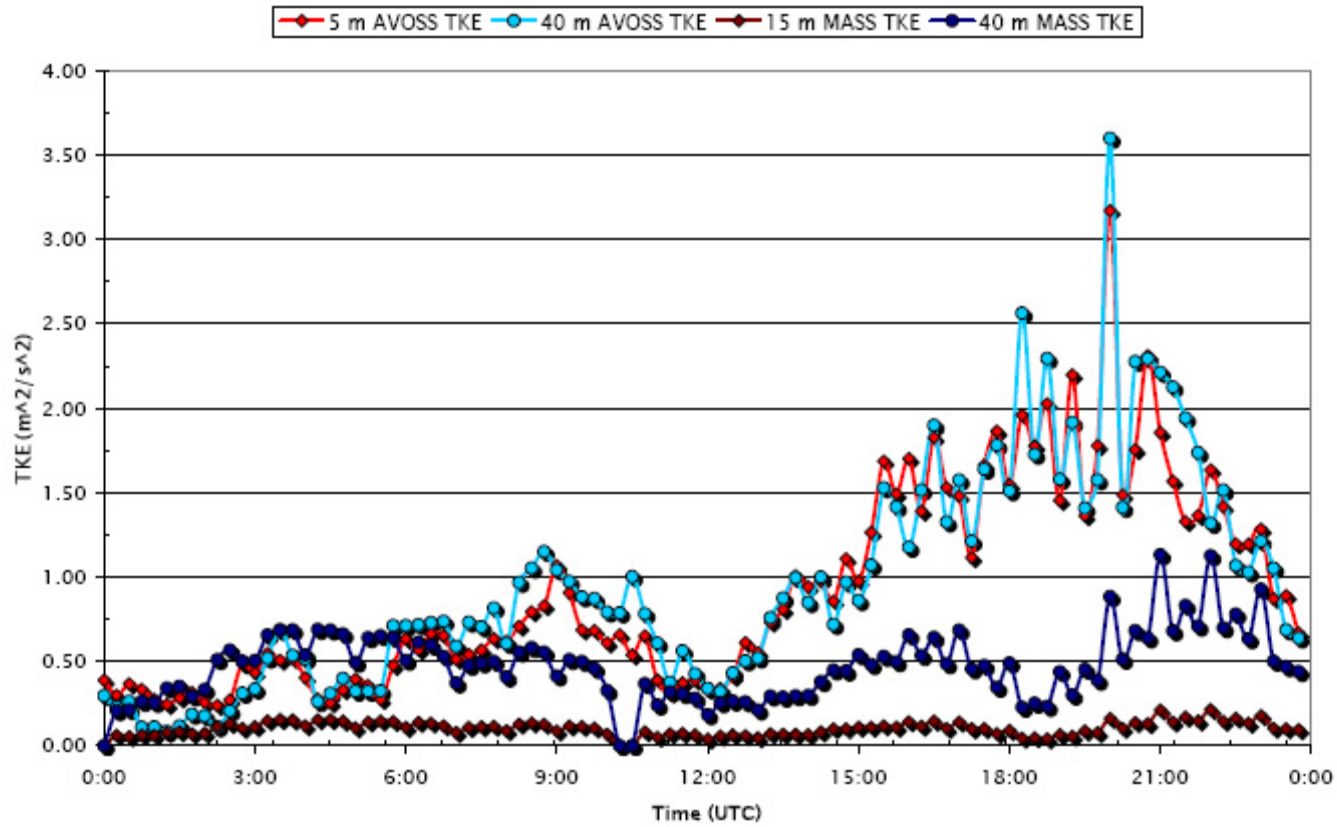


Figure 14: 17 NHMASS 1 km from 00-00 UTC 17-18 September 1997 (17\_36\_00) time series plot of 5/15 and 40 m TKE vs. time from the model simulation and AVOSS tower data.

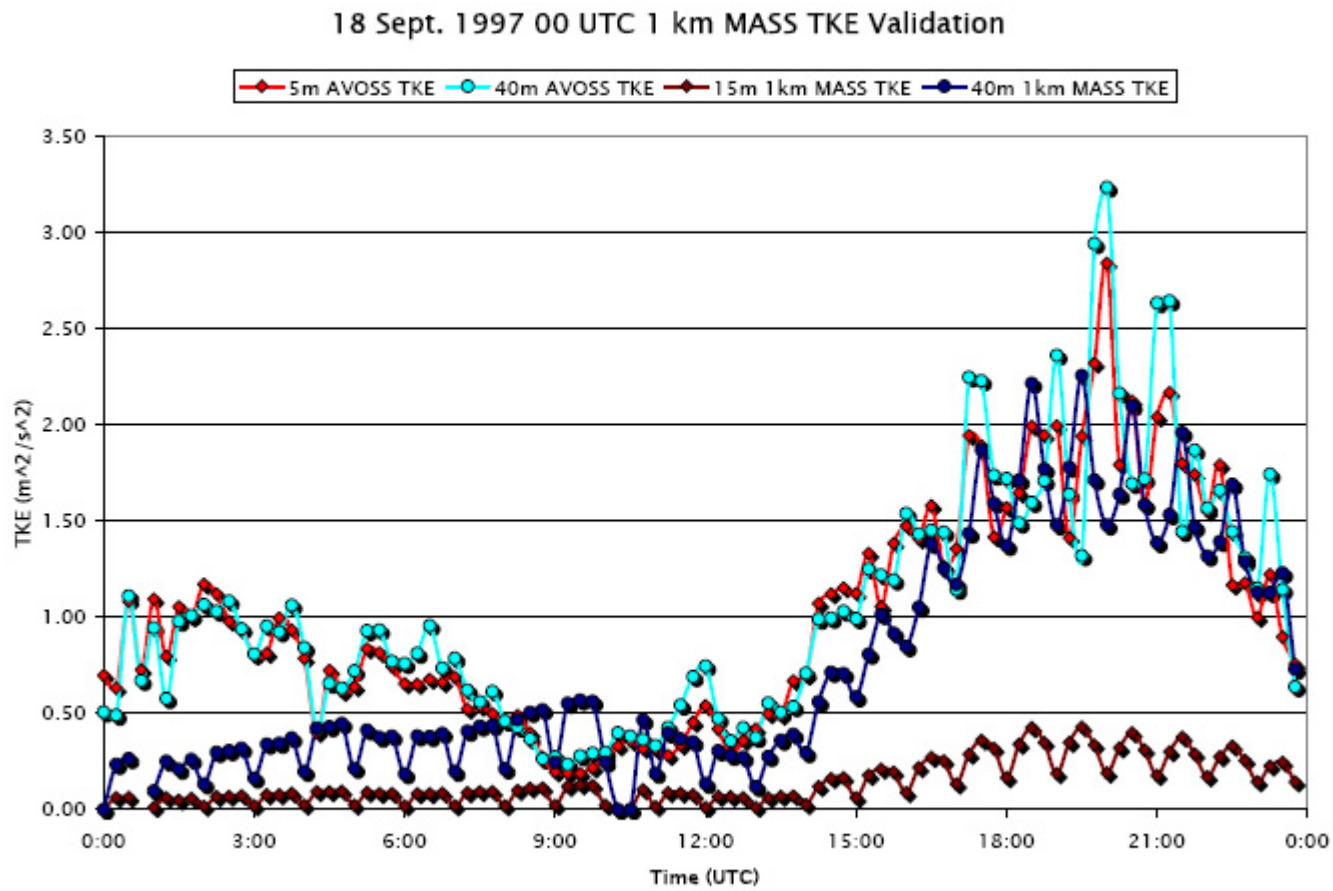


Figure 15: As with Fig. 14, but for 00-00 UTC 18-19 September 1997.

### 19 Sept. 1997 00 UTC 1 km MASS TKE Validation

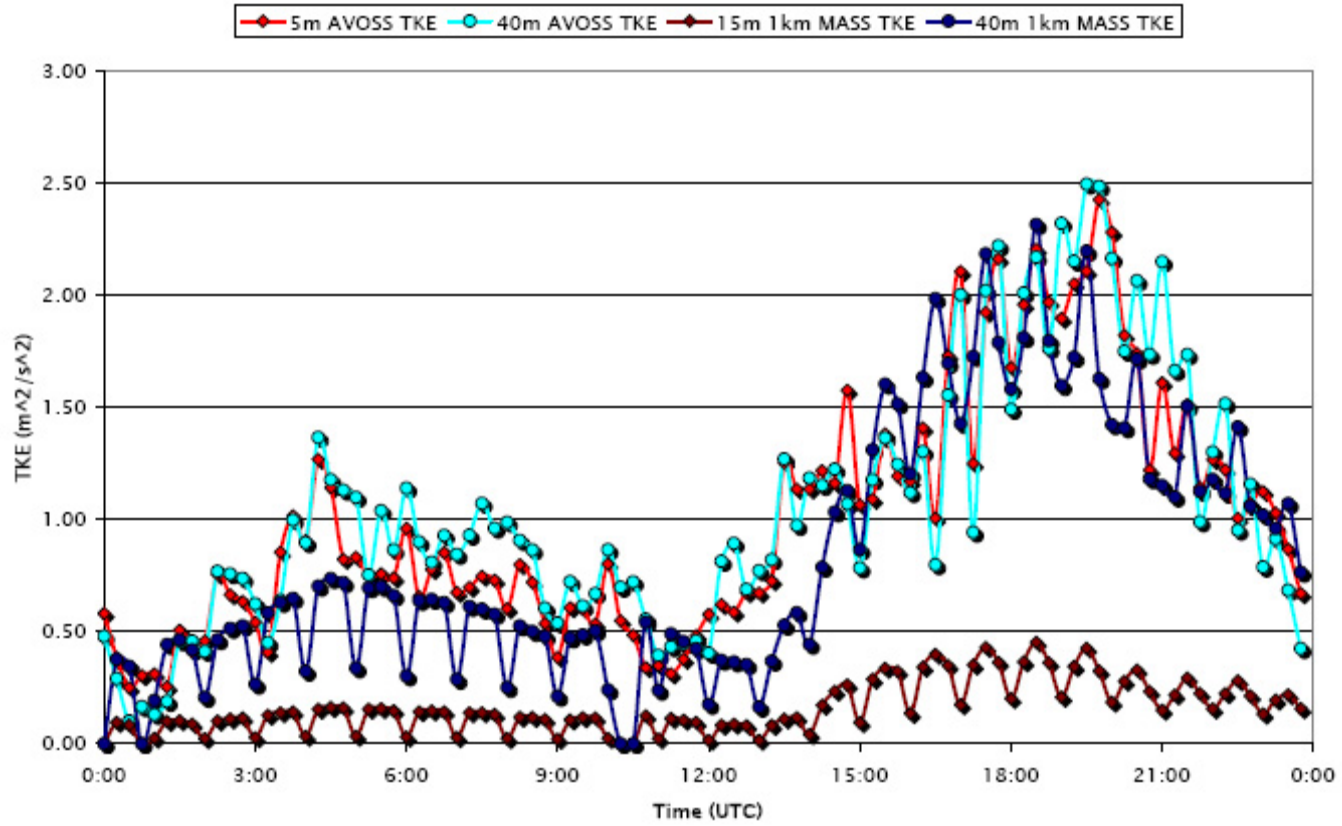


Figure 16: As with Fig. 15, but for 00-00 UTC 18-19 September 1997.

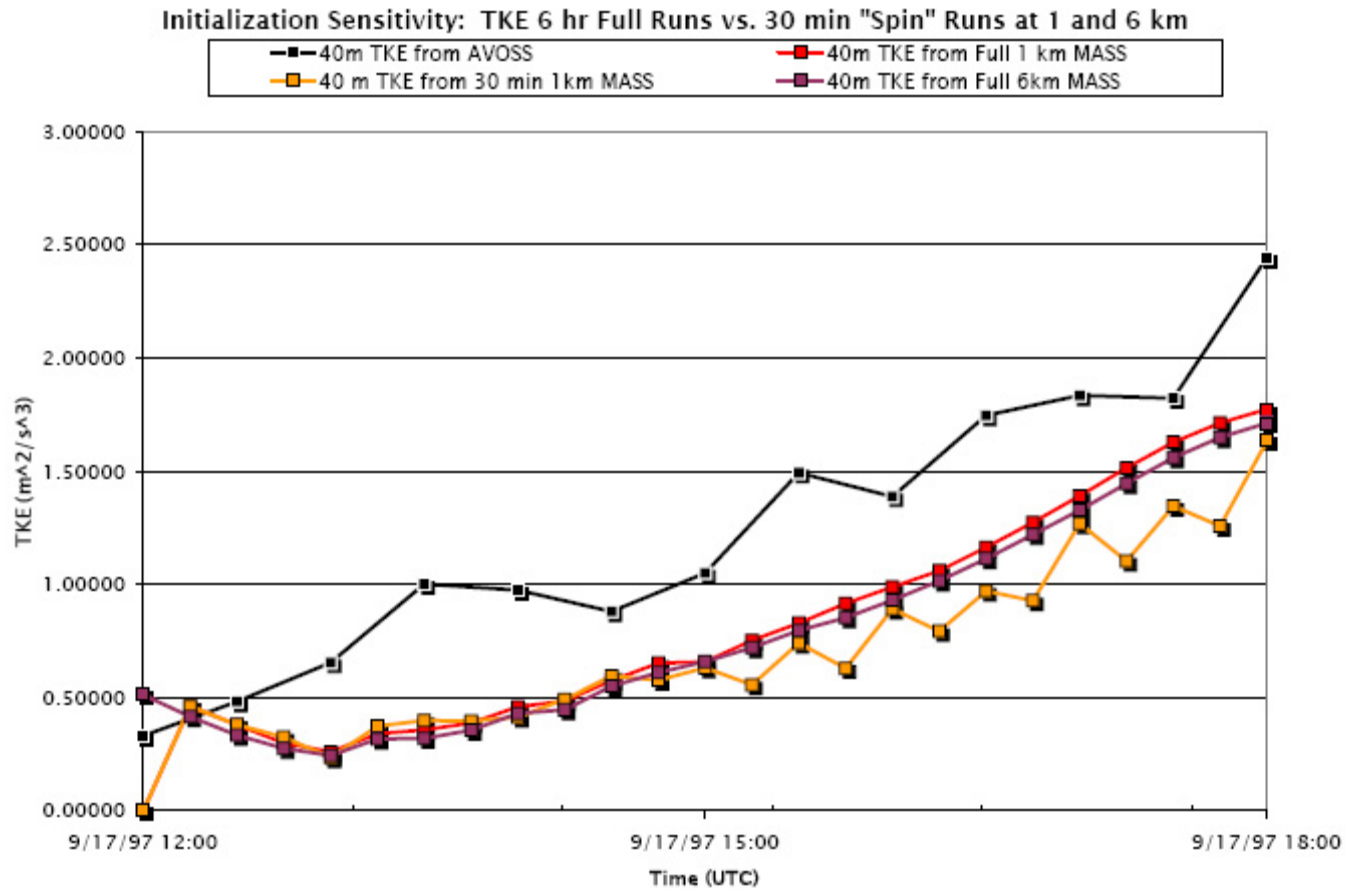


Figure 17: Sensitivity to initialization structure comparing the 30-min “spin” runs against observations (AVOSS) and from continuously integrated 6 and 1 km runs valid from 17\_06\_00 from 12 UTC-18 UTC 17 September 1997.

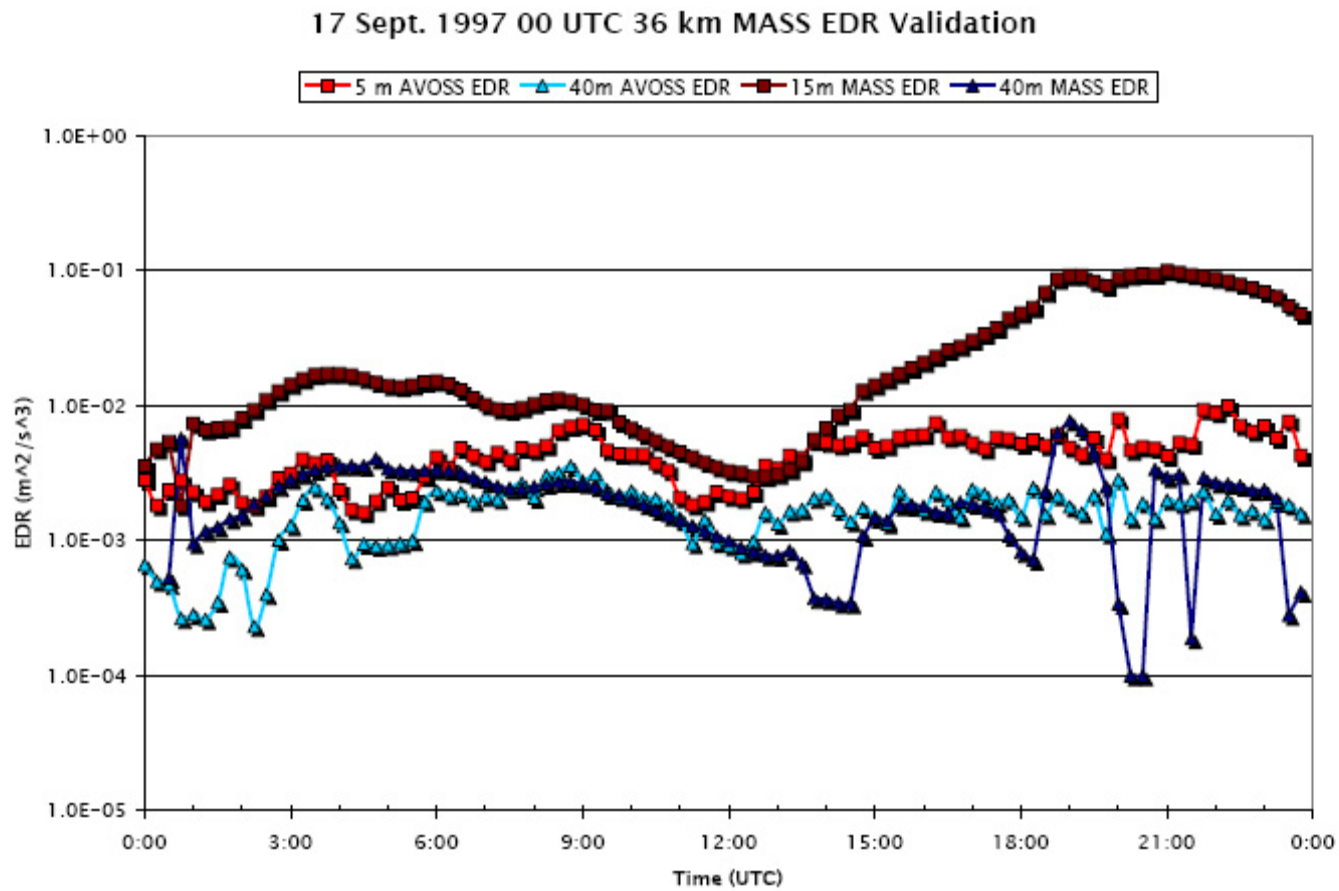


Figure 18: 17 NHMASS 36 km from 00-00 UTC 17-18 September 1997 (17\_36\_00) time series plot of 5/15 and 40 m eddy dissipation rate (EDR, log scale) vs. time from the model simulation and AVOSS tower data.

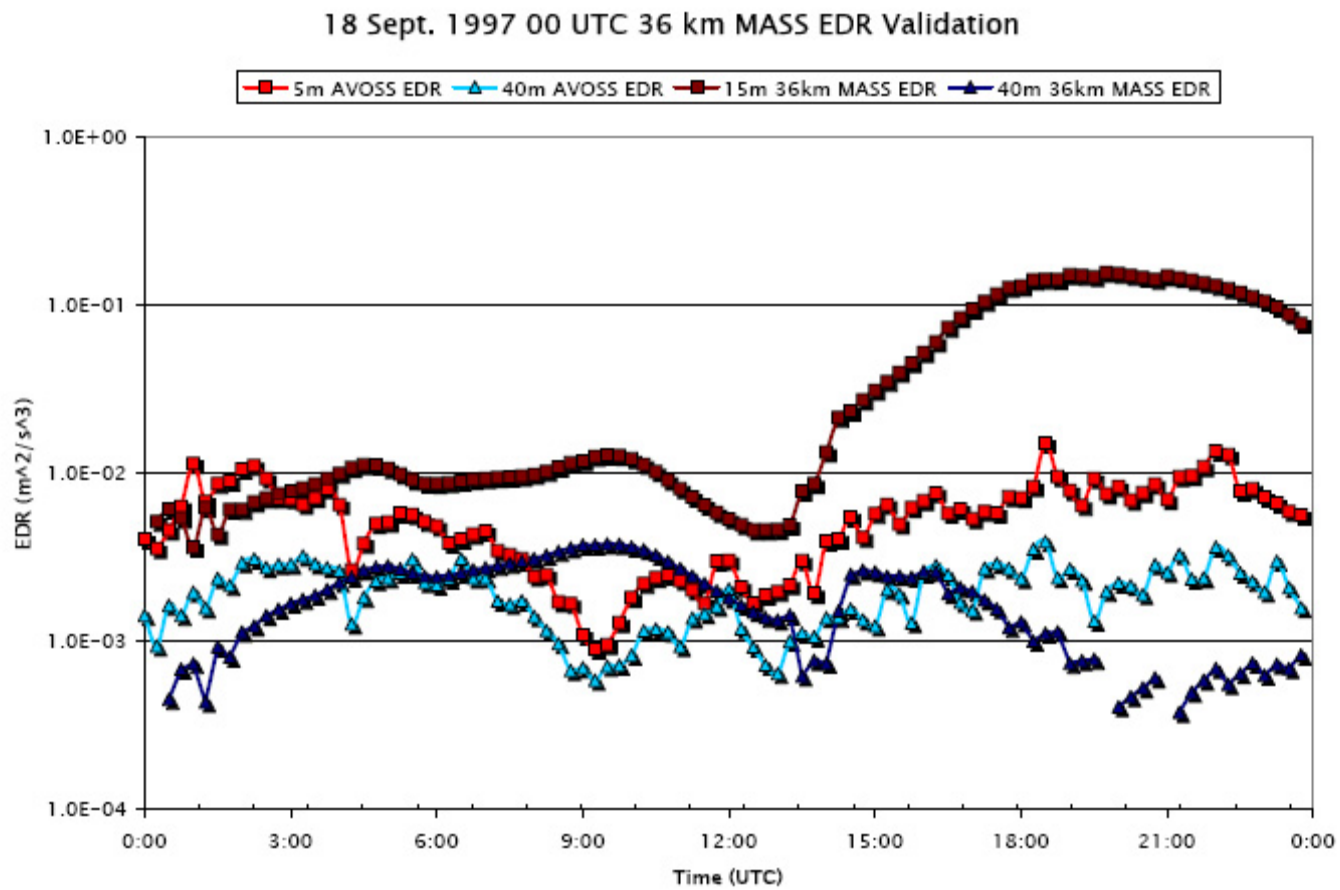


Figure 19: As with Fig. 18, but for 00-00 UTC 18-19 September 1997.

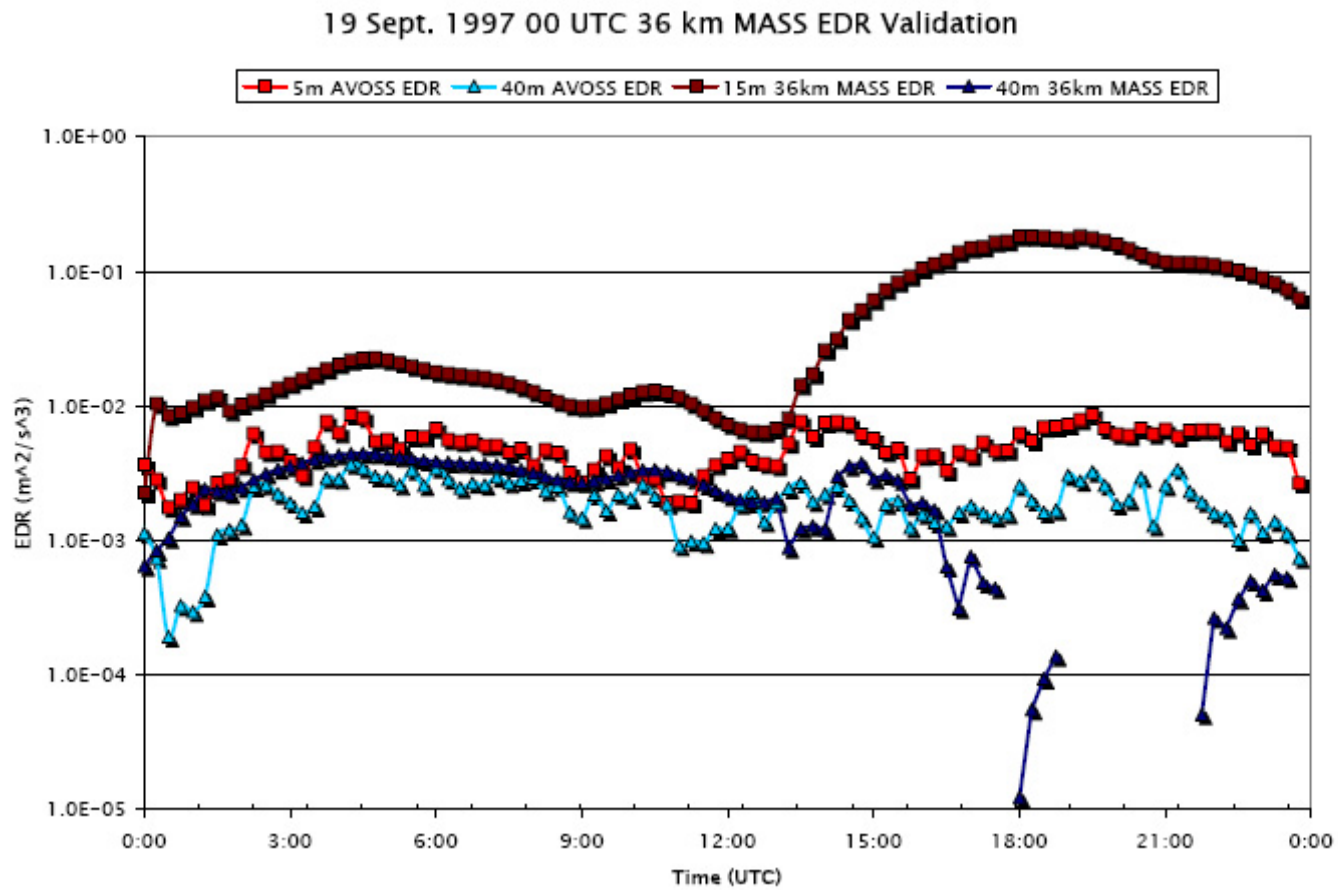


Figure 20: As with Fig. 19, but for 00-00 UTC 18-19 September 1997.

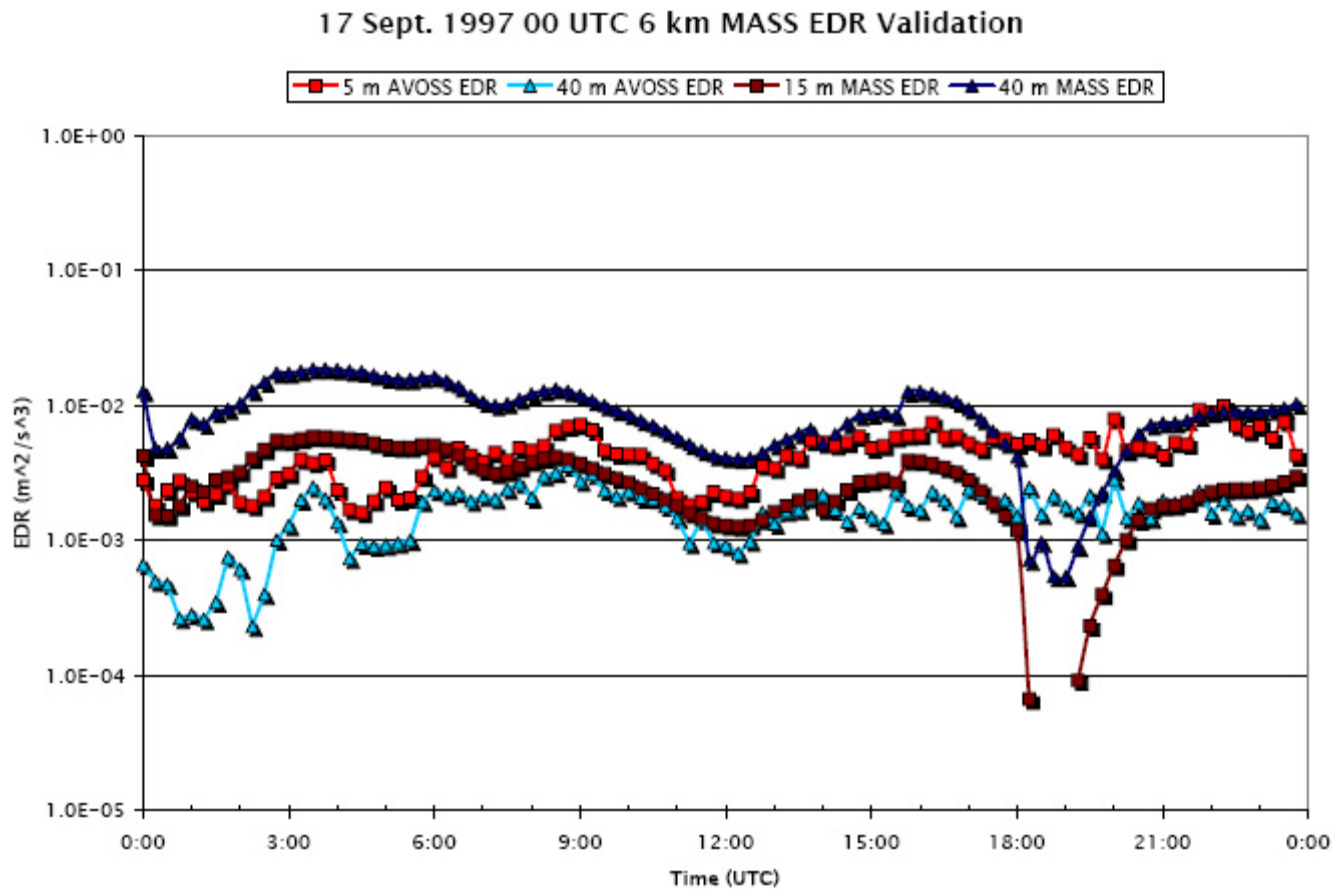


Figure 21: 17 NHMASS 6 km from 00-00 UTC 17-18 September 1997 (17\_6\_00) time series plot of 5/15 and 40 m eddy dissipation rate (EDR, log scale) vs. time from the model simulation and AVOSS tower data.

### 18 Sept. 1997 00 UTC 6 km MASS EDR Validation

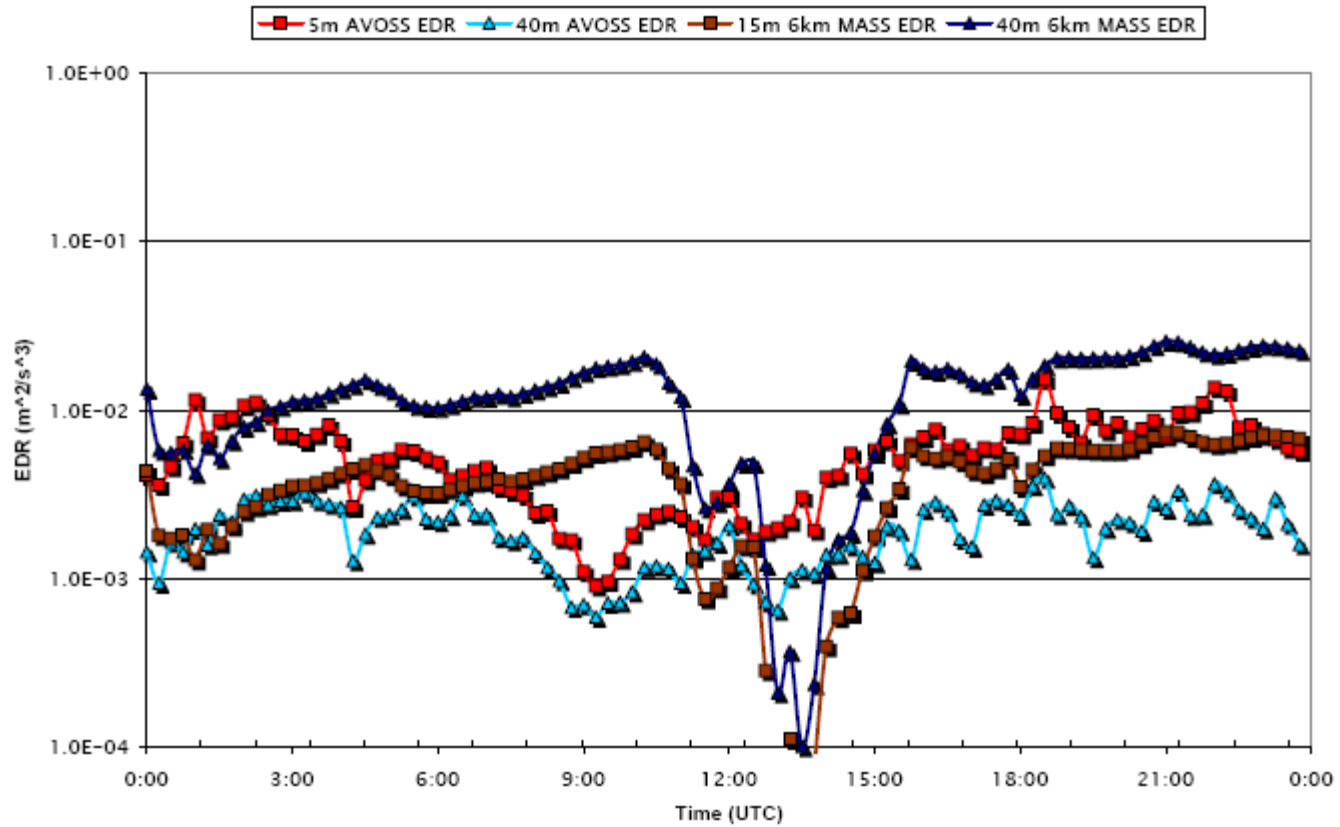


Figure 22: As with Fig. 21, but for 00-00 UTC 18-19 September 1997.

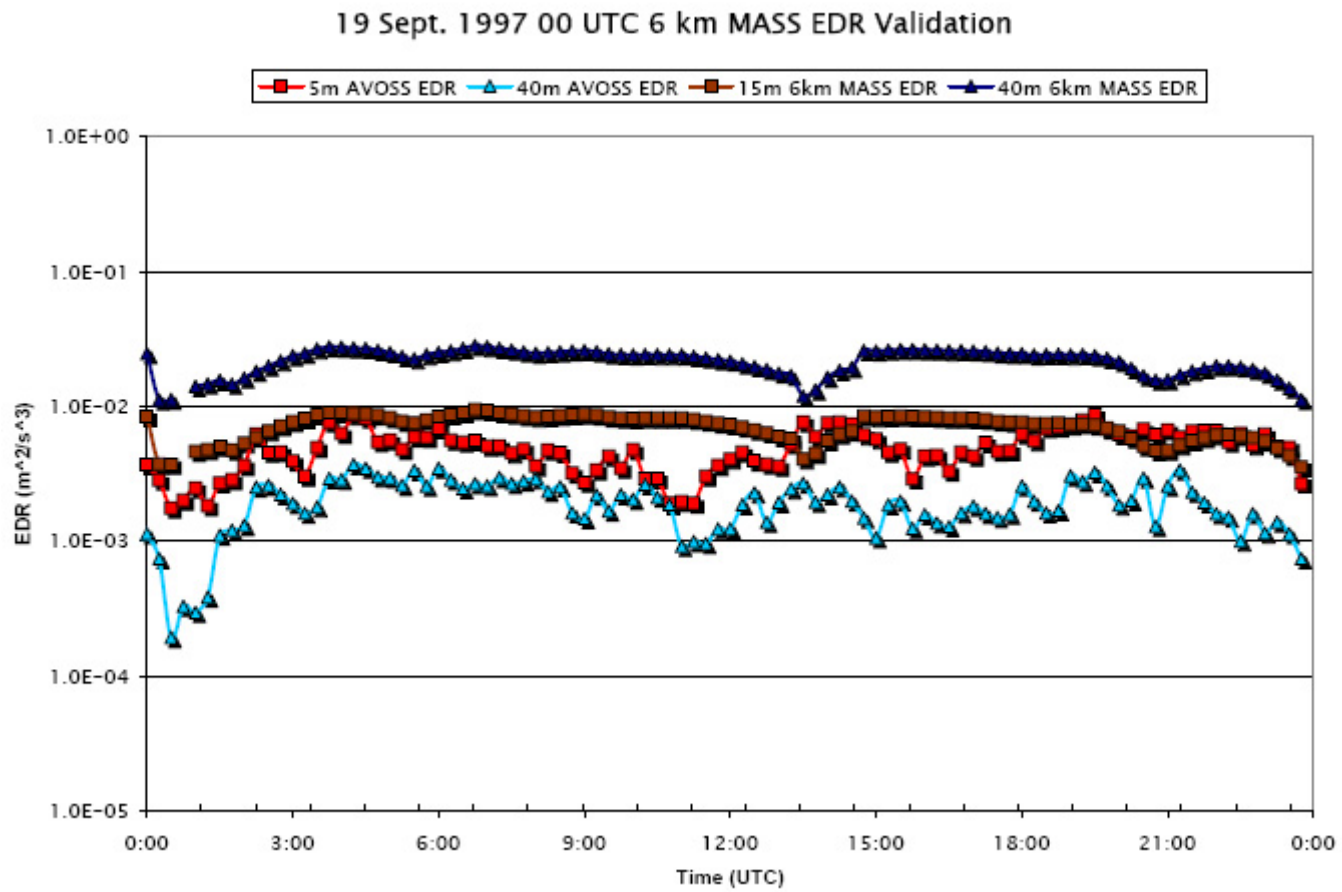


Figure 23: As with Fig. 22, but for 00-00 UTC 19-20 September 1997.

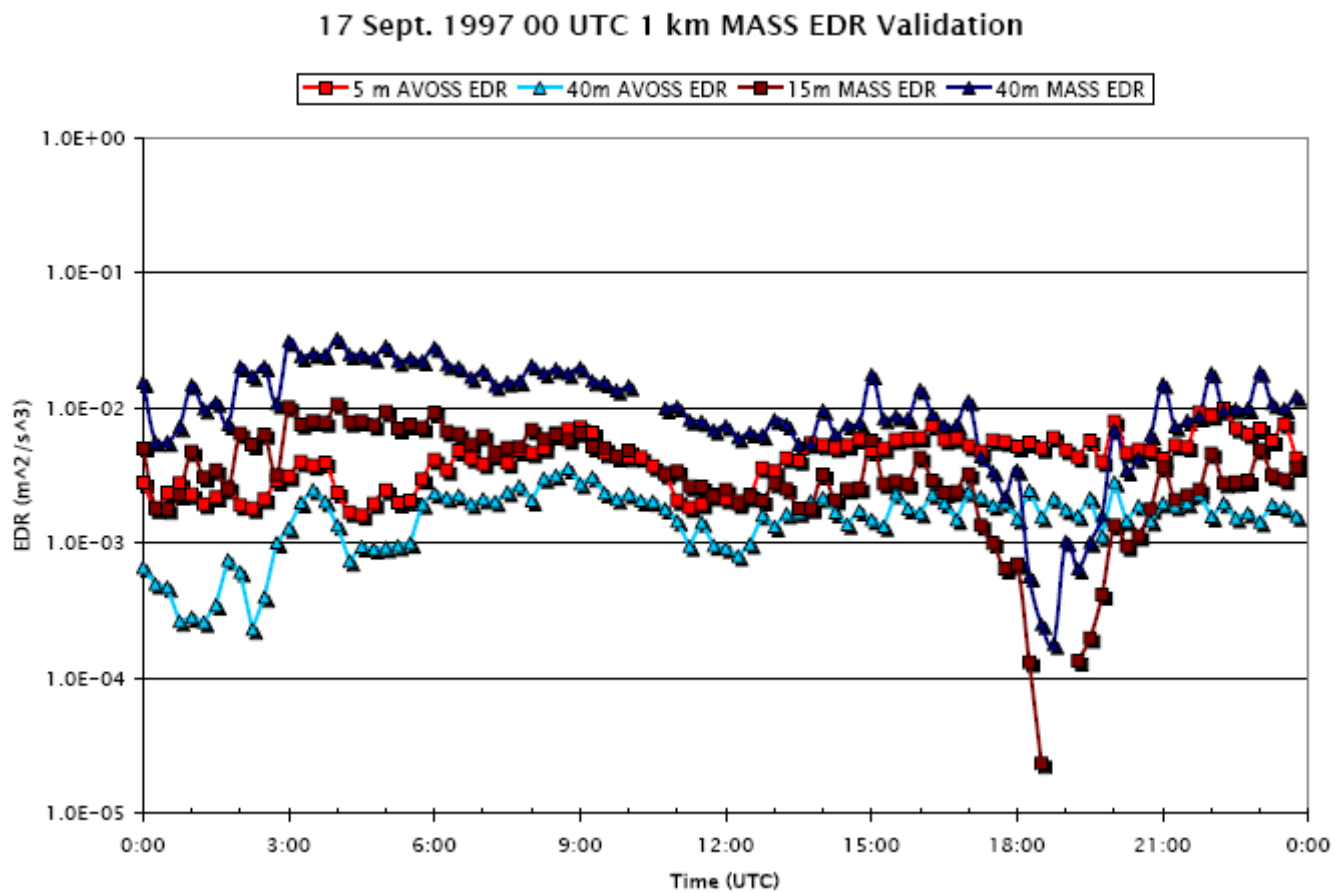


Figure 24: As with Fig. 20, but for 1-km (17\_01\_00) valid 00-00 UTC 17-18 September 1997.

### 17-18 Sept. 1997 12 UTC 36 km MASS TKE Validation

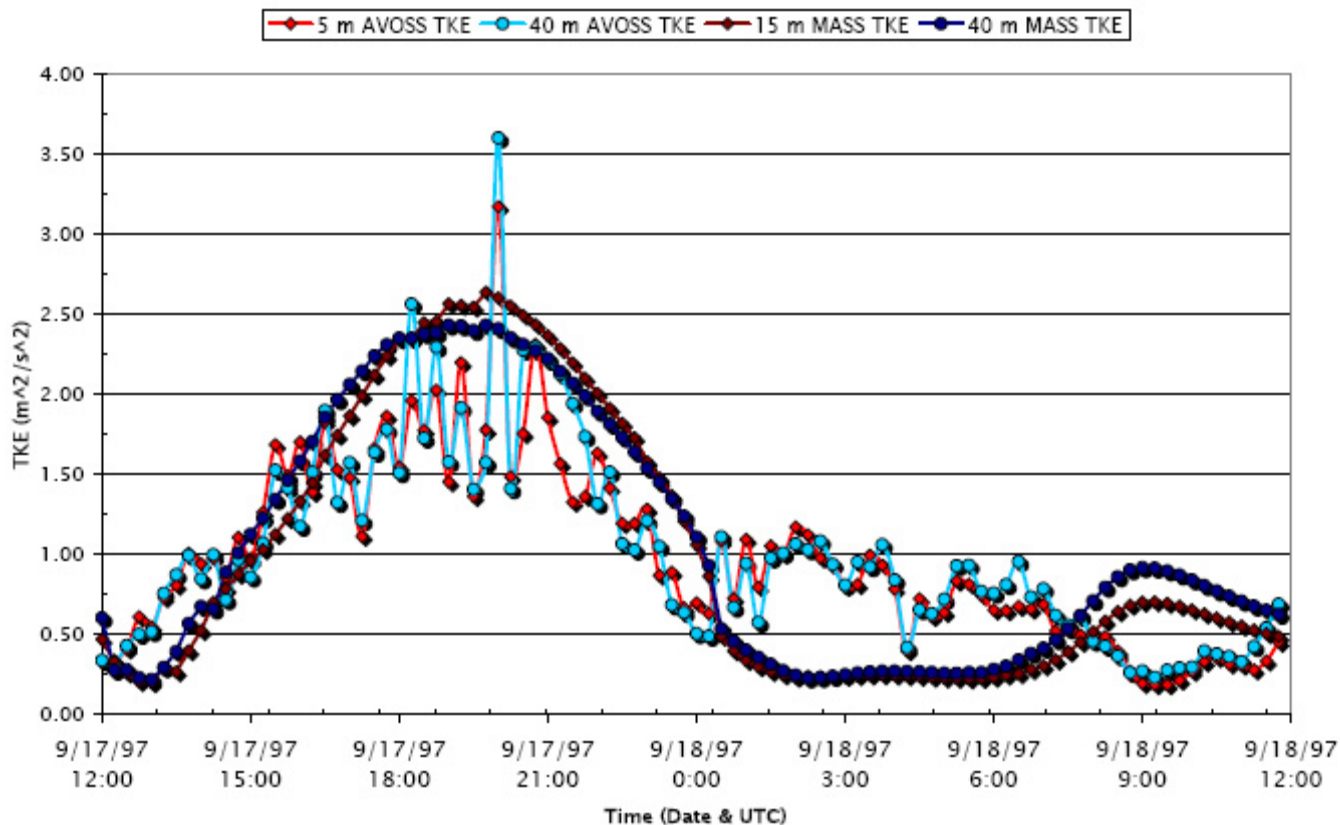


Figure 25: 17 NHMASS 36 km from 12-12 UTC 17-18 September 1997 (17\_36\_00) time series plot of 5/15 and 40 m TKE vs. time from the model simulation and AVOSS tower data.

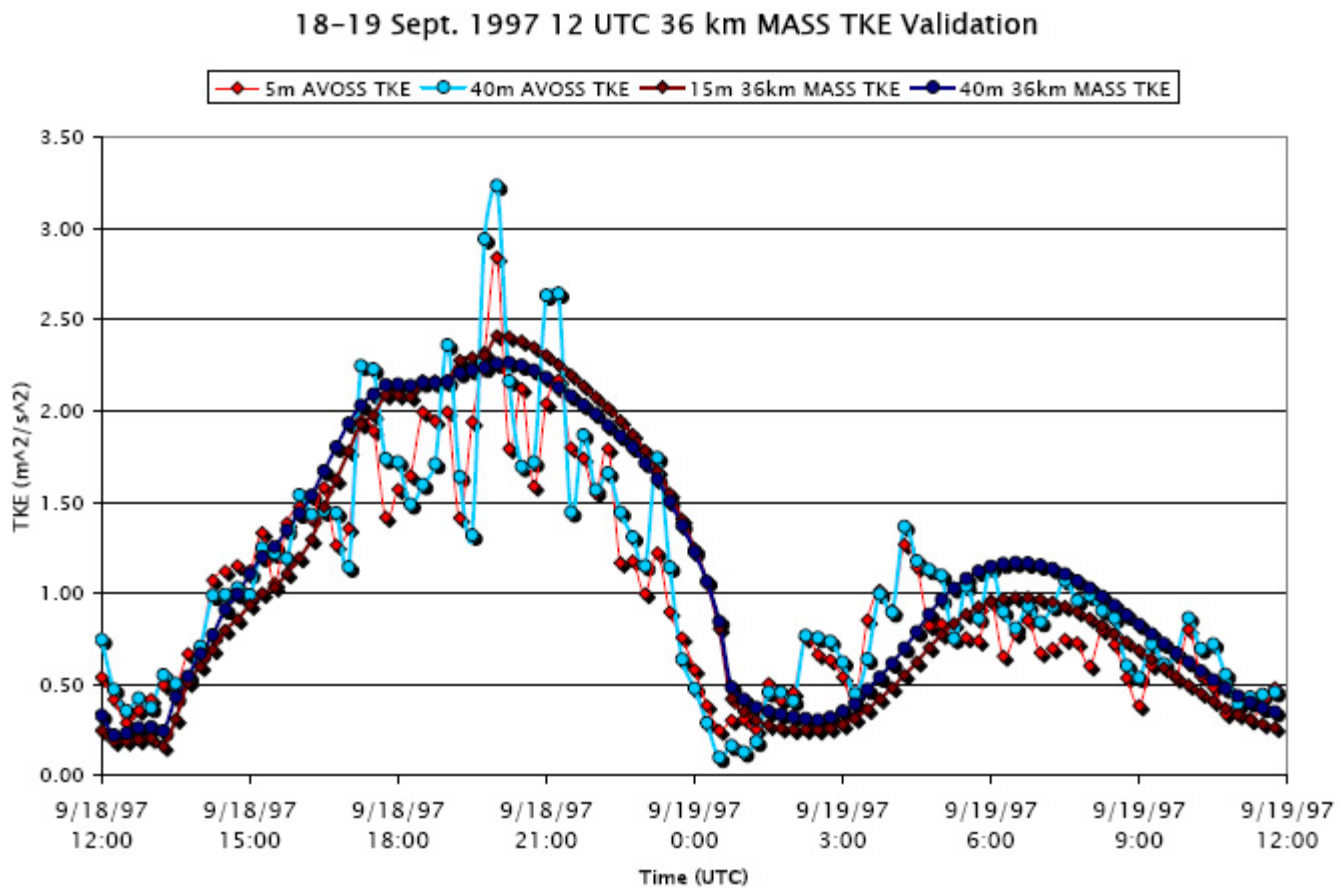


Figure 26: As with Fig. 25, but for 00-00 UTC 18-19 September 1997.

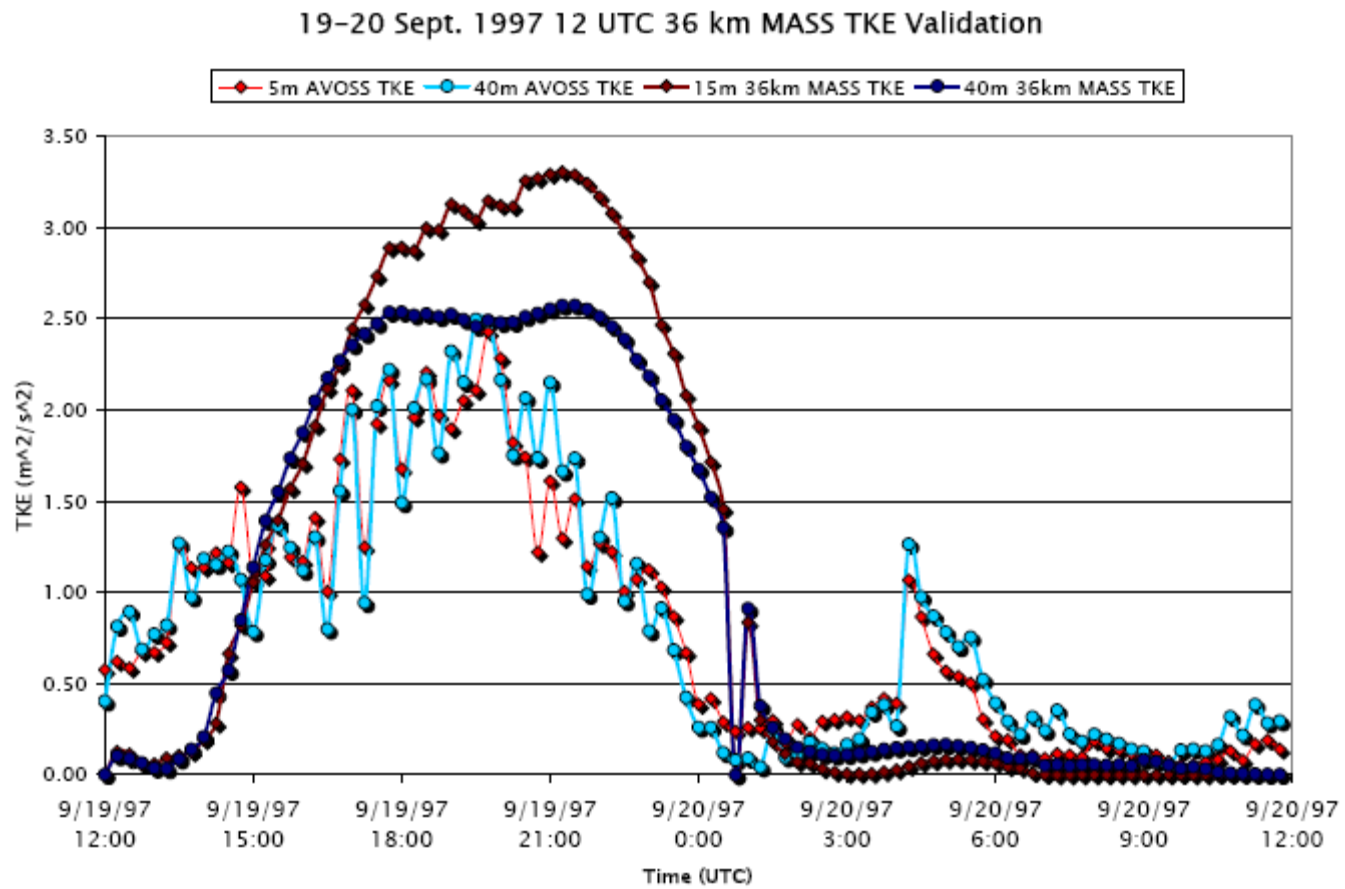


Figure 27: As with Fig. 26, but for 00-00 UTC 18-19 September 1997.

### 17-18 Sept. 1997 12 UTC 6 km MASS TKE Validation

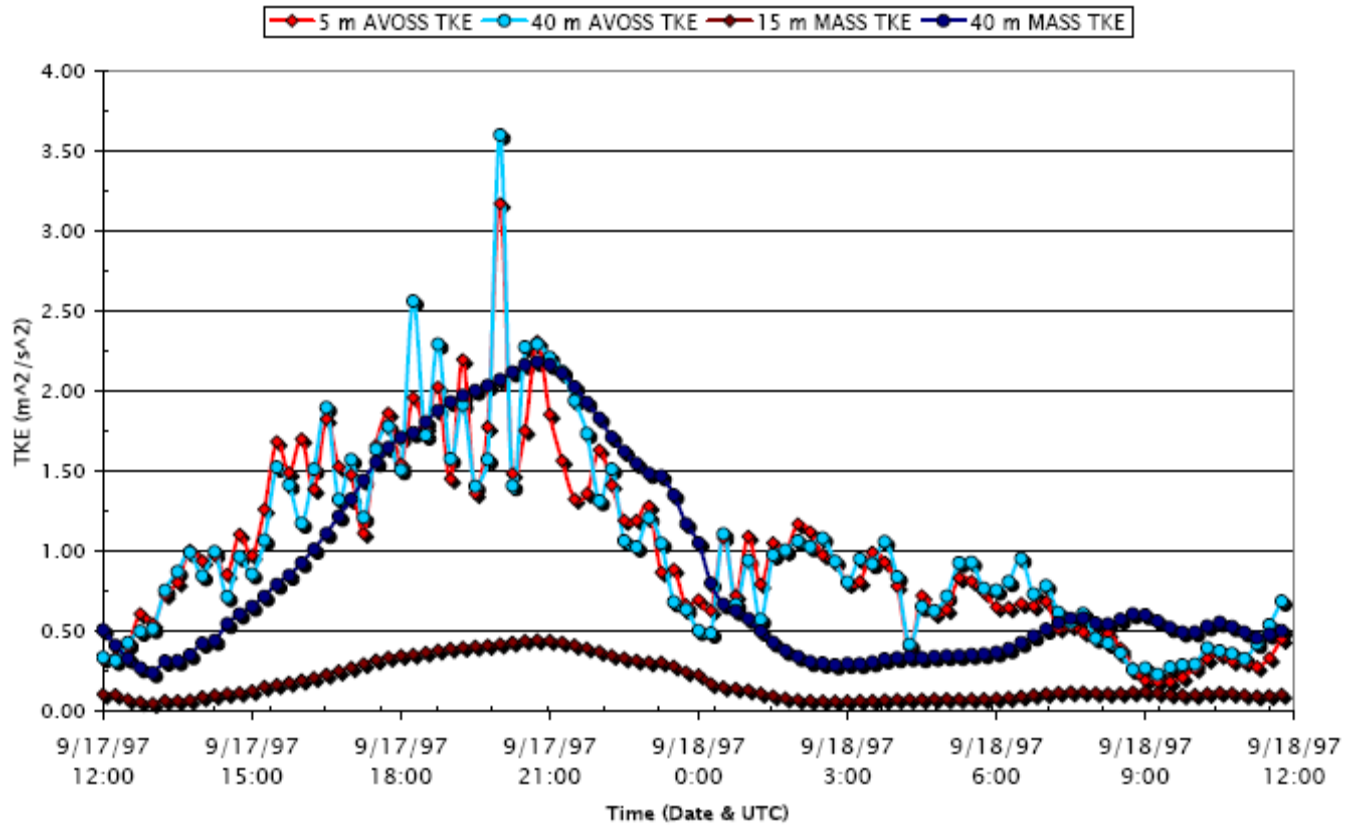


Figure 28: 17 NHMASS 6 km from 12-12 UTC 17-18 September 1997 (17\_36\_00) time series plot of 5/15 and 40 m TKE vs. time from the model simulation and AVOSS tower data.

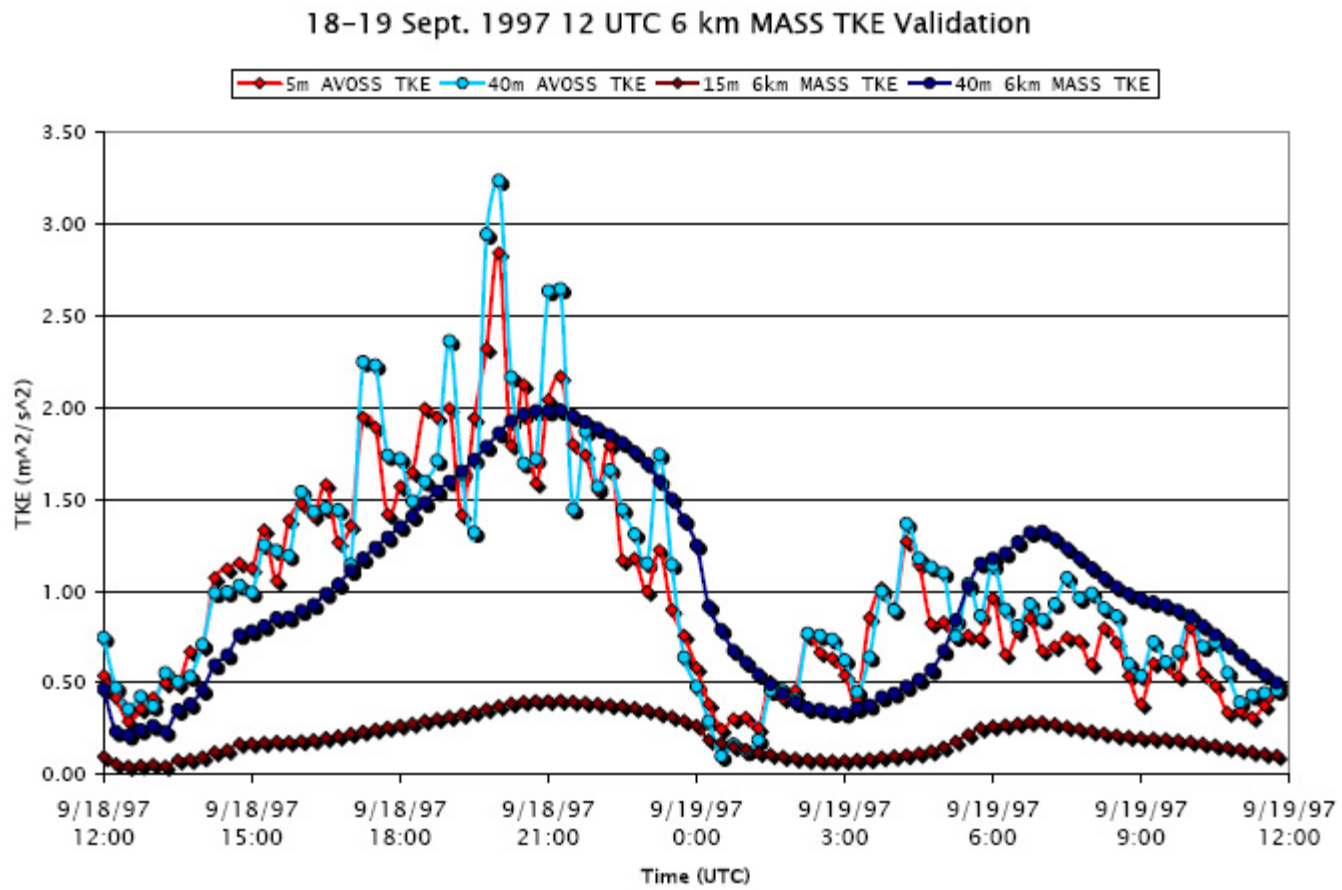


Figure 29: As with Fig. 28, but for 12-12 UTC 18-19 September 1997.

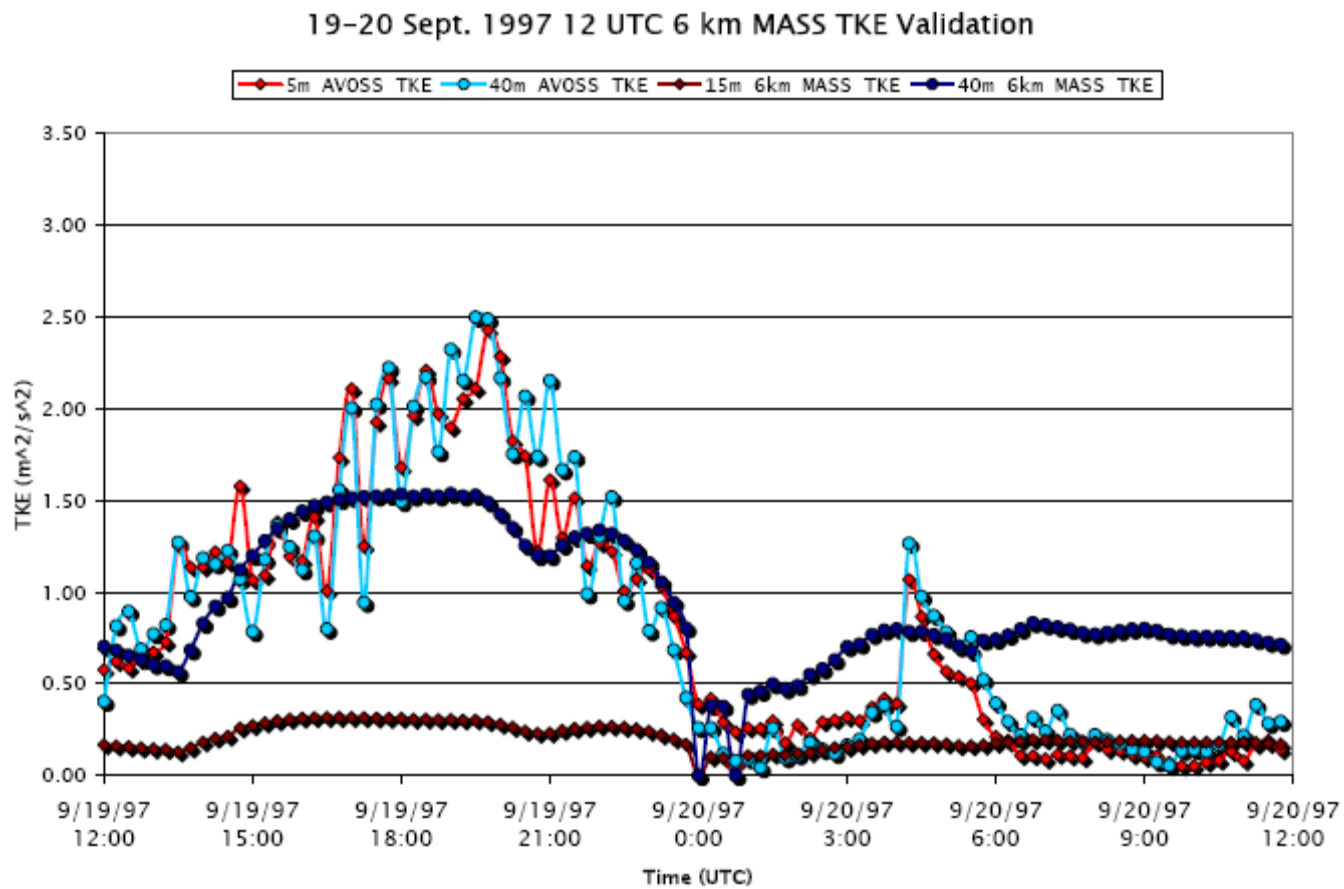


Figure 30: As with Fig. 29, but for 12-12 UTC 19-20 September 1997.

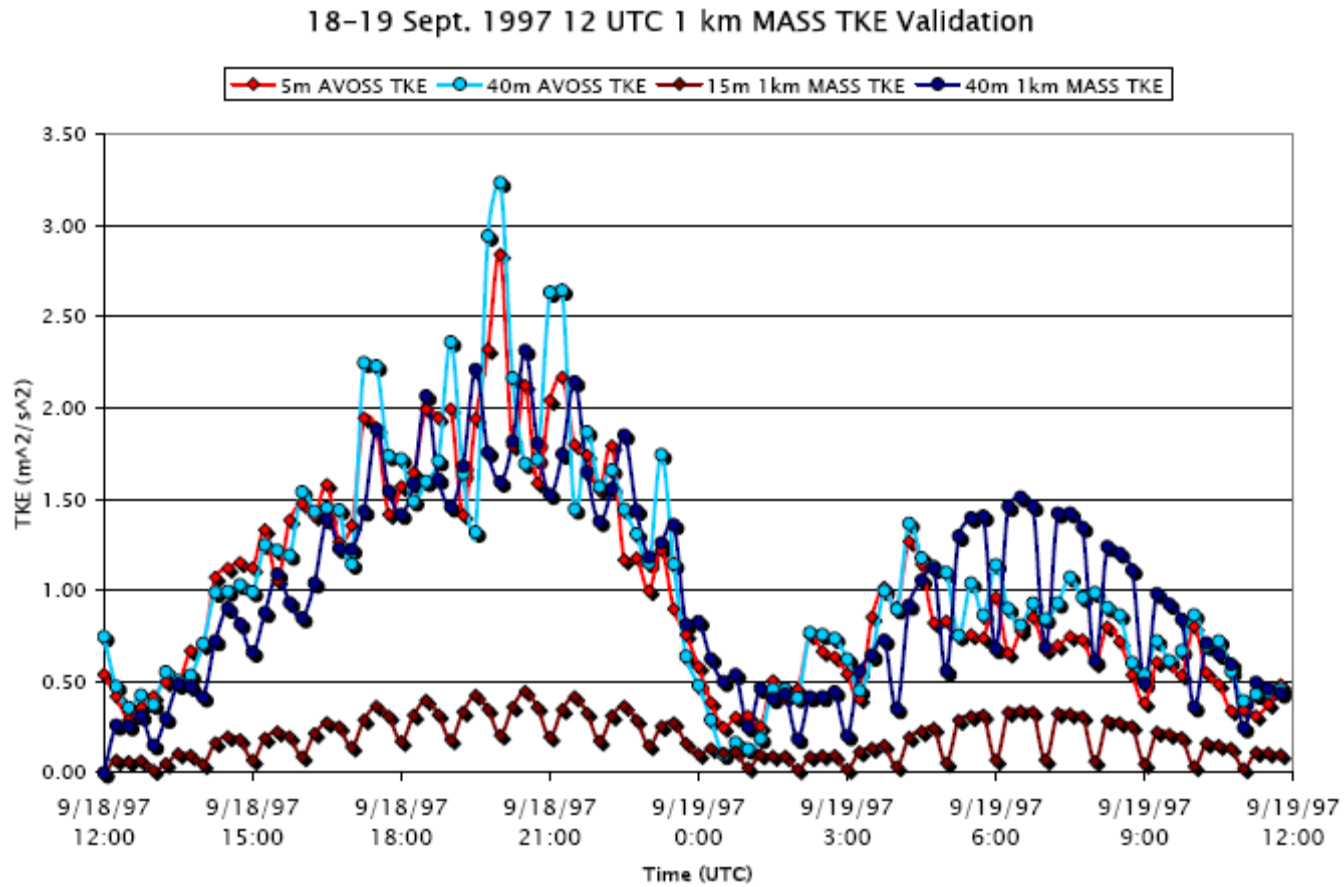


Figure 31: 17 NHMASS 1 km from 12-12 UTC 18-19 September 1997 (18\_36\_00) time series plot of 5/15 and 40 m TKE vs. time from the model simulation and AVOSS tower data.

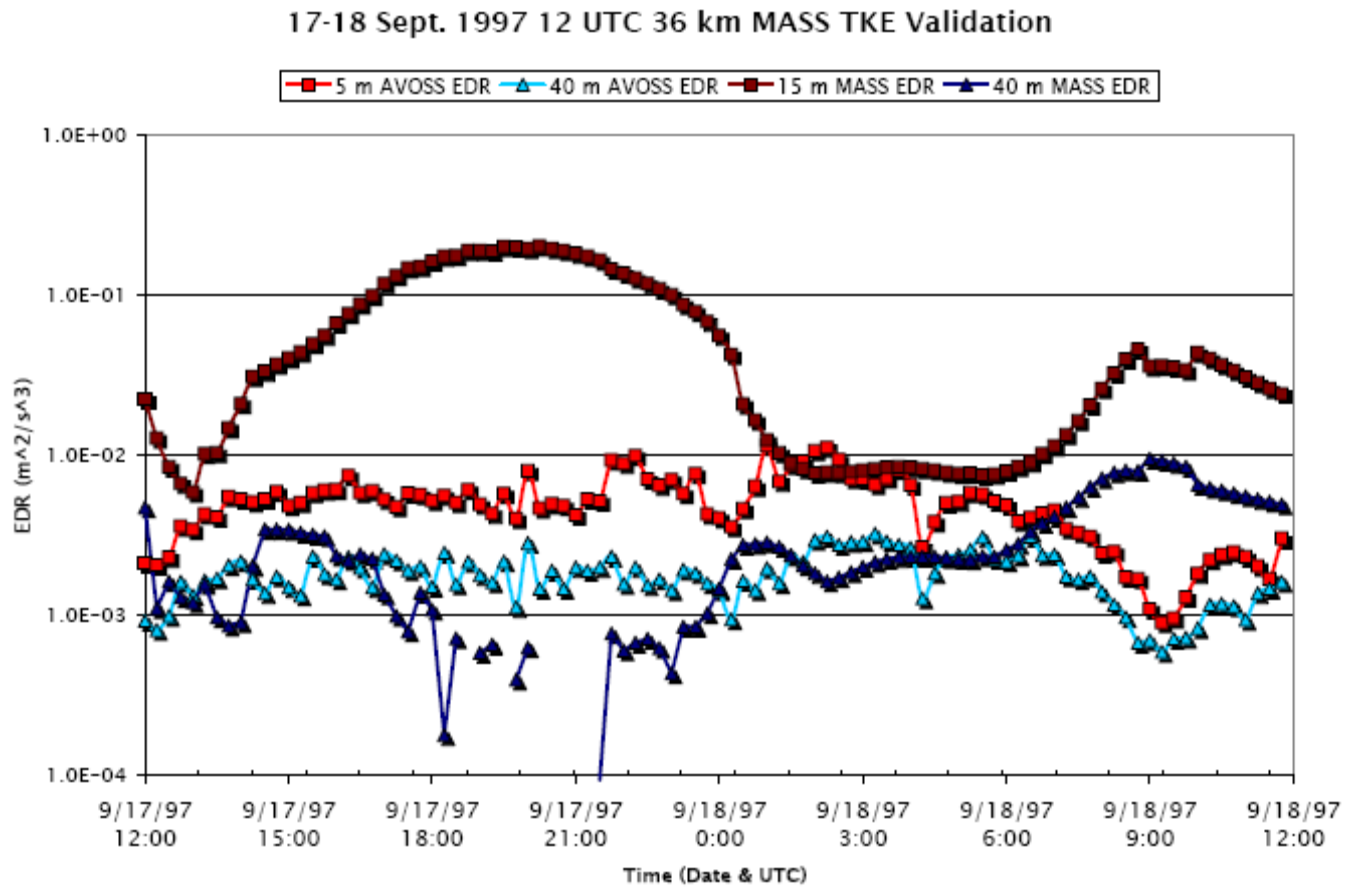


Figure 32: NHMASS 36 km from 12-12 UTC 17-18 September 1997 (17\_36\_12) time series plot of 5/15 and 40 m eddy dissipation rate (EDR, log scale) vs. time from the model simulation and AVOSS tower data.

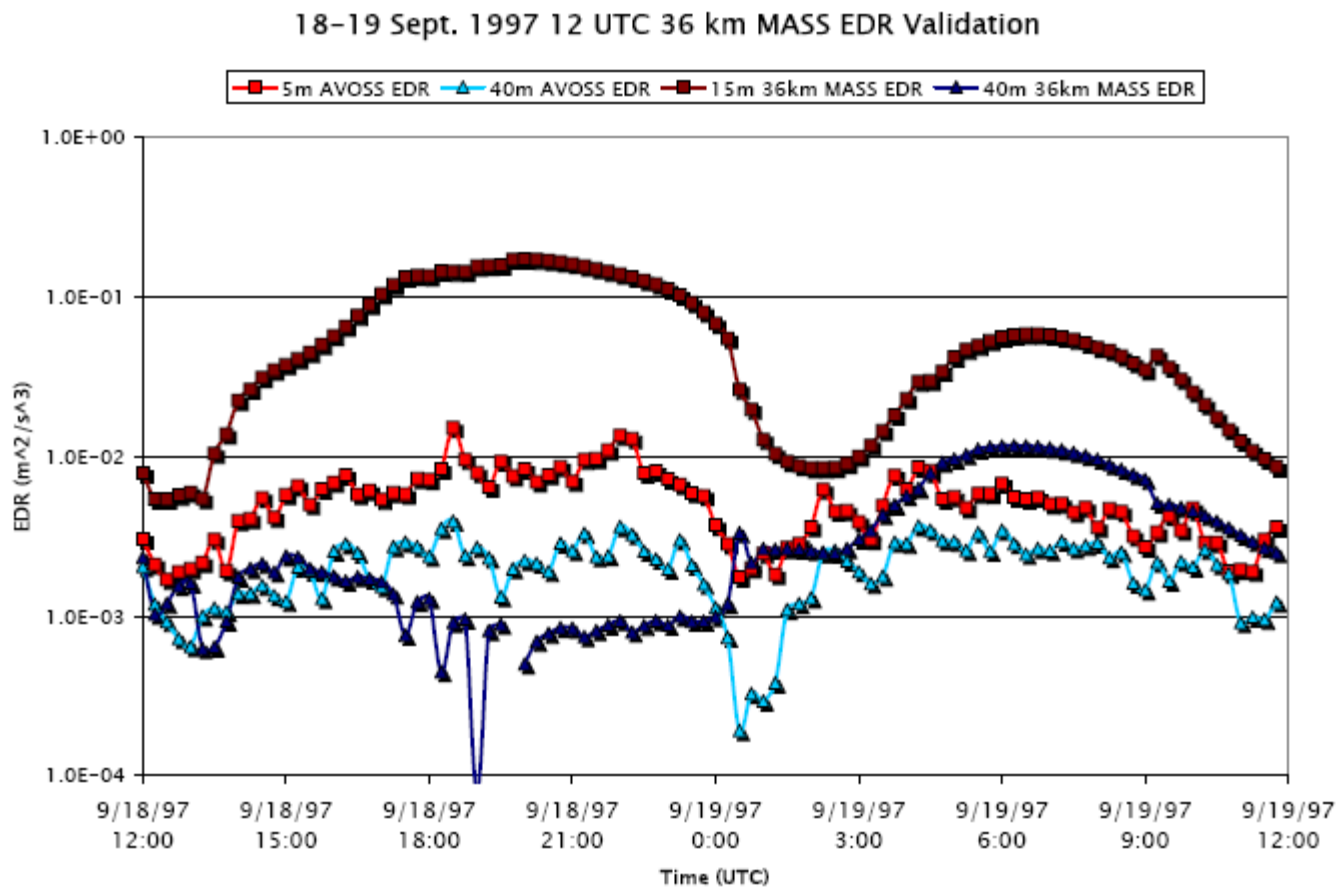


Figure 33: As with Fig. 32, but for 00-00 UTC 18-19 September 1997.

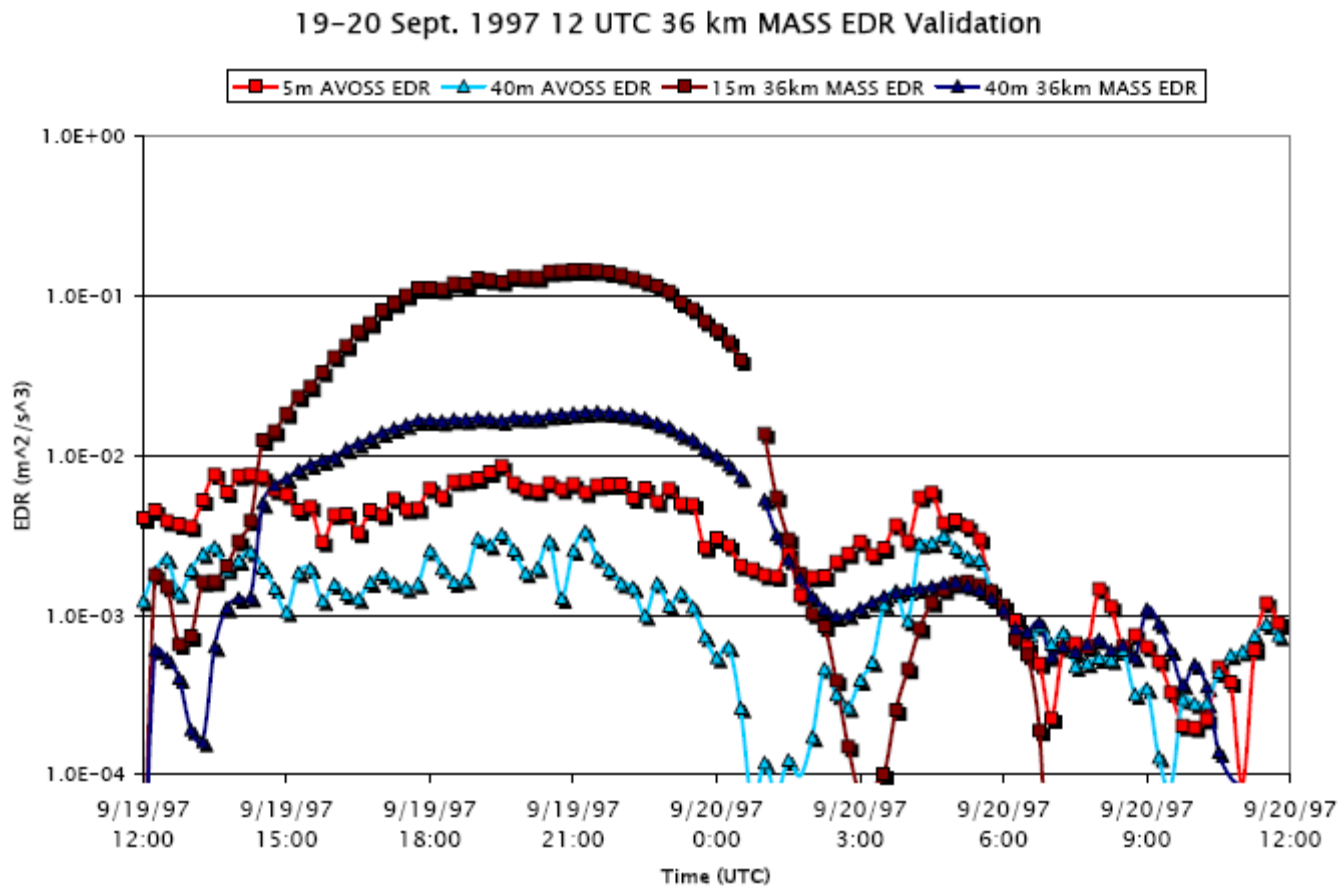


Figure 34: As with Fig. 33, but for 00-00 UTC 18-19 September 1997.

### 17-18 Sept. 1997 12 UTC 6 km MASS EDR Validation

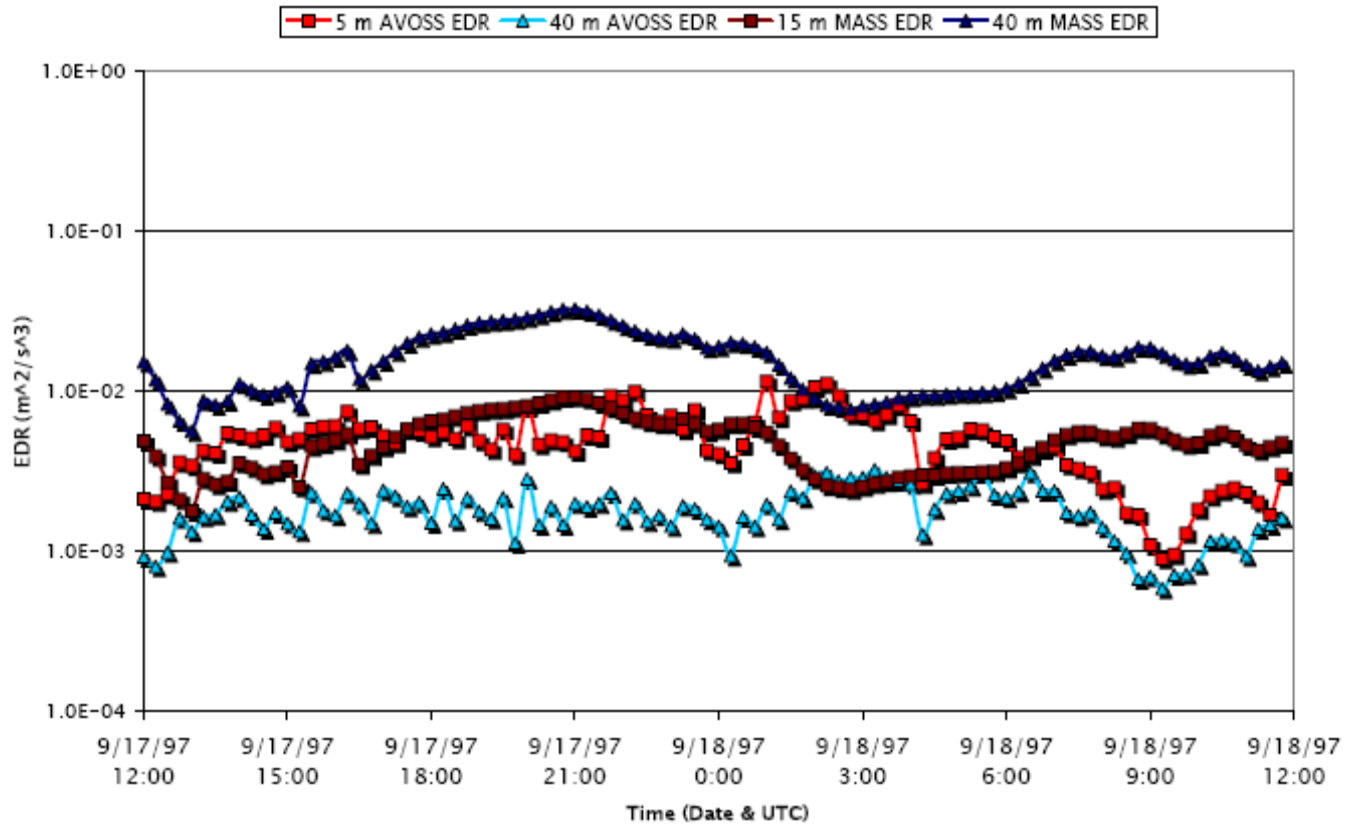


Figure 35: 17 NHMASS 6 km from 12-12 UTC 17-18 September 1997 (17\_06\_12) time series plot of 5/15 and 40 m eddy dissipation rate (EDR, log scale) vs. time from the model simulation and AVOSS tower data.

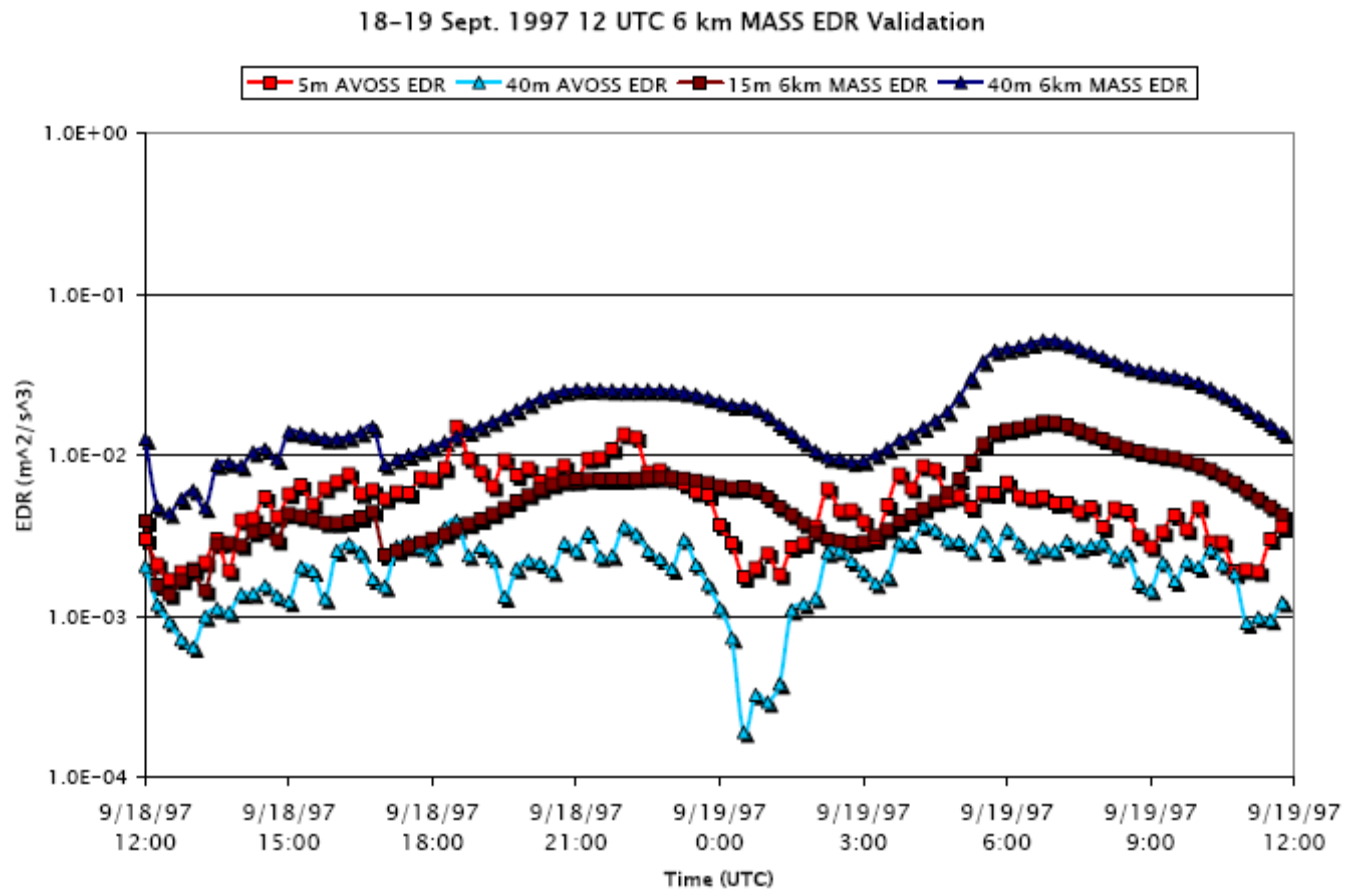


Figure 36: As with Fig. 35, but for 00-00 UTC 18-19 September 1997.

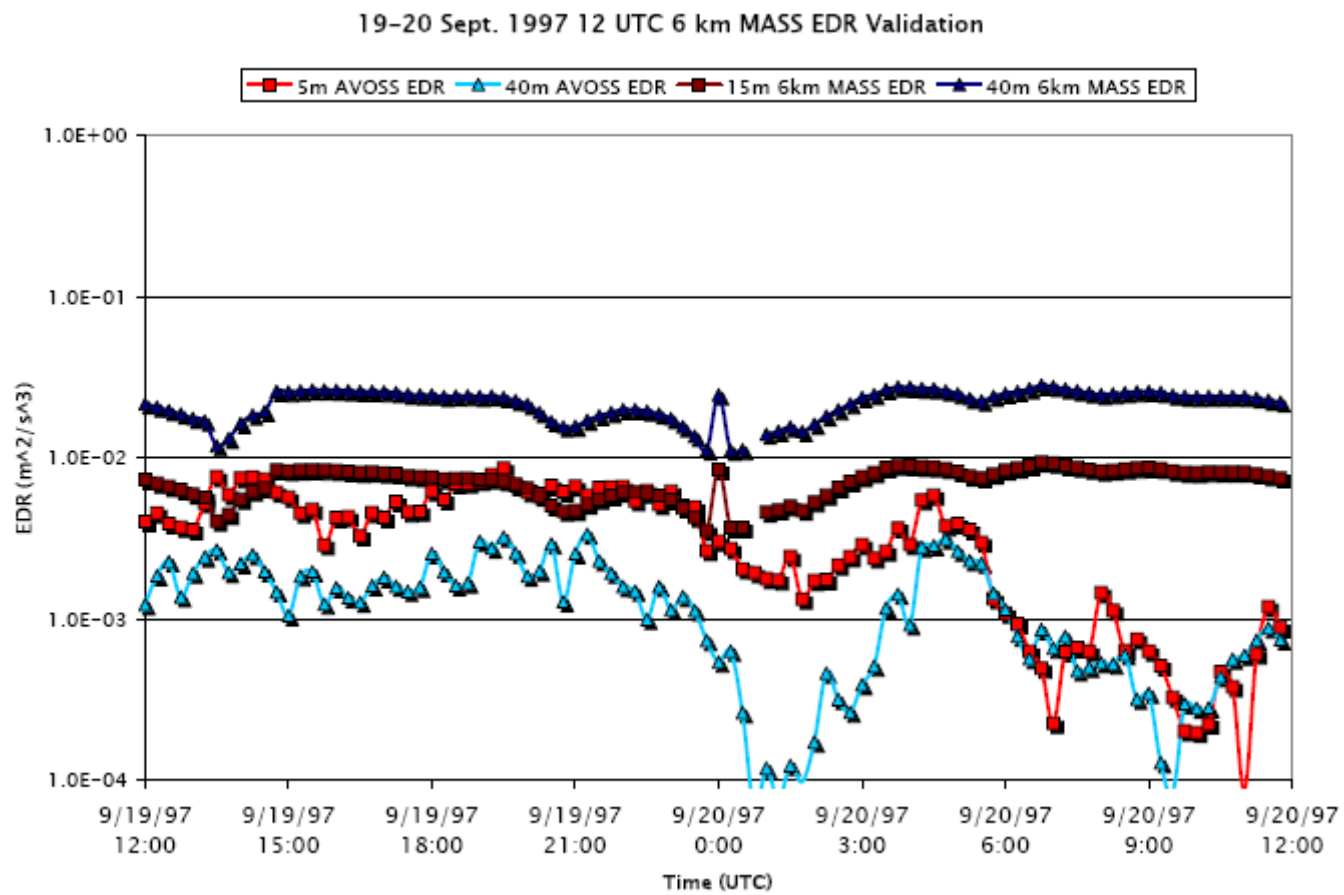


Figure 37: As with Fig. 36, but for 00-00 UTC 19-20 September 1997.

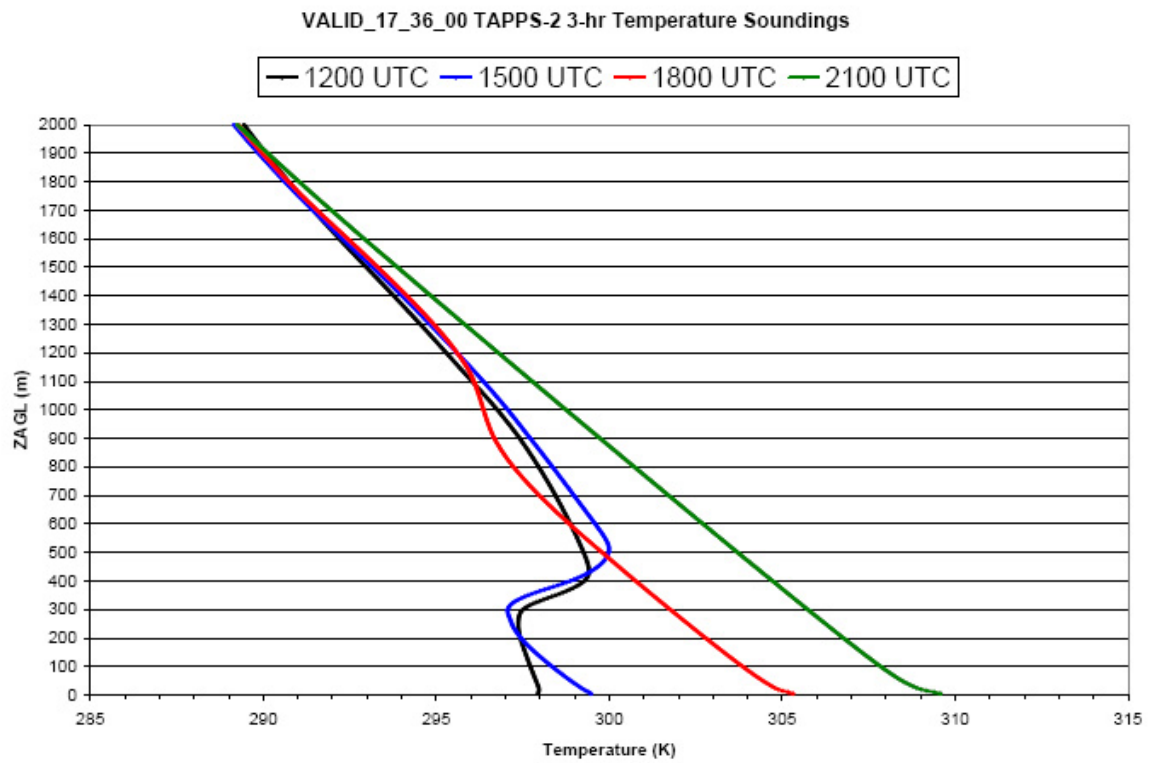
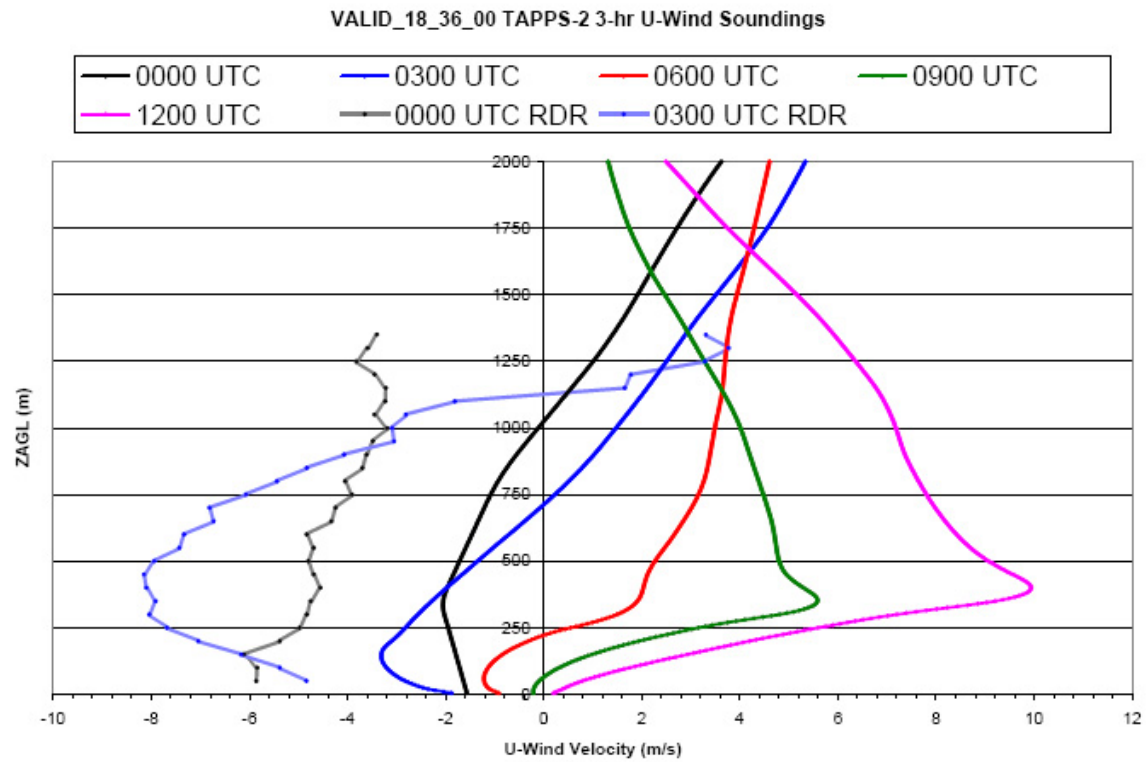
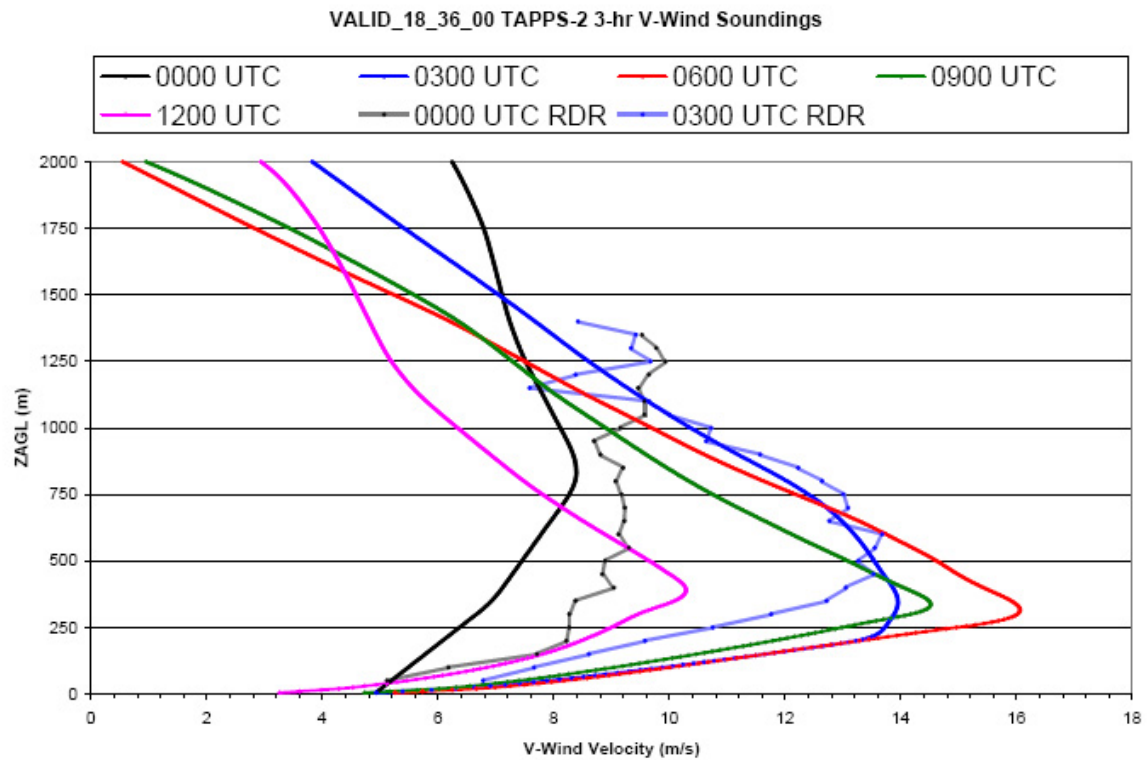


Figure 38: Temperature sounding evolution from 17\_36\_00 valid 12-21 UTC 17 September 1997 plotted at 3-hr intervals.



**Figure 39: Crosswind (u) wind sounding evolution from 18\_36\_00 valid 00-12 UTC 18 September 1997 plotted at 3-hr intervals. In addition, observations from the FWD radar are plotted at 00 and 03 UTC (color match).**



**Figure 40: Headwind (v) wind sounding evolution from 18\_36\_00 valid 00-12 UTC 18 September 1997 plotted at 3-hr intervals. In addition, observations from the FWD radar are plotted at 00 and 03 UTC (color match).**

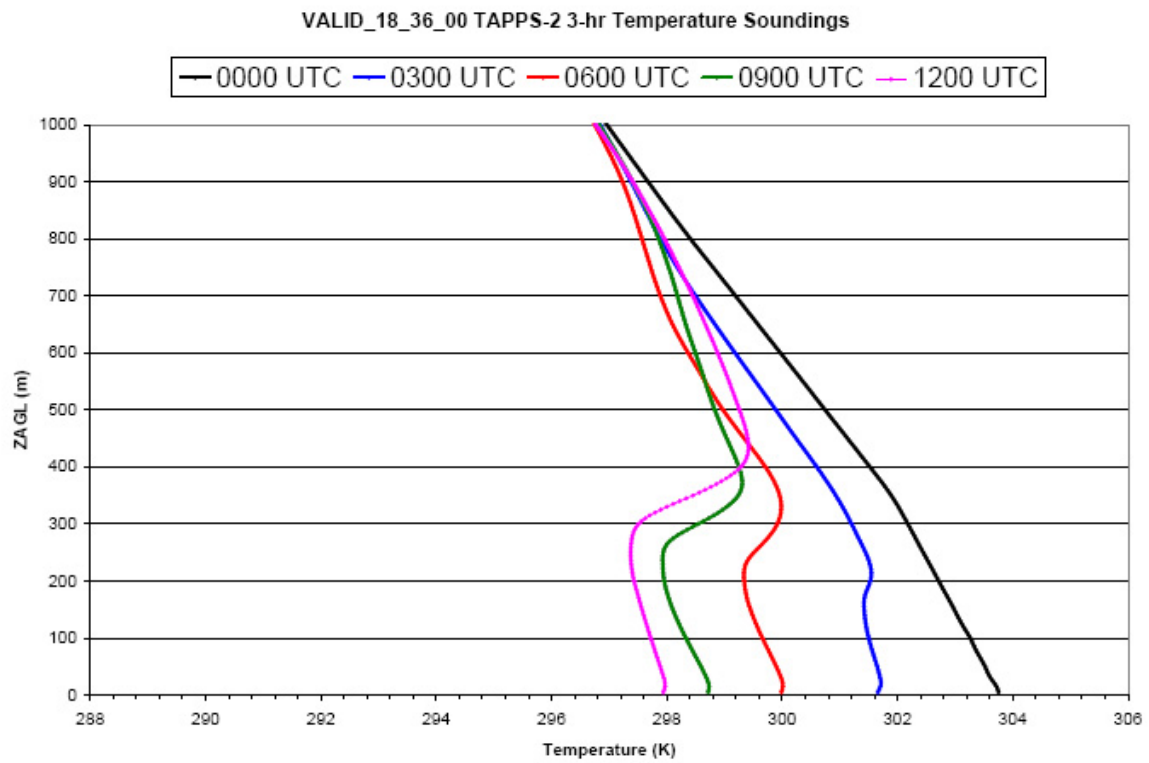


Figure 41: Temperature sounding evolution from 18\_36\_00 valid 00-12 UTC 18 September 1997 plotted at 3-hr intervals.

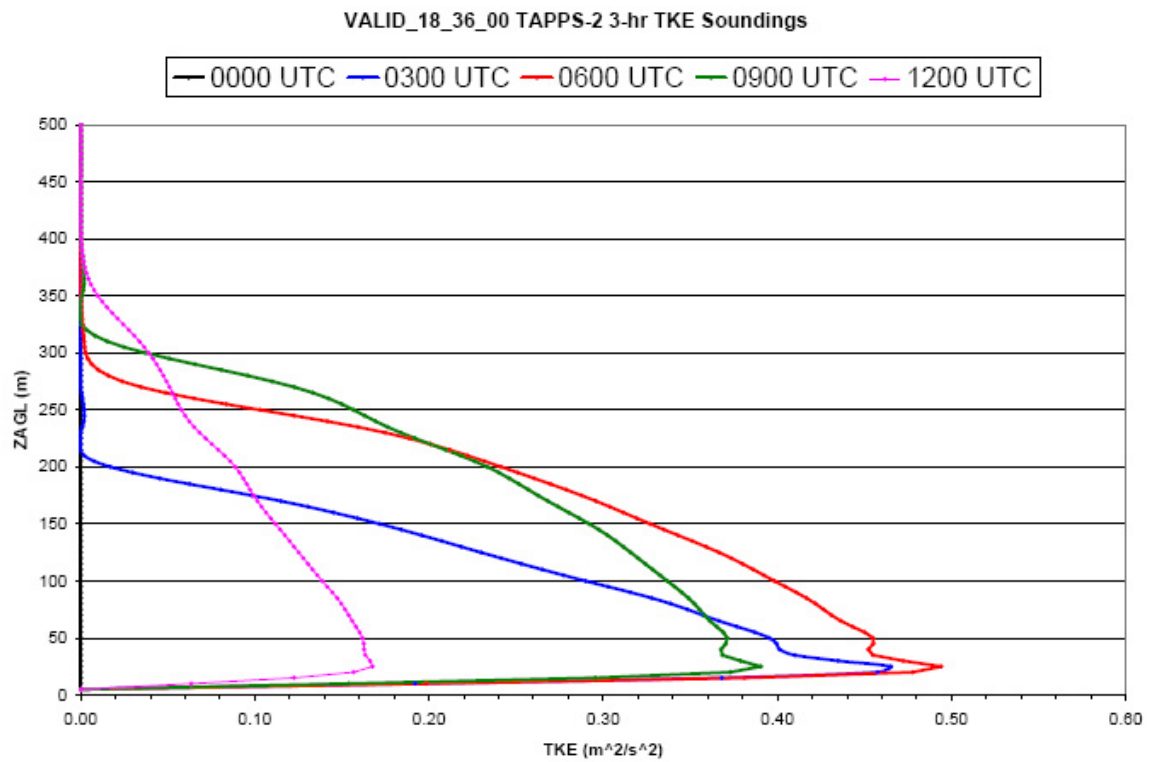


Figure 42: TKE sounding evolution from 18\_36\_00 valid 00-12 UTC 18 September 1997 plotted at 3-hr intervals from the surface to 500 m, near the height of the DLLJ.

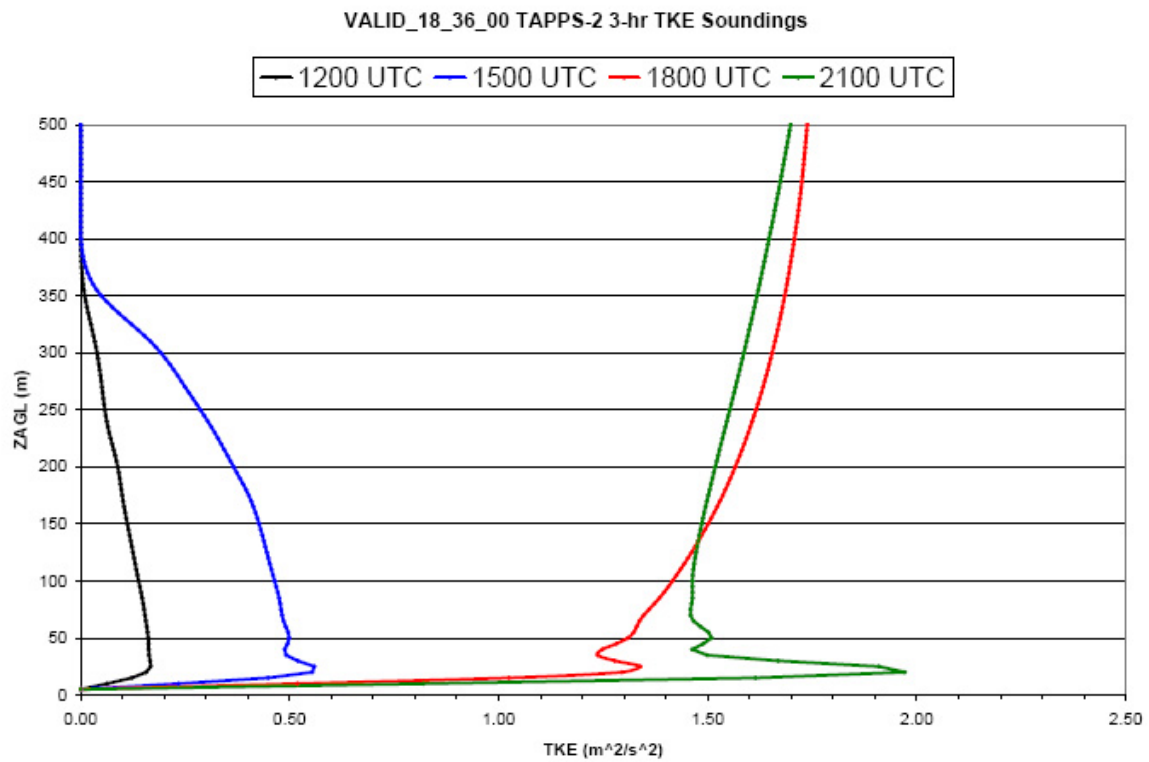


Figure 43: EDR sounding evolution from 18\_36\_00 valid 00-12 UTC 18 September 1997 plotted at 3-hr intervals from the surface to 500 m, near the height of the DLLJ.

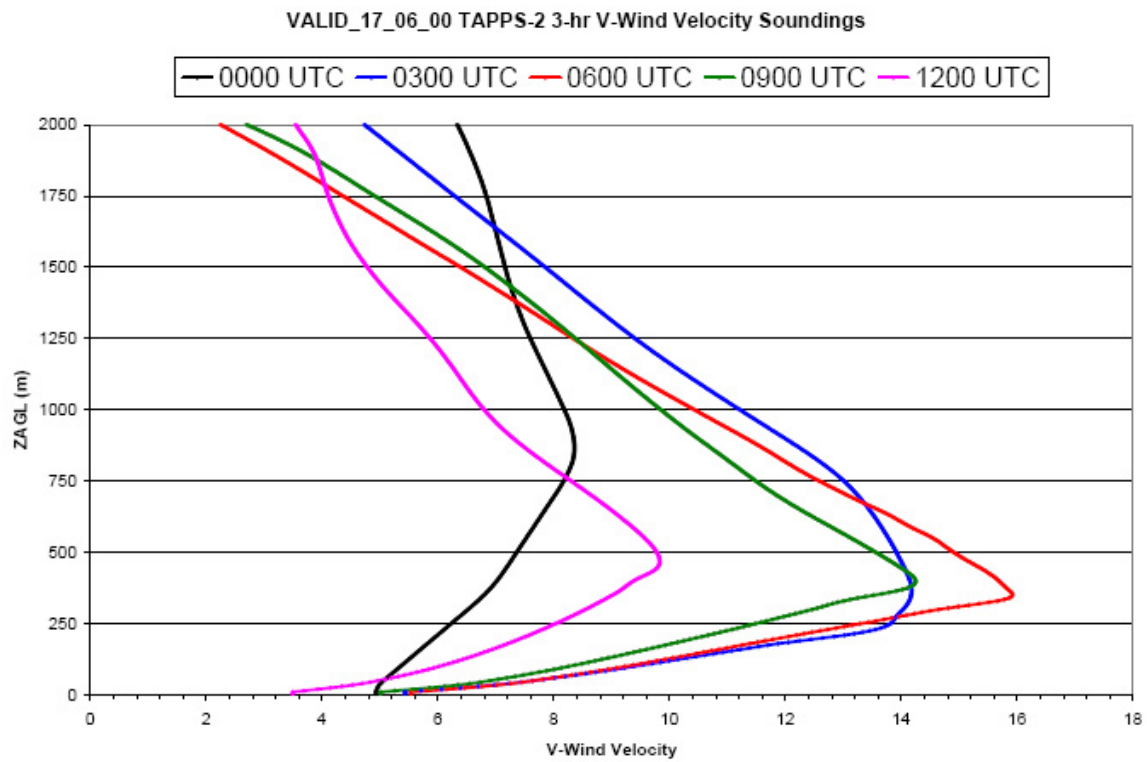


Figure 44: Headwind (v) wind sounding evolution from 17\_06\_00 valid 00-12 UTC 17 September 1997 plotted at 3-hr intervals.

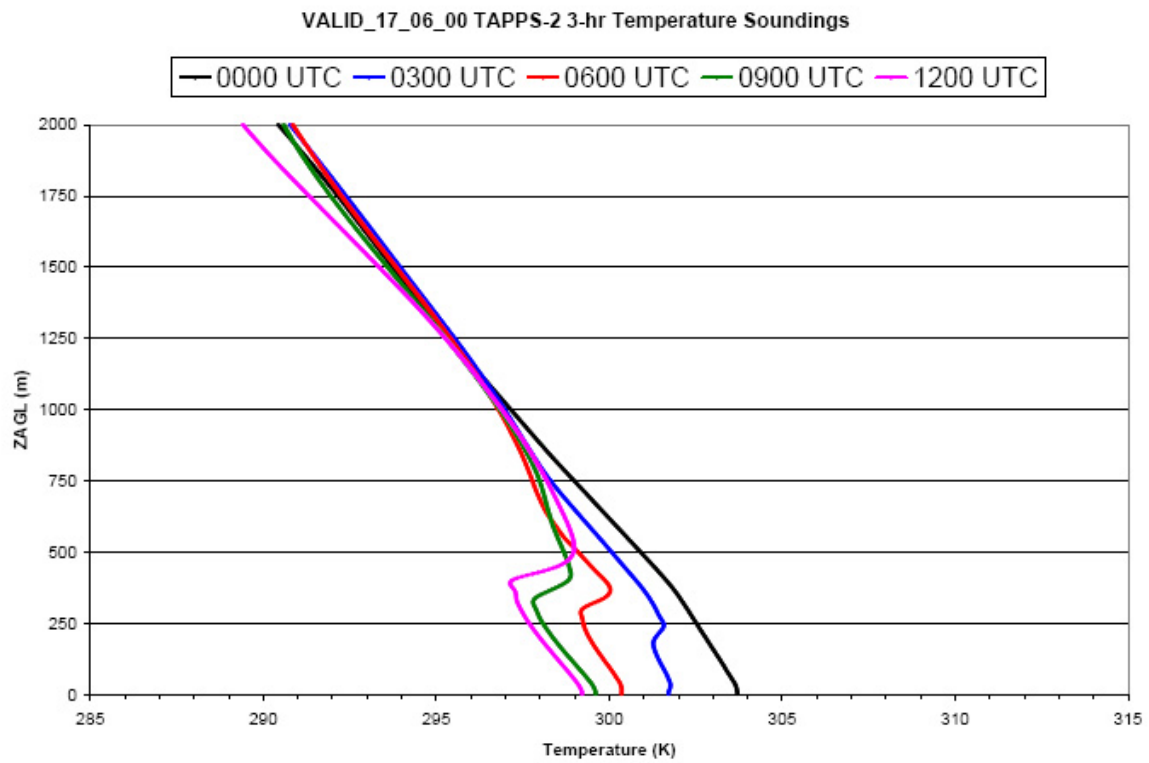


Figure 45: Temperature sounding evolution from 17\_06\_00 valid 00-12 UTC 17 September 1997 plotted at 3-hr intervals.

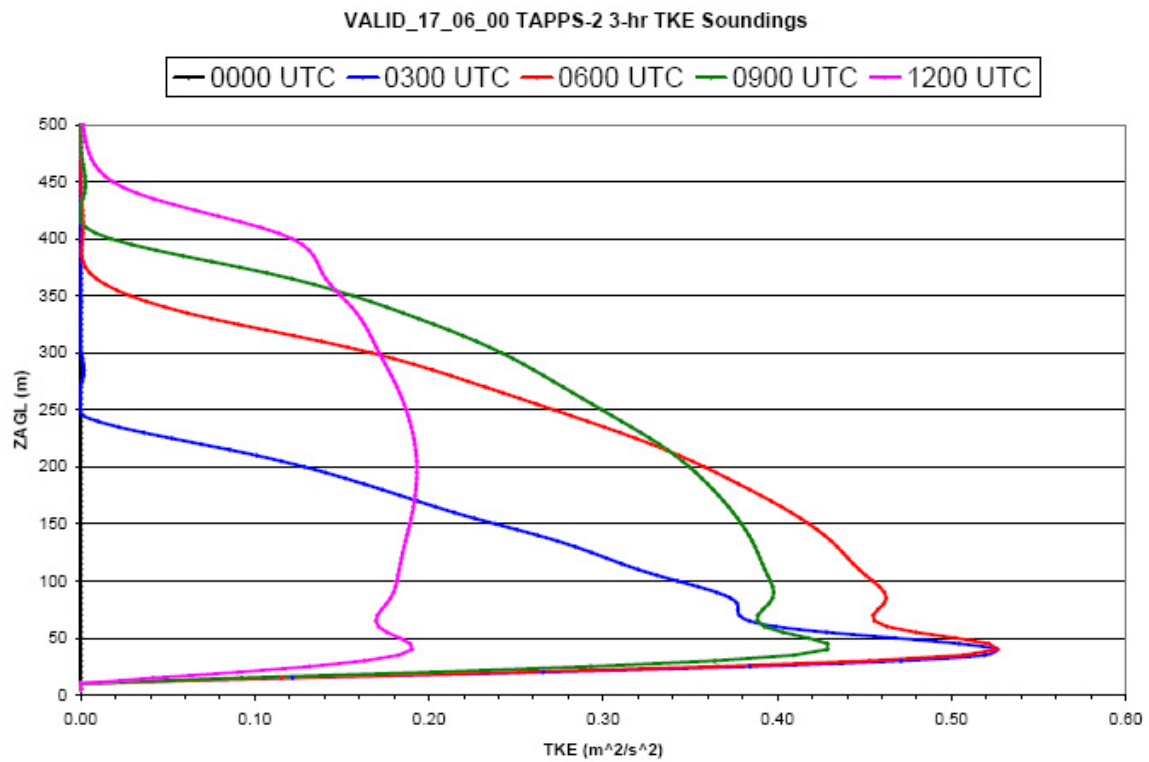


Figure 46: TKE sounding evolution from 17\_06\_00 valid 00-12 UTC 17 September 1997 plotted at 3-hr intervals.

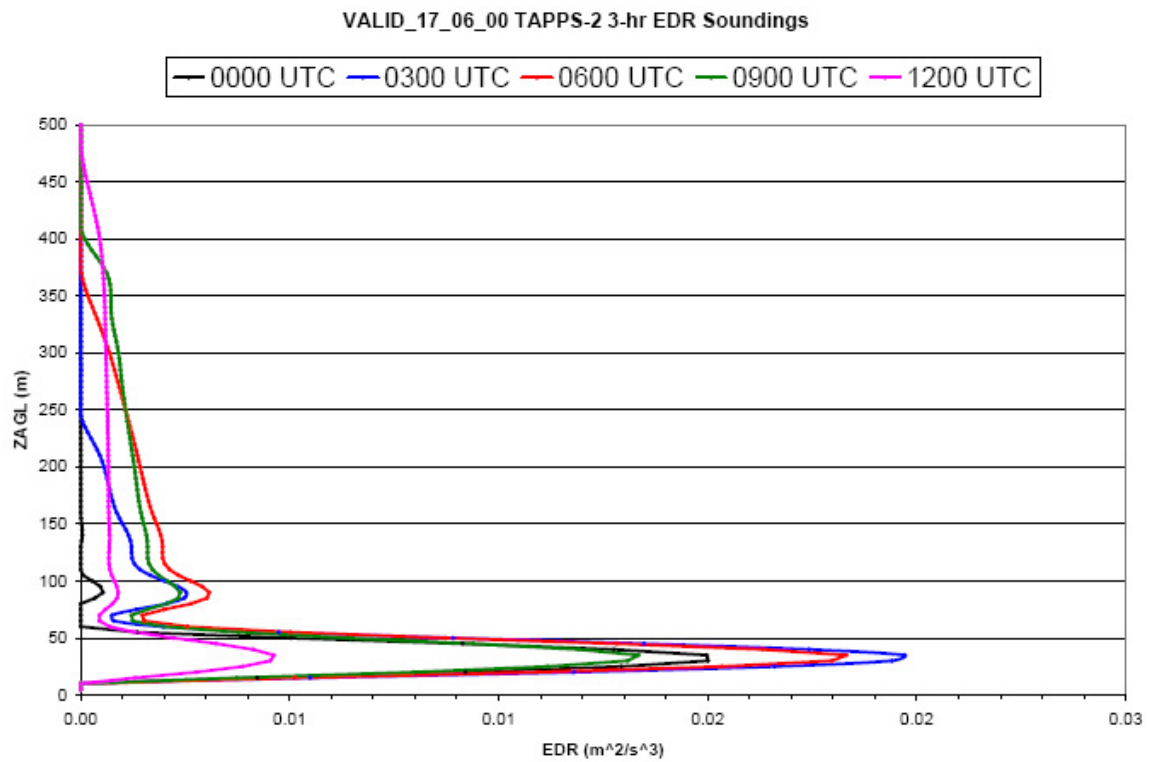


Figure 47: EDR sounding evolution from 17\_06\_00 valid 00-12 UTC 17 September 1997 plotted at 3-hr intervals.

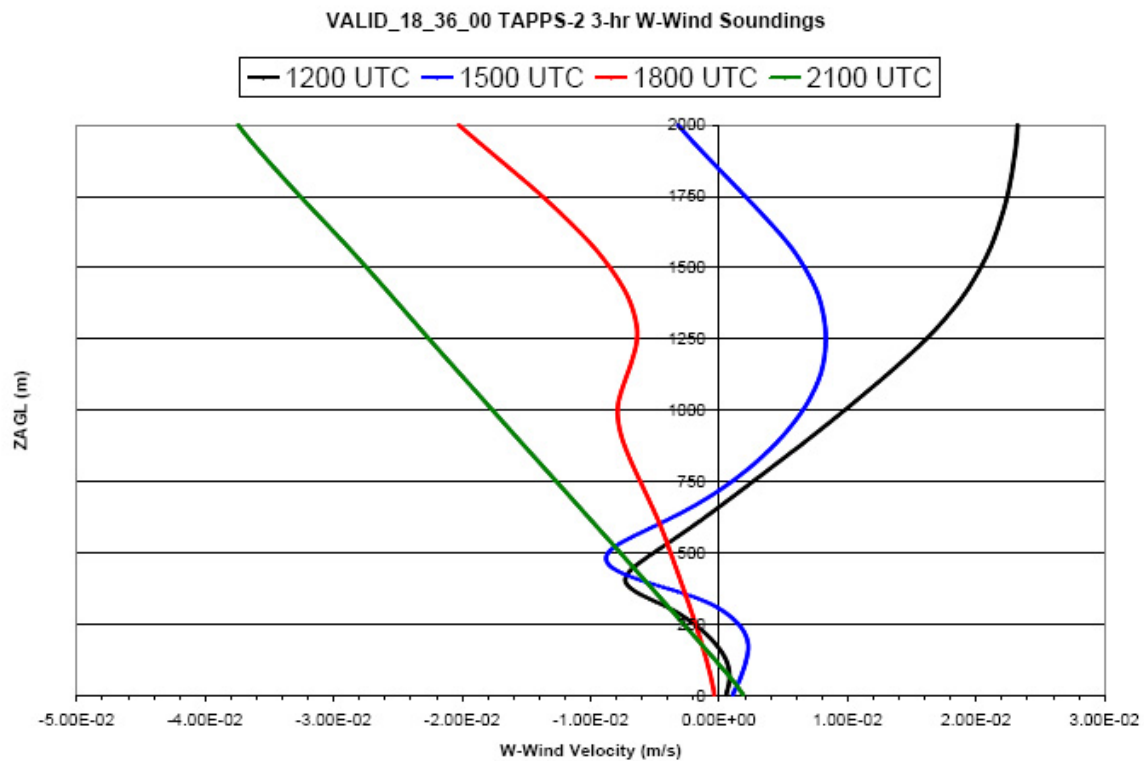


Figure 48: Vertical sounding evolution of vertical velocity (w) from 18\_36\_00 valid 12-00 UTC 18 September 1997 plotted at 3-hr intervals.

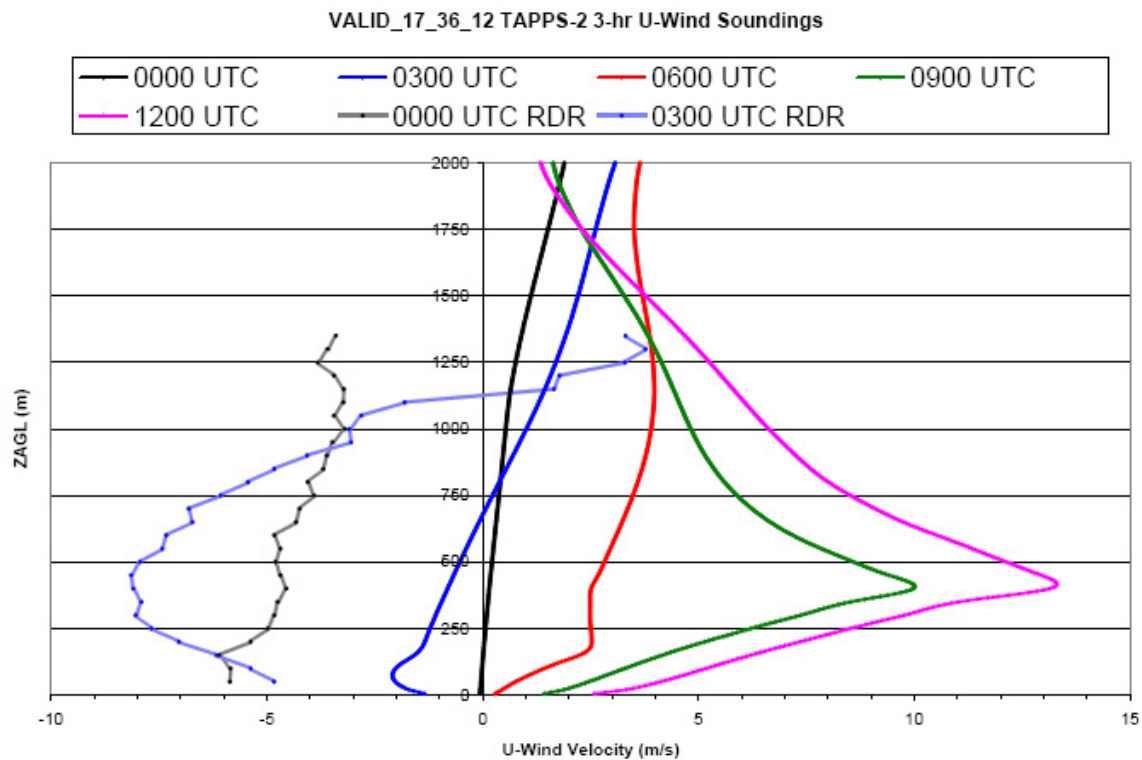


Figure 49: Crosswind (u) wind sounding evolution from 17\_36\_12 valid 00-12 UTC 18 September 1997 plotted at 3-hr intervals. In addition, observations from the FWD radar are plotted at 00 and 03 UTC (color match).

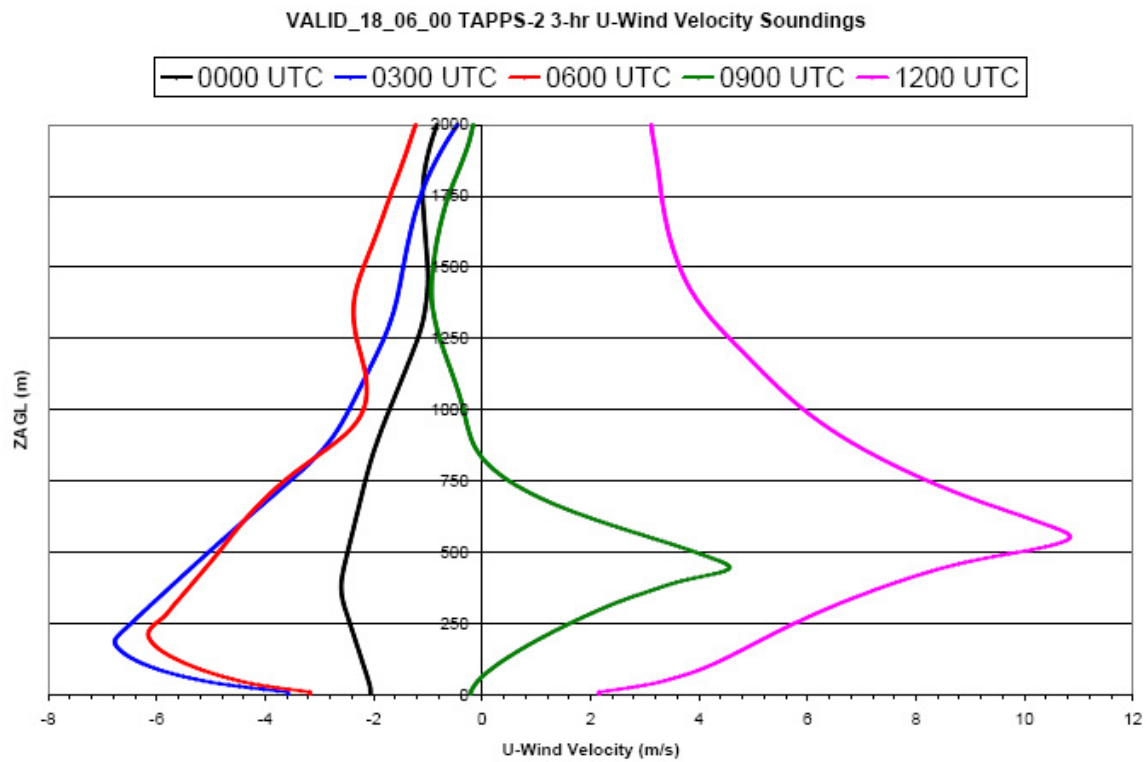


Figure 50: Crosswind (u) wind sounding evolution from 18\_06\_00 valid 00-12 UTC 18 September 1997 plotted at 3-hr intervals.

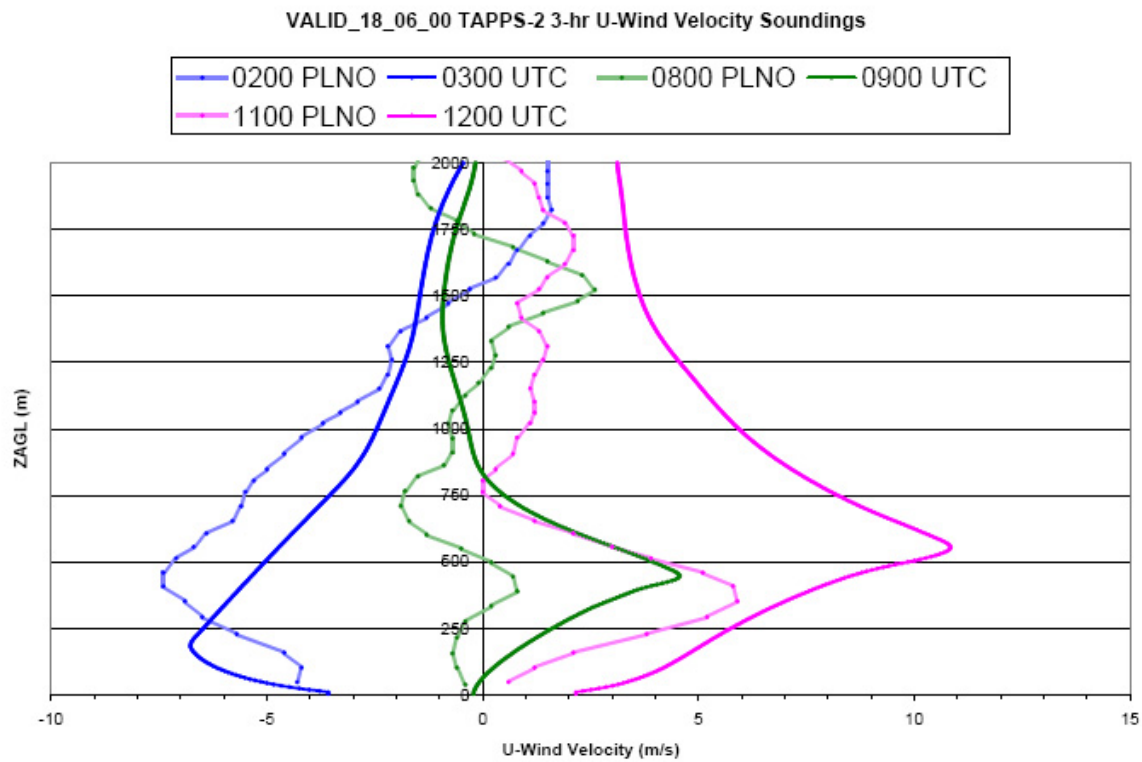


Figure 51: Crosswind (u) wind sounding evolution from 18\_06\_00 valid 00-12 UTC 18 September 1997 plotted at 3-hr intervals, with a color coordinated comparison to the PLNO soundings taken near the time plotted in the model simulations (lighter colors).

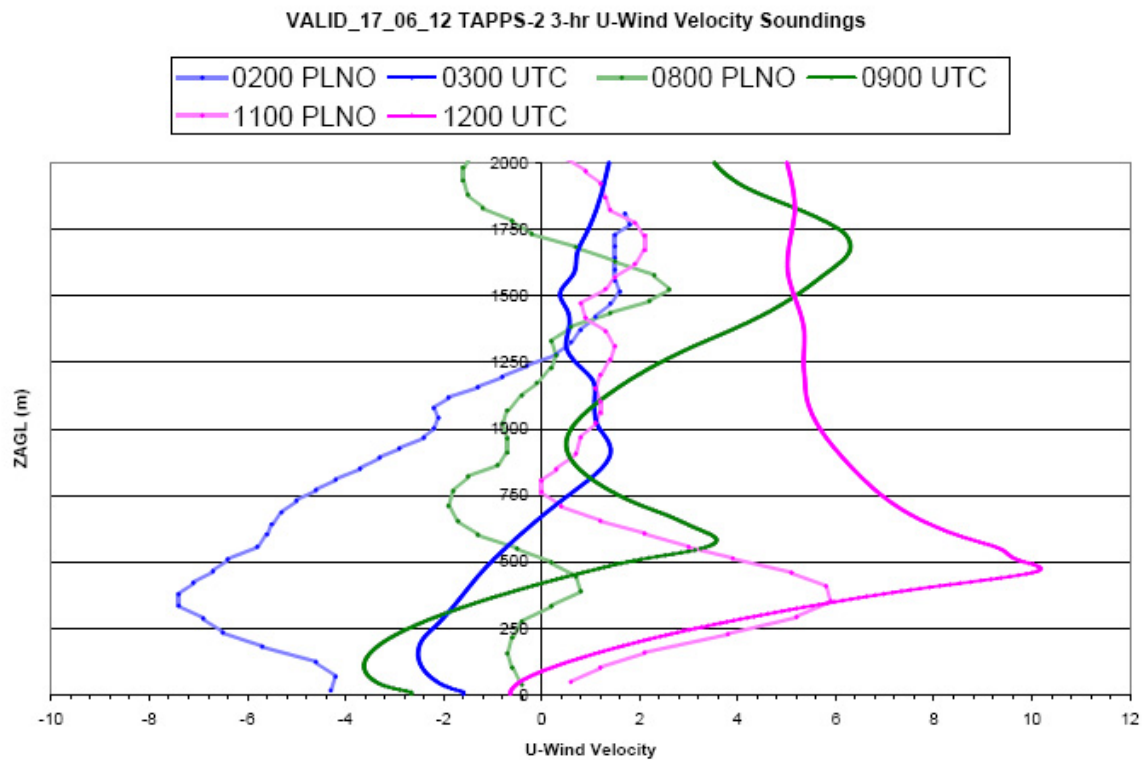


Figure 52: Crosswind (u) wind sounding evolution from 17\_06\_12 valid 00-12 UTC 18 September 1997 plotted at 3-hr intervals, with a color coordinated comparison to the PLNO soundings taken near the time plotted in the model simulations (lighter colors).

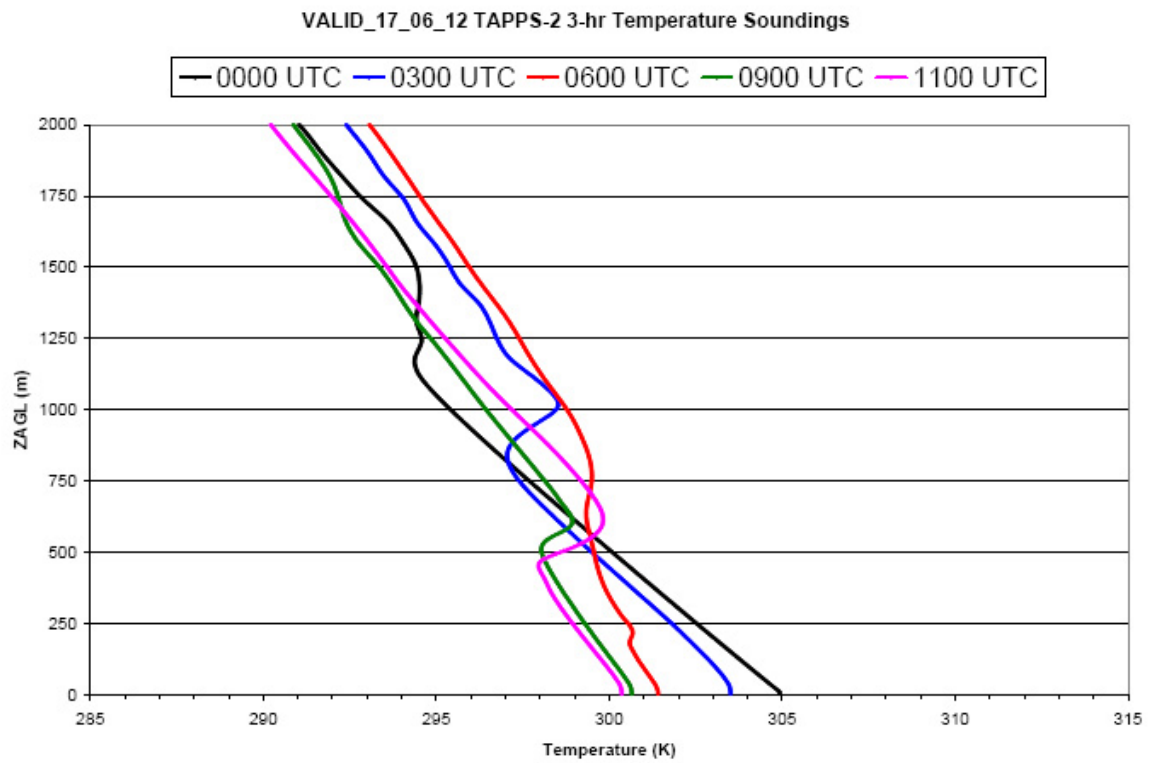


Figure 53: Temperature sounding evolution from 17\_06\_12 valid 00-12 UTC 18 September 1997 plotted at 3-hr intervals.

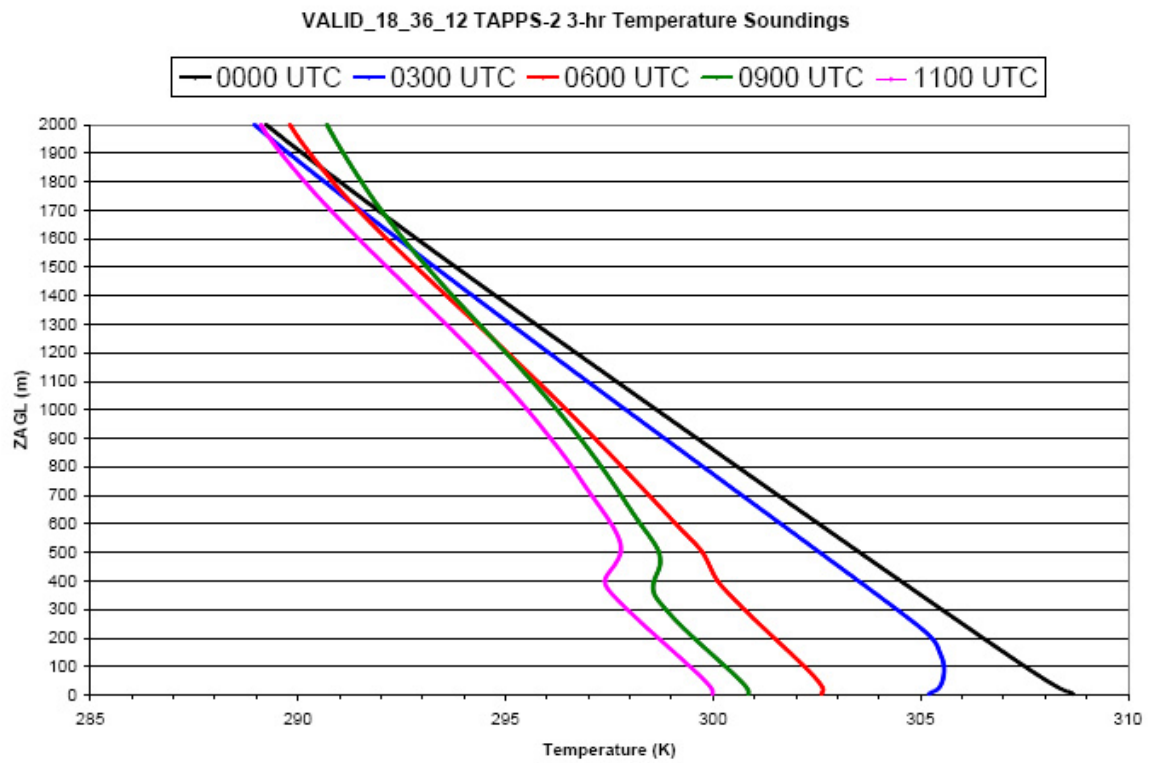


Figure 54: Temperature sounding evolution from 18\_36\_12 valid 00-12 UTC 19 September 1997 plotted at 3-hr intervals.

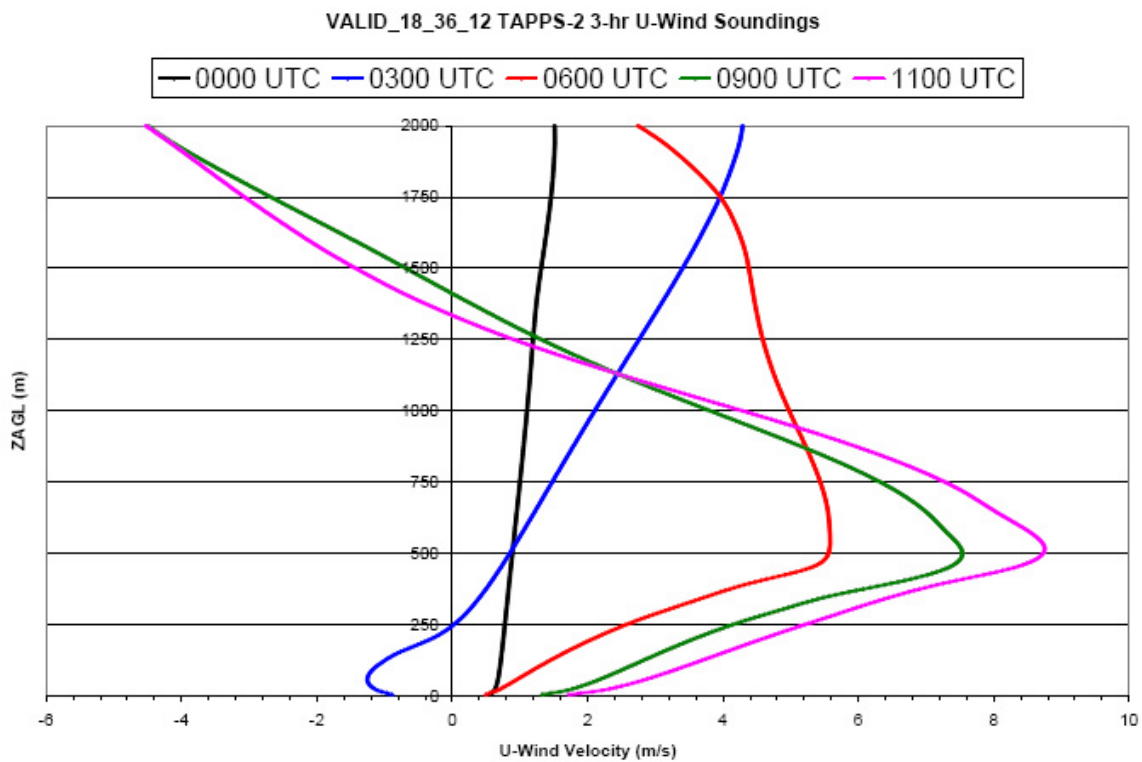
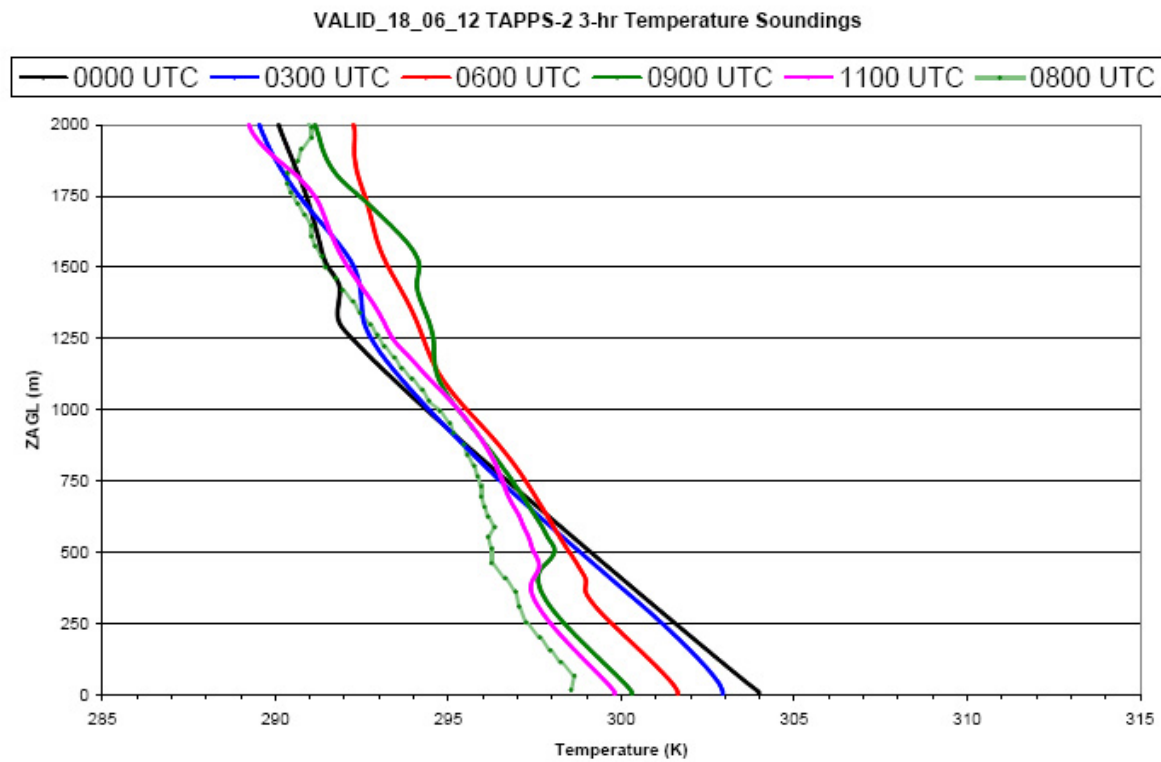


Figure 55: Crosswind (u) wind sounding evolution from 18\_36\_12 valid 00-12 UTC 19 September 1997 plotted at 3-hr intervals.



**Figure 56: Temperature sounding evolution from 18\_06\_12 valid 00-12 UTC 19 September 1997 plotted at 3-hr intervals. The temperature profile from 08 UTC at PLNO is also included.**

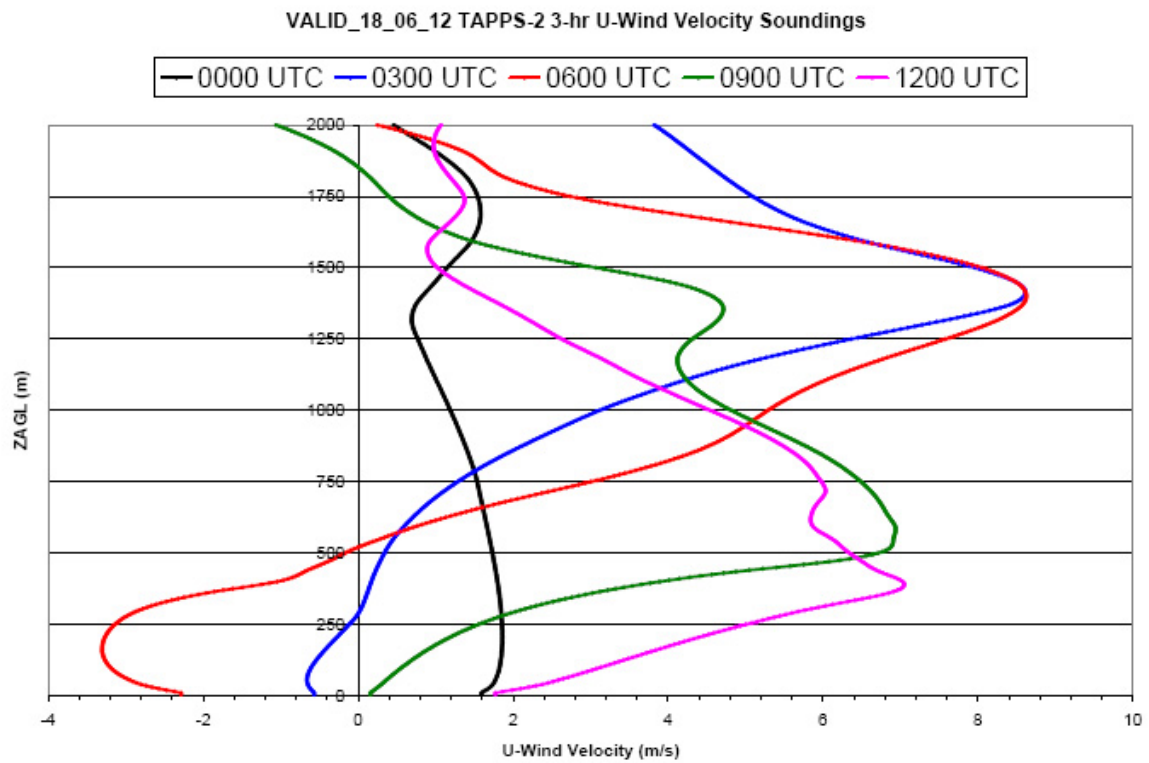


Figure 57: Crosswind (u) wind sounding evolution from 18\_36\_12 valid 00-12 UTC 19 September 1997 plotted at 3-hr intervals.

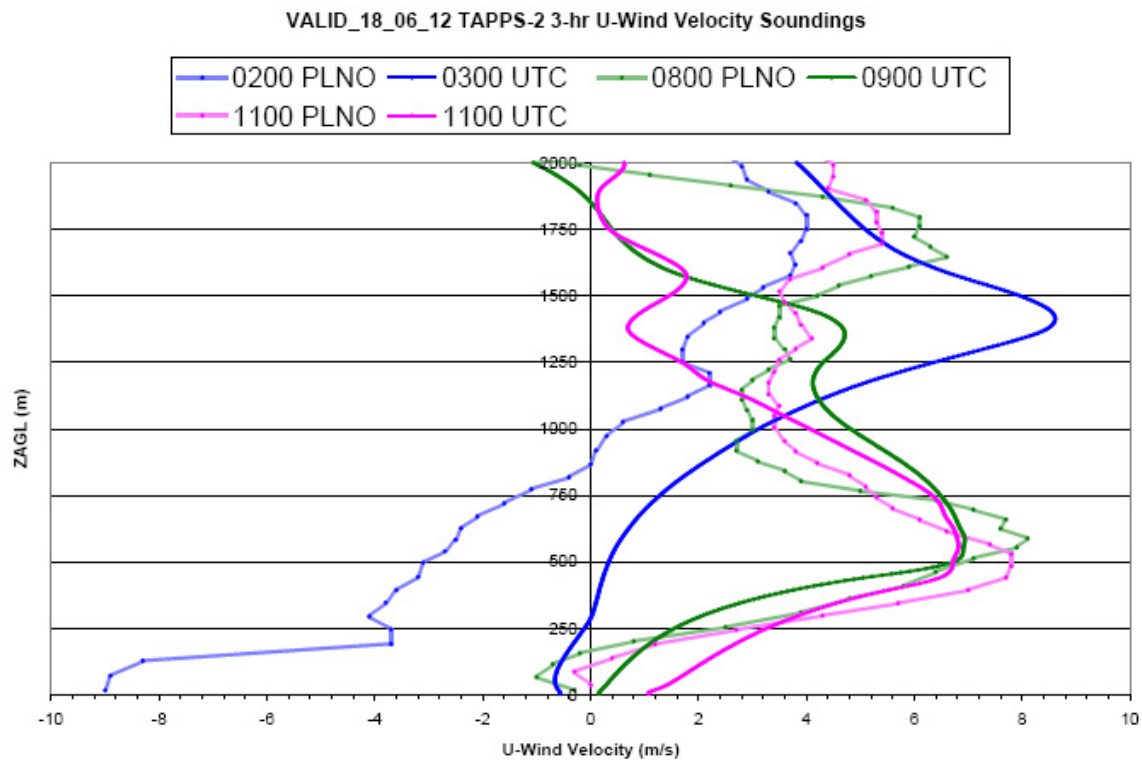


Figure 58: Crosswind (u) wind sounding evolution from 18\_06\_12 valid 00-12 UTC 18 September 1997 plotted at 3-hr intervals, with a color coordinated comparison to the PLNO soundings taken near the time plotted in the model simulations (lighter colors).

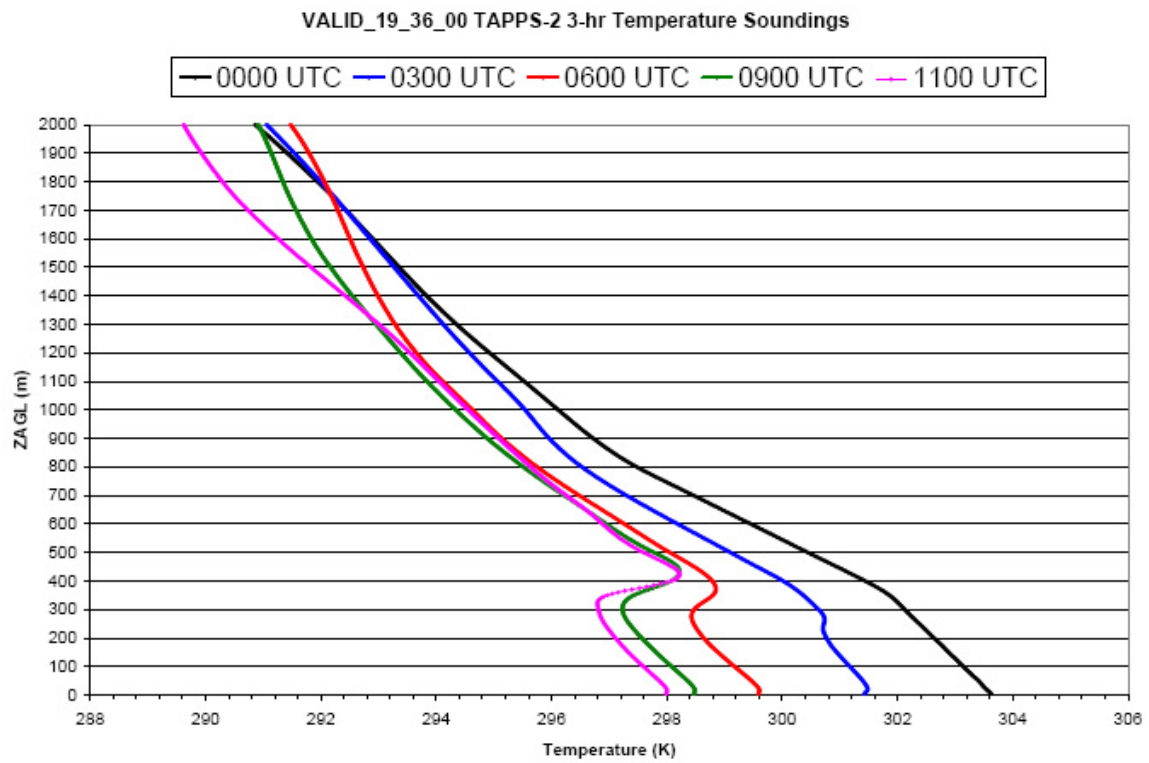


Figure 59: Temperature sounding evolution from 19\_36\_00 valid 00-12 UTC 19 September 1997 plotted at 3-hr intervals.

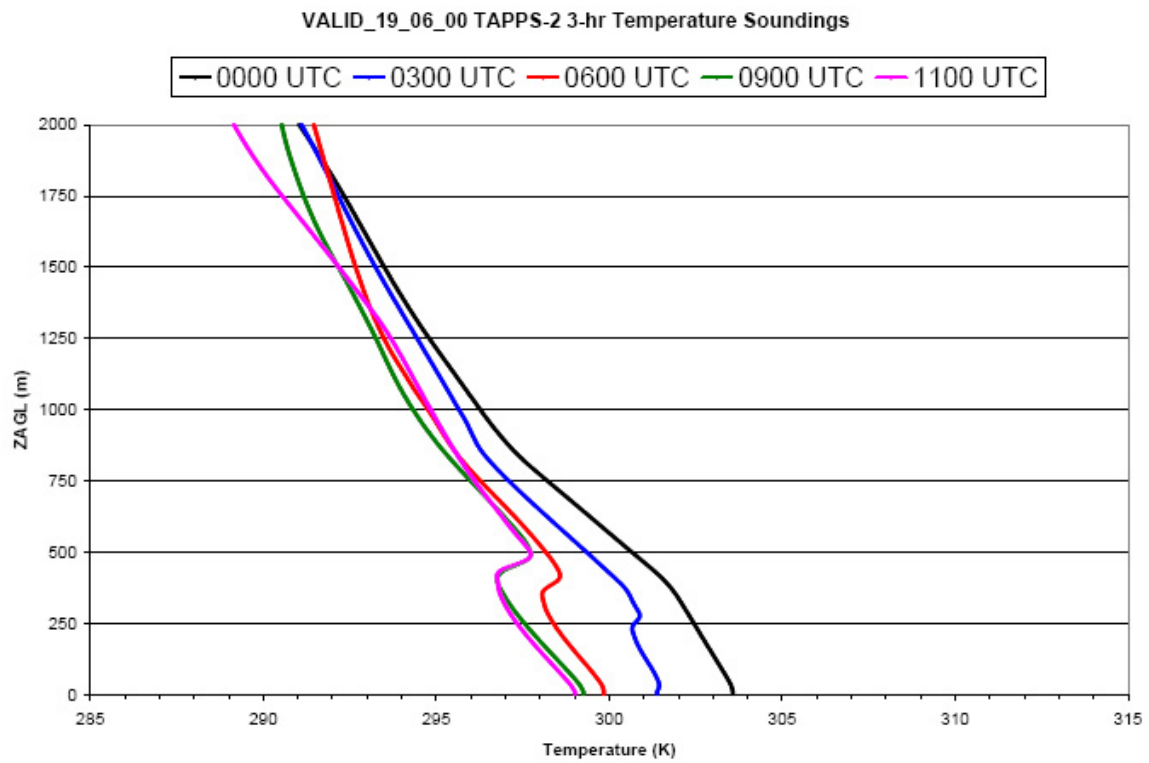


Figure 60: As with Fig. 59, but for 19\_06\_00.

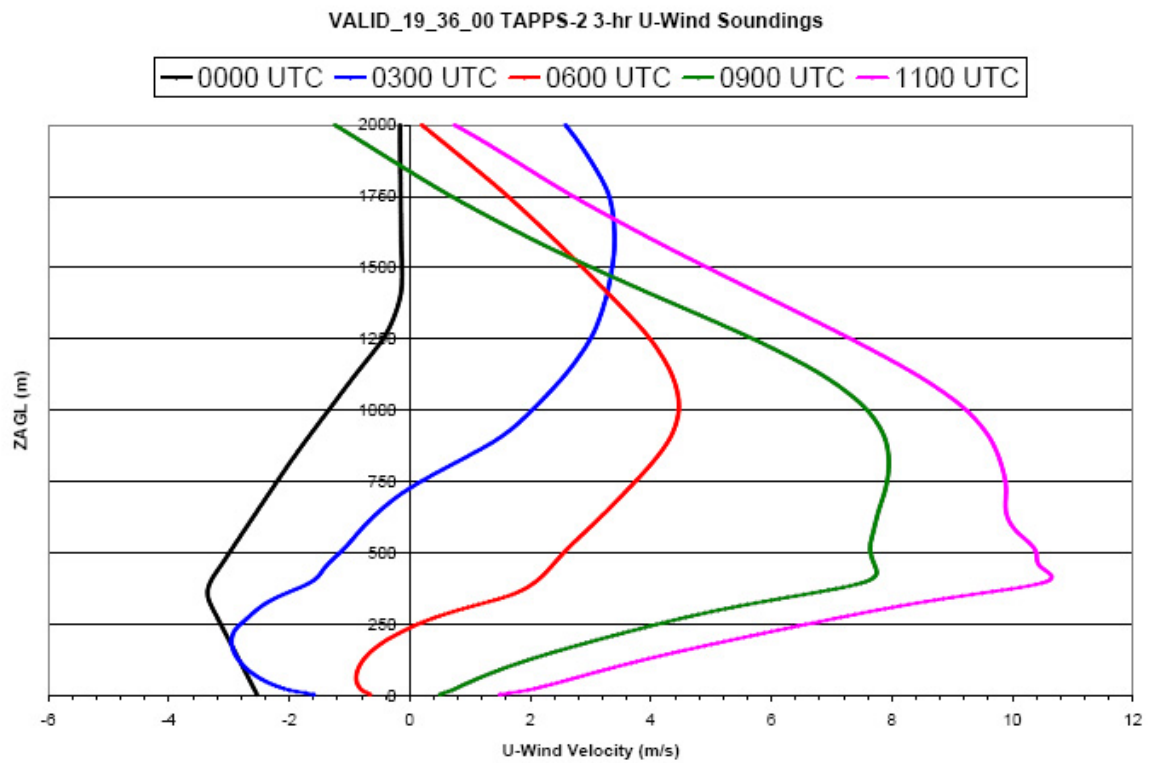


Figure 61: Crosswind (u) wind sounding evolution from 19\_36\_00 valid 00-12 UTC 19 September 1997 plotted at 3-hr intervals.

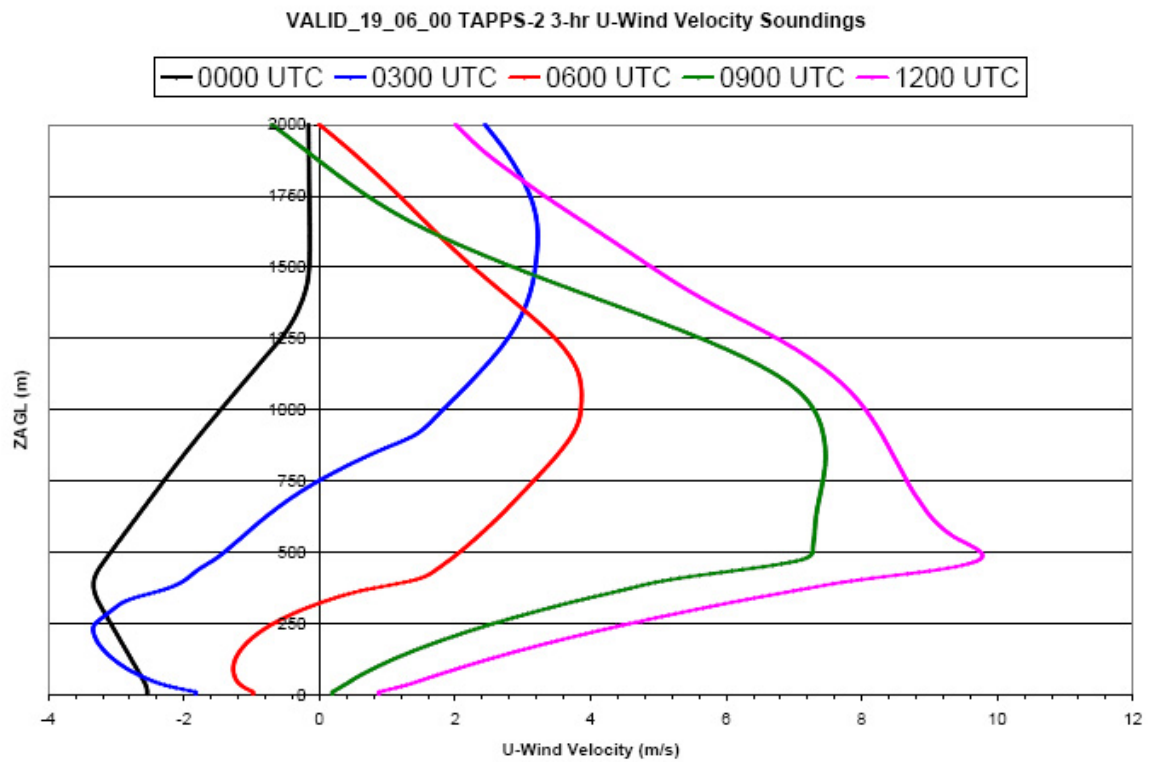
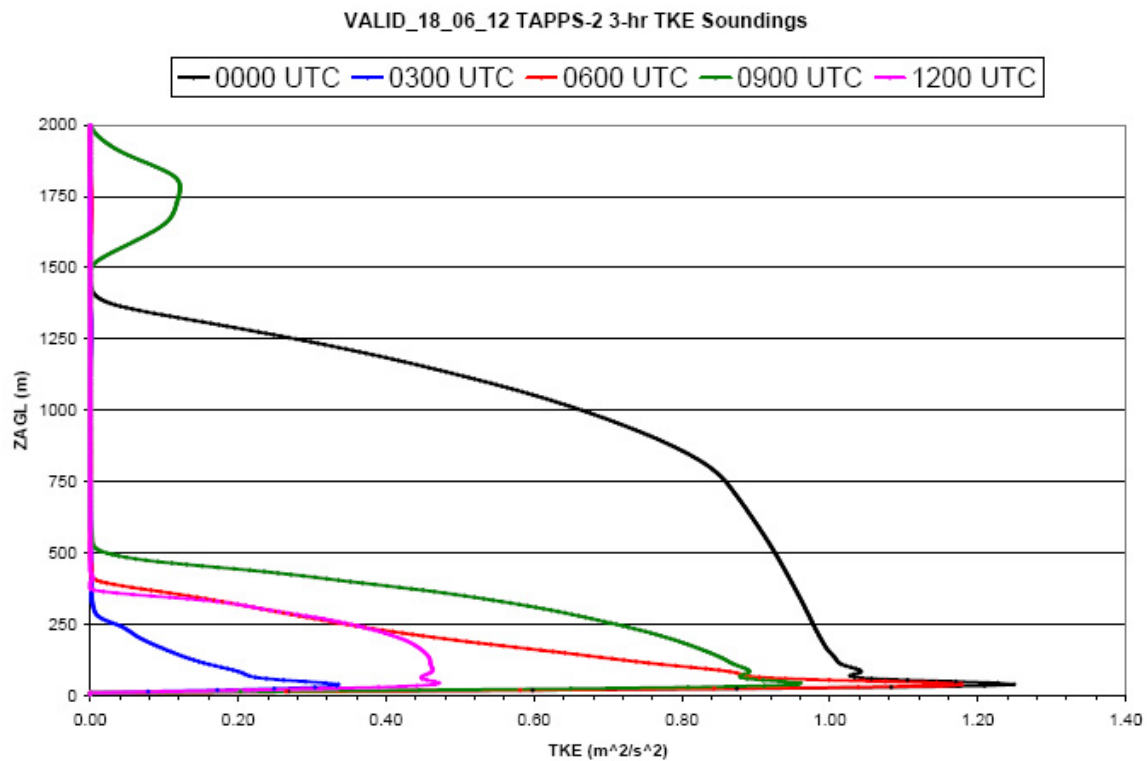
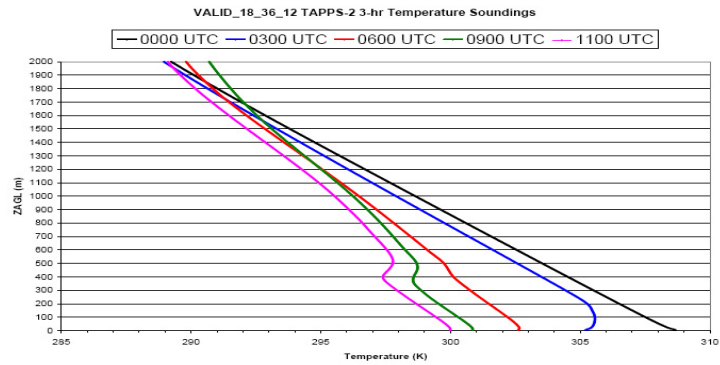


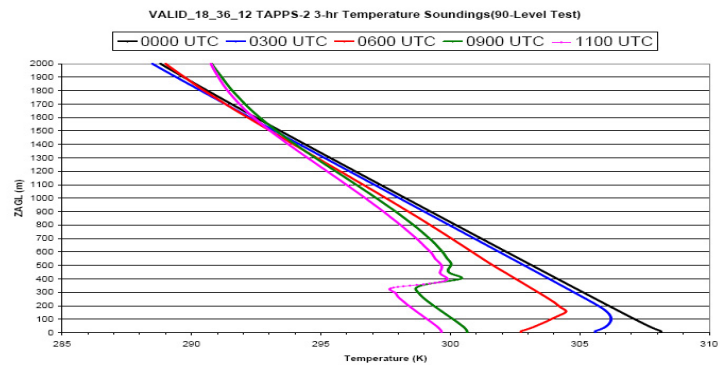
Figure 62: As with Fig. 61, but for 19\_06\_00.



**Figure 63: TKE sounding evolution from 18\_06\_12 valid 00-12 UTC 17 September 1997 plotted at 3-hr intervals. Note the secondary increase of TKE above 1.5 km at 09 UTC in association with a secondary cross-wind maximum at 1.5 km.**

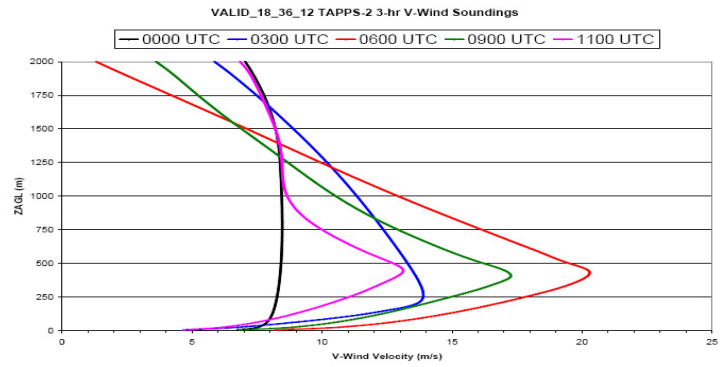


(a)

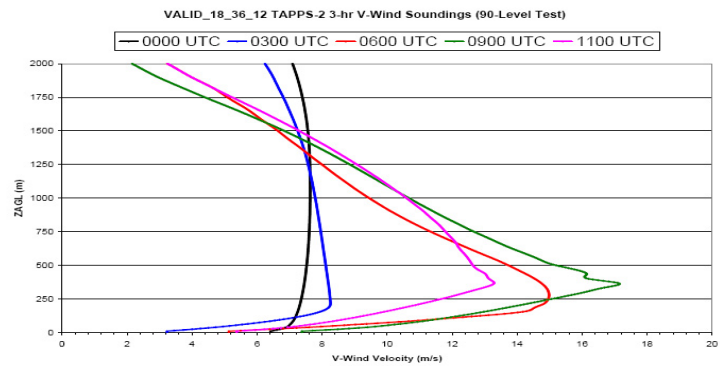


(b)

Figure 64: 18\_36\_12\_CTRL (a) and 18\_36\_12\_TST (b) 3-hr nocturnal inversion evolution from 00-12 UTC 19 September 1997. Note that while both profiles have similar curves between 00-03 UTC, the 90-level 18\_36\_12\_TST simulation develops a stronger inversion faster than the CTRL.

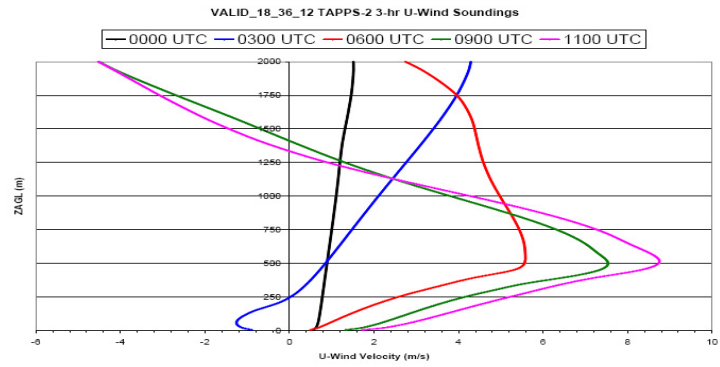


(a)

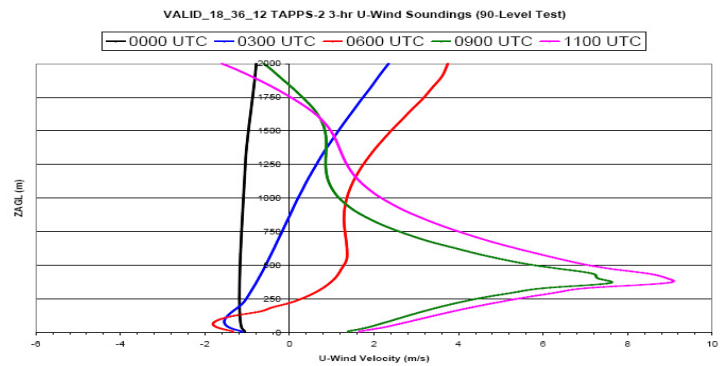


(b)

Figure 65: 18\_36\_12\_CTRL (a) and 18\_36\_12\_TST (b) 3-hr headwind velocity soundings from 00-12 UTC 19 September 1997.

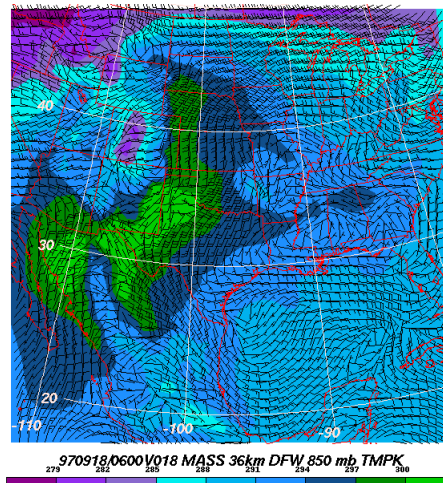


(a)

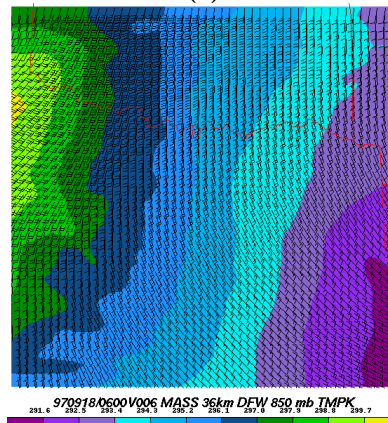


(b)

Figure 66: 18\_36\_12\_CTRL (a) and 18\_36\_12\_TST (b) 3-hr crosswind velocity soundings from 00-12 UTC 19 September 1997.

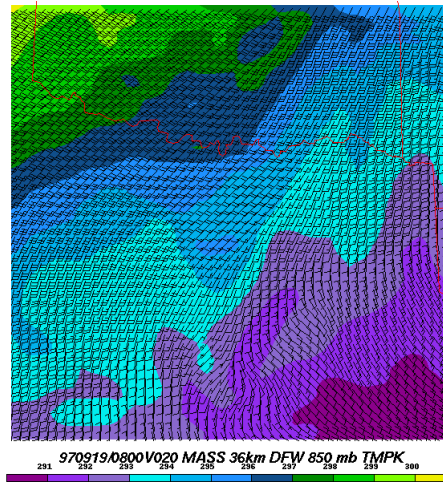


(a)



(b)

Figure 67: 850 hPa temperature (color fill) and winds from 17\_36\_12 and 18\_06\_00 valid 06 UTC 18 September 1997 across the Southern Plains. Note that the temperature gradient northwest of DFW is oriented east to west, particularly in 18\_06\_00.

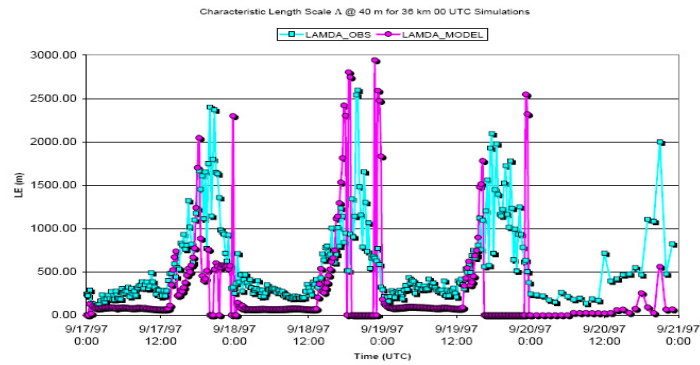


(a)

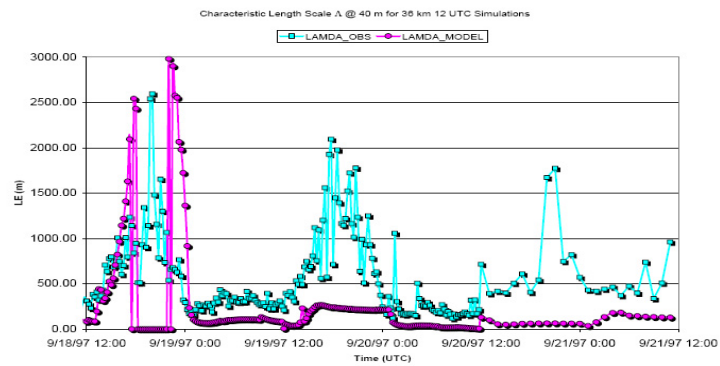


(b)

Figure 68: As with Fig. 67, but for (a) 08 UTC 19 September from 18\_06\_12 and (b) 08 UTC 20 September 1997 from 19\_06\_12. Note the shift in temperature gradient at 850 h-Pa to a more north to south orientation, coincident with the veering LLJ.

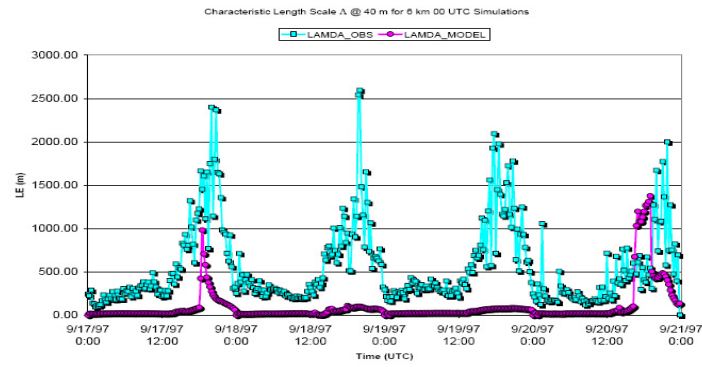


(a)

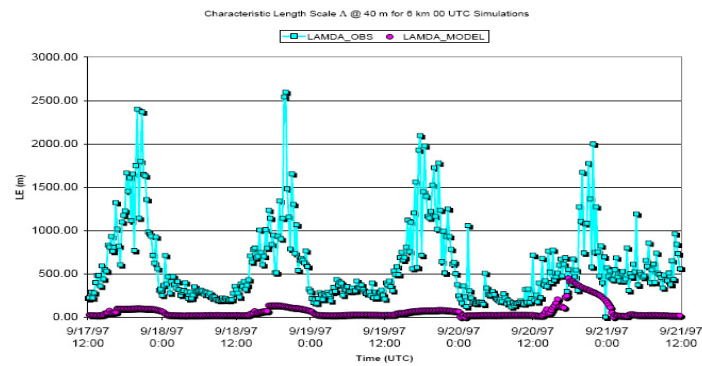


(b)

Figure 69: Derived characteristic mixing length  $\Lambda$  at 40 meters from AVOSS tower observations (light blue curve) and (a) 36 km 00 UTC simulations and (b) 36 km 12 UTC simulations, valid 17-21 September 1997.

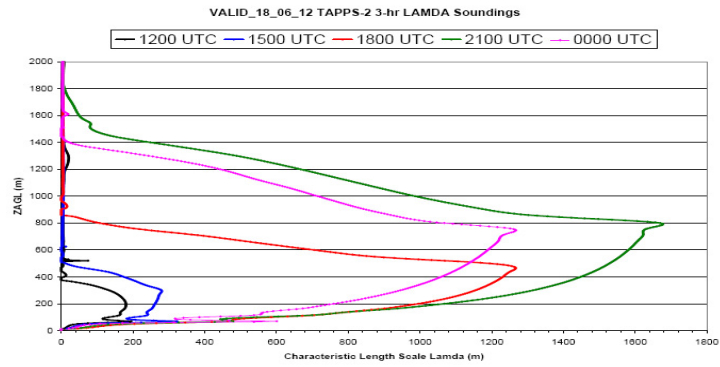


(a)

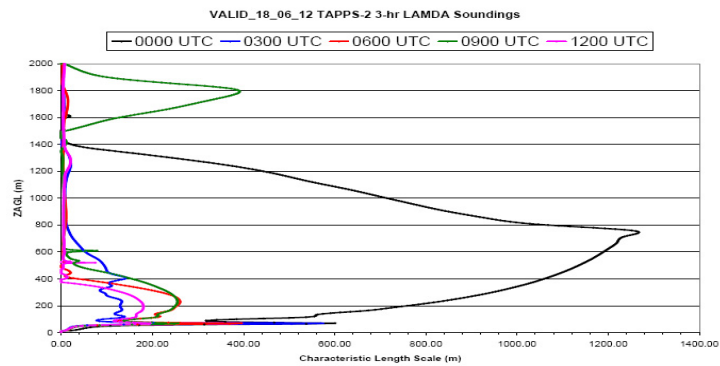


(b)

Figure 70: Derived characteristic mixing length  $\Lambda$  at 40 meters from AVOSS tower observations (light blue curve) and (a) 6 km 00 UTC simulations and (b) 6 km 12 UTC simulations, valid 17-21 September 1997.



(a)



(b)

Figure 71: Derived characteristic mixing length  $\lambda$  soundings from 18\_06\_12 for (a) 12-00 UTC and (b) 00-12 UTC 19 September 1997.

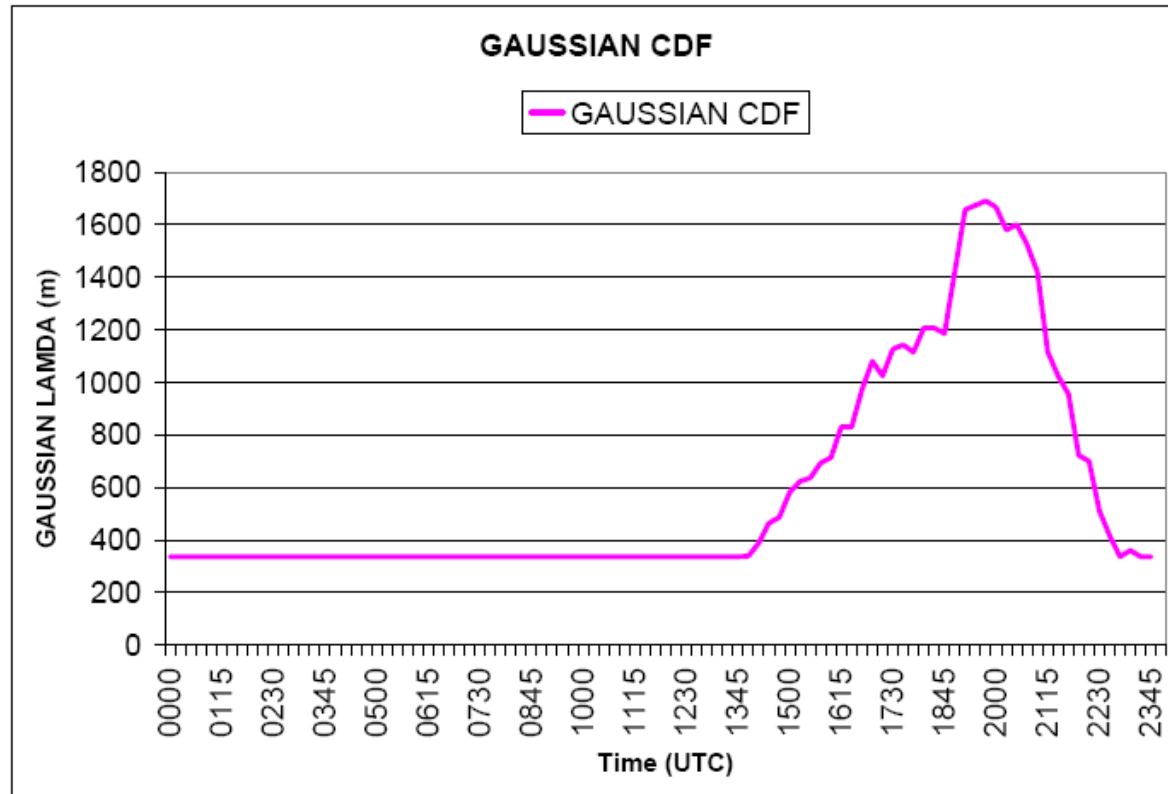


Figure 72: Gaussian cumulative distribution function showing the characteristic mixing length  $\Lambda$  used to produce GAUSS EDR values.

EDR Sensitivity: 36km 40-m 12 UTC NHMASS Simulations  
 1200 UTC 17- 1200 UTC 18 September 1997  
 (DFW Airport)

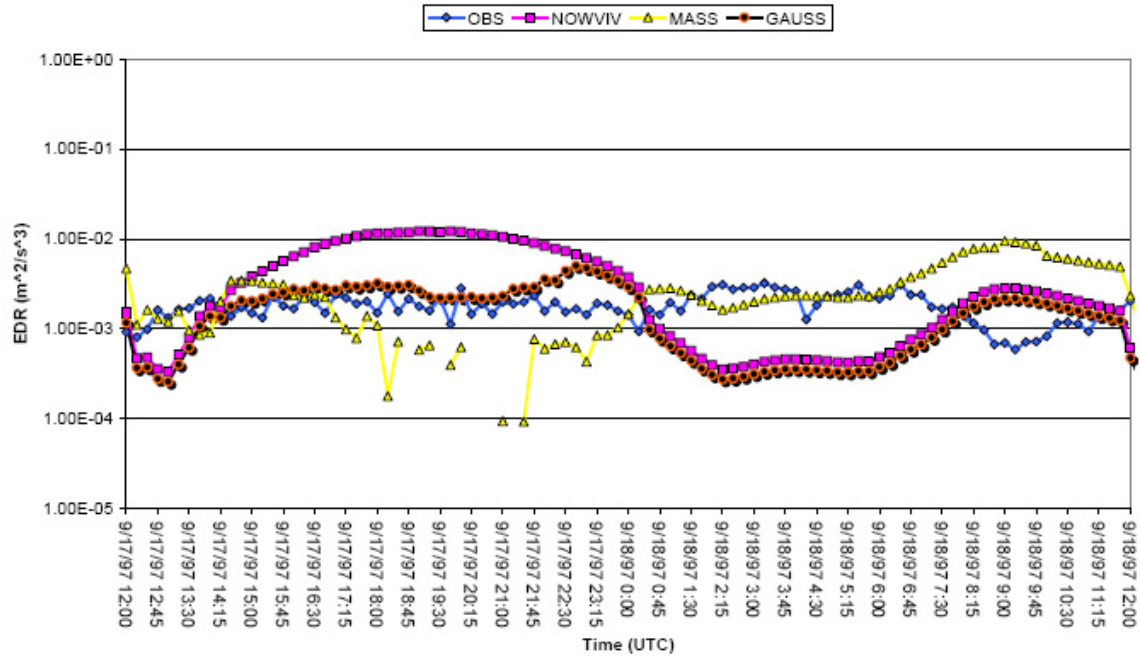


Figure 73: EDR sensitivity time-series plots for 17\_36\_12 valid 00-12 18 September for the observed values (blue circles), NOWVIV (pink squares), MASS (yellow triangles), and GAUSS (black circles).

EDR Sensitivity: 36km 40-m 12 UTC NHMASS Simulations  
 1200 UTC 18- 1200 UTC 19 September 1997  
 (DFW Airport)

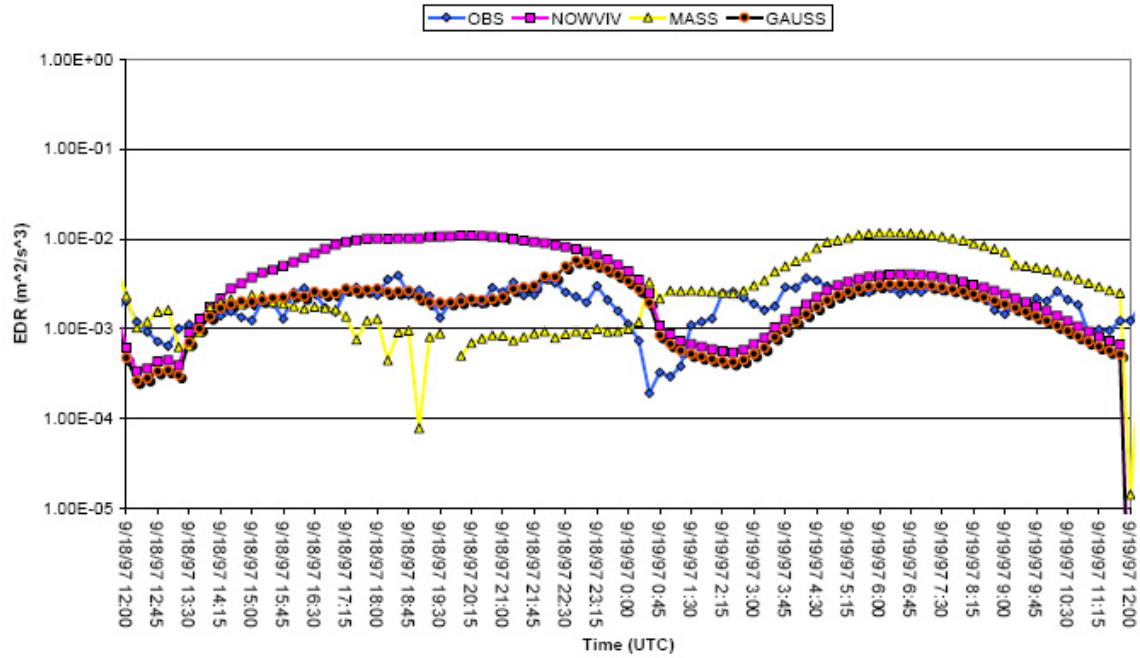


Figure 74: EDR sensitivity time-series plots for 18\_36\_12 valid 00-12 19 September for the observed values (blue circles), NOWVIV (pink squares), MASS (yellow triangles), and GAUSS (black circles).

EDR Sensitivity: 36km 40-m 12 UTC NHMASS Simulations  
 1200 UTC 19- 1200 UTC 20 September 1997  
 (DFW Airport)

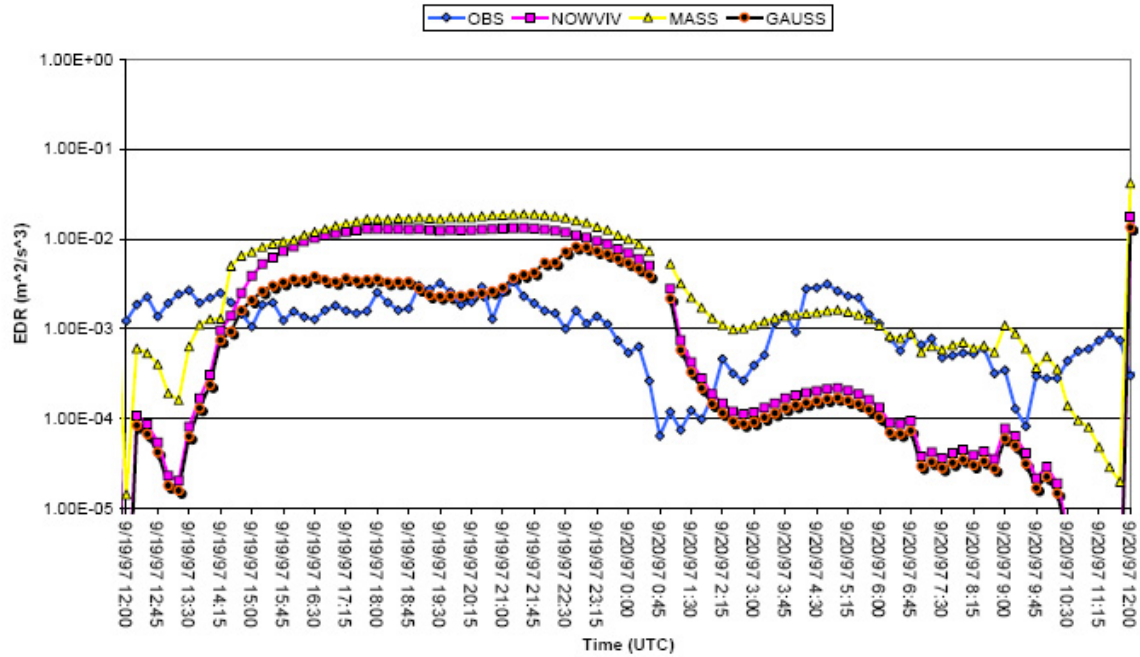


Figure 75: EDR sensitivity time-series plots for 19\_36\_12 valid 00-12 20 September for the observed values (blue circles), NOWVIV (pink squares), MASS (yellow triangles), and GAUSS (black circles).

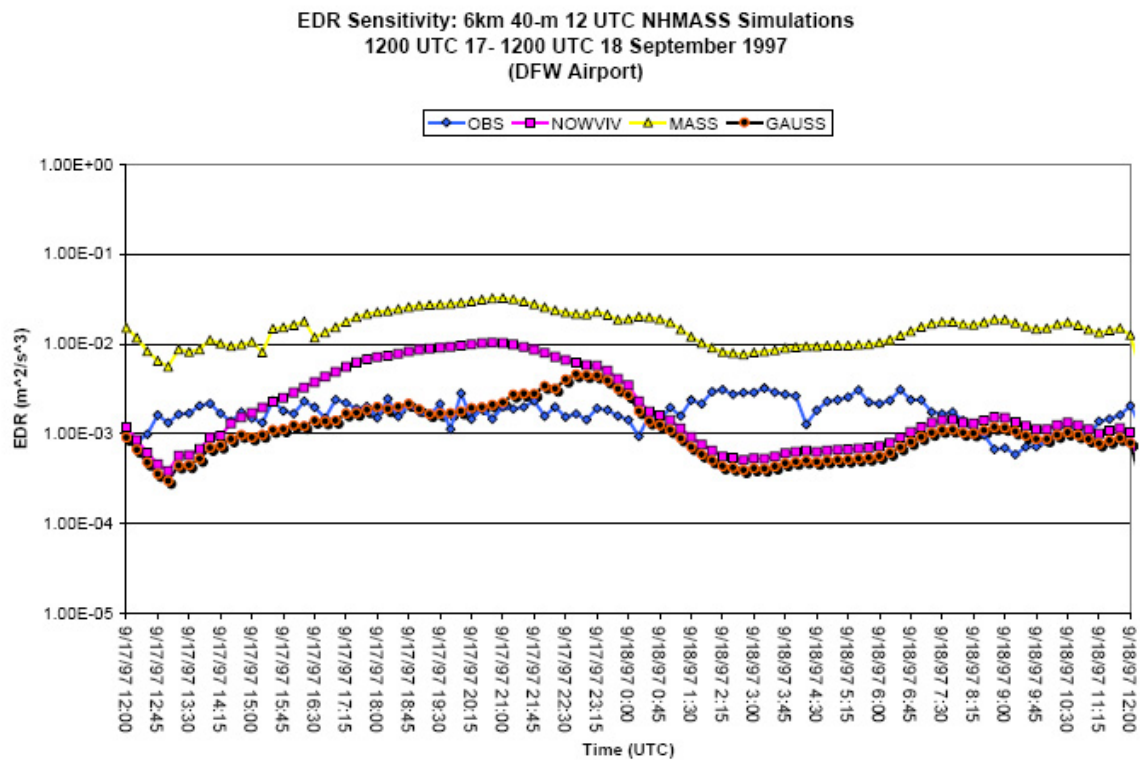


Figure 76: EDR sensitivity time-series plots for 17\_06\_12 valid 00-12 18 September for the observed values (blue circles), NOWVIV (pink squares), MASS (yellow triangles), and GAUSS (black circles).

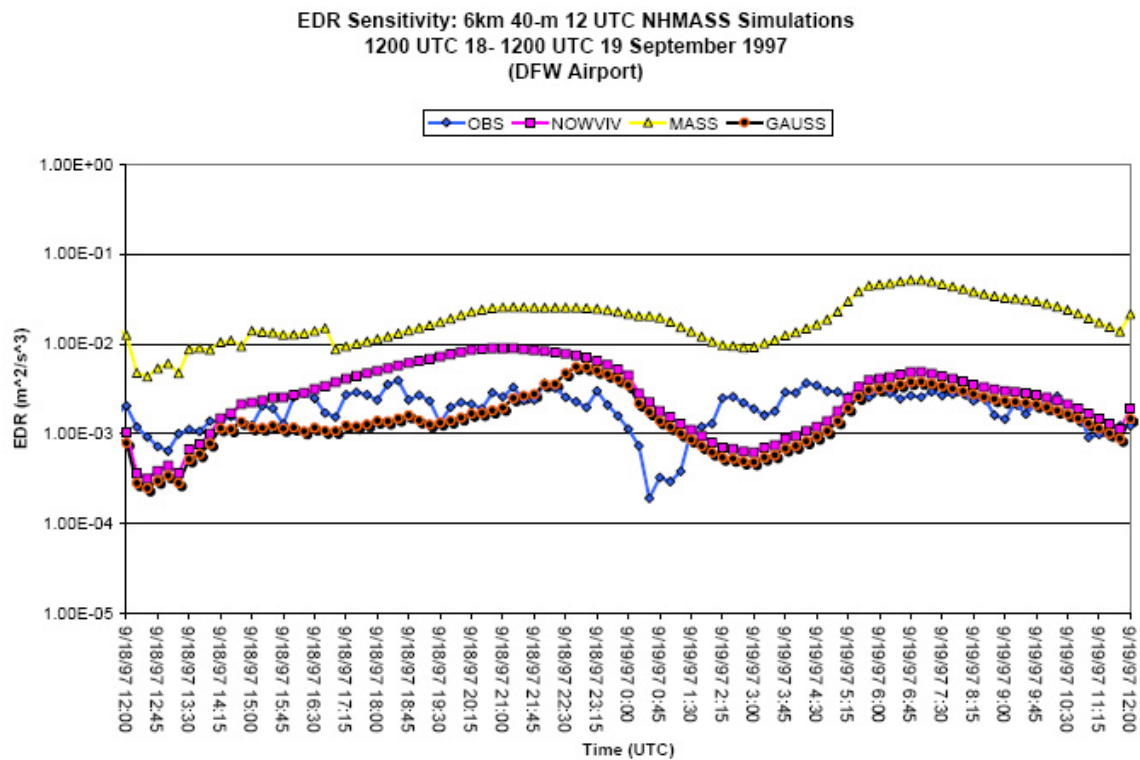


Figure 77: EDR sensitivity time-series plots for 18\_06\_12 valid 00-12 19 September for the observed values (blue circles), NOWVIV (pink squares), MASS (yellow triangles), and GAUSS (black circles).

EDR Sensitivity: 6km 40-m 12 UTC NHMASS Simulations  
1200 UTC 19- 1200 UTC 20 September 1997  
(DFW Airport)

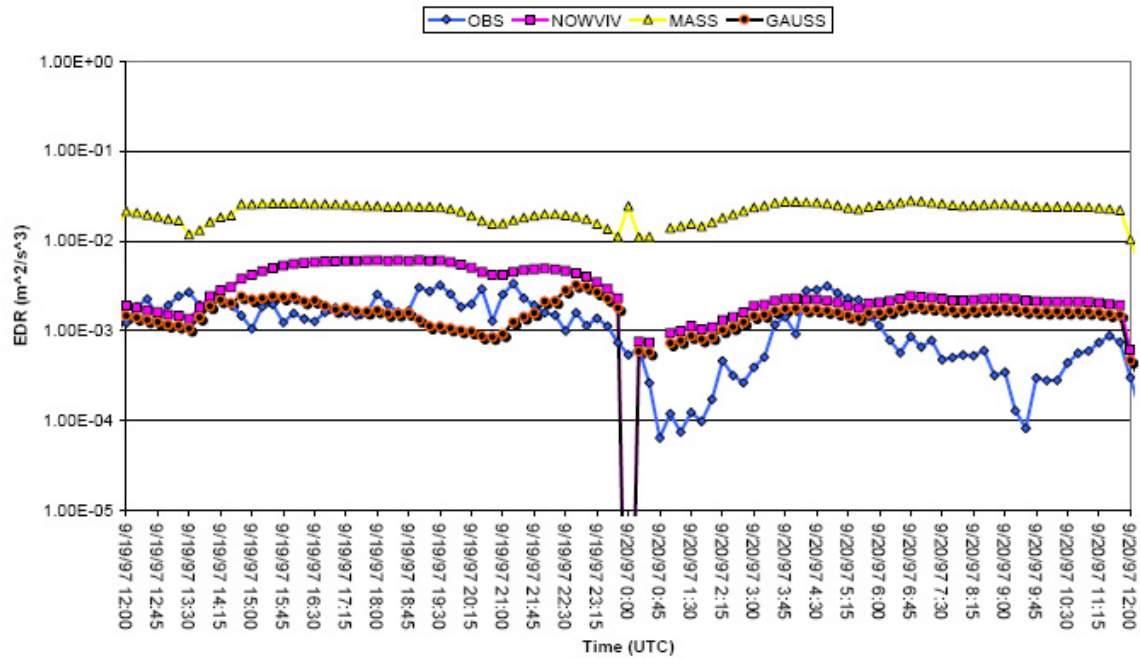


Figure 78: EDR sensitivity time-series plots for 19\_06\_12 valid 00-12 20 September for the observed values (blue circles), NOWVIV (pink squares), MASS (yellow triangles), and GAUSS (black circles).

### **3. Investigations of Numerically-Simulated Turbulence Diagnostics in the Upper Troposphere and Lower Stratosphere**

#### **1. Introduction**

The forecasting of turbulence is of great importance to safety and productivity in aviation meteorology, and is a source of extensive research with many applications. In particular, turbulence forecasting has become a regularly used tool by the National Weather Service (Ellrod and Knapp 1992) and the NOAA Forecasting System Laboratory (Marroquin 1998), where model-generated dependent fields are used to derive indices based on turbulent kinetic energy (TKE) and eddy dissipation rate (EDR). Historically, the focus of research on the evolution of TKE and EDR has been on the planetary boundary layer (PBL), i.e., the lowest one to three kilometers of the atmosphere. Turbulence, however, can occur at any level within the atmosphere and pose a significant threat to aircraft that fly in the upper troposphere and lower stratosphere. A recent study performed by the National Transportation Safety Board revealed that turbulence at upper levels (mostly above 6 kilometers) was responsible for 257 fatalities, 830 injuries, and an average annual loss of \$93 million dollars over a 10 year span from 1990-2000 (e.g. Eichenbaum 2003).

The scale of the turbulence often responsible for the injuries and damage that occurs to aircraft is much smaller than the resolvable scales of operational

numerical weather prediction models. As discussed in Koch et al. (2005), the turbulence in both clear air and near convection (CAT and CIT, respectively (note Kaplan et al. 2004(a,b)) resulting from turbulent eddies most commonly responsible for aviation turbulence above the boundary layer have horizontal scales of ~100-300 meters. To directly resolve such features using numerical models that approach large-eddy simulation (LES) systems using a one-to-one (1:1) horizontal to vertical grid ratio may aid in capturing some, but not all, turbulent generation features. Despite the microscale nature of the turbulence problem, the energy cascade that occurs on the synoptic to mesoscale makes the prediction of turbulence possible using tools that do not directly resolve microscale turbulence features. By identifying the features and fundamental processes that are part of the energy cascade to smaller scales meaningful prognostic turbulence predictions can be made.

The processes that generate and maintain turbulence within the upper troposphere and lower stratosphere are coupled with vertically propagating inertia gravity waves initiated by energy sources within the lower to mid troposphere and by jet stream dynamics near the tropopause (e.g. Koch et al. 2005). In particular, two distinct sources of wave generation, deep moist convection and large amplitude mountain waves, modify their surrounding thermodynamic and kinematic profiles resulting in significant three dimensional fluxes of energy that are capable of upper-atmospheric penetration. Several previous studies have examined the convective and mountain wave problems and their associated features. Lin and Li (1988) used a cloud model to generate

idealized simulations of a supercell thunderstorm to investigate the role of elevated heating on sheared flow present when a “V-shaped” cloud pattern occurs, which was shown to be associated with severe thunderstorms. The V-shaped cloud pattern is hypothesized to be a source of turbulence and was found to be a result of a quasi-steady moist convective updraft in Lin and Li (1988) which, at times, produces overshooting tops into the lower stratosphere and attendant gravity waves. The V-shaped profile was found to be sensitive to the mean wind speed, stratification, and hydrostaticity. The gravity waves varied in intensity when a sponge layer was added to the model lid to mimic the affect of the stratosphere on the profile. Lin and Li (1988) hypothesized that the V-shaped anvils were generated by upstream propagating gravity waves originating at the updraft source. A study by Detwiler and Heymsfield (1987) detailed small-scale turbulence aircraft encounters along the edge of anvils during the observational CCOPE campaign, and very little turbulence in the “shadow” region behind the updraft. In Kaplan et al. (2005a), a 44 case studies of severe aviation accidents, in which either passengers or crew members were injured or the plane was damaged, revealed that out-of-cloud convectively induced turbulence (CIT) was the second most common factor associated with aviation accidents in the study. The pilots visually reported the presence of deep moist convection within a 100 km radius and were avoiding the “weather”. The study illustrated the importance of out-of-cloud CIT in situations where pilots were attempting to avoid convection. Recent studies of out-of-cloud CIT by Lane (2001) and Lane et al. (2003) used idealized high resolution simulations that illustrated regimes of turbulence just

above the initial overshooting top associated with deep convection and a region of turbulence associated with breaking vertically propagating gravity waves 2-3 kilometers above the tropopause. Lane et al. (2003) used very low horizontal grid spacing to derive explicit momentum variances and perturbations from the grid for an analysis of “explicitly” resolved turbulent kinetic energy (TKE). A continuation of this work in Lane and Kneivel (2005) revealed that the gravity waves generated by the numerical model and their affect on the momentum flux (derived explicitly) in the lower and middle stratosphere were highly sensitive to horizontal grid spacing.

Previous mountain wave studies have detailed turbulence in the lower stratosphere as well. Lilly and Lester (1974) used observational data from aircraft to reveal sporadically-turbulent gravity waves generated by terrain over southern Colorado that reached heights of up to 17 kilometers. Leutbecher and Volkert (2000) performed a numerical simulation of an aircraft-related turbulence incident linked to orographically-induced gravity waves with heights up to 20 kilometers. Most recently, Clark et al. (2000) detailed observational and numerical modeling evidence of turbulence in the upper troposphere and lower stratosphere on 9 December 1992 as part of a downslope windstorm and aviation accident near Boulder, Colorado. From the favorable juxtapositioning of jet streak dynamics and a vertically propagating gravity wave mountain wave regime, Clark et al. (2000) hypothesized a “downburst” of turbulence resulted in a DC-8 aviation incident that resulted in the loss of an engine and wing from the aircraft.

As shown in studies by Lane et al. (2003) and Clark et al. (2000), the use of numerical modeling has greatly increased our understanding of upper atmospheric turbulence. In order to close the equations of motions, which is required to integrate operational and research mesoscale models with time, a sub-grid scale mixing scheme is employed to control instabilities and approximate turbulent motion between grid points. To address this issue, various approximation parameters have been derived to represent the fluxes of momentum and heat through the models' boundary layer scheme (e.g. Yamada and Mellor 1975, Stull 1988). The majority of work done in previous literature have focused on developing approximations for the second moment fluxes for the boundary layer, which are then used in vertical integration to resolve turbulence at upper levels. The flux parameterizations are then incorporated into an approximated version of the TKE tendency equation to prognostically predict turbulence at the next time step in the simulation. The approximations made to the TKE tendency equation, which are manifested in the appropriate closure scheme used for the second moment fluxes, are often of lower order to increase computational efficiency. In addition, since the majority of work on deriving appropriate approximations for the second moment fluxes has been done in the boundary layer, they more appropriately represent turbulence evolution within the PBL. The sub-grid scale parameterization schemes are thus not necessarily designed for application to higher resolution problems, particularly at higher altitudes above the PBL.

Because the forecasting of clear-air turbulence (CAT) or convectively-induced turbulence (CIT) is of great importance to commercial aviation, many previous studies have addressed the issue of accurately representing turbulence at upper levels in numerical models. The most common approach taken in previous studies centers on estimates of turbulence that result from unresolved scales of motion by approximating the TKE equation from model-derived fields. Marroquin (1998) developed a diagnostic turbulent kinetic energy formulation (hereafter, DTF3) to approximate the TKE equation evolution at upper levels on the grid-scale. The prognostic TKE tendency equation (DTF3) is approximated using a steady-state approach derived from numerical model output independent of the TKE generated within the sub-grid scale. The formulation, along with approximately twelve other such indices (including the North Carolina State University index, hereafter NCSU1), were used to develop a statistically-based weighted CAT prediction system for operational numerical models. The system, known as the integrated turbulence forecasting algorithm (ITFA), produces graphical turbulence guidance (GTG) products from the 20-km Rapid-Update Cycle (RUC) model at mid and upper levels which can be used to prognostically predict areas of possible turbulence generation (e.g. Sharman et al. 1999, 2000, 2002, 2006).

Following the previous work of Marroquin (1998), Koch et al. (2005), Sharman et al. (1999, 2000, 2002, 2006), a direct grid-scale turbulence forecasting algorithm is being developed in coordination with the United States Air Force at North Carolina State University. The algorithm, described in Section

3, is based off of estimates of turbulence derived from numerical model output similar to those of previous studies (e.g., Marroquin 1998, Sharman et al. 2006). In order to evaluate the model's capability in handling turbulence evolution at upper levels using direct post-processing algorithm, case studies of two different upper atmospheric turbulence generation regimes, moist convection and mountain waves, are analyzed. The case studies are examined using a very fine spatial and temporal configured non-hydrostatic mesoscale numerical model. The increased temporal and spatial nature of the simulations, that approach LES scale, allows for a series of explicit turbulence calculations such as the individual TKE tendency terms to be performed. By calculating the turbulence explicitly, insight on the physical processes that generate turbulence in the two vastly different case studies can be investigated and quantified through diagnostics calculations. The explicit turbulence calculations are also being tested as part of an automatic grid-nesting algorithm capable of capturing upper-atmospheric turbulence features responsible downward energy cascade, which, when violently dissipated on the microscale, pose a threat to high-altitude flying aircraft.

This study has three specific aims. The first is to express and resolve features that generate turbulence in the upper troposphere and lower and middle stratosphere that could produce significant aviation turbulence. Case studies from two vastly different forcing regimes are presented where aviation turbulence poses a threat to high-altitude flying aircraft. These cases are then examined using a numerical model and turbulence diagnostics from the stratosphere are then explored. The second is to address the numerical model's ability to forecast

turbulence at atmospheric levels beyond the boundary layer, thus testing the utility of the sub-grid scale flux approximations against more direct computational methods that quantify grid-scale turbulence. To do this, comparisons between the model parameterized momentum and heat fluxes and explicitly calculated fluxes will be made for each of the cases. In addition, results related to the sensitivity to the type of Reynolds' averaging technique used in the explicit calculations is also presented. The third is to compare and quantify the turbulence generation in two vastly different forcing regimes and identify the most important mechanisms responsible for turbulent tendency. The explicit calculations of the individual terms within the TKE tendency equations allows for direct quantification of the different turbulence contributions and a comparison of scale between the two different forcing regimes.

The rest of the paper is organized as follows. In Section 2, the convective and mountain wave case studies used in the investigation are described from an observational point of view. The numerical model configuration and the explicit turbulence calculation algorithm and associated methodology are described in Section 3. In Section 4, the results from the convective case study, the 12-13 December 2002, large-amplitude gravity wave/convective line are presented. In Section 5, the results from the mountain wave case study, 9 December 1992, are presented. Section 6 details the conclusions from both case studies and recommendation for the project.

## **2. Observational Overview of Case Studies**

The research project funded by the United States Air Force's Research Laboratory is designed to develop operational techniques for the improved prediction of lower stratospheric turbulence generation. Two of the cases used in this study are the 12-13 December 2002 large amplitude gravity wave/convective line case and the 9 December 1992 Colorado Front Range downslope windstorm/aviation accident case. Both cases have the benefit of a wealth of observational data despite the fact that no field program was deployed at the time of the incidents.

### *2.1: 12 December 2002 Convective Case*

On 12-13 December 2002, several large amplitude surface gravity waves developed and moved from portions of central Texas through northern Mississippi. The synoptic and mesoscale environment in southeastern Texas and western Louisiana was favorable for the genesis of mesoscale gravity waves similar to the pre-existing research paradigms where favorable jet streak dynamics (Uccellini and Koch 1987) and wave ducting mechanisms (i.e., a strong stable layer) can lead to mesoscale gravity wave generation (Zhang et al. 2004). Upper air analyses derived from the North American Regional Reanalysis (NARR) dataset valid 12 UTC 12 December 2002 reveal the potential coupling of the right entrance region of a potent polar jet streak over Louisiana/Mississippi and an approaching left exit region of a subtropical jet streak over northern Mexico and the western Gulf of Mexico (e.g., Fig. 1) at upper levels (300 hPa). Surface analyses (Fig. 2) from the western Gulf Coast reveal a strong stationary

frontal boundary, with a cool, moist and strongly stable air mass north of the boundary across southeastern Texas and western Louisiana, an ideal configuration for wave ducting. The jet configuration would allow for enhanced upper level divergence and deep moist convection within the warm sector south of the boundary, support rapid and deep surface cyclogenesis along the boundary, and provide the genesis mechanism for large-amplitude surface gravity waves north of the boundary within the stable layer.

Surface gravity waves passed over several NOAA Global Positioning System (GPS) microbarogram pressure stations along the Gulf of Mexico and Southeast United States. Figure 3 shows a Google Earth composite plot of the time and magnitude of the pressure rise/fall couplet associated with gravity waves whose signal is observed at the surface across Texas, Louisiana, Arkansas and Mississippi on 12-13 December 2002. The first observational evidence of a gravity wave occurs in far southeastern Texas on the morning of 12 December. Figure 4 is a four-panel plot of GPS stations arranged in chronological order from Houston, TX (HOU, Fig. 4(a)) at 1500 UTC 12 December, east/northeast through the southeast Texas sites of Ledbetter (LED, Fig. 4(b)) and Palestine (PAL, Fig. 4(c)), and into the Western Louisiana site of Lafayette (LAF, Fig. 4(d)) at 0300 UTC 13 December. Several of the gravity waves had maximum pressure rise/fall couplets of 6-9 hectopascals (hPa) over a 2-3 hour span during the afternoon of 12 December in southeastern Texas. During this time period, upper-level dynamics from the couplet jet structure initiated deep moist convection trailing southwest from a rapidly developing

surface cyclone along the Texas coast. NOAA NWS Level II radar imagery from the morning hours of 12 December from HOU (Fig. 5) show the development of deep moist convection along the southeast Texas coast and Western Gulf of Mexico south of a stationary boundary. To the north of the boundary, a band of steady stratiform precipitation was present as a result of lift over the cool stable layer across far southeast Texas and western Louisiana. As the surface cyclone deepened and surface heating increased, a mature convective line moved eastward along the Texas Gulf Coast. Around 2130 UTC 12 December, reflectivity and velocity imagery from the Lake Charles, LA (LCH) radar show a rapid erosion of stratiform precipitation north of the boundary and behind the main convective line south of the boundary across Jasper, Newton, San Augustine, and Sabine County Texas (Fig. 6). The precipitation continues to erode with eastward extent and by 2330 UTC 12 September, has eroded as far east as Evangeline Parish Louisiana, leaving the area of interest near the stationary boundary and surface cyclone completely devoid of precipitation. The erosion of precipitation is attributed to rapid descent of momentum associated with a large-amplitude gravity wave generated from the coupled jet structure, which has been documented in other studies (e.g., Zhang et al. 2004).

Spectrum width data, which has been used as a proxy for atmospheric turbulence in radar observations in previous studies, show several wave packets at a vertical beam tilt of  $1.5^\circ$  along the stationary boundary just northeast of the LCH radar across eastern Calcasieu and western Jefferson Davis Parish, Louisiana between 2145-2215 UTC 12 September (Fig. 7). Immediately

preceding the wave feature, the subsidence associated with the descent of the large amplitude gravity wave erodes the precipitation, and induces increased spectrum width velocity variance at vertical tilts as high as  $4.0^\circ$ , indicating the possibility of turbulence at these levels near the radar. Turbulence signatures at upper levels were also captured with the National Oceanic and Atmospheric Association (NOAA) profiler network stationed across southeast Texas and western Louisiana. Figure 8 shows vertical profiles of wind and horizontal velocity variance from PAL and LED on 12-13 December 2002, with evidence of descent within the jet core at both locations. The profiler also shows the presence of an oscillating surface wind between the surface and 2-3 kilometers within the stable layer, which, in the absence of a progressive surface front, has been shown by previous studies to indicate the passage of mesoscale gravity waves (Zhang et al. 2004, Suffern 2005, 2006). At upper levels, increased horizontal velocity variance is seen at the level of the tropopause and coupled jet structure (i.e., 10-12 kilometers), corresponding with periods of precipitation at the sites. In particular, enhanced velocity variance at PAL in the 9-11 kilometer layer between 1900-2200 UTC 12 December corresponds with a period of deeper convection near the site. Above the tropopause, increased velocity variance is also present as high as 16 kilometers, indicating the possibility of a regime of turbulence in the lower stratosphere. The rapid descent of the “dry slot” as a result of the large amplitude gravity wave and attendant precipitation erosion ends the velocity variance signature previously at upper levels on the profiles.

Recent studies by Eckermann et al. (2005) and Eckermann and Wu (2005) have shown the use of the Advanced Microwave Sounding Unit (AMSU), which is a cross-track scanning passive microwave sounder deployed on the NOAA 15-18 weather satellites, in detecting gravity waves in the lower stratosphere. Data from the AMSU satellite are used frequently in numerical weather prediction (NWP) models, and have been shown to improve initial conditions on the global scale and can enhance forecast skill (e.g. Baker et al. 2005). The high-resolution AMSU passes allow for detailed radiance measurements across 7 different channels which can provide detailed information about flow perturbations in the upper troposphere and lower stratosphere from 250 hPa (~8 km) to as high as 2.5 hPa (~40 km). Eckermann et al. (2005) hypothesized that gravity waves in the lower stratosphere could produce oscillations and perturbations in blackbody radiance (temperature), specifically in the Channel 9 (60-90 hPa level) of the AMSU satellite. To test this hypothesis, Eckermann and Wu (2005) performed NWP simulations of a case where orographically-induced vertically propagating gravity waves were detected by the AMSU satellite over Europe. Horizontal cross-sections taken at the 90 hPa level from the NWP runs revealed two-dimensional oscillating temperature field signals caused by mountain waves that were very similar to the patterns observed in the Channel-9 AMSU imagery. To explore the hypothesis that gravity waves, both in large-amplitude (jet-induced) and small-amplitude (convectively-induced) were present in the lower stratosphere on 12-13 December 2002, a signal may be present in the AMSU data passes. Figure 9 (a,b) displays data

from the Channel 9 (~90 hPa) and Channel 10 (~60 hPa) AMSU passes valid at approximately 1300 UTC 12 December 2002 respectively. A distinct elongated couplet in potential temperature perturbations similar to that shown in Eckermann and Wu (2005) is present in both Channel 9 and Channel 10 imagery at 1300 UTC in the western Gulf of Mexico. The signal seen at 1300 UTC over the Western Gulf is most likely attributable to the large-amplitude gravity wave, seen distinctly in pressure traces and profilers across the region, in the early morning hours of 12 December 2002. At 2200 UTC, as shown in Figure 10, the AMSU data indicates more widespread and sporadic temperature perturbations, at a time where deep moist convection was prevalent along the Gulf Coast. The data indicates that waves are also occurring at these levels, but are of much smaller amplitude and tied primarily to the convection, as will be discussed in Section 4.

From the evidence seen in the GPS microbarogram traces, NOAA profilers, NOAA weather radars, and AMSU satellite data, one can conclude that a large amplitude gravity wave and associated convection on 12-13 December 2002 played a significant role in generating upper tropospheric and lower stratospheric waves. The preponderance of observational evidence suggested that (1) a large and small amplitude mesoscale gravity waves were present near the surface in southeast Texas and western Louisiana within the stable layer north of a stationary boundary/warm front and (2) upper tropospheric and lower stratosphere waves, and possibly turbulence (a function of wave breaking) generated by the surface gravity waves and convection were present at mid and upper levels across the western Gulf of Mexico and Gulf Coast. A full discussion

on the synoptic and mesoscale evolution focuses on the large-amplitude and surface gravity waves are detailed in Suffern (2006).

### *2.2 9 December 1992 Mountain Wave Case*

The other case detailed in this study is that of a categorized (e.g. Brinkmann 1974) downslope windstorm and aviation accident induced by the interaction of jet dynamics and a supercritical mountain wave regime over the Front Range of the Rockies. Between 1300-1315 UTC on the morning of 9 December 1992, surface winds peaking at  $35 \text{ ms}^{-1}$  were measured in Boulder, Colorado. Between 1200-1900 UTC, multiple aircraft encounters of moderate to severe turbulence were reported by pilots (PIREPs) along and just west of the Continental Divide and as far east as Denver, Colorado. A DC-8 cargo plane, flying at an altitude of 9.7 kilometers above mean sea level (MSL), experienced turbulence severe enough to dislodge one of the planes four engines and rip 19 feet of the right wing off at 1510 UTC. Figure 11 is an adapted cross-section view of the PIREP reports taken from Vollmer et al. (2006), marking the location of the DC-8 aviation incident.

On the synoptic scale, the Front Range of the Rockies and eastern Colorado was on the backside of a lifting negatively tilted trough situated over Oklahoma and Texas. At upper levels, the region was in a very diffluent upper tropospheric pattern in advance of a  $75 \text{ ms}^{-1}$  northwesterly polar jet streak moving in from the Pacific Northwest. Rawinsonde observations in the Intermountain West indicated a weak cold frontal passage noted by both adiabatic cooling and increased vertical wind shear in the 4-5 km MSL between

1200 UTC 9 December and 0000 UTC 10 December 1992 (Clark et al. 2000, Vollmer et al. 2006). By 0000 UTC 10 December, the left exit region of the approaching polar jet streak had moved over the region of interest, and the negatively tilted upper-level trough had lifted out into the Mississippi River Valley. The 1200 UTC 9 December 1992 soundings from Denver, Colorado (DEN, Fig. 12a) and Grand Junction, Colorado (GJT, Fig. 12b) reveal an extremely strong inversion near the tropopause layer with significant warming in the lower stratosphere. At DEN, approximately 14°C of warming occurs between the 11.5 and 12.6-kilometer levels and 7°C of warming are present within this same layer at GJT. In addition, differing layers of strong positive wind shear (~37 knots between 8.1 and 9.9 km) and strong negative wind shear (~24 knots between 10.1 and 11 km) are present just below these anomalously warm layers. The shear layers and coincident anomalous warm lower stratospheric layers are no longer present at the next rawinsonde launch at 00 UTC 10 December 1992.

As detailed in previous papers on this case (Ralph et al. 1997, Clark et al. 2000), additional data on lower stratospheric turbulence was available from a NOAA/ ERL/ETL lidar located at Table Mountain, Colorado, approximately 10 kilometers north of Boulder. Due to the increased volcanic material and aerosols injected into the lower stratosphere by the eruption of Mt. Pinatubo in 1991, useful wind data from ground-based lidar instrumentation can be obtained from the tropopause level to near 18 kilometers above ground level (AGL), allowing for detailed wind observations that would otherwise not be possible above 2 kilometers AGL (Bernard et al. 1991, Post et al. 1996, Ralph et al. 1997). The

volcanic aerosols resulted in unusually strong backscattered power in the lidar, particularly in the lower stratosphere (e.g. 9-12 kilometers, Fig. 13). In addition to the increased backscatter above the tropopause level (~10 km), lenticular clouds were observed in the 9-11 kilometer layer 15 kilometers east of the lidar location. Clark et al. (2000) used specially oriented cross-sections to detail observations of a horizontal vortex tube (HVT) near the tropopause level, which included wave-like features, and a Defense Meteorological Satellite Program visible satellite image (not shown) valid 1507 UTC 9 December 1992 revealed parallel cloud bands that correspond to the level of the HVT seen in the lidar observations.

The supercritical mountain wave vertical structure is shown directly in the lidar observations, with a distinct region of flow reversal (to easterly) near 12 kilometers, and a breaking gravity wave 10-15 kilometers west of the lidar location (e.g., Clark et al. 2000, Fig. 13). As shown in Ralph et al. (1997), a pronounced horizontal gradient in radial velocities was detected in both the lidar (Fig. 13) and velocity-azimuth display (VAD) techniques, and this flow pattern maintained itself over the region for several hours between 1200-1900 UTC 9 December 1992. The flow regime on 9 December 1992 is consistent with the findings of earlier aircraft observational papers (Lilly and Kennedy 1973, Lilly and Lester 1974) to be characteristic of large-amplitude gravity waves in the lower stratosphere (Clark et al. 2000). As will be discussed in Section 5, favorable interaction of jet dynamics and orographically-forced vertically propagating waves are hypothesized to generate the turbulence that results from breaking waves observed on 9 December 1992.

### **3. Experimental Design and Methodology**

#### *3.1: Numerical Model Configuration*

To investigate the case studies described in Section 2, the research project funded by the United States Air Force Research Laboratory focused on numerical simulations which employed a special automatic grid nesting technique. The model used in the study is the Non-Hydrostatic Mesoscale Atmospheric Simulation System, hereafter denoted as NHMASS, which is the nonhydrostatic version of the Mesoscale Atmospheric Simulation System (MASS) model. The physics and numerics modules of the MASS model was described in detail in Kaplan et al. (2000) and has been used in both operational and research mode at universities for over 20 years. The MASS model has been used to detail the evolution of the Presidents' Day I (Uccellini et al. 1987) and Presidents' Day II (Kiefer 2005) winter storms, severe weather development in the Southeast United States (Hamilton et al. 1998; Kaplan et al. 1995, 1997, 1998; Koch et al. 1998) and for high resolution boundary layer simulations of environments contributing to wake vortices, as discussed in Chapter 2 (Kaplan et al. 2000, Kaplan et al. 2006).

As described in Kaplan et al. (2005c), the model sigma-level structure was modified to be extended into the stratosphere and can extend as high as 10 hPa. For all the simulations discussed in this paper, the NHMASS was run with 90 vertical levels. The increased vertical resolution within the NHMASS simulations is concentrated in the upper troposphere and lower stratosphere to allow for detailed diagnosis of wave activity. The NHMASS simulations were ran with a

horizontal grid mesh containing 162 grid points in both the x and y directions. The simulations used a one-way nesting algorithm (e.g. Davies 1976), starting with an 18-kilometer simulation initialized with NCEP North American Regional Re-analysis (NARR) dataset with a (1°x1°) resolution. The 18 and 6-kilometer grids used the Kain-Fritsch Cumulus Parameterization Scheme, while the finer-resolution simulations (2 km, 667-m, 222-m, 71-m) used an explicit cumulus parameterization scheme. All of the model simulations used the Lin et al. (1983) microphysics package and the TKE PBL parameterization described by Therry and Lacarrere (1983).

The automatic grid nesting technique, as described in more detail in Suffern (2006), is an ongoing research experiment coupled with the NHMASS model in order to develop a reliable, real-time, automatic grid nesting algorithm designed for upper atmospheric turbulence. Currently, the model uses a combination of three parameters. First, the NCSU1 turbulence index is given by:

$$NCSU1 = [U \bullet \nabla U] \frac{|\nabla \zeta|}{|Ri|} \quad (3.1.1)$$

where  $U \bullet \nabla U$  is shear advection,  $|\nabla \zeta|$  is the magnitude of the vorticity gradient, and Ri is the Richardson number. The NCSU1 formulation is designed to determine layers of neutral static stability important for potential turbulence generation. The NCSU1 turbulence index is used for auto-nesting tools at grid resolutions coarser than a 667-meter horizontal grid resolution. This index has been evaluated in depth as a turbulence forecasting index in the NCAR RAP

GTG system by Sharman et al. (2006). The second parameter used is the vertical variation of the Scorer Parameter (in units of  $m^{-2}$ ), given by:

$$l^2(z) = \frac{N^2}{U^2} - \frac{U_{zz}}{U} \quad (3.1.2)$$

where  $N$  is the Brunt-Vaisalla frequency and  $U$  is the magnitude of the total wind. Currently, the vertical variation of the Scorer Parameter is used for grid resolutions finer than 667-meters. The NCSU1 index was used as the lone autonest parameter (e.g. Kaplan et al. 2005) in the first generation of the autonesting algorithm, and the Scorer parameter variation was added to the second generation algorithm, as detailed in Kaplan et al. (2005). The third parameter to be employed in nesting to 71 m is the eddy dissipation rate. Using thresholds established in previous case studies, the model pre-processor chooses an area of the grid to run inner nests based on these fields at a predetermined model level and forecast time. For the 12 December 2002 case, the model's auto nesting algorithm was used to determine the grids for the 2-kilometer, 667-meter, 222-meter, and 71-meter simulations. Figure 13 shows the auto-nested grids from southeast Texas and western Louisiana. For the 9 December 1992 case, the model's auto nesting algorithm was used, but these simulations are not the subject of this research. Instead, a manual nesting of the inner grids was centered on the aircraft accident location ( $39.65^\circ N$ ,  $105.75^\circ W$ ) on the eastern side of the Front Range of the Rockies. For the purposes of this study, the 2 kilometer, 667-meter, and 222-meter simulations are examined.

### 3.2: The TKE Budget and Explicit Calculations

As discussed in Chapter 2 and Section 3.1 of Chapter 3, the NH-MASS model employs a sophisticated turbulent kinetic energy-based scheme to resolve turbulence features on the sub-grid scale. Using Stull (1988, the turbulent kinetic energy (TKE) is defined as:

$$e = \frac{1}{2} u_i'^2 = \frac{1}{2} (u'^2 + v'^2 + w'^2) \quad (3.2.1)$$

where  $u_i'^2$  is the three-dimensional variance of the wind. Because the model starts from a quiescent state, the NHMASS model sets the TKE to a constant value of  $e_{NHMASS} = 0.001$  for  $z = 0, t = 0$  and  $e_{NHMASS} = 0$  for  $z > 0, t = 0$  above the surface when the model is initialized. The model is then integrated forward in time using a prognostic equation which describes the time tendency of kinetic energy change within the system. Derived from the equations of motion, the time-tendency of turbulent kinetic energy is expressed as (e.g. Stull 1988):

$$\frac{\partial \bar{e}}{\partial t} = -\bar{u} \frac{\partial \bar{e}}{\partial x} - \bar{v} \frac{\partial \bar{e}}{\partial y} - \bar{w} \frac{\partial \bar{e}}{\partial z} + \frac{g}{\theta_v} \overline{(w'\theta_v')} - \overline{(u'w')} \frac{\partial \bar{u}}{\partial z} - \overline{(v'w')} \frac{\partial \bar{v}}{\partial z} - \frac{\partial}{\partial z} (\overline{w'e}) - \frac{1}{\rho} \frac{\partial}{\partial z} (\overline{w'p'}) - \varepsilon \quad (3.2.2)$$

The terms on the right hand side of the equation are given as follows, from left to right: *Term 1: U-Advection, Term 2: V-Advection, Term 3: W-Advection, Term 4: Buoyant Production, Term 5: U-Mechanical Shear, Term 5-2: V-Mechanical Shear, Term 6: Turbulent Transport, Term 7: Pressure Perturbations, Term 8: Eddy Dissipation Rate* (e.g., adapted from Stull 1988, Ayra 2001). The over bars denote either a spatial or temporal average of the wind components and TKE, with the primes indicated perturbations from a mean-state value. Term 8, which

is the eddy dissipation rate, always exists whenever the TKE is nonzero and is always a loss term. The rest of the terms in (3.2.2) can either contribute to an overall positive or negative TKE profile. The main TKE budget production terms are Term 4: Buoyancy, Term 5: U-Mechanical Shear, and Term 5-2 V-Mechanical Shear. The other terms, such as the advection of TKE by the mean wind (Terms 1-3), Turbulent Transport (Term 6), and Pressure Perturbations (Term 7), act to redistribute the TKE in the horizontal and vertical and are henceforth not production terms. Therefore, the focus of TKE budget diagnostics discussed herein focus primarily on the three main production terms in 3.2.2. From (3.2.2), it is clear that the TKE budget is not balanced and TKE itself is not a conserved quantity, particularly in complicated atmospheric conditions where the turbulence profiles are not isotropic, stationary, or quasi-homogeneous.

The quantities with primes in (3.2.2) are deviations from the mean state based on a form of Reynolds' averaging. In Reynolds' averaging, any independent variable  $\Omega$  can be decomposed into a "mean-state" quantity and a perturbation from that mean, such that:

$$\Omega' = \Omega - \bar{\Omega} \quad (3.2.3)$$

where  $\bar{\Omega}$  is a mean-state average and  $\Omega'$  is a perturbation from that mean.

Many different forms of Reynolds' averaging may be applied to the independent variables, as discussed in Lin (2007). In terms of turbulence within the boundary layer, most Reynolds' averaging techniques use an ensemble averaging technique, where high frequency data (e.g. 10 Hz) is averaged over 1-to-5 minute spans. For (3.2.2), each parameter and term in the equation can then be

calculated using a pre-specified temporal averaging technique. Since the environment within a numerical model are controlled, the temporal averages can be related become ensemble averages. Adapted from Lin (2007), a temporal average can be identified using:

$$\overline{\Omega}_t = \lim_{T \rightarrow \infty} \frac{1}{T} \int \Omega(x_0, y_0, z_0, t) dt \quad (3.2.4)$$

The temporal averaging technique employed in (3.2.4) is similar to that of Cotton (1986). For the purposes of this study, a temporal averaging technique in which each model simulation into four equally-represented pieces. Because an exact formulation is not possible, the temporal averaging technique is tested for use as part of explicit grid-based diagnostics of the TKE budget, and not directly incorporated into the modeled equations of motion. A significant limitation of the temporal averaging is that the averages only yield four average value fields and thus only provides turbulence information at the end of the temporal averaging period. Another form of averaging, which provides turbulence information as a function of grid spacing, available at every output time, is spatial Reynolds' averaging (e.g. Lane et al. 2003). From Lin (2007), a spatial Reynolds' averaging technique, such as grid-volume averaging, can be defined as:

$$\overline{\Omega} = \frac{1}{\Delta x \Delta y \Delta z \Delta t} \int_x^{x+\Delta x} \int_y^{y+\Delta y} \int_z^{z+\Delta z} \int_t^{t+\Delta t} \Omega dx dy dz dt \quad (3.2.5)$$

The spatial averaging approach given in (3.2.5) quantifies and calculates a total grid average value for each independent variable, and then derives the perturbation quantity by subtracting each grid point value from the average as shown in (3.2.3). In order to capture true grid-scale turbulent features, the spatial

Reynolds averaging benefits from finer resolution between the grid points in three-dimensional space. As shown in prior turbulence literature, a significant limitation of spatial averaging is that the average is inherently a function of the grid spacing length. Thus, the spatial averaging technique is best used on fine spatial resolution runs, such as the ones presented in Lane et al. (2003) and this study. Results from the different Reynolds' averaging techniques are discussed further in Sections 4 and 5.

The focus of the stratospheric turbulence in this study is centered on the quantification and representation on the TKE budget equation using explicit grid-based diagnostics (e.g. (3.2.2)) and the applicability to real-case simulated turbulence features, first presented by Ringley et al. (2005). The three advection terms in (3.2.2), Terms 1,2,3 (U,V,W) advection, are generally assumed to be zero in most numerical models because when spatially or temporally averaged at large scales, the horizontal and vertical gradients of TKE are assumed to be negligible (e.g. Stull 1988). The assumption of horizontal and vertical homogeneity of turbulence is applicable to large-scale motion, where the potential turbulence velocities are much smaller than that of the mean flow. However, these gradients are not necessarily negligible in problems dealing with strong vertical motion and in problems with high frequency turbulence features. (e.g. Stull 1988, Ayra 2001). The TKE PBL scheme described by Therry and Lacarrere (1983) strategically sets the TKE advection to zero, so the affect of advection on the TKE profile is assumed to be negligible regardless of the scale. Thus, the forward integration of the TKE tendency equation would include no

affect of advection at any level within the model. The three middle production terms, Term 4: Buoyancy Production, and Term 5(5-2): U(V) Mechanical Shear, are the most important contributors to turbulence creation and destruction (e.g. Stull 1988, Ayra 2001, Lane et al. 2003). The buoyancy production term is largest in the planetary boundary layer on days where thermal forcing is the strongest. In the stratosphere, the buoyancy production term is extremely important due to the presence of high static stability. In addition, wave amplification has been shown to be critical in previous research particularly near and just above the tropopause (e.g. Lin and Li 1988, Lane et al. 2001, 2003).

An integral part of the buoyancy and shear generation terms are the momentum and heat fluxes, given by the various covariances of velocity and temperature. Because of the complexity and computational restraint that arises due to Reynolds' averaging, the equations of motion that are programmed into numerical models are not closed due to this presence of second-moment turbulent flux terms. The fluxes are parameterized using the gradient transport or K-theory within the NHMASS model, a one to one and a half order closure approximation. The K-theory approximation can be made for any variable, as shown in Stull (1988):

$$\overline{u'_j \xi'} = -K \frac{\partial \xi}{\partial x_j}, j = 1, 2, 3 \quad (3.2.4)$$

The K-theory approximation relates the turbulent flux of the variable with the down gradient of the mean variable that is subjected to the Reynolds' decomposition. For the NHMASS model, a one and a half order closure scheme based off of the work of Yamada and Mellor (1975) is used. The one-and-a-half

order closure keeps the prognostic equation for zeroth-order statistics (e.g., wind, temperature) and retains the equations for variances. The TKE-based PBL scheme employed in the NHMASS model uses (3.2.2) as a combined form of the velocity variance equations. The fluxes in (3.2.2) are parameterized using:

$$\overline{u'w'} = -K_M \frac{\partial \bar{u}}{\partial z} \quad (3.2.5.1)$$

$$\overline{v'w'} = -K_M \frac{\partial \bar{v}}{\partial z} \quad (3.2.5.2)$$

$$\overline{w'\theta'_v} = K_H \frac{\partial \bar{\theta}_v}{\partial z} - \gamma_c \quad (3.2.5.3)$$

where  $\gamma_c$  is the local lapse rate and  $K_M$  and  $K_H$  are the eddy diffusivity coefficients for momentum and heat, respectively, defined as:

$$K_M = \frac{l_k \sqrt{e_{NHMASS}}}{2} \quad (3.2.6.1)$$

$$K_H = 1.35 K_M \quad (3.2.6.2)$$

The local lapse rate term in Eq. 3.2.5.3 is set to zero above the lowest model (surface) layer. The coefficients are functions of the model TKE and the mixing length. The flux parameterizations given by (3.2.5.1)-(3.2.5.3) provide representation for the buoyancy and mechanical shear generation of turbulence via the down-gradient K-theory version of turbulence evolution. For the other terms containing fluxes in (3.2.2), the scheme employs the Therry and Lacarrere (1983) “turbulent kinetic energy flux” parameterization on the turbulent transport and pressure perturbation terms (Terms 6 and 7 in (3.2.2)) given by:

$$\frac{\partial}{\partial z} (\overline{w'e} + \frac{1}{\rho} \overline{w'p'}) = \frac{1}{2} \frac{\partial}{\partial z} (l_k \sqrt{e} \frac{\partial \bar{e}}{\partial z} - \frac{l_e g w_* \overline{w'\theta'}}{2\theta \sqrt{e}}) \quad (3.2.7)$$

where  $l_e$  and  $l_k$  are the characteristic mixing length scales, which are functions of PBL depth, height above ground, stability, and the convective velocity scale  $w_*$ .

Given the approximations and information described in this section, a NH-MASS version of the TKE tendency equation can be written as:

$$\frac{\partial \overline{e_{NHMASS}}}{\partial t} = \frac{g}{\theta_v} (K_H \frac{\partial \overline{\theta_v}}{\partial z} - \gamma_c) + K_M (\frac{\partial \overline{u}}{\partial z})^2 + K_M (\frac{\partial \overline{v}}{\partial z})^2 - (\frac{1}{2} \frac{\partial}{\partial z} (l_k \sqrt{\overline{e_{NHMASS}}} \frac{\partial \overline{e_{NHMASS}}}{\partial z} - \frac{l_e g w_* \overline{w' \theta'}}{2 \theta \sqrt{\overline{e_{NHMASS}}}})) - \varepsilon \quad (3.2.8)$$

The last term in (3.2.8), the eddy dissipation rate, is also parameterized as a function of the model TKE, and is expressed as:

$$\varepsilon_{NHMASS} = \frac{(\overline{e_{NHMASS}})^{3/2}}{8l_e} \quad (3.2.9)$$

As described in Stull (1988), the one-and-a-half order closure scheme allows for the eddy dissipation rate to be a proxy for turbulent intensity, and direct proportionality to the model TKE is noted in (3.2.8). The TKE and EDR that are generated by the model are designed to account for sub-grid scale motions typically found in the real atmosphere, such as thermals and plumes. The buoyant and shear-generated turbulence is generally the highest for these motions within the boundary layer. In addition, the sub-grid scale mixing parameterization helps to reduce numerically-generated instabilities that may cause reflection or model result contamination and failure.

Previous authors such as Lane et al. (2003) and Lane and Kneivel (2005) have used an explicit turbulence calculation scheme to address the grid-scale turbulence by solving for the second-moment fluxes. Due to the limitations invoked by the spatial averaging constraints, the model simulations require a higher resolution spatial and temporal format in order to adequately capture the

features that may produce grid-scale turbulence. The turbulence diagnostics proposed in this methodology are based off of model grid arrays and are not part of the model forward integration. The diagnostics are designed to detect features on the grid-resolvable ( $> 2-4\Delta x$ ) scale which could produce turbulence that threaten high-altitude flying aircraft. For example, the model sub-grid parameterization scheme is employed to diagnose turbulence that occurs between the finite number of points within the model. In the event of wave breaking, the design of the model sub-grid parameterization scheme would allow for significant TKE values to develop. The diagnostic approach introduced here is expected to resolve features that could produce turbulence upon breaking within the model, and in a sense, aids the prognostic prediction of potential turbulence regions that threaten aircraft. The diagnostic calculations are derived using both spatial and temporal Reynolds' averaging techniques. The grid-explicit turbulence diagnostics are hypothesized then to better represent and quantify the small-scale features capable of producing turbulence in the stratosphere upon breaking. In particular, breaking waves near and above the tropopause (as high as 6 kilometers above) generated by overshooting tops have been found to generate significant turbulence (e.g. Lane et al. 2003) capable of damaging aircraft.

#### **4. 12 December 2002 Convective Case Study Results**

##### *4.1 NH-MASS Coarse Grid (MASS18C, MASS6C) Summary*

Following the methodology described in Section 3, the stratospheric version of the NH-MASS model simulated the 12 December 2002 large-

amplitude gravity wave event using a one-way automatic grid-nesting algorithm. The coarsest grid used was 18 kilometers, initialized from the NARR dataset and ran continuously for 36 hours starting at 0000 UTC 12 December 2002 through 1200 UTC 13 December 2002.

For the purposes of this study, the convective case/18-kilometer NH-MASS simulation (hereafter, MASS18C) and the 6-kilometer convective case/NH-MASS simulation (hereafter, MASS6C), are used as both initial and boundary conditions for the higher-resolution simulations, where an explicit turbulence calculation algorithm is tested. Thus, the outer grids will be referred to as the “coarse” grid simulations. In order to understand the evolution of events on the meso-to-microscale, one must understand the synoptic conditions that contribute to the features of interest. As discussed at length in Suffern (2006), the MASS18C simulation does a remarkable job at simulating the synoptic and mesoscale features on 12 December 2002. Figure 15 is a four panel plot of 300-hPa winds and heights valid from 0000 UTC-0000 UTC 12-13 December 2002 from MASS18C. The favorable juxtaposition of the left exit and right entrance regions of the polar and sub-tropical jet streak is apparent in southeast Texas and the western Gulf of Mexico by 1200 UTC 12 December (e.g. Fig.15(a,b)). By 1500 UTC 12 December, deep surface cyclogenesis and attendant deep moist convection develops along the southeast Texas coast and western Gulf of Mexico and rapid strengthening of the downstream jet streak is noted in Figure 15(c,d). The development of large-amplitude gravity waves occurs within the model in response to the jet dynamics and a linear convective system, though

the waves have stronger magnitudes and are coincident with the leading edge of the gust front in the simulation. The lag behind the convection was noted in the observations. Further details on the near-surface and tropospheric gravity waves can be found in Suffern (2006).

The NOAA FSL profiler network and the NARR and RUC data sets indicated the rapid strengthening of an anticyclonically-curved 300 hPa jet streak over eastern Texas, eastern Oklahoma, eastern Kansas, and western Missouri between 1200-2200 UTC 12 December 2002. The wind maxima develops in response to the convection that develops in the left exit region of the sub-tropical jet streak during the early morning and late afternoon hours of 12 December 2002 (e.g. Fig. 15). The MASS18C simulation replicates this process and develops a broader and more intense *upstream* wind maxima (relative to the subtropical jet's exit region) than what was observed (e.g. Fig. 15(c,d)). The jet enhancement seen in this case is very similar to previous work by authors such as Hamilton et al. (1998), where the development of an upstream wind maximum occurred in response to constant elevated heating in the mid troposphere. The deep moist convection, even at a coarse 18-kilometer grid resolution, develops a pronounced wind minimum at upper levels in far southeast Texas near the Louisiana border. The wind minimum occurs in a location where stratospheric gravity waves are indicated by the AMSU satellite data (Fig.9-10) and are heuristically correlated with periods of deeper reflectivity in the radar data, particularly in far eastern Texas and far western Louisiana between 1900-2300 UTC 12 December 2002. The convection that induces both the upstream wind

maximum and the co-located wind minimum in the MASS18C simulation is the focus of the remainder of the higher resolution simulations. As noted in Suffern et al. (2006), when the latent heating within the model was shut off, the convection does not develop and the upstream wind maxima and accompanying gravity waves do not develop.

The NH-MASS model's one-way nesting algorithm uses the MASS18C simulation to provide boundary conditions for the next coarse grid simulation (e.g. MASS6C). The automatic grid nesting algorithm, using the NCSU1 turbulence index at 90 hPa (see Eq. 3.1.1), chose a location to nest the MASS6C simulation. The location chosen by the automatic grid nesting algorithm coincides with a deep moist steady-state updraft along a linear convective system in southeast Texas and western Louisiana. The MASS6C simulation begins at 0800 UTC 12 December 2002 and is integrated forward in time 20 hours to 0400 UTC 13 December 2002. During this time, several convection-related episodes are examined in subsequent higher order runs.

The MASS6C run develops moist convection through the KF cumulus parameterization scheme in the right entrance region of the polar jet stream as early as 1300 UTC 12 December 2002. Graphical and numerical investigations of precipitation that develops early in the model reveal that the convection is cellular in nature and shallow when compared to deeper convective episodes later in the model run. The elevated nature of the convection is to be expected as it is confined to the areas north of the stationary boundary across southeast Texas. Because of the relatively large time and spatial scale within the MASS6C

simulation, the diagnosis of *individual* convective cells is difficult to perform. Nevertheless, the sporadic cellular precipitation features that occur north of the stationary boundary produce accumulated precipitation (both grid and convective type) over the Hill Country of southeast Texas (e.g, Fig. 16). In addition, the development of a downstream wind maximum aloft relative to the subtropical jet exit region begins as early as 1400 UTC 12 December over northern Texas and southern Oklahoma (e.g., Fig. 17). By 1400 UTC, elevated convection develops north of Houston Bay and northwest of Matagorda Bay near the Texas Gulf Coast. Cross-sections potential temperature and wind valid 1400-1800 UTC 12 December reveal the effect of deep moist updrafts on the vertical structure of the upper troposphere and lower stratosphere (e.g. Fig. 18). Stratospheric waves of relative short wavelengths and small amplitudes are generated above and downstream of the convection across the Texas Gulf coast between 1400-1800 UTC 12 December. The individual convective cells that develop between 1400-1600 UTC generates waves as high as 60 hPa in the middle stratosphere. However, the actual cloud boundary does not penetrate above the level of the tropopause (e.g. 100-120 hPa), which supports the evidence that this convection is likely elevated in nature above a region of modest Convective Available Potential Energy (CAPE). The convective tops push the isentropes upward in the cross-section, which is indicative of a deep updraft attempting to penetrate through the tropopause. The period of deeper convection is coincident with the organization of the prior elevated cellular convection into a larger and more organized linear convective line. Despite the output frequency of 1 hr, the upward

and downward motion associated with the overshooting top is still shown in both the moisture and stability fields.

#### *4.2: Deep Moist Convection within the MASS2C Simulation*

As discussed in Section 4.1, a one-way grid nesting technique controlled by the NH-MASS model's automatic grid-nesting algorithm centered a 2-km horizontal grid run (MASS2C) across southeast Texas and western Louisiana (e.g. Fig. 14). The run is initialized at 1900 UTC 12 December 2002 and is integrated for 6 h through 0100 UTC 13 December 2002 with a temporal output frequency of 15 minutes. The region of interest from the MASS6C simulation is the development of a linear convective system across southeast Texas and western Louisiana between 2100-2300 UTC 12 December. As noted within Section 2, the MASS2C configuration uses an explicit precipitation and microphysical scheme for inferring convection, as opposed to the coarser grid results discussed in Section 4.1. Ensemble convective heating within the MASS6C run produced the diverging flow resulting in an area of enhanced NCSU1 turbulence index at 90 hPa, as shown in the NCSU1 turbulence plots in Figure 19. These larger magnitude areas of NCSU1 turbulence index centered the automatic grid nest on a 324x324 kilometer grid with 2-kilometer horizontal resolution in east southeast Texas. Due to the formulation of the explicit turbulence diagnostics, the vertical coordinate for the remainder of the analysis is chosen to be height, specifically, meters above mean sea level. Because the area of interest is near the ocean, the heights discussed are very close to an above ground level height.

To examine the convective evolution across southeast Texas and its impact on the turbulence profile, plots of model-derived turbulent kinetic energy (model-TKE), model-derived reflectivity, and mixing ratio are plotted at various heights. Figure 20 shows a four-panel plot of model TKE and reflectivity from the lowest-model level interpolated height value (250 meters) at 30 minute intervals from 2100-2230 UTC 12 December MASS2C run. A robust linear convective system moves rather quickly northeast of Matagorda Bay, Texas and through far east-southeast Texas by 2100 UTC 12 December. Small cellular-shaped convective features develop and rapidly move northward ahead of the line and some are eventually absorbed as the system propagates eastward. By 2145 UTC, the edge of the linear convection approaches Jasper and Newton County Texas, and the development of a trailing stratiform precipitation region is evident at the 250-meter level around this time. The model-derived TKE is maximized along the leading edge of the convective line, with other maximums noted in the individual convective elements. The strong convergence associated with the gust front initiates TKE values in excess of  $8 \text{ m}^2\text{s}^{-2}$  along the gust front between 2100-2200 UTC (e.g. Fig 20). The leading edge of the convective line crosses the Texas/Louisiana state border and moves across Beauregard Parish in western Louisiana around 2230-2300 UTC, and most notably, across where the WSR-88D would be stationed in Lake Charles, LA (LCH). The line moves across far southwestern Louisiana, and by the end of the model integration at 0100 UTC 13 December, is approaching the western boundary of the model grid. A slight downward trend in reflectivity is noted toward the end of the run, coincident with

the end of surface heating as the solar radiation scheme in the model transitions into a night mode.

As noted in Lin and Li (1988) and Lane et al. (2003), periods of very deep convection capable of penetrating the stratosphere via updrafts that buoyantly overshoot the tropopause are of great interest for aviation turbulence at upper levels. TKE and reflectivity plots from mid-levels (2-6 kilometers, not shown) and upper levels indicate two distinct periods of deep convection within the simulations. The first period of deep convection occurs across Jasper, Newton, and Orange Counties in far east-southeast Texas between 2230-2330 UTC 12 December. In the MASS2C simulation, a cell of interest is noted within the linear convective system in southeastern Orange County, Texas, very close to the Louisiana border, at the 2245 UTC. Plots of reflectivity, model-derived turbulence (Figure 21) mixing ratio, and divergence (Figure 22) at 10 km between 2245-2330 UTC show the development of a V-shaped feature at upper levels that permeates from a convective burst, or “steady-state updraft”, within the linear convective system. The anvil-related particles at 2245-2330 UTC associated with the rest of the convective system are oriented in a southeast to northwest oriented fashion with the exception of the steady-state updraft across southern Orange County. Very large values of the NCSU1 turbulence index are apparent at the 10 km level coincident with the steady-state updraft between 2245-2330 UTC (e.g. Fig. 23). The NH-MASS automatic grid nesting algorithm recognizes this time period and centers the remainder of the high-resolution simulations in

on this convective feature that is derived from the NCSU1 turbulence index in far east-southeast Texas.

At 2230-0100 UTC 12-13 December 2002, another strong steady-state updraft develops in Beauregard and Vernon Parishes in southwest Louisiana. As with the previous steady-state updraft in Orange County, Texas, the precipitation particles at upper levels within the model “anvil” are aligned in a southwest to northeast fashion, as opposed to the rest of the grid, which remain flow-aligned. The steady-state updraft is apparent at multiple upper levels near and just above the tropopause between 2330 UTC 12-0100 13 December. Around 2345 UTC, an area of enhanced reflectivity and several model-derived pockets of TKE in excess of  $20 \text{ m}^2 \text{ s}^{-2}$  occur in Beauregard Parish Louisiana. A very pronounced V-shape is noted in the mixing ratio (e.g. Fig. 23) reflectivity and model-derived TKE (e.g. Fig. 24) fields at upper levels, as high as 12 km. These two steady-state updrafts are the focus of the remainder of the finer-grid simulations discussed in coming sections.

#### *4.3: Fine-Grid Individual Convective Cell Evolution*

##### *4.3.1: MASS667C Simulation Results: Texas and Louisiana Convective Cells*

As discussed in Section 4.2, two deep-moist convective events within the MASS2C simulation trigger the automatic grid-nesting algorithm to center over east southeast Texas and southwestern Louisiana. The first, in east southeast Texas at 2230 UTC, centered a 108x108 kilometer nest with 667-meter horizontal grid spacing, hereafter denoted MASS667C. The MASS667C is initialized at 2200 UTC using the one-way grid nesting algorithm and is integrated

for 2 h through 0000 UTC 13 December with an output frequency of 3-minutes. One significant limitation presented by any grid nesting technique is the removal of precipitation elements at the model initialization time and the corresponding delay resulting from model spin-up. Though the convective forcing of the mass and momentum fields from the MASS2C simulation is fed in through the boundaries as MASS667C integrates forward, the lack of precipitation features at the initial time means that while the convective evolution within MASS667C will be similar to the same area in MASS2C, some differences in the structure and movement of convection may occur.

The MASS667C simulation develops robust convection along the initialized gust front and other confluence axes as early as 2209 UTC, 9 min into the simulation. A ribbon of very high model-derived TKE is coincident along the leading edge of the gust front when significant reflectivity is first detected at a vertical level of 250 m (e.g. Fig. 25). The linear convective system quickly regains similar intensity to MASS2C and propagates eastward into Jasper, Newton, and Orange County Texas. At upper levels below the tropopause (e.g. 6-8 km), several small circular-shaped reflectivity and turbulence banners develop with the first time step (e.g. Fig. 26) and continue through 2230 UTC. The model derived TKE at 8 and 10 km exceed  $20 \text{ m}^2\text{s}^{-2}$  within the convection and spread outward from the original source. The circular shapes denoted areas of convection, but are not steady state and can be taken to represent in-cloud model turbulence features because they are relatively short-lived and advect quickly northward with the mean flow.

At 2233 UTC, the first “deep” steady-state updraft develops across Orange and Jefferson County Texas. At upper-levels (e.g. 8 km), a circular-shaped feature spreads outward in both the model reflectivity and model TKE fields (e.g. Fig. 27). Between 2236-2254 UTC, a very pronounced “v-shape” appearance in both the mixing ratio and model TKE are shown at mid and upper levels. The model-derived TKE at 8 km exceeds  $8 \text{ m}^2\text{s}^{-2}$  in a v-shaped ribbon permeating from the updraft source, suggesting strong turbulent motion at the edge of the anvil. Despite the relative coarse frequency of output, a pronounced “V-shape” to the precipitation particles seen in the model precipitation particle field is present as high as 12 km. In addition, the relationship between the model-derived TKE field and model moisture fields appear to be instantaneous, i.e., a direct correlation between the two is present. The introduction of precipitation particles juxtaposed with model-derived TKE indicates that the model-derived TKE is detecting the presence of in-cloud turbulence at these levels. While the enhanced model TKE disappears at 2254 UTC, the precipitation particles then begin advecting downstream to the northeast, consistent with the remainder of convection in the domain. Near the surface (e.g. 250 m), the model reflectivity, which had been less than or equal to 54 dBz for the first 45 min of the simulation, increases to over 56 dBz between 2245 UTC-2303 UTC and then quickly diminishes. (e.g. Fig. 28(a,b)) The same evidence is also shown in the accumulated precipitation field, showing an enhanced area of accumulated precipitation in the model between 2245-2303 UTC (e.g. Fig 28 (c,d)). The evidence in the model precipitation fields suggest that a period of deep moist

convection occurred between 2236-2254 UTC, followed by weakening of the updraft tower and a reflection in accumulated precipitation between 2245-2303 UTC, giving the cell a total model integration of a little over 30 min.

As the convective line progresses eastward into southwestern Louisiana, the second deep individual convective cell event occurs. At 2321 UTC, two v-shaped turbulence and mixing ratio features rapidly develop at upper levels in Beauregard and Calcasieu Parishes in southwestern Louisiana (e.g. Fig. 29). Between 2321-0000 UTC, the effect of the deep moist convection on the kinematic wind field is very well defined as the anvil spreads out from a circular shape into a v-shape. The first cell over northeastern Beauregard Parish diminishes in both the TKE and mixing ratio fields by 2333 UTC. The second cell over central Calcasieu Parish persists with a v-shape structure through the end of the model run. As noted with the other convective cell in Texas, the model-derived TKE and model-moisture particles have a direct temporal relationship, with model-derived TKE values exceeding  $20 \text{ m}^2\text{s}^{-2}$  along the edge of the anvil and at the updraft source. As noted previously, the V-shape of the moisture particle field is reminiscent of the V-shaped anvil structures described in Lin and Li (1988) where precipitation particles within the anvil are advected downstream of the updraft by the mean wind in a “V-pattern” due to the presence of a quasi steady-steady updraft. The V-shaped model anvil feature in Louisiana is persistent and particles emanate in a V-shape through the end of the model run, in contrast to the prior convective cell in Texas, which only lasts for a short time. The V-shaped anvil develops as fast moving inertia gravity waves propagate

downstream from the updraft source, similar to the idealized modeling results presented in Lin and Li (1988). Analysis of cross-sections and proximity soundings (see Section 4.3) across the region suggest a mean tropopause level of approximately 11 km, indicating that the model-precipitation particles seen in model derived reflectivity and mixing ratio at heights at or above 12 km would likely be introduced by deep moist convection disturbing the tropopause surface, with increased moisture content above the tropopause level being introduced by brief updraft overshoots ( in the absence of any other significant stratospheric moisture source). In addition, the instantaneous relationship between the appearance of model-derived TKE and precipitation particles near and below the tropopause indicate that the model TKE scheme is resolving potential in-cloud turbulence associated with the convection. Because the model's automatic grid nesting algorithm was sensitive to the first steady-state updraft in Texas at 2230 UTC, the MASS222C simulation grid does not cover this second convective cell, despite the fact the Louisiana cell has increased longevity and strength. Lower stratospheric turbulence characteristics of the steady-state updraft over Louisiana are discussed in Section 4.4.

#### *4.3.2: MASS222C Simulation Results: Texas Convective Cells*

The NHMASS automatic grid nesting algorithm chose the first steady-state updraft in Orange County, Texas to center a 35.9x35.9 km grid for a 222-meter simulation, hereafter MASS222C. The model initializes at 2212 UTC and integrates forward for 44 min through 2256 UTC, bracketing the development and intensification of the individual convective cell in Orange County. The high-

resolution nature of this run is achieved with near 1:1 horizontal to vertical grid resolution output and model output frequency of 1 min.

As discussed in Section 4.3.1, a significant limitation of the nesting algorithm is the need for model spin-up for the convective cell. In addition, some differences in convective evolution are noticeable between the MASS667C and MASS222C runs. At the initial time, a very well resolved gust front with near-surface model-derived TKE values in excess of  $8 \text{ m}^2\text{s}^{-2}$  are seen in Newton County Texas north of the convective cell of interest. Convection starts with the first time step, and the first significant precipitation reaches the surface at 2220 UTC, 8 min into the simulation. Extremely high values of near-surface model-derived TKE are also noted at 2220 UTC, exceeding  $20 \text{ m}^2\text{s}^{-2}$ , which develop on the leading edge of the gust front along the Texas/Louisiana border (e.g. Fig. 30). At upper levels between 8-10 km, a circular reflectivity region in extreme northeastern Orange County, Texas begins developing at 2220 UTC. In the next few output times, the convective cell rapidly develops and spreads outward in a very well resolved v-shaped pattern, with TKE values exceeding  $20 \text{ m}^2\text{s}^{-2}$  along the periphery of the model anvil and near the updraft source (e.g. Fig. 31). By 2231 UTC, however, the v-shaped anvil feature erodes and the remaining elevated mixing ratio signal is advected downwind quickly. Near the surface, significant divergence occurs in the same region between 2231-2234 UTC, signaling the weakening of the cell. Enhanced reflectivity and accumulated precipitation occurs just north of the divergent region between 2234-2239 UTC .

Shortly after the first cell diminishes at 2231 UTC, a secondary cell develops farther back from the leading edge of the gust front starting at 2245 UTC. The convective cell quickly develops a v-shaped structure with very high TKE values around the periphery (e.g. Fig. 32). The effect of the steady-state updraft is very noticeable in the wind field, as significant flow splitting occurs at upper levels associated with the convective cell. The flow on the eastern side of the v-shape remains due southwesterly, while flow on the western side of the v-shape is deflected southerly and occasionally southeasterly. The type of flow divergence around the updraft is similar to that of flow splitting around an orographic feature and has been noted in previous studies (e.g., Lin 2007). Enhanced reflectivity values occur downstream of the anvil but no significant surface-based divergence is seen through the end of the model run, indicating the convective cell is yet to completely weaken through the end of the model integration.

#### *4.4 Model-Derived Turbulence Characteristics in the Stratosphere*

Given the presence of deep updrafts that persisted for over 30 min within the model simulation, the next issue addressed is the effect of the diabatic heating on the kinematic and thermodynamic structure of the upper troposphere and lower stratosphere, particularly related to CIT generation. The model-derived TKE at mid-and-upper levels below the tropopause (e.g. at or below 11 km) is coincident with areas of strongest reflectivity in all of the convective cells noted in MASS2C, MASS667C, and MASS222C. At any point within the simulation, a direct relationship between model precipitation or moisture fields and model-

derived TKE is noted. In addition, there appears to be a direct relationship between the magnitude of the model-derived TKE and precipitation distribution, as strengthening (weakening) trends within the convective cells trigger increases (decreases) in model-derived TKE. This type of turbulence and model precipitation particle relationship is consistent with many in-cloud turbulence models suggesting that the strongest turbulent motions are located near the updraft source and within the cloud boundary.

Above the tropopause height, however, analysis of model-derived TKE reveals that turbulence is noticeably small despite the presence of relatively strong horizontal shear at 12-16 km heights. Cross-sectional analysis of model-derived TKE (e.g. Fig. 33) and virtual potential temperature ( $\theta_v$ ) indicate that gravity waves are generated well into the stratosphere (as high as 18 km) but no signal of model-derived TKE above  $1 \text{ m}^2\text{s}^{-2}$  is seen above the tropopause. Scaled analysis of the TKE reveal that while the values are small, the model-parameterized TKE is able to detect the initial upper tropospheric and lower stratospheric response to the updraft. As discussed in Section 4.3, the very small values of TKE may be attributable to the absence of model cloud fields. The model-derived TKE values are, on average, between  $10^{-2}$  and  $10^{-3} \text{ m}^2\text{s}^{-2}$  at heights at or above 11 km and appear to have the same footprint as the convective v-shaped anvil at lower levels. Previous studies such as Lane et al. (2003) have suggested that out-of-cloud convectively-induced turbulence (CIT) can occur 1-2 km above overshooting tops within deep moist convection and upon wave breaking due to gravity waves induced by the convection. Results

discussed in Section 4.3 revealed that overshooting tops similar to the idealized overshooting tops in Lane et al. (2003) are present, and thus, modes of CIT above the tropopause are possible. In addition, observational data from the AMSU satellite discussed in Section 3 indicate that gravity waves were present in association with the convection across the Texas Gulf Coast on 12-13 December 2002.

To investigate the contributions to model-derived TKE in the simulations, the NH-MASS post-processing algorithm was modified to extract individual components responsible for the contributions to model-derived TKE tendency discussed in Section 2. The model parameterized “U-Momentum Flux” (eq. 3.2.5.1), “V-Momentum Flux” (eq. 3.2.5.2), “Heat-Flux” (eq. 3.2.5.3), and “TKE-Flux” (eq. 3.2.5.8) are extracted to determine their overall contribution to the TKE profile. The fluxes are examined at or near tropopause level, and at higher altitudes where possible instances of CIT may occur and could threaten high-altitude flying aircraft. Because the one-way nesting algorithm induces similar convective trends, the results across the fine-grid simulations (i.e., MASS2C, MASS667C, and MASS222C) are consistent, and therefore, results from the MASS667C and MASS222C are only presented.

An examination of four-panel plots from the MASS667C showing all of the relevant model parameterized turbulent fluxes are shown between 2212-2248 UTC in Figure 34.. The previous instances of updrafts perturbing the 8-10 km surfaces are shown very well in heat fluxes that are scaled by a factor of  $10^2$ . Rather than discussing each individual instance, a discussion of the overall flux

profile is necessary because in general, all of the flux profiles are consistent with each particular convective cell. Values of momentum flux are seen co-located with any precipitation particle element, consistent with the direct relationship between cloud boundaries and model-derived TKE in Section 4.3. For the v-shaped anvils discussed in Section 4.3, the U-momentum flux generates positive (negative) on the western (eastern) side of the cloud boundaries. The V-momentum flux generates the exact opposite profiles in TKE contribution, with negative (positive) flux on the eastern (western) side of the cloud boundaries. The momentum flux contributions are then advected downstream with the mean wind. The momentum flux profiles appear to be controlled strictly by the presence of convection in the model, which in turn generates a positive or negative wind shear based on the wind component and position relative to the updraft. Thus, low mean values of wind shear at upper levels would contribute to small values of momentum flux, leading to TKE profiles that may underestimate the strength of the turbulence potential within the stratosphere.

The heat flux plots reveal a strong positive flux signal at the source of the updraft when the motion first comes through the level. Negative fluxes then spread outward in a v-shape from the original updraft source, and the heat flux is thus mostly negative in the domain outside of regions where updrafts are located. The profiles seen in the heat flux field suggest that, as expected, positive potential temperature perturbations induced by rising motion contribute to positive TKE contribution ( $w' > 0$ ) and sinking motion within the anvil produces negative TKE contribution ( $w' < 0$ ). The exact opposite profile is seen in the TKE-

flux field. The TKE flux is negative at the updraft source and positive almost everywhere else in the domain, except for a few locations downwind of the updraft. Because the TKE-flux field is a combination of turbulent transport and pressure perturbations, a thorough analysis of the TKE contribution is not possible without bifurcating the term within the model TKE scheme.

Examination of the flux plots at higher levels was conducted at 1 km intervals from 11 km to 20 km. Only brief instances of flux signal, even scaled by a factor of  $10^2$ , are seen throughout the duration of the model run (e.g. Fig. 35). In addition, no discernable wave signal is found, though the fluxes are usually bracketed with a positive/negative TKE contribution. Since the model fluxes make up the terms responsible for TKE generation in the TKE tendency equation, a further analysis of the model flux signal at upper levels is found in Section 4.5, where the explicit fluxes and TKE tendency equation terms are investigated.

The NCSU1 and NCSU2 turbulence indices (see Section 3), often used in NHMASS diagnosis of upper-level turbulence, are examined at 1 km intervals within the stratosphere. The turbulence indices (e.g. Fig. 36) are plotted against mass divergence in the lower and middle stratosphere. Both the NCSU1 and NCSU2 turbulence indices are able to pick up on individual convective cells penetrating a layer, but the field becomes more sporadic once an anvil becomes established. The presence of so many different convective towers makes tracking individual signals difficult, as the index fields become noisy as the model integrates forward. The divergence profile, however, shows a much more

interesting signal not seen in the model-derived TKE or turbulence index fields. The first steady-state updraft that occurs in southern Orange County, Texas generates significant divergence that spreads outward from the steady-state updraft and moves into Calcasieu Parish, Louisiana during the 2248-2306 UTC time period. The positive/negative divergence couplet is seen as low as 8 km (e.g. Fig. 37) through the tropopause (i.e. 11 km), and into the middle stratosphere, as high as 20 km. Examination of the geopotential height field on constant pressure surfaces confirm that the effect of the diabatic heating is shown in the middle stratosphere, with significant height rises on the order of 100 m occur on the 30 hPa surface (~22-24 km) coincident with the steady-state updrafts in both Texas and Louisiana (e.g. Fig. 38). Despite the effect of the diabatic heating on the overall profile of the lower and middle stratosphere, no NCSU1 or NCSU2 turbulence index is found above 600 (units) in the 18-20 km layer. The effects of the convection are best seen in the divergence field, where convergence/divergence couplets on the order of  $\pm 2 \times 10^{-4} \text{ s}^{-1}$  are noted moving outward from the same spatial location as the steady-state updraft at lower levels. The same type of signal in the divergence and NCSU1/2 turbulence fields are seen with the second steady-state updraft from 2339-0000 UTC (12-13 December) over Beauregard and Calcasieu Parish, Louisiana.

The divergence patterns seen at upper levels are consistent with the results of the idealized modeling study in Lane et al. (2003), where gravity waves generated by the overshooting top emanated outward from the source at levels well above the tropopause. Though no direct observational evidence exists of

CIT within the stratosphere, observations presented in Section 2 suggest that gravity waves were present in the stratosphere and were coincident with periods of deep moist convection. Thus, the NH-MASS simulations production of gravity waves in the lower and middle stratosphere are consistent with observations, and such features could pose a threat to high-altitude flying aircraft if CIT is generated.

Analysis of the potential temperature field suggested that waves were indeed generated and, upon breaking, could produce CIT above the tropopause within the model simulations. However, no significant model-derived TKE is produced at upper levels despite the presence of gravity waves in the stratosphere. The absence of significant TKE suggests that no wave breaking and subsequent overturning occurred during the model simulations. Though no CIT would be produced without the wave breaking, the identification of possible CIT features is important to operational modeling of the convection. The model-derived TKE fields, made of the parameterized fluxes in the PBL scheme, are not able to identify these possible CIT features. Instead, the relationship between cloud particles and TKE suggested that the NH-MASS model TKE scheme appears to only be effective within the actual convection and cloud pattern.

#### *Section 4.5: Explicit Grid-Based Turbulence Experiments*

##### *4.5.1: Introduction*

In Section 4.4 a strong relationship has been established, independent of horizontal resolution in the NH-MASS simulations within cloud boundaries, between convection and indices, which have a history of association with aviation

turbulence, From the mass divergence and NCSU1 and NCSU2 turbulence indices, however, the presence of strong divergent flow and possible locations of CIT generation is noted in the lower and middle stratosphere (e.g., 11-20 km) from gravity waves generated during periods of overshooting tops within individual convective cells across Texas and Louisiana from 2200-0100 UTC 12-13 December 2002.

In order to investigate the contributions to possible CIT within the lower and middle stratosphere, an explicit calculation of the TKE tendency equation using both spatial and temporal Reynolds' averaging techniques are performed. To resolve the features that could generate CIT within the lower and middle stratosphere on the grid-scale, a one-to-one horizontal to vertical grid ratio is desired, based on results in direct numerical simulations and large-eddy simulations (Stull 1988). Though the original model sigma configuration does not have a direct one-to-one grid ratio, the calculation of the explicit turbulence fields can be performed at the conclusion of the integration and interpolated to achieve grid-relative turbulence fields that approach the grid ratio desired. Thus, the vertical grid in the model is interpolated to 250-meter resolution from the surface through 22 km. Therefore, the MASS2C simulation has a grid ratio of 8:1, making the output from the explicit turbulence fields too coarse for an accurate analysis. The MASS667C simulation, however, has a grid ratio of ~1.5:1, allowing for a full diagnosis of the grid-scale turbulence representation not possible in the outer grids. The MASS222C simulation has a grid ratio of .88:1, slightly below the desired one-to-one grid relationship. However, output from the MASS222C

simulation is investigated based on the very fine horizontal resolution and the proximity to the desired one-to-one relationship. For the remainder of this section, the output from the explicit turbulence calculations is presented for the MASS667C and MASS222C simulations only.

#### *4.5.2: Temporal Reynolds' Averaging Results*

As discussed in Section 3, two different Reynolds' averaging techniques were explored in the explicit turbulence calculations. First, a temporal averaging scheme was performed where the individual model run (e.g., MASS667C, MASS222C) is broken into four individual equal time segments. The independent variables ( $u, v, w, \theta_v$ , etc.) are then averaged into four-segments, where averages of 30 min (11 min) are performed for the MASS667C (MASS222C) simulations. Figure 39 shows an entire atmospheric view of averaged u-component wind speed from the MASS667C simulation. The average velocity profile has a distinct shift in value near the surface where the gust front is located. As the model integrates forward and the leading edge of the convective line propagates eastward, the average u-wind field changes abruptly between averaging times due to the shift in wind direction behind the linear convective system. Examination of the associated flux fields (e.g. Fig. 40), calculated at each time during the integration, reveal a sharp change in sign and magnitude along the edge of the outflow as the averaging time segment changes. The effect of averaging-time segment shift is apparent at levels above the outflow and significantly alters the interpretation of the associated potential turbulence field in the lower stratosphere. For example, at upper levels, the affect of the temporal

averaging adversely changes the momentum-flux profiles at levels near the tropopause. The averaging scheme can identify the individual steady-state updrafts at the beginning of the MASS667C several output times before they actually are represented in the model-parameterized flux field. The temporally averaged fluxes increase coincident with the introduction of convective motions at these levels, as illustrated in Section 4.3. The pattern repeats itself as the averaging time changes, with individual convective features appearing in the flux field before they actually occur within the model. Such inconsistency within the explicit flux fields may cause the NHMASS auto nesting algorithm to choose an incorrect time to situate an inner nest and hereby lessening the quality of the simulation. Therefore, complete diagnosis of the mesoscale features responsible for potential turbulence generation in the upper troposphere and lower stratosphere are diluted by the explicit time averaging. Despite the limitation in the time averaging, some useful information is gained regarding the wave activity in the lower stratosphere. From the averaged virtual potential temperature field ( $\theta_v$ ) in the lower stratosphere, gravity waves generated by the convection are present as high as 16 km, suggesting the presence of potential turbulence generation well above the height of the tropopause (e.g. 11 km). Examination of the MASS222C flux fields reveals the exact same averaging problem. As expected, the MASS222C model parameterized fluxes show more detail than that of the MASS667C, indicating that the increase in horizontal grid resolution does have bearing on the features generating turbulence. However, there is not a

discernable difference in structure in the explicit time-averaged flux fields between the MASS667C and MASS222C.

To test the utility of a time-based averaging scheme, a series of flux fields were generated using a single-time based average as opposed to the segmented approach aforementioned. Complete evaluation of the flux fields in both the MASS667C and MASS222C simulations using either a single or segmented Reynolds' time averaging approach does not produce realistic flux fields based on the wave features and convection present within the model. Specifically, the derived explicit flux fields are quite noisy and splotchy, with no discernable positive/negative couplets following wave packets in the lower stratosphere. The source of error in the derived explicit flux fields comes from the use of a single or segmented time-average to base the calculations for the perturbation fields. Because the flux fields are the dominant control on the TKE tendency equation terms, the use of the time-averaged calculated TKE tendency equation terms is also significantly diluted by the flux fields. In addition, the splotchy nature of the fields and the substantial changes in overall flux magnitude at the switch of averaging time does not lend itself useful to an algorithm for automatic grid nesting. Therefore, the time-averaged Reynolds' fluxes are not useful in diagnosing potential turbulence generation for the 12 December 2002 case.

#### *4.5.3: Spatial Reynolds' Averaging Results: Flux Contributions*

The second Reynolds' averaging approach uses a spatially-based average, where the values of the dependent variables are summed at each grid point for all the available output times. A single grid-based average value is

calculated at each time throughout the simulation as a culmination of values from the associated grid points. Using the methodology outlined in Section 3, a perturbation value of the dependent variable in question is generated for each individual three-dimensional point within the model for each output time. In order to eliminate the physical inconsistency that arose with the four-segmented time-averaging approach, the single grid-based average is not used in the TKE tendency equation. Instead, the full model fields and derived fluxes are used in the calculation. Because the fluxes and derivatives in the TKE tendency equation require an “average”, the use of the full model fields may introduce some mathematical inconsistency. However, because the goal of the research is to investigate the model’s ability to predict turbulence potential for use in an automatic grid nesting algorithm, a diagnostic approach (i.e., identification of potential CIT) is taken to quantify the TKE tendency equation. The overall magnitude of the flux contributions are not discussed herein to avoid redundancy, since the fluxes are the centerpiece of the TKE tendency equation terms discussed in Section 4.5.4.

Using perturbations derived from the spatially-averaged Reynolds’ variables, a direct side-by side comparison of the model versus explicit momentum, heat, and turbulent fluxes are analyzed for various vertical levels in the upper troposphere and lower stratosphere. The first analysis of the explicit spatially-averaged flux is performed for the convective cell in east southeast Texas at 2242-2300 UTC 12 December. At vertical levels between 8-10 km, which is below the level of the tropopause, the model and explicit u-momentum

flux fields (e.g. Fig 41) show remarkable consistency, particularly in terms of the temporal distribution of the fluxes. Unlike the temporal Reynolds' averaging, the timing of flux contributions are coincident with the convection punching through the vertical layer, as seen in the model fluxes and particle fields. An important distinction between the two flux calculations, however, is the spatial extent and structure of the turbulence contribution. In the MASS667C simulation, very similar overall turbulence contributions between the model and the explicit scheme are found with the first steady-state updraft over east southeast Texas between 2242-2312 UTC, but the model-parameterized fluxes show a much broader and smoother area of potential turbulence, coincident with the cloud features discussed in Section 4.3. The explicit fluxes show more structure and detail, and are concentrated with gradients in virtual potential temperature. The representation of the explicit flux fields indicate that the spatial Reynolds' averaging for the MASS667C scheme appears to be capable of resolving potential turbulence features on the grid-scale and do appear somewhat independent of the actual in-cloud turbulence. At 2257 UTC, several minutes after the original steady-state updraft in east southeast Texas, the model flux fields at 10 km continue to show the in-cloud anvil turbulence contributions and possible gravity waves spreading downstream from the original updraft tower in a kidney-bean v-shape pattern. In addition to the anvil portion of the overshooting top, the explicit fluxes show potential turbulence being generated along the edge of the cloud boundary, where a 4 K gradient in virtual potential temperature is noted between 10-16 kilometers (e.g. Fig. 42).

As the updraft weakens and the precipitation particles spread downstream, the model parameterized fluxes also weaken and move with the mean flow, while the explicit fluxes indicate that the potential turbulence, aligned along a gradient in virtual potential temperature along the periphery of the cloud boundary, is spreading eastward into Louisiana. The potential turbulence signal shows a discernable tight positive/negative couplet consistent with that of a propagating gravity wave. In addition, the potential turbulence aligned along this “micro-front” is aligned somewhat perpendicular to the mean flow (e.g. Fig. 42). The results show similar patterns to that of Lane et al. (2003) where gravity waves spread outward from the updraft tower capable of producing turbulence, and Kaplan et al. (2005a), where reports of turbulence-related incidents occurred frequently in cloudy air along the periphery of deep moist convection. At 2327 UTC, the secondary steady-state updraft in Louisiana occurs, and the signal from the “micro-front” feature is no longer visible.

The aforementioned patterns remain consistent in the momentum, heat, and turbulence flux fields through the upper troposphere and lower stratosphere to a height of 12 km, just above the tropopause level. In the lower and middle stratosphere, the signal from the model parameterized fluxes is much weaker and appears to be tied directly with the steady-state updraft at lower levels. In the explicit fields, however, the effect of the diabatic heating in the upper troposphere reveals wave-like structures in the lower stratosphere (i.e., 14-16 km) and mimics the divergence profiles in the middle stratosphere (i.e., 16-20 km). The wave-like features contain a positive/negative/positive flux contribution in very small spatial

scales above and just downstream of the convection and appear just after the overshooting tops (e.g. Fig. 43). The potential turbulence features move much more quickly than the flux contributions in the model-parameterized fields and contain more detailed spatial structure. Specific details on these features are deferred to the discussion on TKE tendency in the next section.

The flux contributions in the MASS222C simulation reveal the same pattern as shown in the MASS667C, but with increased spatial structure in the horizontal. As The steady-state updraft at 2222-2230 UTC along the Texas/Louisiana border generates an impressive gravity that quickly spreads upstream of the updraft, generating a distinct wave-couplet in flux contributions. The same signal is found along the Jasper/Newton County border at 2240-2249 UTC with another updraft punching through the 8 km layer. As seen in the MASS667C, several episodes of distinct wave-like features are found in the lower and middle stratosphere (i.e., 14-18 km) above and just downstream of these steady-state updrafts. The model parameterized flux fields in the MASS222C simulation, shown in Fig. 44 for the steady-state updraft at 8 km along the Jasper/Newton County line, show very broad areas of flux contribution and highly-resolved cloud boundary edges outlined by all of the flux fields (i.e.,  $u$ ,  $v$ ,  $\theta_v$ ,  $e$ ). The flux contributions are attributable to the precipitation particles at this level as the flux field erodes and spreads upstream with the mean flow when the updraft weakens.

The comparison of the model-parameterized flux fields to an explicit spatial calculation suggest that: (1) the model-generated TKE appears to be

solely controlled by the presence of cloud-boundary features at and near the tropopause height; (2) the explicit spatial fields are able to resolve fine wave-like structures in the lower and middle stratosphere not shown in the model-parameterized fluxes; (3) the disparity between the model and explicit fluxes in the middle and lower stratosphere are likely controlled by the strength of the overall shear. Since the magnitude of the shear is so small in the lower and middle stratosphere, the generation of turbulence by the model scheme is suppressed and tied, through parameterizations, to the convection below. The low values of mean wind shear also contribute to the smoother flux values when a signal is present within the model scheme

#### *4.5.3: Spatial Reynolds' Averaging Results: MASS667C Investigation*

The flux contributions shown in the lower and middle stratosphere are then incorporated into an explicit calculation of the turbulent kinetic energy tendency equation discussed in Section 2. In addition to the fluxes, several derivatives must also be calculated in order to construct a diagnostic grid-explicit TKE tendency equation. The spatial derivatives are done on the order of 667 m (222 m) for the MASS667C (MASS222C) simulations. The vertical derivatives, such as u and v-mechanical shear, second-moment fluxes (i.e., TKE and pressure perturbations), etc. are calculated to an interpolated height of 500 m every 250 m, with the exception of the lowest and highest model layer. The 250-m vertical resolution of the derivatives allows the overall resolution of the explicit TKE budget to approach that of a 1:1 ratio. For the purposes of this manuscript,

the results from the MASS667C are presented only; the results from the MASS222C simulation were similar.

#### *4.5.3.1: MASS667C Explicitly Calculated Horizontal Advection Terms*

For the MASS667C simulation, the horizontal advection terms, Term 1: U-Advection, Term 2: V-Advection and Term 3: W-Advection, are calculated and examined for the both steady-state updrafts over east southeast Texas between 2230-2251 UTC 12 December and over extreme southwest Louisiana from 2330-0000 UTC 12-13 December. Because the results are relatively consistent for both cases, a general discussion is provided and the case is referenced in the attendant figures, except when cross-sections are discussed.

The model-derived TKE, representing the model-parameterized TKE gradients on the sub grid scale, are used in the calculation. Due to the assumption of horizontal homogeneity, the contribution of horizontal advection of TKE is zero in the model-derived TKE calculation. The explicit grid-scale TKE tendency terms, however, suggest that the contribution to TKE tendency from the horizontal advection terms may not necessarily be negligible. As shown in Figure 45, the potential TKE tendency from horizontal advection (i.e., Terms 1 and 2) can be as high as  $1.6 \times 10^{-1} \text{ m}^2\text{s}^{-3}$  at the time of updraft penetration over Orange County, Texas (i.e., 2233 UTC) and average between  $4\text{-}8 \times 10^{-2} \text{ m}^2\text{s}^{-3}$  between 8-12 km along the periphery of the cloud boundaries. As shown in Figure 45, the response to the grid-explicit turbulence diagnostics does have a delay in the vertical, suggesting the scheme's ability to accurately diagnose the vertical propagation of the effect of deep moist convection on the turbulence profile in the

lower stratosphere. Above 12 km, however, very little contribution from horizontal advection is noted. The contribution to the explicit TKE profile from Term 3: W-Advection is, as expected, strongly tied to the presence of either strong rising (sinking) motion during the strengthening (weakening) phase of the updraft. However, the vertical gradients in model-TKE are relatively small, and thus, Term 3 is an order of magnitude smaller than Terms 1 or 2. Generally, the contribution from W-advection ranges from  $1 \times 10^{-2} \text{ m}^2\text{s}^{-3}$  at the point of updraft penetration to  $6\text{-}8 \times 10^{-3} \text{ m}^2\text{s}^{-3}$  along the periphery of the cloud boundary for the first steady-state updraft over Orange County, Texas. Above 12 km, however, the trace of horizontal and vertical advection mimics the model-derived TKE, and is sporadic and not co-located with the potential turbulence features seen in the explicit fluxes. Thus, the concentration of horizontal and vertical advection to the TKE (Terms 1,2,3) is primarily aligned along the cloud boundary and overshooting top at and near the tropopause level. In a cross-sectional view cut through the Texas steady-state updraft, shown in Fig. 46-48, the effect of the diabatic heating on the lower and middle stratosphere is clear and more information about the potential turbulence generation is revealed. The maximum value of horizontal and vertical contributions for the first quasi-steady state updraft coincide with the maximum in diabatic heating, at 2245 UTC at a height of 10.5 kilometers. Term 1 and 2 contributions exceeding  $\pm 3 \times 10^{-2} \text{ m}^2\text{s}^{-3}$  arranged around the level of maximum heating, extending into the lower stratosphere to heights as high as 13.5 km (e.g. Fig. 46 and 47). The vertical advection of TKE, shown in Term 3, is an order of magnitude smaller than the horizontal terms and mostly negative around and

over the maximum in diabatic heating (e.g. Fig. 48). The most significant positive contribution from Term 3 occurs at the level of the overshooting top, where the isentropes bend into the stratosphere. The pattern in Term 3 suggests that the maximum value of TKE from the sub grid scale model calculation is located at the tropopause level based on the sign reversal within Term 3. In addition, a ribbon of TKE production via advection is noted along the leading edge of the gust front extending upward into the convection, indicating that horizontal and vertical gradients in sub grid TKE are present along the leading edge of the linear convective system. No other contribution to the TKE profile above  $\pm 2.5 \times 10^{-3} \text{ m}^2\text{s}^{-3}$  are seen in either the horizontal or vertical TKE advection terms. The patterns shown in Fig. 46-48 for the first steady-state updraft are identical to the explicit TKE profiles for the advection terms seen in the Louisiana steady-state updraft between 2315-0000 UTC 12-13 December. In the second overshooting top examined, the cell does not weaken through the end of the model simulation. However, distribution of the horizontal and vertical advection terms around the updraft is consistent with that of cross-sections made for the second steady-state updraft in Texas.

The horizontal and vertical advection terms shown in the cross-sections for both the Texas and Louisiana steady-state updrafts show that: (1) the overshooting top in the steady-state updrafts extend up to about 12 km, but produces gravity waves at and below 16 km; (2) the contribution of TKE from the sub grid scheme is restricted to the levels at or near the level of diabatic heating and overshooting top, and at lower levels, along the leading edge of the gust

front; (3) the TKE signal from the advection terms disappear as the gust front moves out away from the updraft and the convective cell dies. The signals seen in the advection terms are to be expected considering the model-derived TKE is used in the solution of the terms. Thus, one may wish to consider the maintenance of TKE along the edge of the cloud boundaries as a possible source of danger for aircraft flying near or around deep moist convection, as shown in observational reports in Detwiler and Heymsfield (1987) and Kaplan et al. (2004a). The results also suggest that the advection of TKE around convective cells may play a minor, yet non-negligible, role in the overall turbulence contribution, and the assumption of horizontal homogeneity may not necessarily be valid. The results are an extension of the hypothesis of Taylor (1938) that suggests horizontal homogeneity would be invalid in situations where the turbulence velocity is on the same order as the mean flow, which is noted in many of the flux contribution plots shown in Section 4.3. Though Terms 1-3 do not produce or destroy turbulence, the re-distribution of TKE in the lower and middle stratosphere around the periphery of deep moist convection in both the horizontal and vertical play a non-negligible role in altering the TKE profile critical to upper aviation turbulence forecasting.

#### *4.5.3.2: Explicitly Calculated Production Terms*

From authors such as Stull (1988) and Ayra (2001), the most important terms in turbulent kinetic energy contribution in the boundary layer are buoyancy and mechanical shear production terms, represented by Term 4: Buoyancy Production, Term 5: U-Mechanical Shear, and Term 5-2: V-Mechanical Shear. In

the upper troposphere and lower - middle stratosphere, the sharp increase in static stability accompanying the transition from the troposphere into the stratosphere and shear accompanying the decrease in overall mean wind speed near the tropopause suggest that these terms may also have a secondary maximum in this region. Thus, the buoyancy and mechanical shear production of potential CIT in the TKE tendency equation are investigated. The production terms are hypothesized to play the most important role in turbulence generation and also provide crucial information about the evolution of possible CIT in the stratosphere. Though the explicit turbulence calculations were performed for all of the fine-resolution simulations, a particular case investigation from the MASS667C simulation is presented with emphasis on the two periods of deep moist convection over Orange County, Texas (2230-2300 UTC) and Beauregard and Calcasieu Parish, Louisiana (2330-0000 UTC 12-13 December).

At levels near the tropopause (e.g., 8-10 km), the buoyancy production naturally mimics the patterns of heat-flux discussed in Section 4.3, outlining the v-shaped anvil and updraft feature near the Texas-Louisiana border between 2236-2254 UTC. The buoyancy production is around 1-2 orders of magnitude higher than the advection terms, with maximum values approaching  $1.6 \text{ m}^2\text{s}^{-3}$  at the updraft core and downstream in the v-shaped anvil. The buoyancy production is mostly positive except in very thin layers around the edge of the cloud boundary. As shown in Figure 49, a series of gravity waves, demarked by positive/negative/positive buoyancy production, spread rapidly upstream of the updraft core between 2230-2300 UTC. In the remainder of the domain, several

other wave-like features in the buoyancy production field are noted behind the linear convective system spreading northward, with distinct turbulence generation ranging from  $\pm 4 \times 10^{-1} \text{m}^2\text{s}^{-3}$ .

The production of TKE via u (v) mechanical shear, labeled as Term 5 (5-2) in the TKE tendency equation in Section 3, is calculated using 500-m deep second order finite-difference derivative approximations for the wind shear and explicit u and v-momentum fluxes. As seen in the buoyancy production term, TKE is also produced within gravity-wave like features in the lower stratosphere. Gradients in mechanical shear production, exceeding  $\pm 1.6 \times 10^{-1} \text{m}^2\text{s}^{-3}$ , occur frequently with the updraft and convectively-induced outflow (e.g. Fig. 50 (51)) all throughout the model domain. Near the updraft, the mechanical shear production of turbulence approaches  $1 \text{m}^2\text{s}^{-3}$ , which suggests that the mechanical shear production of CIT is on the same order of magnitude as the buoyant production. The overall magnitude of turbulence production via mechanical shear is highest in the v-mechanical shear term lower stratosphere, attributable to strong southerly flow (i.e., strong v component) behind the linear convective system where gravity waves are being produced by the convection.

As discussed in Section 3, the model TKE comes from a series of parameterizations of the turbulent fluxes, such as the u and v momentum flux, and is then fed into the general form of the TKE tendency equation. As shown in Eq. (3.5.3.1-3.5.3.2), the momentum fluxes are parameterized using the wind shear in the u and v components, respectively. The NHMASS model form of TKE, following Therry and Lacarrere (1983), then has the u and v-mechanical

shear production terms to be the square of the vertical wind shear (i.e.,  $(\frac{\partial u}{\partial z})^2, (\frac{\partial v}{\partial z})^2$ ). If the magnitude of the vertical wind shear is less than  $10^{-1} \text{ s}^{-1}$ , the value of mechanical shear production must also be less than  $(-K_M 10^{-1} \text{ s}^{-1})$ . In the explicit calculation algorithm, however, no such restriction on the mechanical shear production is made. The magnitude of the wind shear with respect to the horizontal components is, on average, about an order of magnitude smaller than the explicitly-derived momentum fluxes, with u and v wind shear in the lower stratosphere averaging around  $4 \times 10^{-2} \text{ s}^{-1}$ , except with locally higher maxima near the updraft. As seen in the flux plots in Section 4.4, the momentum flux is on the order of  $10^1 \text{ m}^2\text{s}^{-2}$ . Thus, the contribution to the TKE budget from the mechanical shear terms is controlled primarily by the use of the explicitly-derived momentum flux, which allows for the evolution of potential CIT features in the lower and middle stratosphere independent of the mean wind shear value.

Examining the steady state updrafts from a cross-sectional perspective, a significant amount of buoyantly-produced turbulence is apparent throughout the troposphere and lower stratosphere. Positive (negative) buoyancy production of turbulence is noted to line up with areas of strong rising (sinking) motion attributable to the sign of  $w'$ . In particular, strong positive buoyancy production brackets the area of maximum rising motion and level of maximum diabatic heating in east Southeast Texas around 2239-2245 UTC between 8-10 km. Just above the updraft, the overshooting top is noted by negative buoyancy production, where the parcel restoration effect caused by the presence of the stratosphere induces high values of negative  $w'$  and positive  $\theta_v'$ . In the lower

stratosphere, evidence of gravity waves are seen in the isentropes and buoyancy production field following the upward push of isentropes, mimicking the overshooting top (e.g. Fig. 52).

The production of CIT from the  $u(v)$  mechanical shear within the cross-sections is highest in the boundary layer along the eastward-propagating gust front. Mechanical shear production of turbulence is also bracketed around the maximum in diabatic heating (e.g. Fig. 53 (Fig. 54)), which is consistent with the buoyancy production fields. As noted in the plane view, the magnitude of the  $V$ -mechanical shear production is higher than the  $U$ -mechanical shear production and is on the same scale as the buoyancy production, i.e.,  $10^{-1} \text{ m}^2\text{s}^{-3}$ . A small pocket of negative  $v$ -mechanical shear production is noted above the overshooting top between 15-16 km in Texas (e.g. Fig. 53). The pocket of negative turbulence generation disappears as the convection weakens, while higher values of mechanical shear production remain along the leading edge of the gust front.

By 2300 UTC, the overshooting top is no longer visible in the cross-section and the gust front at lower-levels outraces the updraft core across east southeast Texas. The buoyancy production of turbulence in the upper troposphere and lower stratosphere ceases, and the pocket of negative  $v$ -mechanical shear production disappears in the middle stratosphere. After the convection is completely gone, however, one particular wave-like feature of interest remains present in the lower stratosphere. The feature, demarked by a train of positive and negative buoyancy and mechanical shear CIT production, is

noted along the eastern periphery v-shaped anvil of the steady-state updraft in Louisiana. The same feature is also present between 2300-2330 UTC in Beauregard Parish Louisiana in the 8-12 km layer in both plane and cross-sectional views. The wave-like feature is aligned in a northeast-to-southwest fashion with the mean flow ahead of the linear convective system, and is apparent as high as 14 km with buoyancy production of turbulence between  $\pm 6 \times 10^{-1} \text{m}^2 \text{s}^{-3}$  throughout the layer. The mechanical shear production terms suggest that a gradient in both u and v wind shear, on the order of  $6 \times 10^{-2} \text{s}^{-1}$ , is present in the 8-12 km layer, with the gradient vector reversing from east (west) in the u (v) mechanical shear terms (e.g. Fig. 55). Despite the gradient reversal, a wave-like couplet in mechanical shear production of turbulence occurs in both terms as the wave propagates eastward into Louisiana (e.g. Fig. 55). V-Mechanical shear production of turbulence approaches  $2 \times 10^{-1} \text{m}^2 \text{s}^{-3}$ , which is the same scale or production seen immediately over the convection in the prior analysis. Cross-sections of the next steady-state updraft across Beauregard Parish Louisiana between 2300-0000 UTC 12-13 December show the wave-like feature propagating through the lower stratosphere between 11-16 km in all three CIT production terms. Between 2321-2333 UTC, cross-sections through the linear convective system in southwestern Louisiana indicate: (1) an updraft core ahead of the main convective line is present and generates both positive and negative buoyancy and mechanical shear production around the updraft; (2) the gravity-wave feature generated by the previous convective cell in Orange County, Texas, remains in the lower stratosphere between 11-16 km with a distinct wave-

like couplet of CIT generation in both plane and cross-sectional view; (3) a significant updraft core develops when the leading edge of the convective system combines with the previous smaller updraft core ahead of the main line at 2330 UTC. The updraft core generates positive buoyancy production (e.g. Fig. 56) throughout the entire depth of the troposphere with the exception of the very top of the updraft, due to negative virtual potential temperature perturbations within the overshooting top. The convective tower generates gravity waves in the lower stratosphere responsible for both positive and negative buoyancy production bracketing the updraft and these gravity waves spread outward away from the overshooting top, very similar to the idealized results presented in Lane et al. (2003). As noted in the previous steady-state updraft, a pocket of negative  $v$ -mechanical shear (e.g. Fig 57) turbulence production occurs in the middle stratosphere between 15-16 km. As one approaches the end of the model simulation, the convection begins to decrease in intensity in the cross-section and the overshooting top is no longer present. Accordingly, the production of TKE via buoyancy and mechanical shear also deteriorates and by 2357 UTC is diminishing quite rapidly over the level of maximum diabatic heating. The aforementioned pocket of  $v$ -mechanical shear production immediately above the overshooting top also disappears, as noted in the Texas steady-state updraft an hour prior.

Higher up in the middle stratosphere, several instances of gravity wave signals with distinct wave-like potential CIT couplets, are present as high as 16 km for both of the steady-state updrafts. As seen in Section 4.3, the model

seems to generate smoother and broader areas of turbulence contribution from the fluxes that sum up to TKE on the order of  $10^{-2} \text{ m}^2\text{s}^{-2}$ . The explicit fields, however, generate wave-like structures in the buoyancy and mechanical shear production terms that have smaller spatial structures (e.g. Fig. 58), which one might expect is more realistic for gravity waves generated by convection in the middle stratosphere. The gravity waves appear upstream and one-to-two model output times after the overshooting tops, suggesting the gravity waves may be vertically propagating through the lower stratosphere. At heights of 18-20 km, the explicit buoyancy production fields are very similar to the divergence profiles discussed in Section 4.3, where very pronounced outward-propagating waves are shown coincident with the overshooting tops below. Above 16 km, the mean flow acquires a more westerly component, and thus, the u-mechanical shear term becomes the more important of the two shear production terms. The waves seen in the 18-20 km layer contribute potential turbulence on the order of  $\pm 6 \times 10^{-1} \text{ m}^2\text{s}^{-3}$ , which is quite significant for the middle stratosphere (e.g. Fig. 59). The model parameterized fields, on the other hand, have very little signal above 16 km and are not co-located with the outward divergence profiles seen in the explicit fields. The analysis of TKE contribution in the middle stratosphere (i.e., at or above 16 km) suggest that the model parameterized fields are much smaller in magnitude and do not follow the same pattern as the divergence and explicit buoyancy and mechanical shear production fields. Because the lone variable in the model parameterized fluxes is the magnitude of the shear (for the mechanical shear terms) and stability (for the buoyancy term), the results suggest that the

model-derived shear and stability estimations alone do not resolve the potential CIT features seen in the explicit grid-scale scheme in the absence of wave breaking within the model. Though the model parameterized scheme can identify the updraft and important upper atmospheric response to the overshooting top, the outflow-related gravity waves, particularly within the strong gradient in virtual potential temperature between the Texas and Louisiana updraft cores, are better resolved with the grid-explicit calculated diagnostics.

The two steady-state updrafts detailed in Texas and Louisiana on 12-13 December 2002 produce buoyancy and mechanical shear potential turbulence on the order of  $10^{-1}\text{m}^2\text{s}^{-3}$ , which is 1-2 orders of magnitude higher than the turbulence generation from the advection terms. The potential turbulence from the buoyancy and mechanical shear production terms in the explicit calculations are also an order of magnitude or more larger than the sub grid scale turbulence that is generated by the MASS model PBL scheme. Based on the structure and evolution of the potential turbulence fields from the explicit calculation versus the sub grid scale model parameterized fields, the explicit fields appear to provide more realistic gravity wave structure and subsequent potential CIT representation in the lower and middle stratosphere. The eastward-propagating gravity wave in the lower stratosphere is very well resolved in both the buoyancy and mechanical shear production fields, contributing the same scale of potential turbulence as seen within the convection that produced it. In addition, the gravity wave and convectively-induced divergence in the middle stratosphere are more realistic in the explicit scheme than in the parameterized scheme. The model-parameterized

scheme is unable to resolve the same potential CIT features seen in the explicit calculations due to the parameterizations of turbulent fluxes. The explicit calculations, on the other hand, benefit from grid-scale explicit fluxes which produce potential CIT from buoyancy and mechanical shear on the order of  $10^{-1} \text{ m}^2\text{s}^{-3}$ , which is quite substantial for the lower and middle stratosphere. The explicit calculation algorithm also resolves potential CIT features not directly present in the model scheme which could impact high-flying aircraft, such as the eastward-propagating gravity wave in the 11-14 km layer which occurs between the two steady-state updrafts.

#### *4.5.3.3: Turbulent Transport and Pressure Perturbation Contributions*

The advection terms discussed in Section 4.5.3.1 are viewed as the transport of pre-existing turbulence in the horizontal and vertical. In the same manner, the turbulent transport (Term 6) and pressure perturbation (Term 7) effect on the TKE profile is viewed as the vertical redistribution of turbulence via transport from turbulence itself and pressure correlations. The derivatives used in the explicit calculations are done over a 500-m depth, and the sub grid scale model-derived turbulence ( $\epsilon$ ) and pressure perturbation ( $p'$ ) are used in the calculation of the explicit turbulent transport (Term 6) and pressure perturbation (Term 7) respectively.

Horizontal plane and cross-sectional views of turbulent transport indicate that the term is an order of magnitude or more smaller than the production terms discussed in Section 4.5.3.2, and are about the same order of magnitude as the advection terms discussed in Section 4.5.3.1. Since the sub grid scale turbulence

is used in the calculation, the similarity to the advection terms is expected. The vertical gradients in turbulent transport ( $w'e'$ ) are also one to two orders of magnitude smaller than the gradient in mean wind or stability that was calculated in the production terms. The turbulent transport term is highest near the core of the updraft and then decreases as the waves generated by the convection spread downstream in the lower stratosphere (e.g. Fig. 60). The maximum turbulent transport contribution is around  $1.6 \times 10^{-2} \text{ m}^2\text{s}^{-3}$  at the updraft core between 8-10 km. Above 12 km, however, the turbulent transport term drops below  $10^{-2} \text{ m}^2\text{s}^{-3}$  throughout the lower and middle stratosphere except in very small pockets behind the linear convective system. The profile of turbulent transport is consistent with the model derived-TKE plots discussed in previous sections; since very little turbulence is being generated by the model scheme, small to negligible values of vertical gradients in turbulent flux are expected. Thus, one can conclude that the turbulent transport term would be largest where the perturbation vertical velocity and model-derived TKE are juxtaposed. As expected, the highest values of turbulent transport are located near and just below the tropopause within or immediately surrounding the deep moist convection.

Analysis of the pressure perturbation term (Term 7) from the explicit calculated scheme suggests that Term 7 is on the same order of magnitude as both the advection and turbulent transport terms. As described by Stull (1988), the pressure perturbation or “pressure correlation” term, like its counterparts on the  $10^{-2}$  scale, is a redistribution term. The pressure perturbation term contributes

to the TKE tendency in the same locations with respect to space and times as the production terms (Terms 4, 5, and 5-2) do, suggesting a strong dependence on  $w'$ . Unlike the turbulent transport term, a signal above 14 km is evident, albeit weak, in the pressure perturbation term. The maximum value of turbulence generation via pressure perturbations is  $2 \times 10^{-2} \text{ m}^2\text{s}^{-3}$  in the middle stratosphere collocated with the gravity wave features discussed in Section 4.5.3.2 (e.g. Fig. 60). The differences in profiles between the turbulent transport and pressure perturbation fields are important because the model scheme parameterizes them together. The results of the explicit scheme suggest that the turbulent transport and pressure perturbation terms may not necessarily follow the same distribution as one would expect based off of the parameterized results. However, to fully diagnose the utility of combining these two terms together, the explicit grid scale TKE derived from the velocity variances needs to be integrated forward as part of the model turbulence calculation. Due to complexities in re-programming the model PBL scheme and programs that calculate turbulence, this sensitivity test is not performed and is deferred to future work.

## **5. 9 December 1992 Mountain Wave Case Results**

### *5.1 9 December 1992 NH-MASS Simulation Introduction*

Following the methodology described in Section 3 and the convective case described in Section 4, the stratospheric version of the NH-MASS model simulated the 9 December 1992 mountain wave/stratospheric turbulence episode event using a one-way grid-nesting algorithm. The coarsest grid, as in the 12 December 2002 case, was 18 kilometers, initialized from the NARR Regional

Re-analysis dataset and ran continuously for 24 hours starting at 0000 UTC 9 December 1992 through 0000 UTC 10 December 1992 on a 100x100x90 grid structure. The 6 km grid, initialized and updated using the one-way grid nesting algorithm, is integrated for 18 hr from 0600 UTC 9 December to 0000 UTC 10 December 1992. The subsequent finer resolution grids, 2 km (hereafter, MASS2M), 667 m (MASS667M), and 222 m (MASS222M), are evaluated using the explicit grid turbulence diagnostics applied in Section 4 for the 12 December 2002 convective case. All of the NHMASS simulations diagnosed using the explicit grid turbulence diagnostics are centered on the location of the aircraft accident, discussed in Section 2, at 39.64 N, -105.58 W. Thus, the simulations evaluated in this section are focused on the location of a significant aviation danger from the observations.

As discussed in Clark et al. (2000) and Vollmer et al. (2006), the favorable juxtaposition of upper level divergence due to the interaction between a synoptic-scale jet streak and orographically-produced gravity waves in the Front Range of the Rockies are hypothesized to initiate an extreme aviation turbulence hazard within the 9-10 km layer on 9 December 1992. In particular, Clark et al. (2000) hypothesized that a “downburst” of turbulence, initiated from an unstable layer in the 11-12 km layer on 9 December 1992, was forced downward to the 9-10 km layer in large part due to the favorable jet streak/mountain wave interaction. Using the NHMASS model, Vollmer et al. (2006) revisited Clark et al. (2000)’s proposed mechanism by evaluating the 9 December 1992 event using higher vertical and horizontal resolution with specific interest on the unstable layer

above the accident level. In the coarse grid simulations, Vollmer et al. (2006) showed the propagating jet streak impinging on the terrain of Northern Colorado at 1500 UTC at 18 km. Based on the results from the finer grid simulations, discussed in terms of the explicit grid turbulence diagnostics herein, Vollmer et al. (2006) proposes a three-stage process for the formation of environment that contributed to the multiple aviation turbulence reports and the significant aviation accident on 9 December 1992. The evaluation of the explicit grid-based turbulence diagnostics for the 9 December 1992 case is provided in this manuscript to: (1) evaluate the sources and profiles of model-generated turbulence in the 9 December 1992 case; (2) determine the differences in turbulence profiles between the model parameterized and explicit-grid scale diagnostic calculations; (3) compare the explicit-grid based turbulence diagnostics to the convective case presented in Section 4.

#### *5.2 9 December 1992 MASS2M/MASS667M Explicit Turbulence Diagnostics*

Using the methodology outlined in Section 3 and following the same analysis techniques described for the 12 December 2002 case in Section 4, the 9 December 1992 fine grid simulations are subjected to the explicit-grid turbulence diagnostics. The 2-kilometer grid mesh (hereafter, MASS2M), was initialized at 1200 UTC 9 December 1992 on a 162x162x90 grid mesh and integrated for 12 hr through 0000 UTC 10 December 1992. Evaluation of the model TKE in the upper troposphere and lower stratosphere from MASS2M shows the model-derived TKE scheme develops turbulence exceeding  $18 \text{ m}^2\text{s}^{-2}$  in the 10-12 km layer in a banner originating across the higher terrain of Grand County that

spreads southeastward with the mean flow across Northern Clear Creek and Gilpin County, Colorado between 1400-1500 UTC 9 December 1992 (e.g. Fig. 61). Because this area is just upstream of the accident location, the flow-aligned TKE will be further diagnosed in the MASS667M and MASS222M simulations. In the 12-16 km layer, sporadic turbulence is found immediately on the lee side of the Front Range on the far eastern side of the MASS2M grid (e.g. Fig. 62). The TKE signals on the far eastern side of the grid appear rather splotchy and devoid of structure, making a complete analysis of their origin difficult. Despite the pulse nature of TKE maxima in the 14-16 km layer, general areas of TKE between 1-3  $\text{m}^2\text{s}^{-2}$  develop in both the lee of the Front Range and among the higher terrain of Grand County, Colorado. Above 16 km, very little signal in TKE is noted from the model scheme. The results suggest that the interaction of the mountain wave and impinging jet streak from the northwest is generating a turbulence signal in the lower and middle stratosphere. In addition, the model-generated TKE signal within the mountain wave case is stronger than the convective case. As will be demonstrated later, the overturning of several vertically propagating wave packets in the lower and middle stratosphere contribute to this higher TKE signal in the mountain wave case. The wavelengths of the disturbances in the mountain wave case appear large enough to generate turbulence from the parameterized fluxes. Since the MASS2M has a horizontal to vertical grid ratio much greater than 1, the explicit turbulence diagnostic scheme is not analyzed in significant detail and is deferred to the finer resolution simulations.

The MASS667M simulation was integrated on a 162x162x90 grid using the NHMASS model, initialized using the one-way grid nesting algorithm at 1400 UTC 9 December for 2 hr through 1600 UTC 9 December with 3-minute output. The MASS222M simulation, evaluated further in cross-sectional views later in the section, was initialized using the same grid structure at 1430 UTC and integrated for 1 hr through 1530 UTC on 9 December 1992 with 1 minute output. The configuration of start times was set in order to bracket the time of the accident (i.e., 1507 UTC) in the middle of the simulations. As with the outer coarse grids, MASS667C was set with the center of the grid at the accident location and did not employ the automatic grid nesting algorithm. Using an analysis technique developed for the convective case, direct comparisons between the model-parameterized fluxes and the explicitly-calculated fluxes were examined in horizontal plane views at vertical levels near and above the accident height (i.e., 9.75 km). Examination of the vertical levels above the accident level is crucial to Clark et al. (2000)'s hypothesis of a turbulent "downburst", that will be explored later.

As seen in the plots from the MASS2M run, the majority of TKE production from the model parameterized scheme is flow-aligned and originates from a terrain gradient between Gilpin and northern Clear Creek counties. The ribbon of elevated TKE values originates from a terrain gradient near the Gilpin/Clear Creek/Grand county borders in the MASS2M and MASS667M simulations. The terrain gradient develops significant flow-aligned negative u-momentum (e.g. Fig. 63), v-momentum (e.g. Fig. 64), and heat (e.g. Fig. 65) flux

contributions that remain quasi-steady and fixed in space and time in the 11-12 km layer, with the highest production coming from the v-momentum flux term (e.g. Fig. 64). The TKE-flux term generates the only positive flux, suggesting that the turbulent transport term in the model is moving to destroy turbulence in the lower stratosphere. Analyses of the terrain maps of Colorado (e.g. Fig. 66) reveal that the model parameterized fluxes are generating TKE over the higher terrain of Grand County, Colorado, and is then advected downstream via the mean flow across Clear Creek and Gilpin Counties. The explicit flux profiles, however, have a much different spatial distribution in the lower stratosphere. The u-momentum (e.g. Fig. 63), v-momentum (e.g. Fig. 64), and heat (e.g. Fig. 65) fluxes have both positive and negative contributions that are twice that of the model parameterized fields. The explicit fields are primarily negative over the higher terrain west of the Front Range, consistent with the TKE production in the model parameterized fields. The biggest difference between the two flux fields occur in the Front Range, across southern Boulder and central Jefferson County, Colorado. The steepest terrain gradient, oriented almost due north-south in this area of the Rockies, is located across Boulder and Jefferson Counties within the MASS667M grid. In the MASS667M, the virtual potential temperature contours are aligned with the terrain gradient across southern Boulder and central Jefferson counties throughout the simulation. Several small wave-like structures, which generate both positive and negative flux contributions, are visible along and east of the terrain gradient and attendant virtual potential temperature gradient across central Jefferson County at the 9-12 kilometer level. Some of the wave-like

features move quickly to the east, quasi-perpendicular to the flow, while others remain stationary along the terrain gradient in Jefferson County. The moving (stationary) wave-like features visible in the 9-12 km layer along and east of the Front Range are associated with the propagating (stationary) mountain wave/hydraulic jump modes, as discussed in Vollmer et al. (2006). The results suggest that the model TKE scheme exclusively resolves turbulence generated by the higher terrain to the west, while the explicit scheme is able to capture features associated with the terrain gradient along the Front Range at the levels near and above the accident location.

The spatial-Reynolds' averaging technique, discussed in both Sections 2 and 4, are employed on the model output from MASS667M and MASS222M for 9 December 1992. The calculation of the horizontal and vertical advection of TKE from Terms 1-3 (see Section 3 and Section 4) near the accident height (i.e. 9.75 km) represent the transport of the model-generated TKE on the grid-scale. The horizontal advection terms near the height of the accident (i.e. 9.75 km) in the MASS667M simulation show the production/destruction of turbulence emanating from point sources, which are likely individual model-resolved mountain peaks, across southwestern Grand and southeastern Boulder County Colorado throughout the model integration. The TKE production is oriented northwest to southeast with a distinct switch in orientation between the u and v advection terms. In Term 1 (Term 2), the TKE is being produced on the northern (southern) side of the banner, and is being destroyed on the southern (northern) side of the banner (e.g. Fig. 67). The magnitude of horizontal advection does approach  $10^{-1}$

$\text{m}^2\text{s}^{-3}$ , suggesting that the affect of horizontal advection on the TKE budget may not necessarily be negligible on small scales, as was found in the convective case in Section 4.

The major production terms, buoyancy (Term 4) and mechanical shear (Terms 5 and 5-2), are also examined in detail for the 9 December 1992 case. Below 9 km, very little positive or negative TKE budget contribution is noted from the three major production terms in both MASS667M and MASS222M. In the 9-11 km layer, the buoyancy (e.g. Fig. 68) and u (v) mechanical shear (e.g. Fig. 69,70) production term reveals negative buoyancy production on the  $10^{-1} \text{ m}^2\text{s}^{-3}$  scale along the higher terrain in southwest Grand County and along the Front Range terrain gradient in Central Jefferson County. The buoyancy and mechanical shear production terms also show that small-scale potential turbulence features are being produced in the same location where the model-generated TKE is highest across Grand County, propagating southeastward into Clear Creek and Gilpin Counties throughout the model integration. The value of the mean wind shear exceeds  $\pm 1.6 \times 10^{-2} \text{ s}^{-1}$  west of the Front Range in the banner, indicating that the magnitude of the mean wind shear in the 9-11 km layer is sufficiently high enough for significant turbulence production within the model-parameterized TKE scheme. In the lower stratosphere (i.e., 12-16 kilometer layer), the generation of TKE within the model scheme shifts to areas east of the Front Range, where several fast-moving distinct wave features are noted within all three production terms (e.g. Fig. 71), while TKE generation farther west across Grand County, in the higher terrain, remains quasi-stationary.

All three production terms show strong potential turbulence features along the edge of the Front Range, particularly near Interstate-70 in central Jefferson County, between 1430-1530 UTC 9 December 1992. Throughout the entire model integration, the three production terms appear to be on the  $1.5 \times 10^{-1}$  scale in the lower and middle stratosphere, indicating that the mechanical shear production of turbulence plays a more prominent role in the mountain case than the convective case. The V-mechanical shear term is actually highest in southern Jefferson County, where the potential turbulence is quasi-stationary, suggesting that the difference in flow-direction across this portion of the Front Range can alter the TKE budget profile. Above 16 km, the only signal from the explicit TKE budget calculations appears along I-70 in Central Jefferson County, coincident with the features at lower levels, in the U-Mechanical shear term. Cross-sections, which cut through the transient features noted in the 12-16 km layer in MASS667M, shown in Figure 72, reveal transient wave-like features responsible for both production and destruction of TKE in the explicit budget within a pronounced unstable layer located between 14-16 km. The unstable layer was noted in both Clark et al. (2000) and Vollmer et al. (2006) across the Front Range. While some TKE budget contributions are noted from turbulent transport (Term 6) and pressure perturbations (Term 7), the contributions were one to two orders of magnitude smaller than the other production terms. The pressure perturbation terms, however, are used to analyze the three-stage development process that is hypothesized to be responsible for the aviation accident on 9 December 1992 from Vollmer et al. (2006).

### 5.3 9 December 1992 MASS222M Explicit Turbulence Diagnostics

Analysis of the horizontal plane view of the explicit TKE budget terms in MASS222M reveal mostly quasi-stationary turbulence production in the grid associated with the higher terrain east of the Front Range and along the Palmer Divide. Since this information was already shown in MASS667M, the focus of the analysis shifted to the evolution of the TKE budget in the cross-sectional view. Cross-sections of each explicitly-calculated term were cut through the accident location, and revealed two distinct unstable layers, between 11-12.5 km and 15.5-17 km in MASS222M. The horizontal and vertical advection terms only produce signals near overturning isentropes (i.e. Fig. 73) within the unstable layers, indicating that the horizontal and vertical advection of TKE is important in episodes of potential wave breaking. The signal in the horizontal and vertical advection terms indicates that the model-derived TKE gradients are highest (1) near the surface topographic features and (2) where potential dynamic instability is present, i.e., areas of possible wave overturning. The three major production terms (e.g. Fig. 74-76) all reveal a distinct mountain-wave structure with hydraulic jump, similar to those shown in Lin and Wang (1996). Lin and Wang (1996), however, used an idealized study with an isolated two-dimensional mountain, and here, the topography is much more complex. Some similarity is shown to the mountain wave regime where  $l > k$  (Durran 1990, Lin 2007), where vertically propagating gravity waves occur above and just downstream of the orographic feature within the boundary layer. The buoyancy and mechanical shear terms have positive/negative couplets within the boundary layer near the terrain and

upward through 18 km over the individual terrain features. The largest areas of potential turbulence, as resolved from the explicit-grid based calculation, appear over the higher mountain peaks just below the two aforementioned unstable layers

East of the Front Range and across the Palmer Divide, an elevated region of turbulence generation is noted in the 10-11 kilometer layer over the lower elevations. In the boundary layer, particularly in the U-Mechanical shear term, the TKE budget appears to change and move more rapidly along the leading edge of the Front Range in the lee within the boundary layer and aloft (e.g. Fig. 75). The region in question has been determined from vertical velocity and potential temperature cross-sections (e.g. Fig. 77) to be the area of a developing hydraulic jump in the MASS222C simulation. The hydraulic jump becomes first established at 1438 UTC, and the faster-moving features noted in the isentropes and various TKE production terms respond to the propagating hydraulic jump mode in both the boundary layer and aloft between 1440-1515 UTC 9 December. During this time, small wave-like undulations are present in a cascade of downward momentum within the downslide wind portion of the jump (e.g. Fig. 77). At 1515 UTC, however, indications of wave-overturning at the 11.25 km level over the Palmer Divide leads to a quasi-steady state of TKE production below the wave overturning level and within the boundary layer most apparent in the U-Mechanical shear term. The shift in TKE budget profiles in the Palmer Divide between 1500-1530 UTC are attributed to a shift in hydraulic jump mode from the developing phase (1440-1515 UTC) to a quasi-stationary mode (1515-1530

UTC). The shift in hydraulic jump mode is also quite apparent in the vertical velocity fields (e.g. Fig. 76) and model-derived TKE in MASS667M (e.g. Fig. 78) from the same time periods shown in the explicit grid-based calculations. The TKE from the model grid-based scheme remains between 1-2  $\text{m}^2\text{s}^{-2}$  prior to 1515 UTC, and then approaches 4  $\text{m}^2\text{s}^{-2}$  at the 11-11.5 km layer after 1515 UTC (e.g. Fig. 77). The change in TKE production in the 11-12 km layer over the Palmer Divide was seen below the level of wave-overturning, suggesting the shift in hydraulic jump mode directly affects the TKE profile aloft. The results are similar to theoretical work by authors such as Clark and Peltier (1984) where idealized numerical modeling simulations suggested a resonant amplification mechanism generated severe downslope wind via resonance between upward and downward propagating waves between the surface and the wave-induced critical level aloft (e.g. Vollmer et al. 2006). The wave-like undulations noted in the analysis are hypothesized to be upward propagating waves within the downslope wind portion of the hydraulic jump, which then resonates to the critical level (i.e., 11-12 km) where wave breaking can occur. The model-generated turbulence occurs after wave breaking in the 11-12 km level, consistent with the TKE evolution within the explicitly-calculated diagnostics. The transition of the hydraulic jump into a quasi-steady state and subsequent intensification along the leading edge of the Front Range is consistent with the three-stage process in the development of severe downslope winds in Scinocca and Peltier (1993), where wave breaking aloft acted to intensify the downslope winds near the surface. The hydraulic jump establishment occurs near the time of the DC-9 cargo jet accident

(1509 UTC), though much farther east of the actual accident location. The results from the explicit-grid based calculations from the Palmer Divide area illustrate the utility of the explicit TKE diagnostics being used in conjunction with the model derived TKE in resolving important potential turbulence feature (i.e., the hydraulic jump) that could threaten aircraft flying near and around mountain wave regimes.

The 9 December 1992 mountain wave case explicit-grid TKE budget diagnostics produced potential turbulence that was, on average, one to two orders of magnitude smaller than the convective case in Section 4. As shown in the convective case, the dominant production term was buoyancy. In the mountain wave case, the production terms were on the same order of magnitude overall, with the U- mechanical shear term providing more signal in the middle stratosphere and in the cross-sectional analysis in MASS222M. The explicit grid based diagnostics from the mountain wave case were able to resolve both quasi-steady potential turbulence production from the mountain peaks and standing mountain waves, as well as rapidly evolving mountain-wave features, such as the hydraulic jump along the leading edge of the Front Range. The model parameterized TKE scheme produced smoother and slower evolving TKE features east of the Front Range, while the explicit grid-based calculations suggest the waves are more transient and evolve quicker. The model-parameterized scheme produces flow-aligned TKE banners from higher terrain across Grand County, Colorado in the MASS2M and MASS667M simulations that are also noted by the explicit calculation diagnostics. The flow-aligned TKE generated by the higher terrain across Grand County, Colorado appear to have

finer spatial detail in the model-derived calculations than the explicit grid diagnostics, suggesting some information may be lost between grid points in the diagnostic calculations. In MASS222M, the TKE in the vertical cross-sections from the model parameterized scheme were highest with overturning isentropes and the TKE generated from the establishment of a steady-state hydraulic jump regime, indicating the model's ability to accurately diagnose the presence of very fine-scale turbulence. The explicit grid-based diagnostics were able to handle both the standing and evolving mountain wave features throughout the entire atmosphere, appearing during and after the shift in mountain wave regime seen in the model-derived TKE. Therefore, the use of both the model-derived TKE and explicit-grid based turbulence diagnostics can aid in accurately forecasting areas of potential turbulence generation in highly-complex and high-resolution problems such as the 9 December 1992 mountain wave case.

## **6. Conclusions**

A detailed investigation of turbulence evolution in the upper troposphere and lower stratosphere are presented for two different modes of potential turbulent generation: deep moist convection and mountain wave regimes. Observations from radar, lidar, satellite, and aircraft pilot reports from both cases suggested that extreme turbulent motions which threaten high altitude flying aircraft were present in the upper troposphere and lower stratosphere. In the 12 December 2002 case, satellite data capable of sensing gravity waves in the upper atmosphere indicated that a significant amount of wave activity was present above and in the proximity of deep moist convection, which, upon

breaking, could produce aircraft-damaging turbulence. In the 9 December 1992 case, a DC-9 cargo plane lost an engine and part of a wing flying near the mountain waves produced in the lee of the Rocky Mountains.

Using a non-hydrostatic meso- $\beta$  model with a model lid extending well into the middle stratosphere, a comprehensive numerically-based investigation of the turbulence evolution in the upper atmosphere was performed. Using the finest model resolution, which approached LES-scale, explicit grid-based turbulence diagnostics examining the flux of momentum, heat, and turbulence were calculated and compared to the model parameterized fluxes generated by the PBL scheme. The explicitly-derived fluxes were then used to create diagnostic calculations of seven terms in the TKE budget equation. The diagnostic TKE budget calculations were expected to provide important information regarding the expected evolution of TKE and the processes contributing to the evolving turbulence profile.

The explicit grid-based turbulence diagnostics employed two different kinds of Reynolds' averaging techniques: temporal and spatial. Evaluation of the model parameterized fluxes using the temporal averaging technique revealed that a significant bias occurred in the flux calculations due to the switch in average value fields. Using a quasi-volume average technique, the spatially-derived turbulent fluxes provided more realistic evolution of potential turbulence features on the grid-resolvable scale than the temporally-derived fluxes for both cases.

In the 12 December 2002 case, comparisons between the spatially-derived turbulent fluxes and the parameterized versions generated by the model PBL scheme were analyzed with respect to two strong convective cells across within the model across southeast Texas and southwest Louisiana. The model-parameterized fluxes were highest in the upper troposphere coinciding with the actual model-resolved cloud features generated by the convection. Above the tropopause, very little signal in the model parameterized fluxes were found, and as such, the model-derived TKE remained below  $0.1 \text{ m}^2\text{s}^{-2}$ . The model parameterized scheme did detect the initial upper tropospheric and lower stratospheric response to the updraft cores, but failed to diagnose other important potential CIT features. In the explicit turbulent flux calculations, signal was present within the actual model-resolved cloud features, consistent with the parameterized version, and in vertically-propagating gravity waves lower and middle stratosphere. The explicit-flux calculations, coupled with the isentropic analysis, showed that convectively-induced gravity waves were present in the lower and middle stratosphere emanating from the convective updraft, and, in some cases, overshooting tops. The results are similar to the idealized modeling study of Lane et al. (2003), where gravity waves were shown several kilometers above the tropopause spreading out in all directions. Though the isentropic surfaces unambiguously showed the gravity wave features, the model parameterized momentum fluxes were unable to resolve the fine-scale structure and evolution of the lower stratospheric waves.

A diagnostic version of the TKE budget equation was then derived from the spatially-averaged momentum, heat, and turbulence fluxes. The vertical and horizontal advection of TKE, Terms 1-3 in the TKE budget, suggested that while the contribution to the overall TKE profile was small, the overall change to the TKE budget may be non-negligible, particularly around periphery of v-shaped anvils generated by the strongest convective updrafts. The three major production terms all revealed wave-like TKE generation within gradients in virtual potential temperature in the lower and middle stratosphere. Overall, the buoyancy production of TKE was highest in the upper atmosphere, around 2 orders of magnitude higher than any of the vertical or horizontal redistribution terms and 1 order of magnitude higher than the mechanical shear generation terms. Between the development of two deep convective updrafts, an eastward-propagating gravity wave was generated in the lower stratosphere along the edge of a v-shaped anvil from the first convective cell in southeast Texas. Horizontal plane and cross-sectional analysis revealed the wave propagating almost in phase with the surface outflow. The explicit TKE budget diagnostics resolved the feature well, while the model parameterized fluxes and subsequent TKE did not. The v-shaped anvil profile most often produced significant wave features in the lower stratosphere, and illustrates their importance to characterizing severe aviation hazards, furthering their importance suggested by Detwiler and Heymsfield (1987), Lin and Li (1988), and Kaplan et al. (2005a). In addition, the actual development of the V-shaped anvils was coincident with upstream

propagating gravity waves from the initial updraft source, similar to the idealized results and hypothesis discussed in Lin and Li (1988).

From the calculation of mechanical shear turbulence generation, it was noted that the values of mean wind shear in both the u and v direction were very small. Since the model parameterized fluxes are based off of the mean wind shear, it is hypothesized that the model-derived TKE calculation's inability to diagnose the features identified in the explicit budget are a result of the small mean wind shear. Though no instances of significant wave breaking occurred in the lower and middle stratosphere, the identification of the important features that could produce turbulence upon breaking is of interest to the Air Force project and the refinement of the automatic grid-nesting algorithm. The results in this study also further the observational case study analysis by Kaplan et al. (2005a), where the second most common report of aviation turbulence incidents occurred *around* the periphery of deep moist convection. Therefore, the identification of potential CIT generation could prove to be a vital addition to the forecasting of aviation turbulence using numerical models. The explicitly-derived TKE budget terms showed the ability to diagnose potential turbulence hazards within the 12 December 2002 case not readily apparent in the model-derived TKE calculations and should be implemented in the automatic grid nesting algorithm when the horizontal and vertical resolution approaches the LES scale.

In the 9 December 1992 mountain wave case, the interaction of a southeast-propagating polar jet streak and a sub-critical mountain wave regime produced significant turbulence in the Front Range of the Rockies. Using the

same numerical modeling technique described for the 12 December 2002 case, evaluation of the model parameterized fluxes and subsequent TKE evolution was shown to be strongly tied to the surface topography and aligned with the mean wind flow near the tropopause and within transient wave features in the Palmer Divide in the lower and middle stratosphere. The explicitly-calculated fluxes and subsequent TKE diagnostics revealed consistent patterns to the model parameterized scheme, but with more spatial detail. The explicit TKE budget diagnostics revealed that the three major production terms were of the same order of magnitude, suggesting that mechanical shear generation of turbulence played a more important role in the mountain wave case than the convective case. The model-parameterized fluxes and explicitly-calculated fluxes were remarkably similar due to the presence of higher mean wind shear, furthering the adage that the overall magnitude of the wind shear strongly controls the model-derived TKE. Cross-sectional analysis from the 222-meter 9 December 1992 case illustrated the ability of the explicit grid diagnostic's ability to resolve turbulence generated within vertically-propagating mountain wave regimes and an important shift in the hydraulic jump in the Front Range, coinciding with an increase in TKE production near the altitude of the DC-9 incident. The model-derived TKE, however, was highest within the boundary layer and in the location of wave breaking in the Front Range, and appeared limited in diagnosing the full range of motion and activity seen in the explicit calculations. As with the convective case, important information regarding the evolution of potential aviation hazards caused by turbulence was gained by employing the explicit grid-

based turbulence diagnostics. Though the TKE profile will be different from case-to-case, the use of the explicit grid-based turbulence diagnostics would be beneficial to identifying the fine-scale features and processes that lead to turbulence generation in the upper atmosphere.

## **7. Acknowledgements**

This research was supported by United States Air Force contract FA8718-04-C-0011. The author wishes to thank the following individuals for their contributions to this specific project: Committee members Dr. Michael Kaplan (University of Nevada), Dr. Yuh-Lang Lin (North Carolina State University), Dr. Sethu Raman (North Carolina State University), and Dr. Gary Lackmann (North Carolina State University). Special thanks are in order for Dr. S. Pal Ayra (North Carolina State University), Ken Waight (MESO, Inc.), and Dr. Michael Brennan (National Hurricane Center) for helpful comments and suggestions and various computing issues.

## 8. References

- Ayra, S. P., 2001: *Introduction to Micrometeorology*. Kuwler Academic Press, 307 pp.
- Bernard, A., D. Demaiffe, N. Mattielli, and R.S. Punongbayan, 1991: Anhydrite-bearing pumicese from Mount Pinatubo: Further evidence for the existnsnce of sulphur-rich magmas, *Nature*, **354**, 139-140.
- Clark, T. L., W. D. Hall, R. M. Kerr, D. Middleton, L. Radke, F. M. Ralph, P. J. Neiman, and D. Levinson, 2000: Origins of aircraft-damaging clear-air turbulence during the 1992 Colorado downslope windstorm: numerical simulations and comparison with observations. *J. Atmos. Sci.*, **57**, 1105-1131.
- ., and W. R. Peltier, 1984: Critical level reflection and the resonant growth of nonlinear mountain waves. *J. Atmos. Sci.*, **41**, 3122-3134.
- Detwiler, A. and A.J. Heymsfield, 1987: Air motion characteristics in the anvil of a severe thunderstorms during CCOPE. *J. Atmos. Sci.*, **44**, 1899-1911.
- Durrán, D. R., 1990: Mountain waves and downslope winds. *Atmospheric Processes over Complex Terrain*, Meteor. Monogr., No. 45, Amer. Meteor. Soc., 59-81.
- Eckermann, S. D. and D. L. Wu, 2005: Imaging gravity waves in lower Stratospheric AMSU-A radiances, part 1: Simple forward model. *Atmos. Chem. Phys.*, **0000**, 0001-17, 2005.
- , J. D. Doyle, J. F. Burris, T. J. McGee, C. A. Hostetler, L. Coy, B. N. Lawrence, A. Stephens, J. P. McCormack, and T. F. Hogan, 2005: Imaging gravity waves in lower stratospheric AMSU-A radiances, Part 2: Validation case study. *Meteor. Atmos. Phys.*, **0000**, 00001-21, 2005.
- Eichenbaum, H., 2003: Historical overview of turbulence accidents and case study analysis. MCR Federal, Inc. Rep. BR-M021/080-1, 82 pp.
- Ellrod, G.P. and D.I. Knapp, 1992: An objective clear-air turbulence forecasting technique: verification and operational use. *Wea. Forecasting*, **7**, 150-165.
- Hamilton, D.W., Y.-L. Lin, R. P. Weglarz, and M.K. Kaplan, 1998: Jetlet formation from diabatic forcing with applications to the 1994 Palm Sunday tornado outbreak. *Mon. Wea. Rev.*, **126**, 2061-2089.

- Leutbecher, M. and H. Volkert. 2000: The Propagation of Mountain Waves into the Stratosphere: Quantitative Evaluation of Three-Dimensional Simulations. *J. Atmos. Sci.*: **57**, 3090–3108.
- Kaplan, M.K., and R.A. Rozumalaski, R.P. Weglarz, Y.-L. Lin, S. Businger, and R.F. Gonski, 1995: Numerical simulations studies of the mesoscale environment conducive to the Raleigh tornado. NOAA Tech. Memo. NWS ER-90, 101 pp.
- , S.E. Koch, Y.-L. Lin, R. P. Weglarz, and R.A. Rozumalaski, 1997: Numerical simulations of a gravity wave event over CCOPE. Part 1: The role of geostrophic adjustment in mesoscale jetlet formation. *Mon. Wea. Rev.*, **125**, 1185-1211.
- , Y.-L. Lin, D.W. Hamilton, and R.A. Rozumalazki, 1998: The numerical simulation of an unbalanced jetlet and its role in the Palm Sunday 1994 tornado outbreak in Alabama and Georgia. *Mon. Wea. Rev.*, **126**, 2133-2165.
- and Y.-L Lin, J.J. Charney, K. D. Pfeiffer, D.B. Ensley, D. S. DeCroix and R. P. Weglarz. 2000: A Terminal Area PBL Prediction System at Dallas–Fort Worth and Its Application in Simulating Diurnal PBL Jets. *Bull. Amer. Meteor. Soc.*, 81, pp. 2179–2204.
- , K.M. Lux, J.D. Cetola, A.W. Huffman, A.J. Riordan, S.W. Slusser, Y.L. Lin, J.J. Charney, and K.T. Waight, 2004: Characterizing the severe turbulence environments associated with commercial aviation accidents. A Real-Time Turbulence Model (RTTM) designed for the operational prediction of hazardous turbulence environments. NASA/CR2004-213025.
- , A. W. Huffman, K. M. Lux, J. D. Cetola, J. J. Charney, A. J. Riordan, and Y.-L. Lin 2005a: Characterizing the severe turbulence environments associated with commercial aviation accidents. Part 1: A 44-case study synoptic observational analyses. *Meteor. Atmos. Phys.*, **88** 129-152.
- , A. W. Huffman, K. M. Lux, J. D. Cetola, J. J. Charney, A. J. Riordan, Y.-L. Lin, and K. T. Waight, 2005b: Characterizing the severe turbulence environments associated with commercial aviation accidents. Part II: Hydrostatic mesobeta scale numerical simulations of supergradient wind flow and streamwise ageostrophic frontogenesis. *Meteor. Atmos. Phys.*, **88** 153-173.
- , Y.-L. Lin, M.T. Kiefer, C.J. Ringley, P.S. Suffern, 2005c: The development of a stratospheric real-time turbulence modeling system. Submitted to AFRL, 7 July 2005. AFRL-VS-HA-TR-2005-1121, 87 pp.
- , Y.L. Lin, C.J. Ringley, Z.G. Brown, P.S. Suffern, M.T. Kiefer, and A.M. Hoggarth, 2006: Wake vortex simulations form a Terminal Area PBL Prediction System (TAPPS). Preprints, *44<sup>th</sup> Aerospace Sciences Meeting*

- and Exhibit*. Reno, NV, AIAA paper 06-0174. American Institute of Aeronautics and Astronautics, 26 pp.
- Kiefer, M.T., 2005: The Impact of Superimposed Synoptic to Meso-Gamma Scale Motions on Extreme Snowfall over western Maryland and northeast West Virginia during the 2003 President's Day winter storm. MS thesis, Dept. of Marine, Earth, and Atmospheric Sciences, North Carolina State University, 204 pp.
- Koch, S.E., D.W. Hamilton, D. Kramer, and A. Langmaid, 1998: Mesoscale dynamics in the Palm Sunday tornado outbreak. *Mon. Wea. Rev.*, **126**, 2031-2060.
- , B. D. Jamison, C. Lu, T.L. Smith, E. I. Tollerud, C. Girz, N. Wang, T. P. Lane, M. A. Shapiro, D. D. Parrish, and O. R. Cooper, 2005: Turbulence and gravity waves within an upper-level front. *J. Atmos. Sci.*, **62**, 3885-3908.
- Lane, T. P., and M.J. Reeder, 2001: Convectively generated and their effects on the cloud environment. *J. Atmos. Sci.*, **58**, 2427-2440.
- , R. D. Sharman, T. L. Clark, and H. M. Hsu, 2003: An investigation of turbulence generation mechanisms above deep convection. *J. Atmos. Sci.*, **60**, 1297-1321.
- , J.C. Kneivel, 2005: Some effects of model resolution on simulated gravity waves generated by deep, mesoscale convection. *J. Atmos. Sci.*, **62**, 3408-3419.
- Lilly, D.K., and P.F. Lester, 1974: Waves and turbulence in the stratosphere. *J. Atmos. Sci.*, **30**, 800-812.
- , and P.J. Kennedy, 1974: Observations of a stationary mountain wave and its associated momentum flux and energy dissipation. *J. Atmos. Sci.*, **30**, 1135-1152.
- Lin, Y. L., R. D. Farley, and H.D. Orville, 1983: Bulk parameterization of the snow field in a cloud model. *J. Climate Appl. Meteor.*, **22**, 1065-1092.
- , and S. Li, 1988: Three-dimensional response of a shear flow to elevated heating. *J. Atmos. Sci.*, **45**, 2987-3002.
- , and T.-A. Wang, 1996: Flow regimes and transient dynamics of two-dimensional stratified flow over an isolated mountain ridge. *J. Atmos. Sci.*, **53**, 139-158.
- , 2007: *Mesoscale Dynamics*. Cambridge University Press (In Press), TBD pp.

- Marroquin, A., 1998: An advanced algorithm to diagnose atmospheric turbulence using numerical model output. Preprints, *16<sup>th</sup> AMS Conference on Weather Analysis and Forecasting*, Amer. Met. Soc., 11-16 January, 2 pp.
- Post, M.J., A. Weickmann, K.R. Healy, R.J. Willis, and C. Grund, 1996: Comparison of Mount Pinatubo and El Chichon volcanic events: Lidar observations at 10.6 and 0.69 microns. *J. Geophys. Res.*, **101**, 3929-3940.
- Ralph, F. M., P. J. Neiman, and D. Levinson, 1997: Lidar observations of a breaking mountain wave associated with extreme turbulence. *Geophys. Res. Lett.*, **24**, 663-666.
- Ringley, C. J., and M.L. Kaplan, Y-L. Lin, P.S. Suffern, 2005: An investigation of turbulent processes in the lower stratosphere. *11<sup>th</sup> Conference on Mesoscale Processes*, Albuquerque, NM, Amer. Meteor. Soc., P3M.2, 6 pp.
- Scinocca, J. F. and W. R. Peltier, 1993: The instability of Long's stationary solution and the evolution toward severe downslope windstorm flow. Part I: Nested gridnumerical simulations. *J. Atmos. Sci.*, **50**, 2245-2263.
- Sharman, R.C., C. Tebaldi, and B. Brown 1999: An integrated approach to clear-air turbulence forecasting. Preprints, *8<sup>th</sup> Conf. on Aviation, Range, and Aerospace Meteorology*. Dallas, TX, Amer. Meteor. Soc., 68-71.
- , G. Weiner and B. Brown, 2000: Description and integration of the NCAR integrated turbulence forecasting algorithm. Preprints, *40<sup>th</sup> Aerospace Sciences Meeting and Exhibit*, Reno, NV, AIAA Paper 00-0493, American Institute of Aeronautics and Astronautics.
- , C. Tebaldi, and B. Brown, 2002: Results from the NCAR Integrated Turbulence Forecasting Algorithm (ITFA) for predicting upper level clear-air turbulence. Preprints, *10<sup>th</sup> Conf. on Aviation, Range, and Aerospace Meteorology*. Portland, OR, Amer. Meteor. Soc., 351-354.
- , -----, G. Weiner, and J. Wolff, 2006: An integrated approach to mid-and-upper level turbulence forecasting. *Wea. Forecasting*, **21**, 268-287.
- Stull, Roland B., 1988: *An Introduction to Boundary Layer Meteorology*. Kulwer Academic Press: 639 pp.
- Suffern, P.S., M.L. Kaplan, and Y-L. Lin, 2005: Numerical simulations of vertically propagating gravity waves in the stratosphere above a hydrostatic large amplitude surface gravity wave on December 12<sup>th</sup>, 2002. *11<sup>th</sup> Conference on Mesoscale Processes*, Albuquerque, NM, Amer. Meteor. Soc., 5 pp.

- , 2006: Interactions of gravity waves and moist convection in the troposphere and stratosphere. MS thesis, Dept. of Marine, Earth, and Atmospheric Sciences, North Carolina State University, 280 pp.
- Therry, G., and P. Lacarrere, 1983: Improving the eddy kinetic energy model for the planetary boundary layer. *Bound.-Layer Meteor.*, **25**, 63–88.
- Uccellini, L.W., and S.E. Koch, 1987: The synoptic setting and possible energy sources for mesoscale wave disturbances. *Mon. Wea. Rev.*, **116**, 2545-2569.
- Vollmer, David R. and Y-L Lin, M. Kaplan. 2006: Investigating the evolution of mountain-induced turbulence along the Colorado Rockies on 9 December 1992. Submitted to: *J. Atmos. Sci.*, 45 pp.
- Yamada, Tetsuji and George Mellor. 1975: A Simulation of the Wangara Atmospheric Boundary Layer Data. *J. Atmos. Sci.*, **32**, 2309–2329.
- Zhang, F., 2004: Generation of mesoscale gravity waves in upper-tropospheric jet-front systems. *J. Atmos. Sci.*, **131**, 845-861.

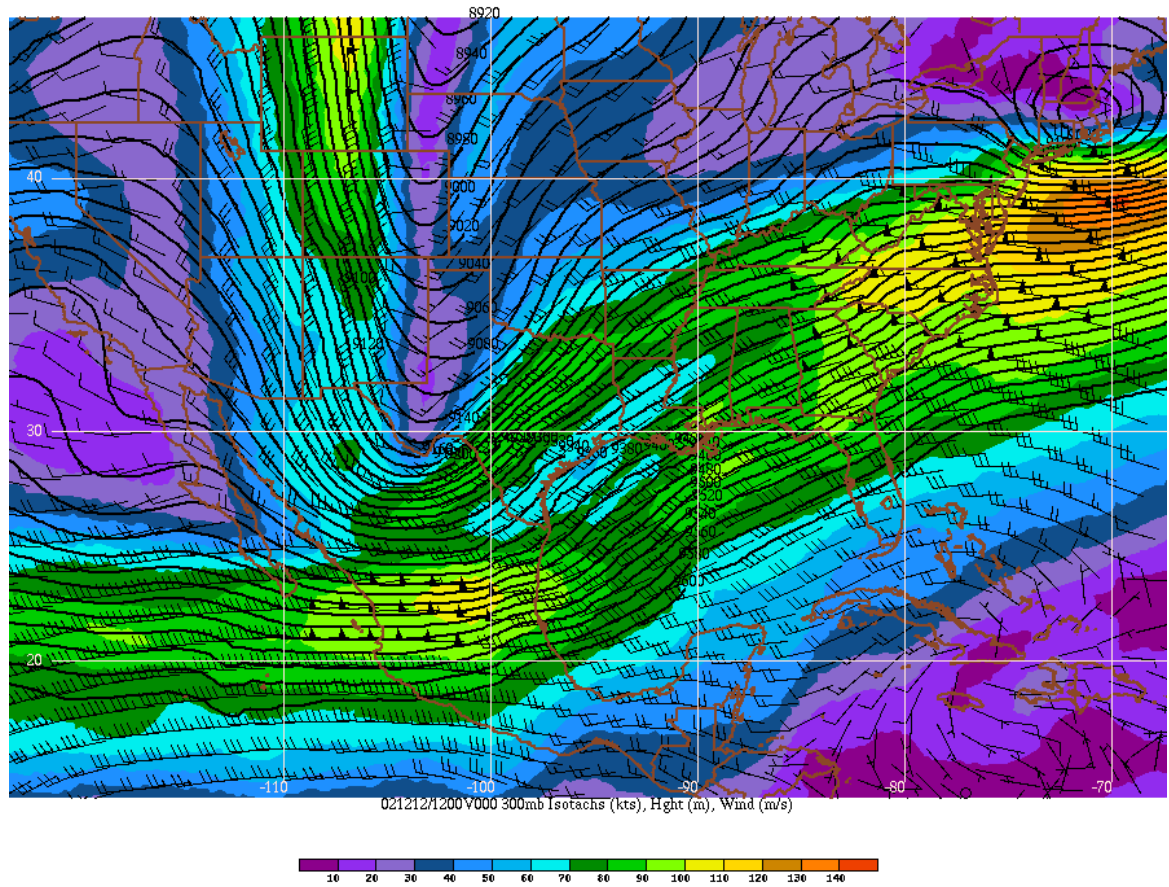


Figure 1: NARR Reanalysis valid 1200 UTC 12 December 2002: 300 h-Pa wind (m/s), isotachs (colored) and height (m). State outlines in dark red, with the region of interest in far Southeast Texas and Southwest Louisiana.

▼ Plymouth State Weather Center ▼

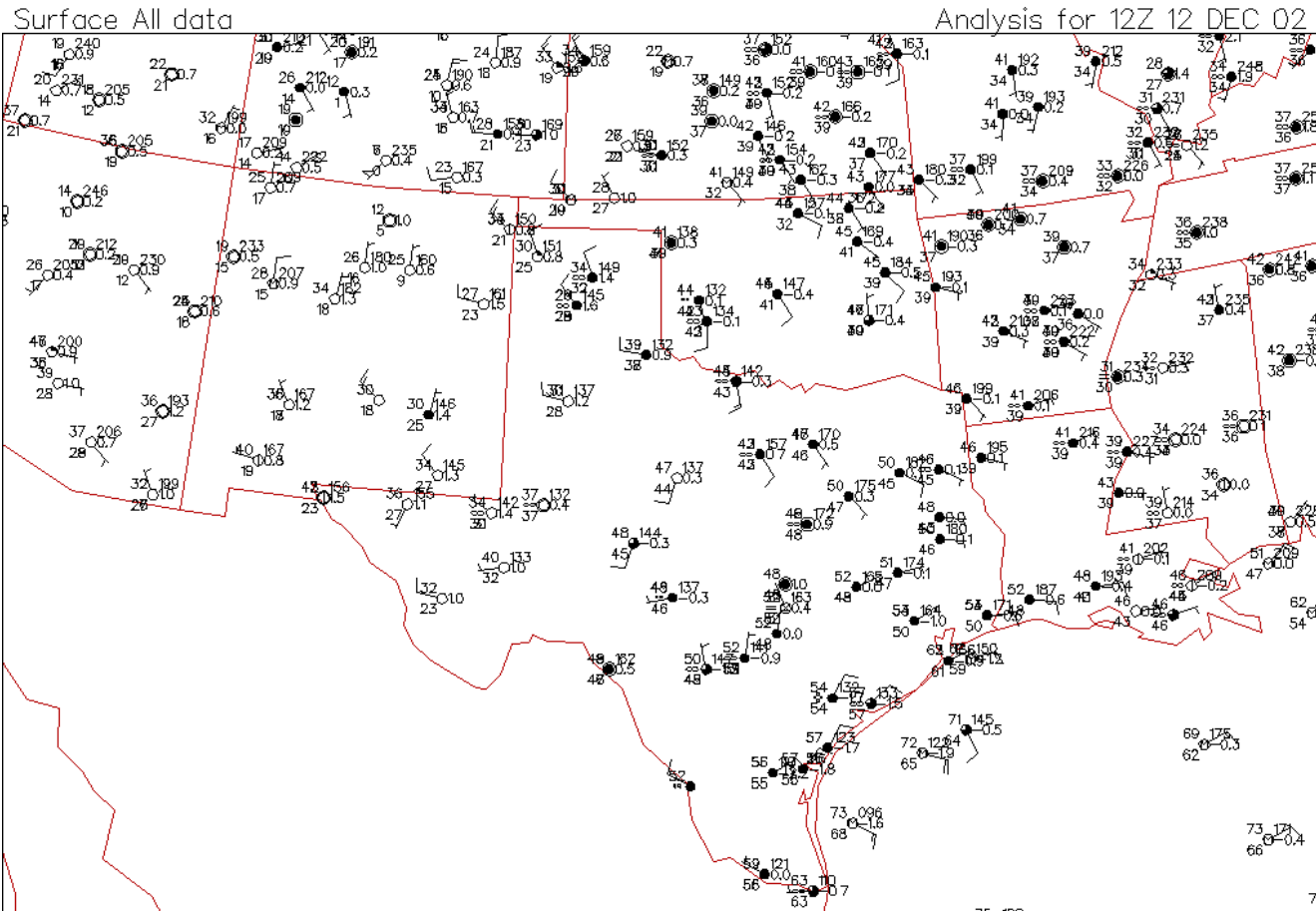


Figure 2: Plymouth State Weather Center archived standard surface data plot valid 1200 UTC 12 December 2002 in the Southern Plains. The strong stable layer north of the warm front is noted along the Texas Coast.

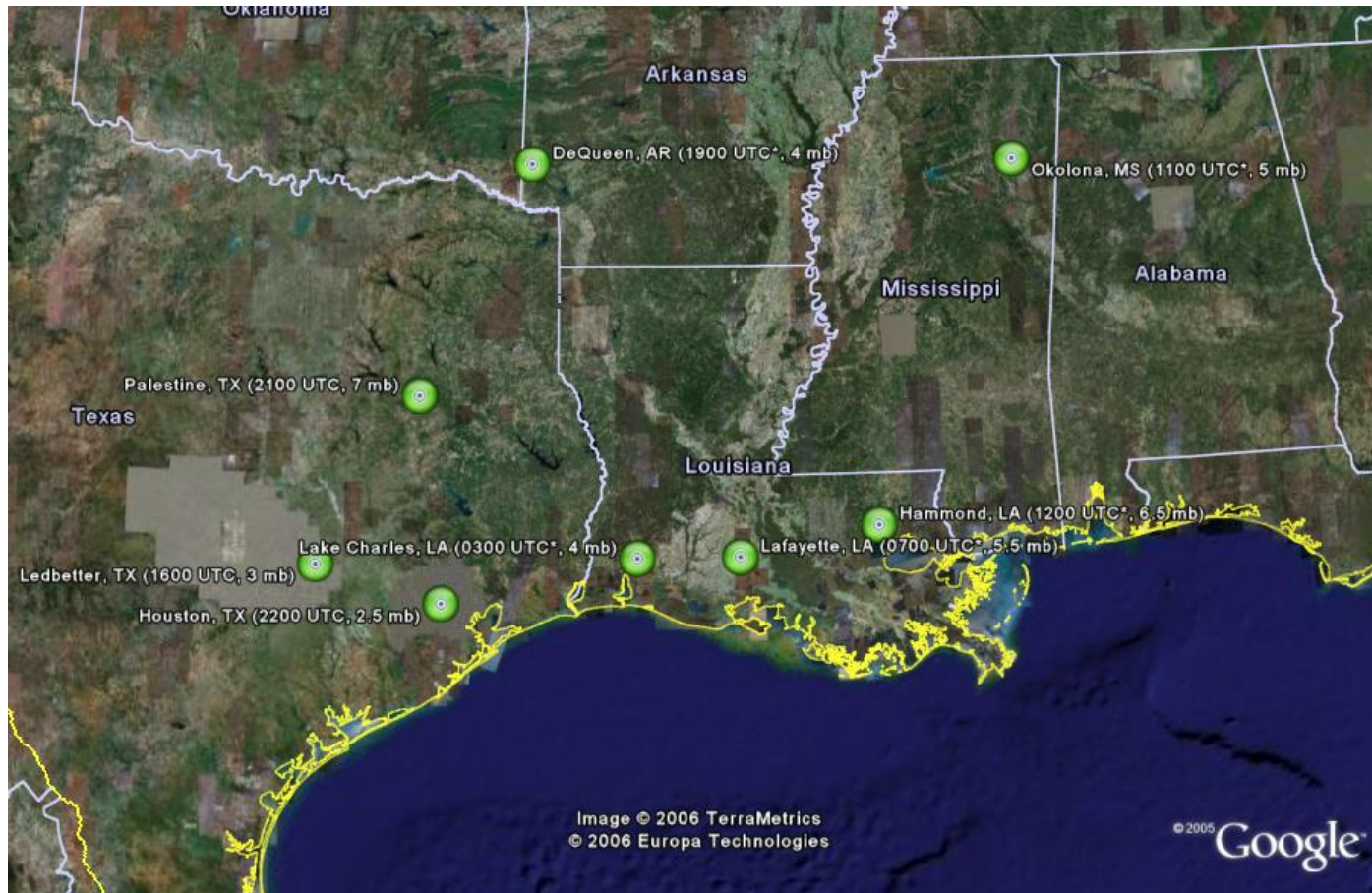
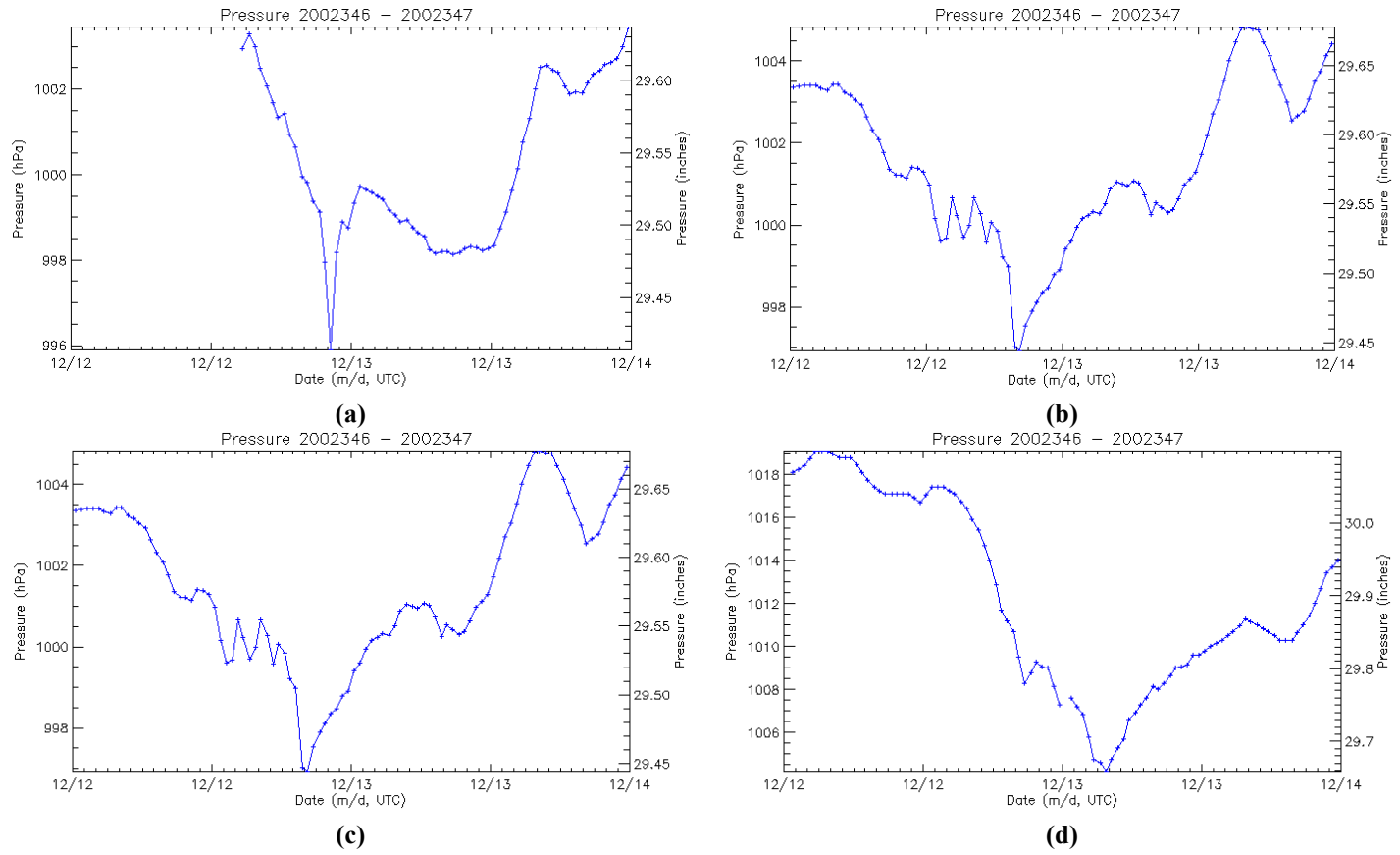
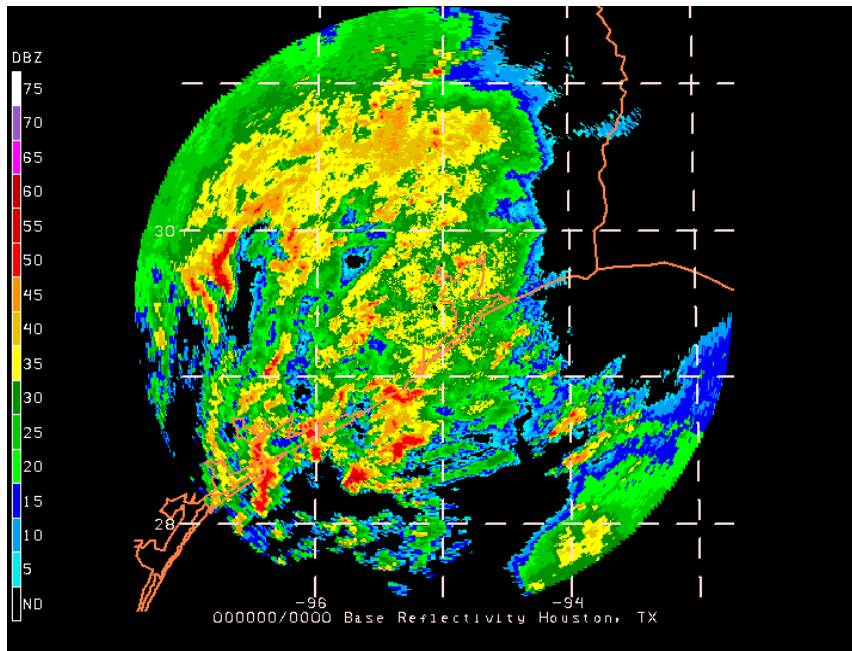


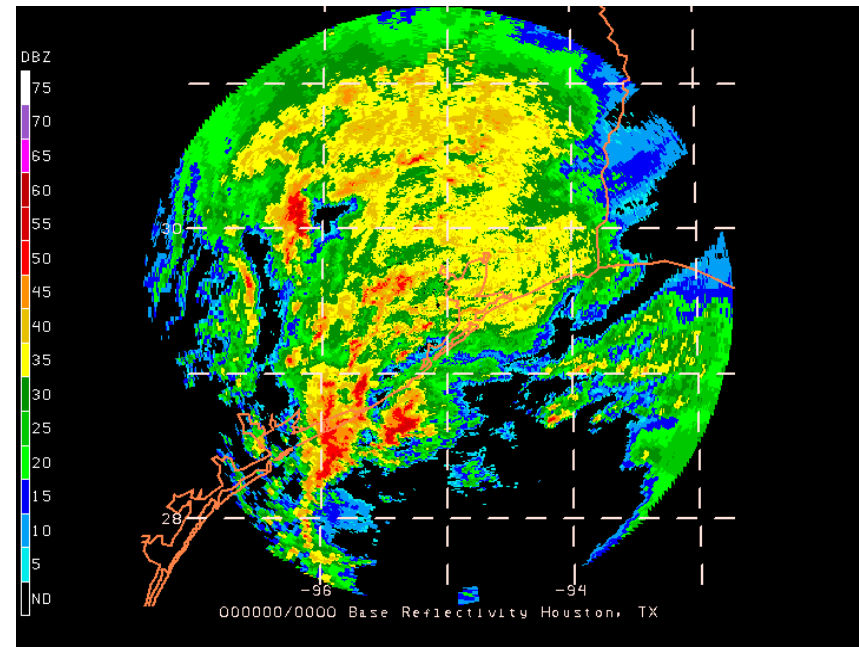
Figure 3: Google Earth composite plot of GPS microbarogram maximum 6-hr pressure falls associated with the large amplitude gravity wave 1200-1900 UTC 12-13 December 2002. Times marked with a \* indicated observations ending on 13 December 2002.



**Figure 4: Four-panel plot of GPS microbarogram traces of pressure vs. time following gravity wave features valid 12 UTC-12 UTC 12-14 December 2002 from (a) Houston (HOU), TX; (b) Ledbetter (LED), TX; (c) Palestine (PAL), TX; and (d) Lafayette (LAF), LA.**



(a)



(b)

Figure 5: NOAA NWS Level-III Base Reflectivity radar data from Houston, TX valid (a) 1603 UTC (b) 1703 UTC 12 December 2002.

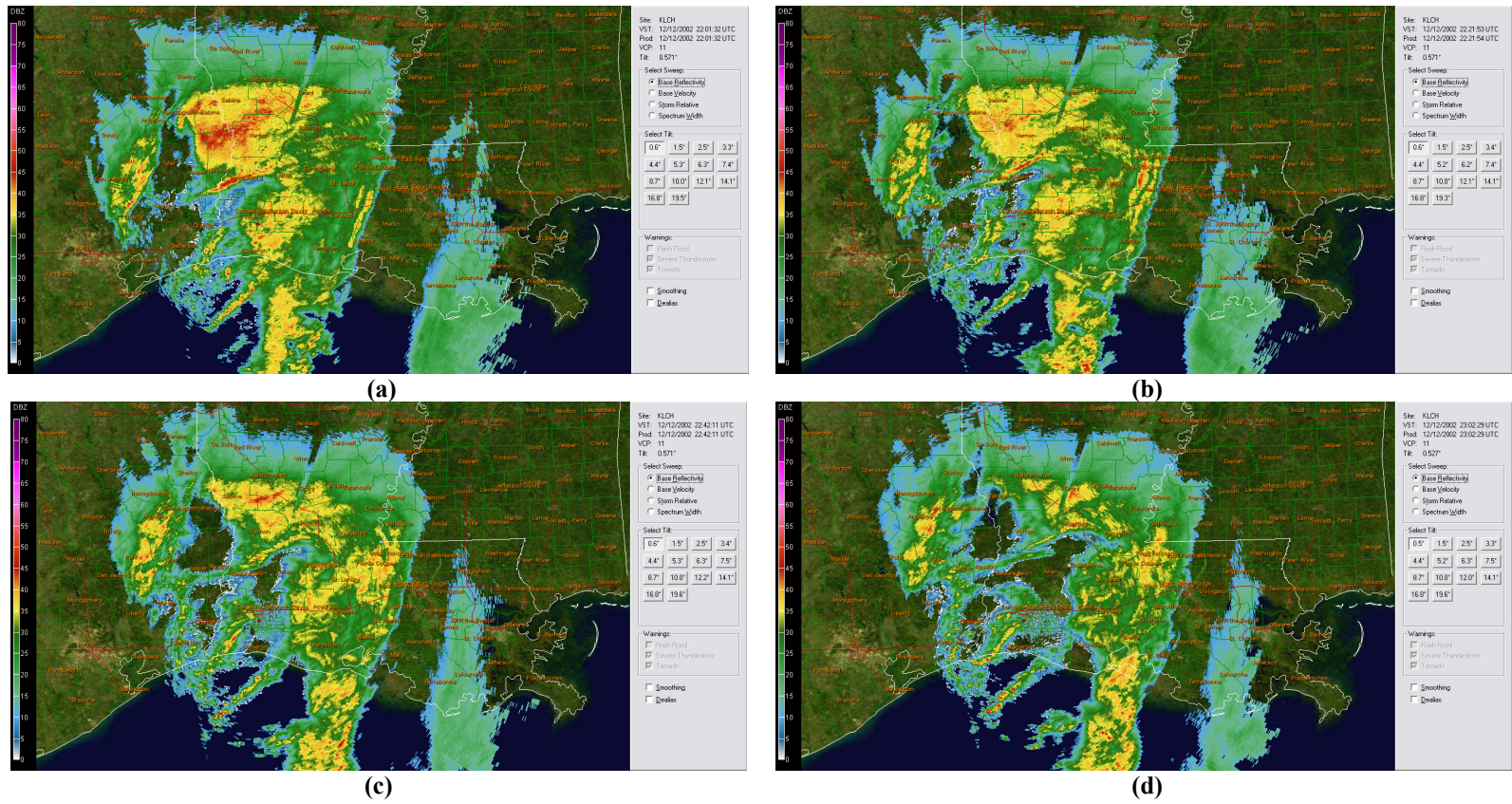
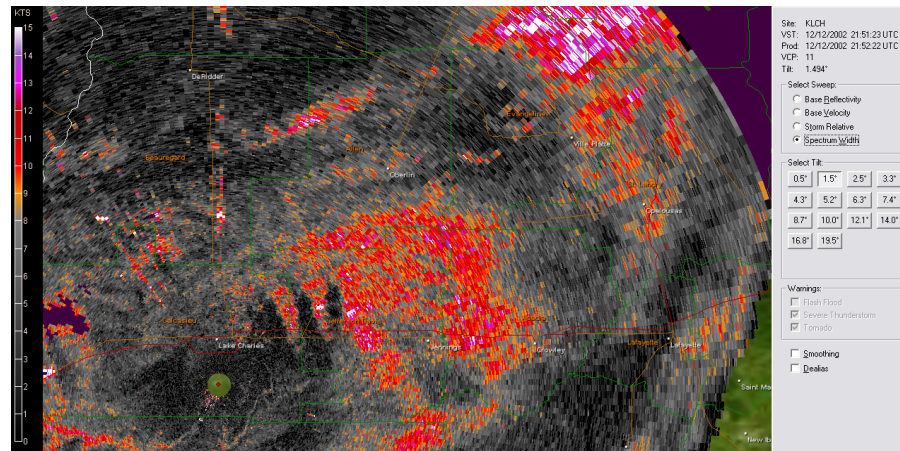
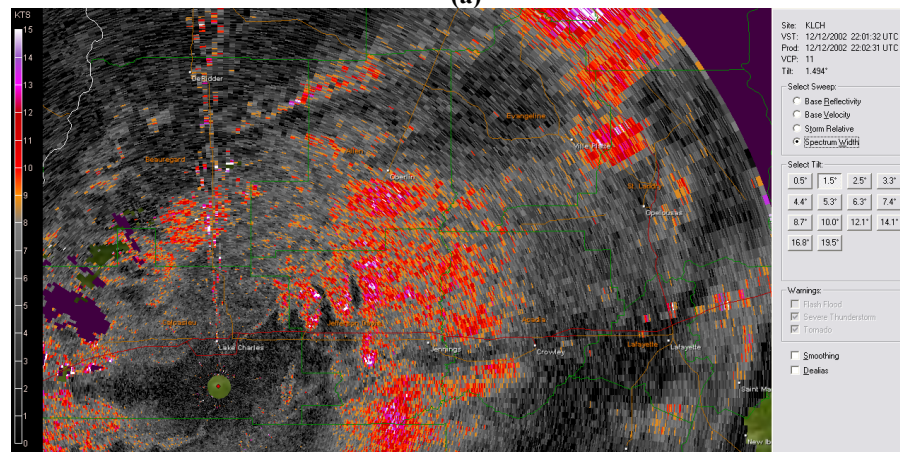


**Figure 6: Four-panel plot of NOAA NWS Level-II Base Reflectivity from Lake Charles, LA (LCH) valid at (a) 2201 UTC; (b) 2220 UTC; (c) 2242 UTC; (d) 2302 UTC, showing the erosion of precipitation north and south of the warm front behind the primary squall line.**

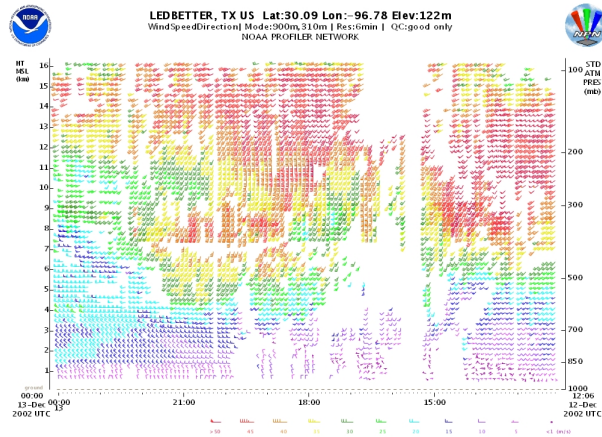


(a)

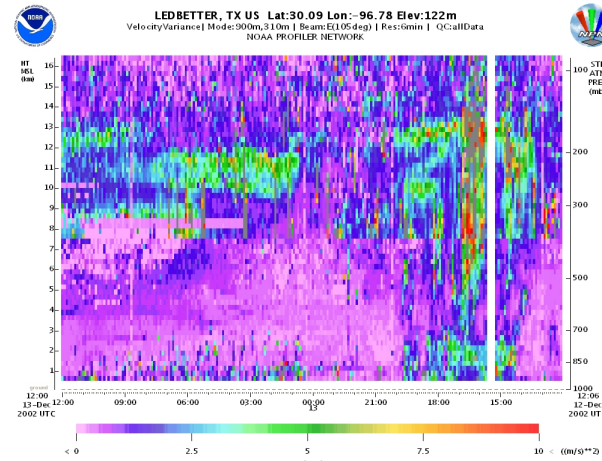


(b)

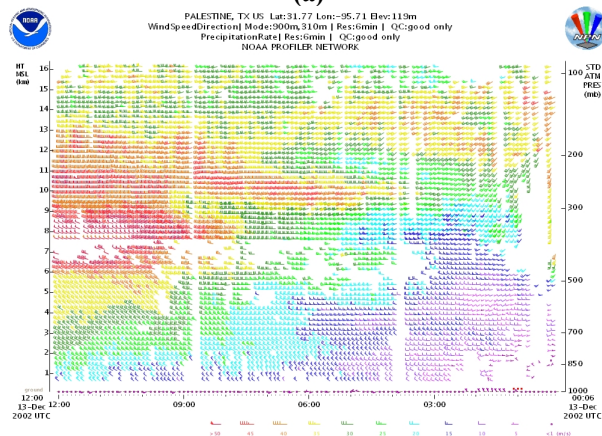
**Figure 7: NOAA NWS Level-II Tilt-2 Spectrum Width (velocity variance) from Lake Charles, LA (LCH) radar valid (a) 2151 UTC; (b) 2201 UTC 12 December 2002. The gravity wave signal is south of the warm frontal boundary and northwest of the radar location.**



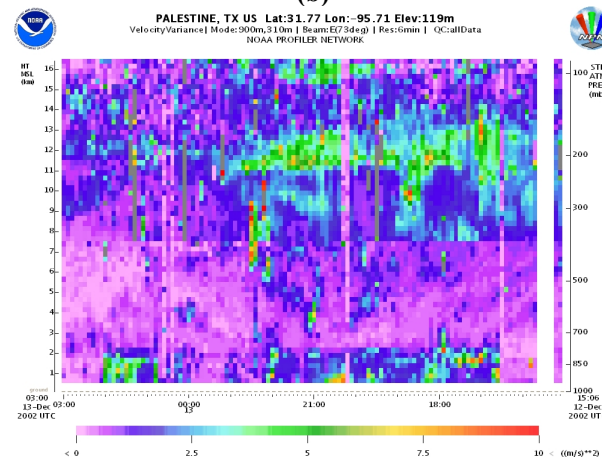
(a)



(b)

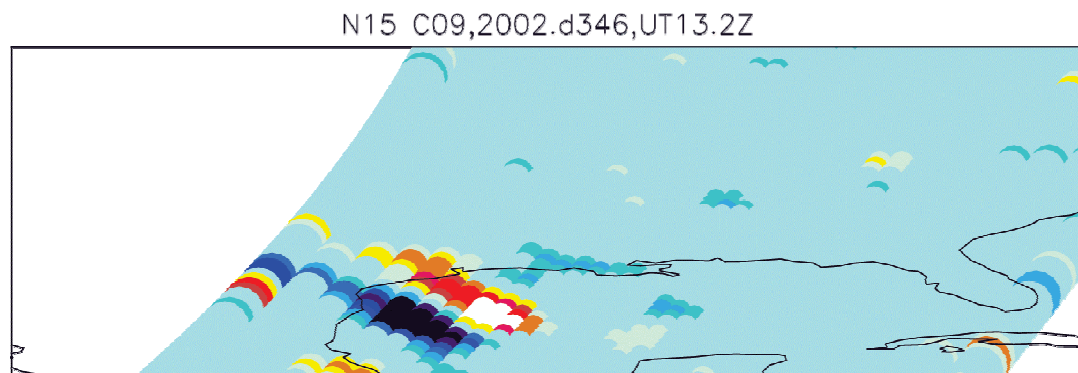


(c)

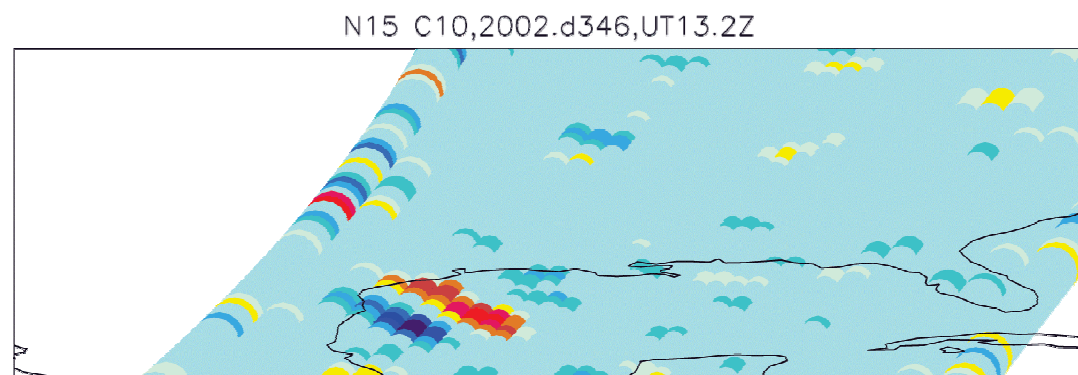


(d)

Figure 8: Four-panel plot of NOAA FSL Profiler data from 12-13 December 2002 from (a) vertical wind profile from PAL; (b) horizontal velocity variance from PAL; (c) as with (a), but for LED; (d) as with (b), but for LED. Time positioned from right to left..

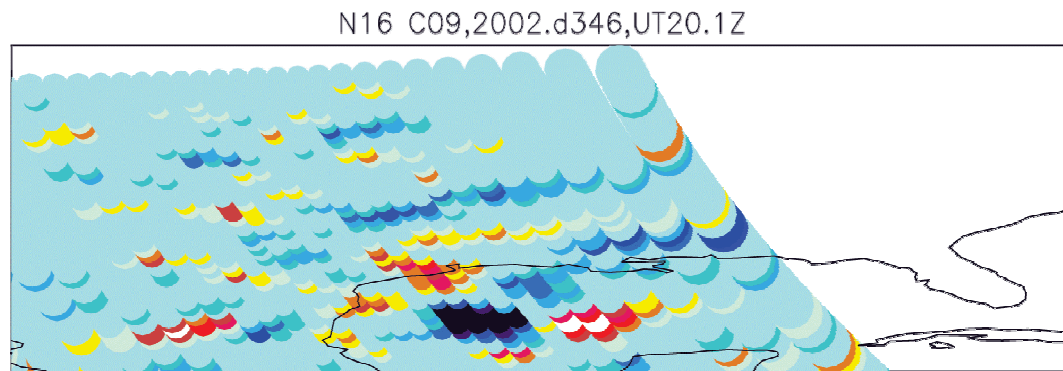


(a)

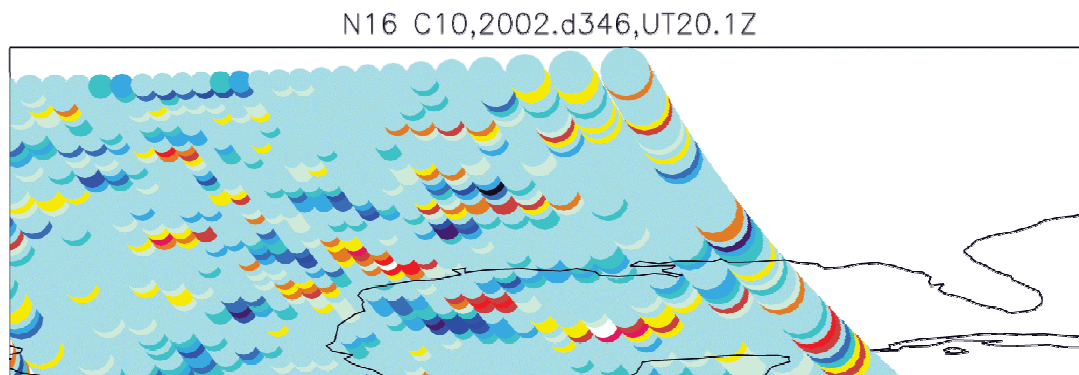


(b)

**Figure 9: AMSU satellite data plots of virtual potential temperature fluctuations valid ~13 UTC 12 December 2002 for (a) Channel 9 (~90 hPa) and (b) Channel 10 (~60 hPa).**



(a)



(b)

Figure 10: As with Fig. 9, but for ~20 UTC in (a) Channel 9 (~90 hPa) and (b) Channel 10 (~60 hPa).

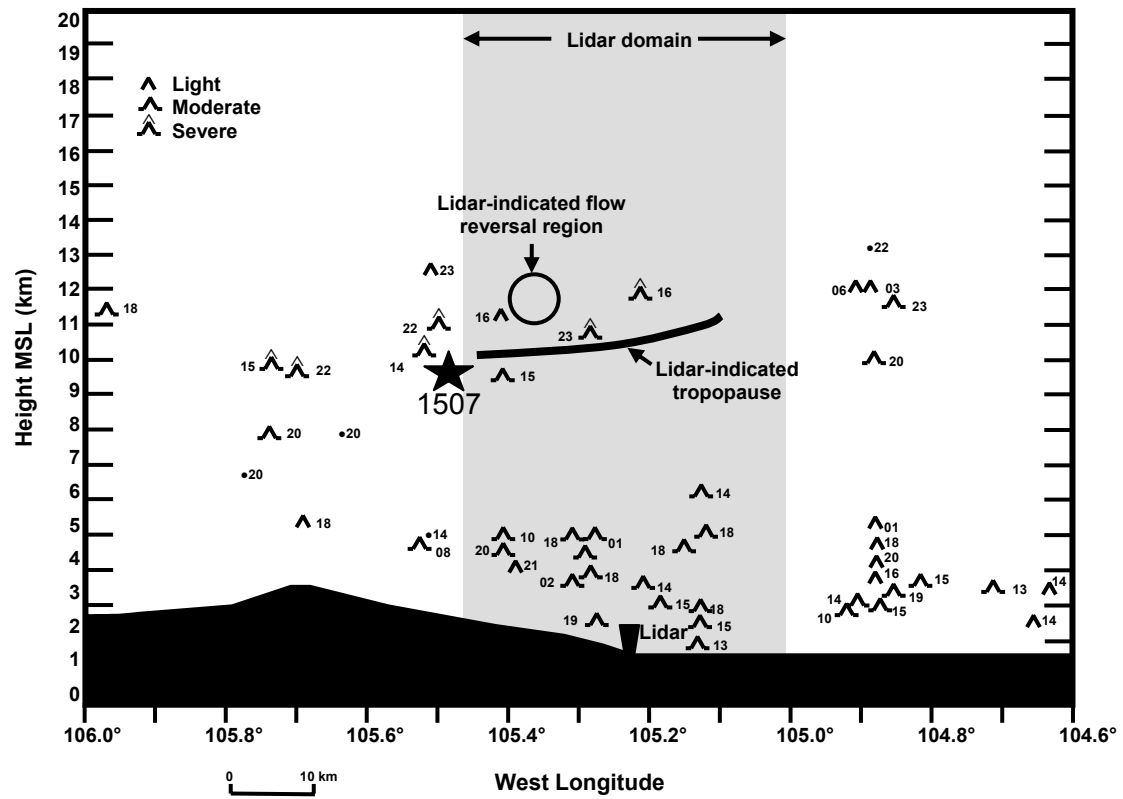
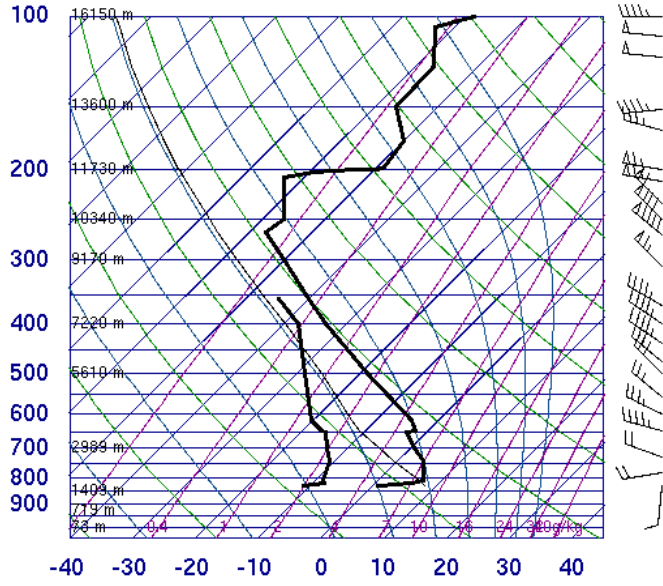


Figure 11: Adapted from Clark et al. (2000), a cross-section through the accident location (indicated by the time and star) of pilot reports of turbulence, lidar position, and lidar-indicated flow reversal region, tropopause and surface topography from 9 December 1992 (Vollmer et al. (2006).

72469 DNR Denver

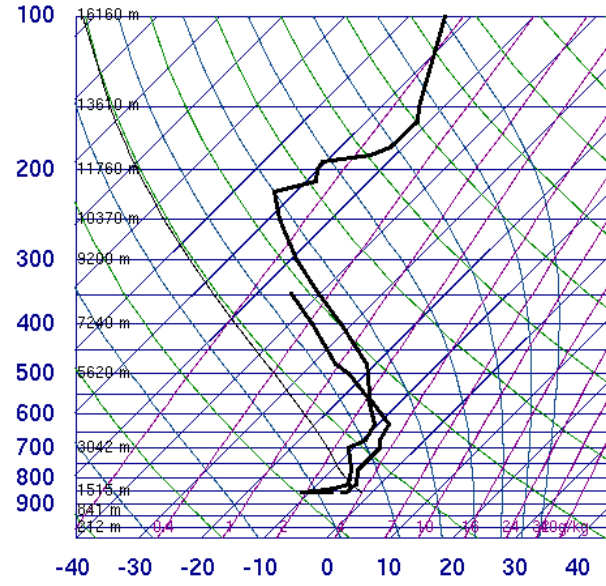


SLAT 39.75  
 SLON -104.  
 SELV 1625.  
 SHOW -9999  
 LIFT 7.34  
 LFTV 7.31  
 SWET -9999  
 KINX -9999  
 CTOT -9999  
 VTOT -9999  
 TOTL -9999  
 CAPE 0.00  
 CAPV 0.00  
 CINS 0.00  
 CINV 0.00  
 EQLV -9999  
 EQTV -9999  
 LFCT -9999  
 LFCV -9999  
 BRCH 0.00  
 BRCV 0.00  
 LCLT 260.9  
 LCLP 636.0  
 MLTH 296.9  
 MLMR 2.37  
 THCK 5537.  
 PWAT 6.22

12Z 09 Dec 1992

University of Wyoming

72476 GJT Grand Junction



SLAT 39.11  
 SLON -108.  
 SELV 1475.  
 SHOW 17.64  
 LIFT 14.88  
 LFTV 15.01  
 SWET 67.00  
 KINX 1.60  
 CTOT 10.60  
 VTOT 15.60  
 TOTL 26.20  
 CAPE 0.00  
 CAPV 0.00  
 CINS 0.00  
 CINV 0.00  
 EQLV -9999  
 EQTV -9999  
 LFCT -9999  
 LFCV -9999  
 BRCH 0.00  
 BRCV 0.00  
 LCLT 266.2  
 LCLP 799.2  
 MLTH 283.8  
 MLMR 2.88  
 THCK 5408.  
 PWAT 10.00

12Z 09 Dec 1992

University of Wyoming

Figure 12: NWS routine radiosondes from (a) Denver, CO (DEN) and (b) Grand Junction, CO (GJT) valid 12 UTC 9 December 1992. Note the pronounced warming in the lower stratosphere in both soundings. Data courtesy of sounding archives at The University of Wyoming.

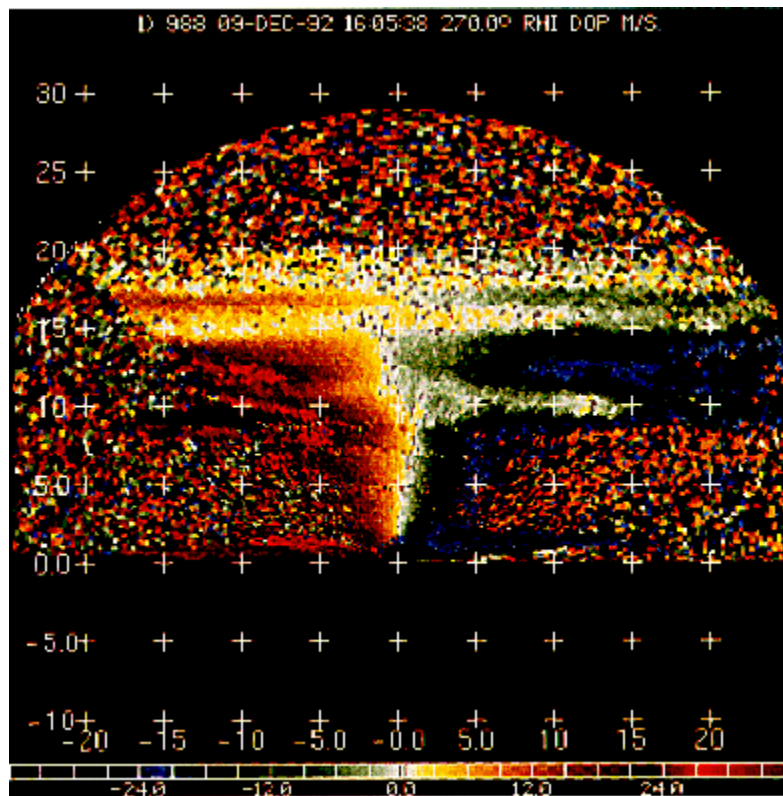
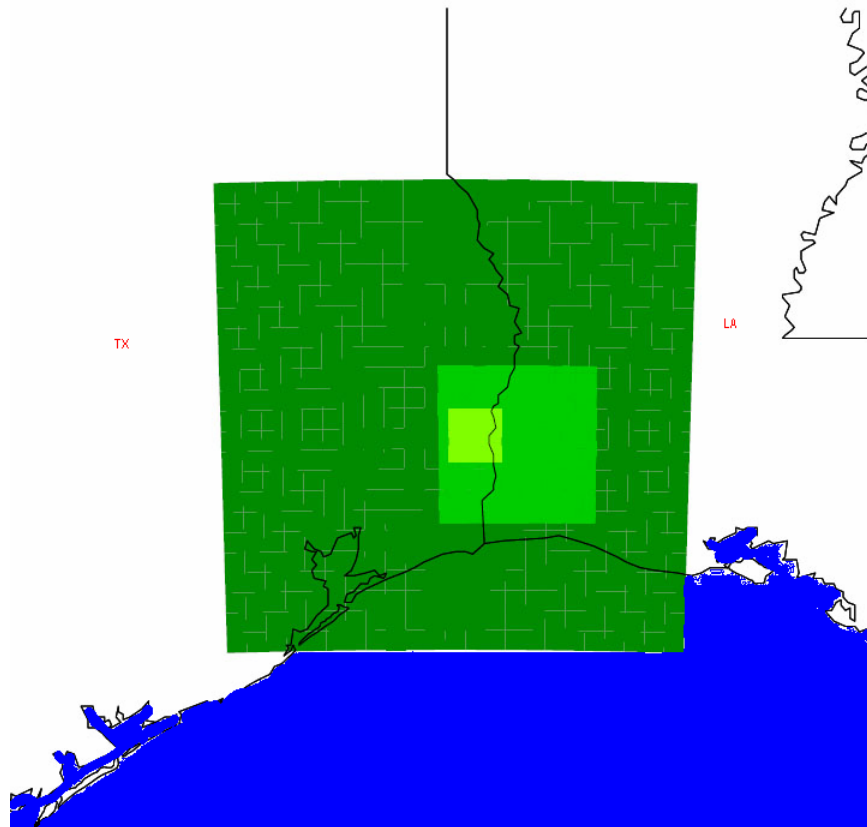
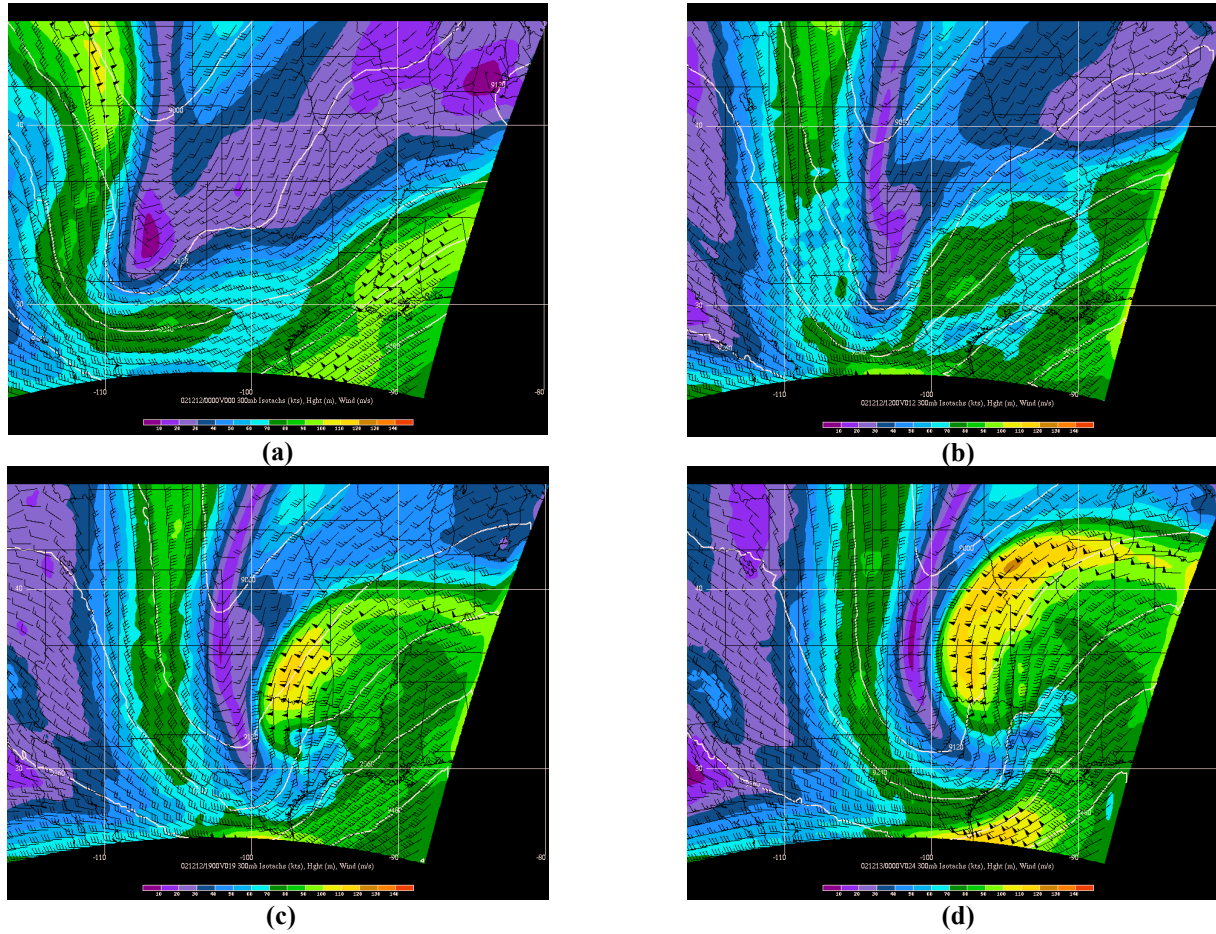


Figure 13: Range-Height Indicator (RHI) plot of radial velocity from NOAA ERL/ETL lidar at Table Mountain Colorado, valid 16 UTC 9 December 1992. Note the reversal of flow within the lower stratosphere ~10 km east and ~10 km above the lidar. Adapted from Ralph et al. (1997).



**Figure 14: NHMASS fine resolution simulations for 9 December 1992 case, shown in the following order: 2 km is the outer portion (white), followed by 667 m (green hatch), 222 m (green), 71 m (bright green). From Ringley et al. (2005).**



**Figure 15: MASS18C 300-hPa winds (barbs), isotachs (color fill), and heights (contoured) valid (a) 0000 UTC; (b) 1200 UTC; (c) 1900 UTC 12 December 2002 and (d) 0000 UTC 13 December 2002.**

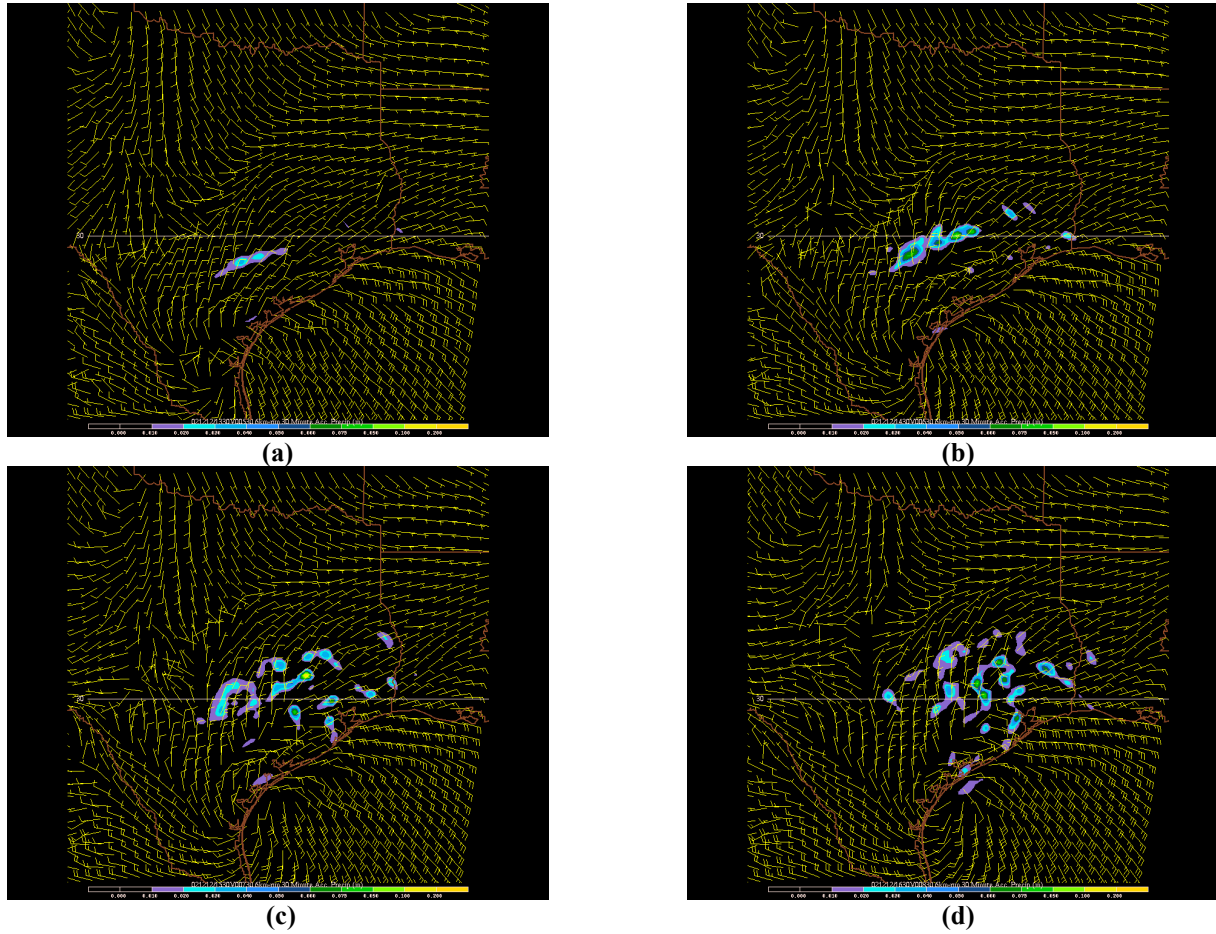


**Figure 16: MASS6C accumulated precipitation (mm) valid (a) 1330 UTC; (b) 1430 UTC; (c) 1530 UTC; (d) 1630 UTC, showing the development of individual convective cells in the Texas Hill Country prior to the development of a strong linear convective system.**

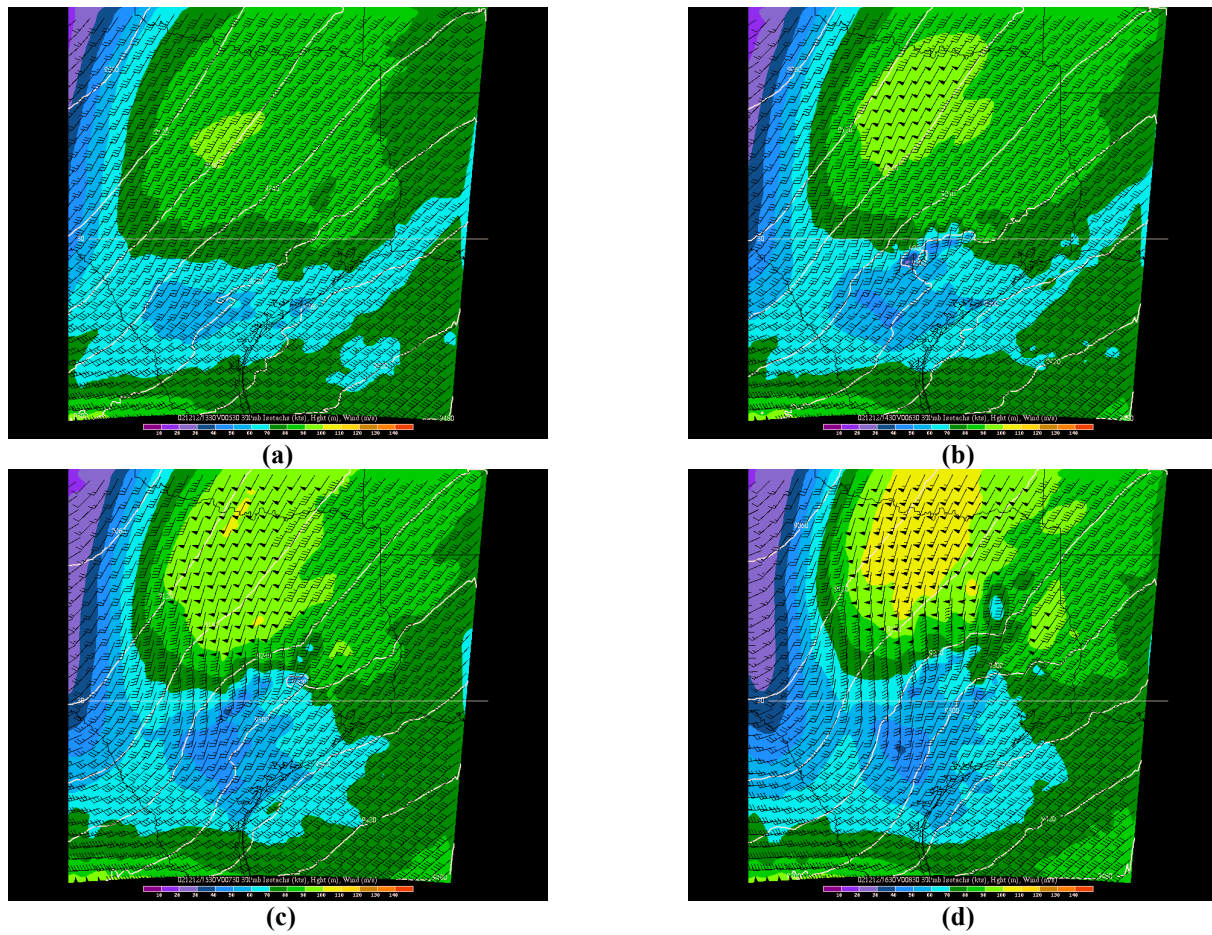


**Figure 17: MASS6C 300 hPa winds (barbs), isotachs (color fill) and heights (white contours) valid (a) 1330 UTC; (b) 1430 UTC; (c) 1530 UTC; (d) 1630 UTC, showing the development of a significant upstream wind maxima over Northern Texas and Southern Oklahoma.**

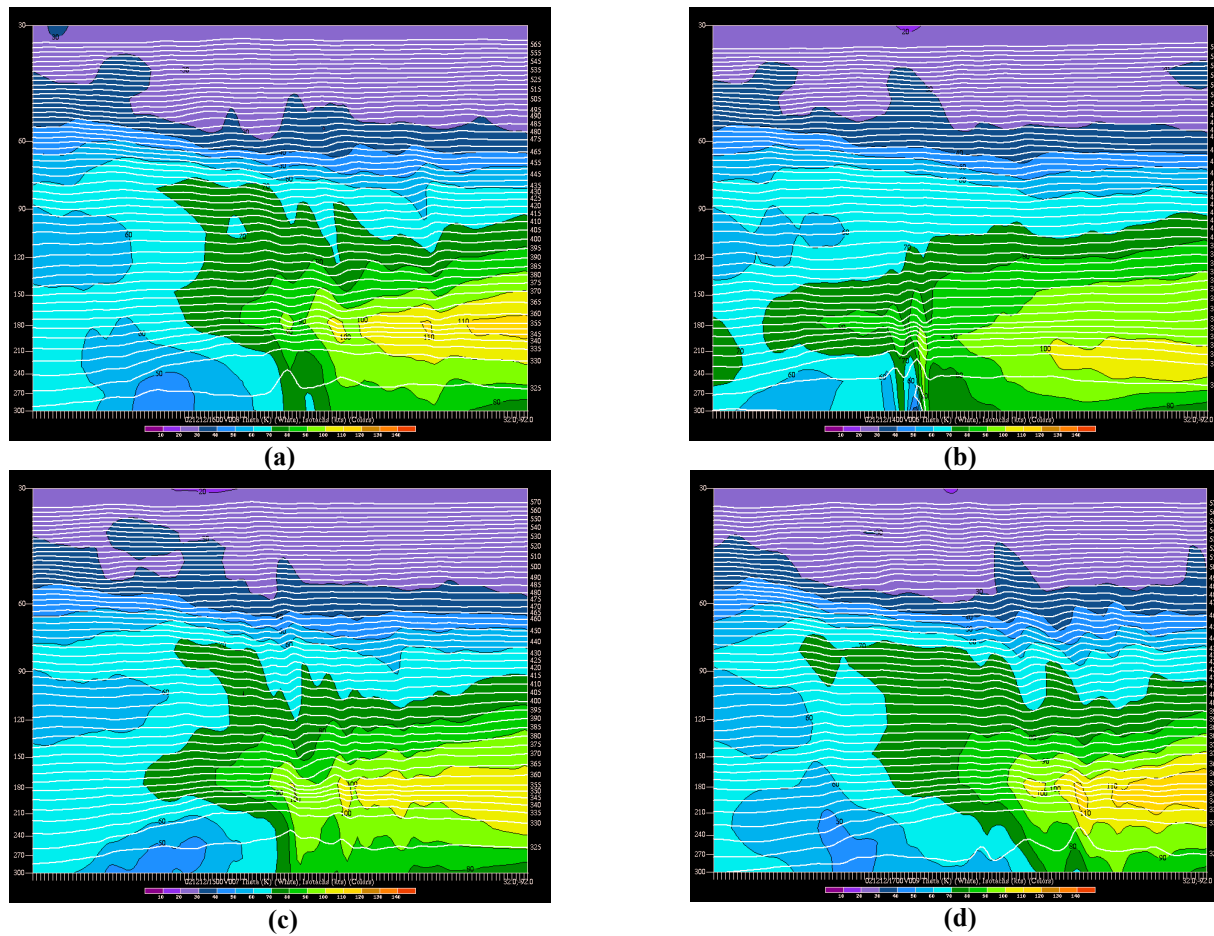


Figure 18: MASS6C cross-sections of isotachs (color fill) and isentropes (white contours) valid (a) 1400 UTC; (b) 1500 UTC; (c) 1600 UTC; (d) 1700 UTC, illustrating the impact of convective bursts within MASS6C on the stratosphere.

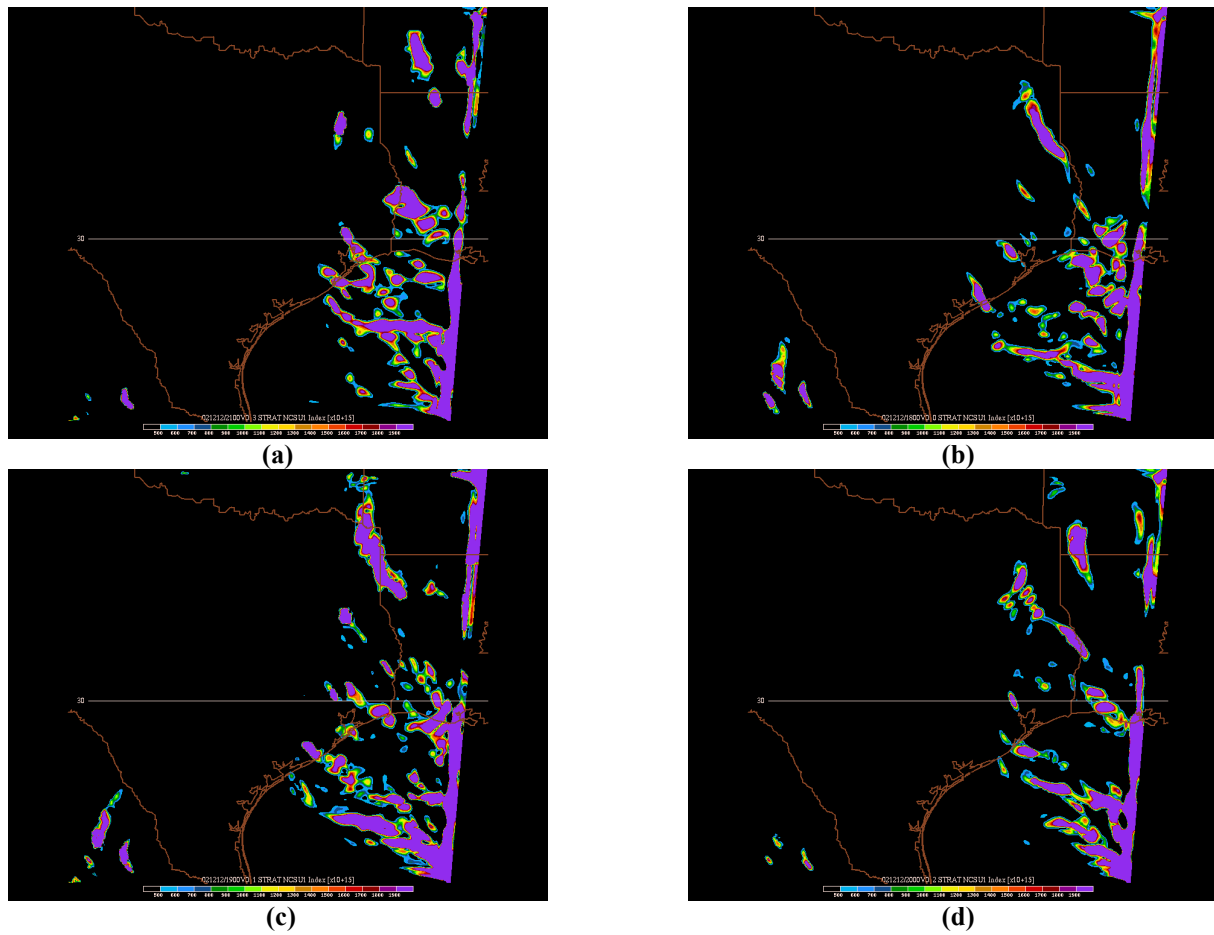


Figure 19: MASS6C NCSU1 turbulence index (color fill) at 90 hPa valid (a) 1800 UTC; (b) 1900 UTC; (c) 2000 UTC; (d) 2100 UTC, showing the region of enhanced NCSU1 in far southeast Texas responsible for triggering the 2-km autonest.

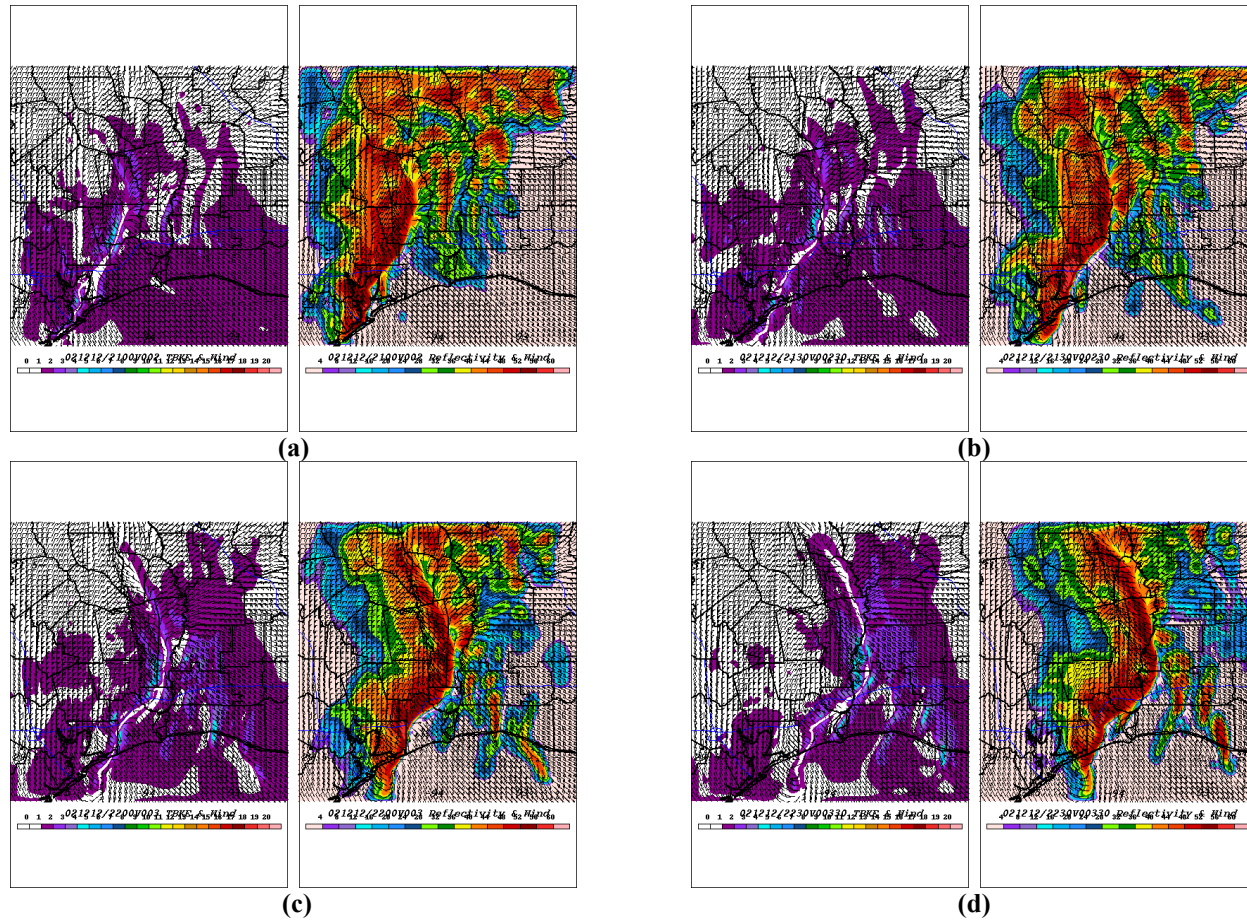


Figure 20: MASS2C composite plots of model-derived TKE (left panel) and model-derived reflectivity (right panel) and wind at 250-m MMSL valid (a) 2100 UTC; (b) 2130 UTC; (c) 2200 UTC; (d) 2230 UTC 12 December 2002.

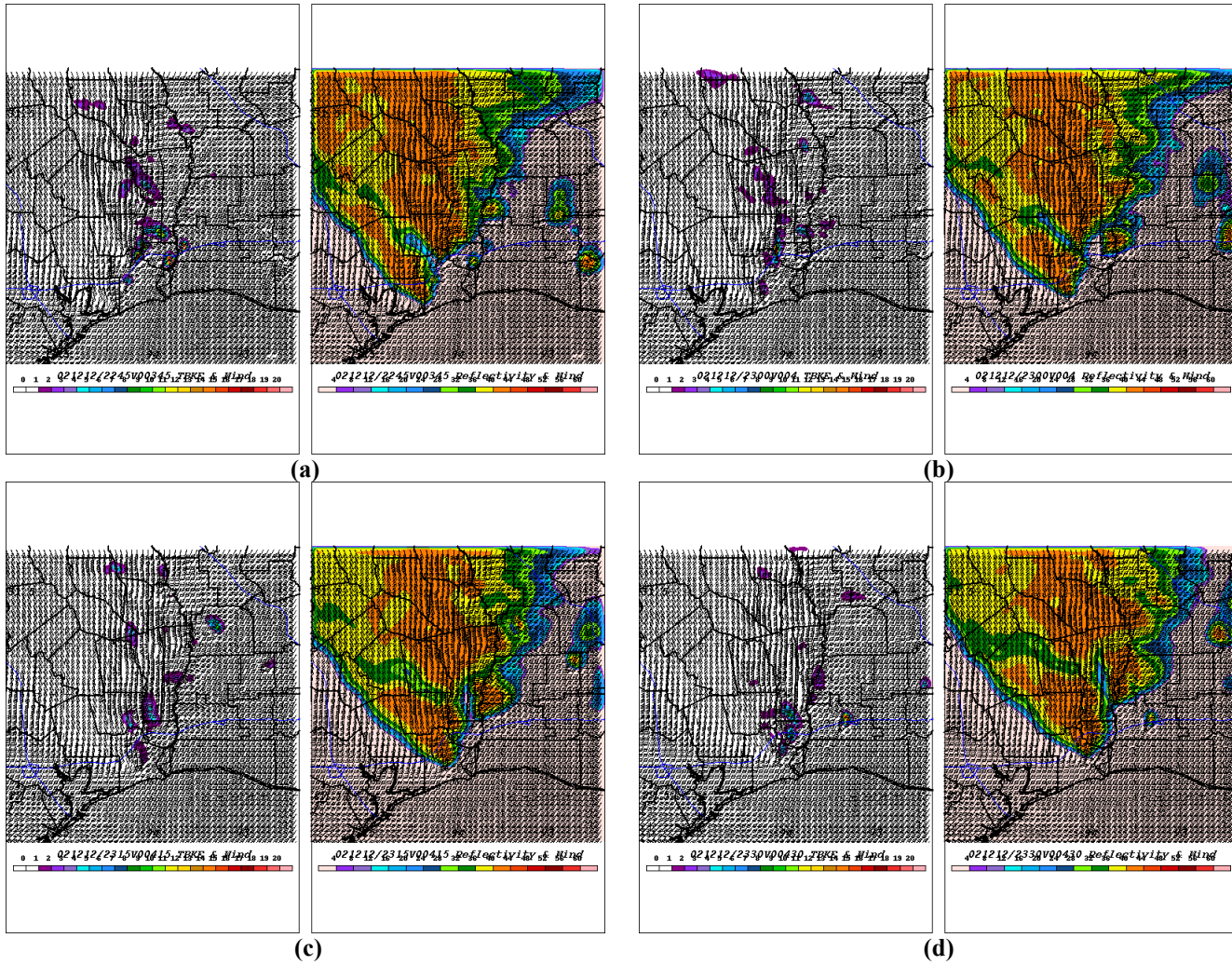


Figure 21: As with Fig. 20, but for 10-km MMSL valid (a) 2245 UTC; (b) 2300 UTC; (c) 2315 UTC; (d) 2330 UTC 12 December 2002.

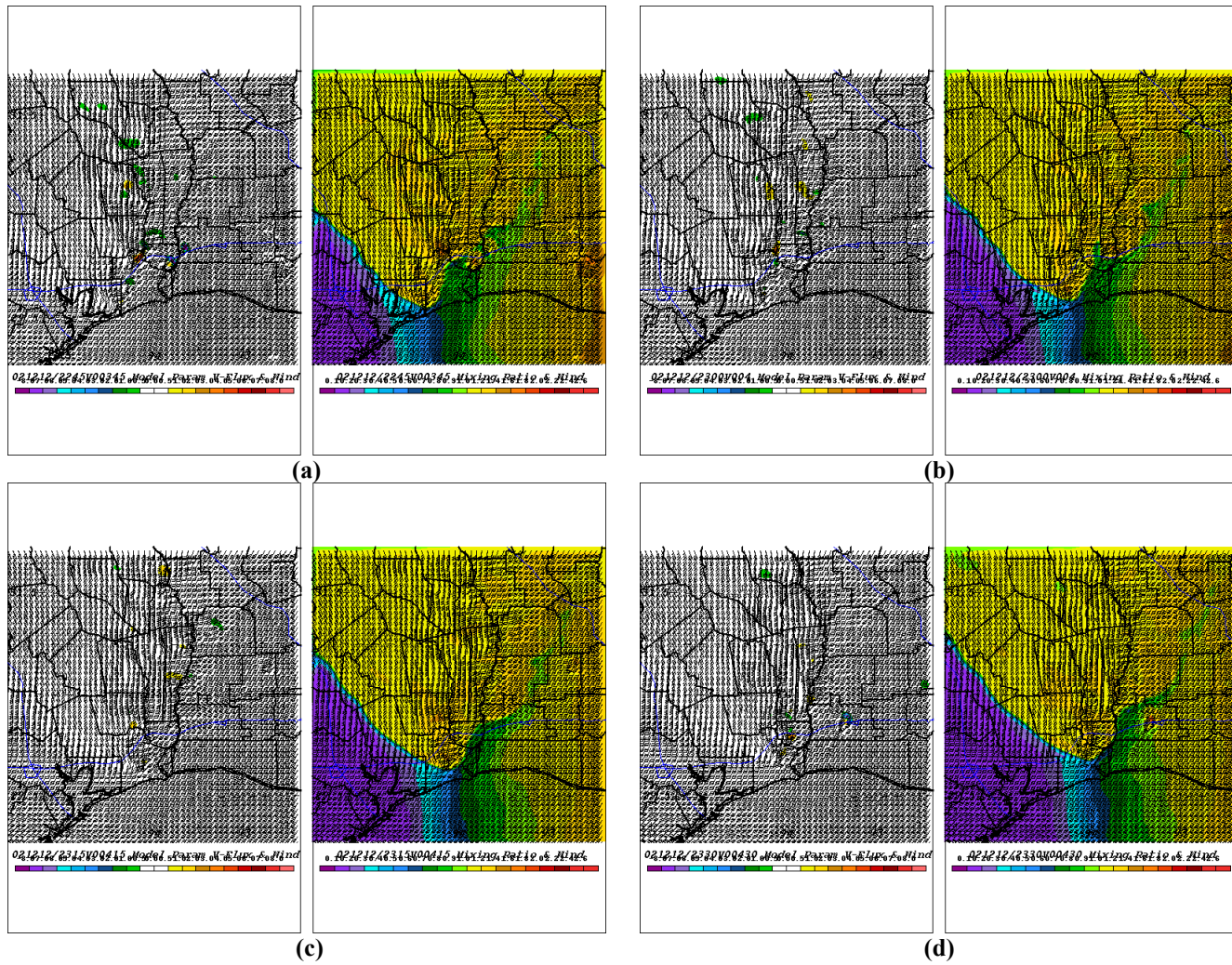


Figure 22: MASS2C composite plots of divergence (left panel) and mixing ratio (right panel) and wind at 10 km MMSL valid (a) 2245 UTC; (b) 2300 UTC; (c) 2315 UTC; (d) 2330 UTC 12 December 2002.

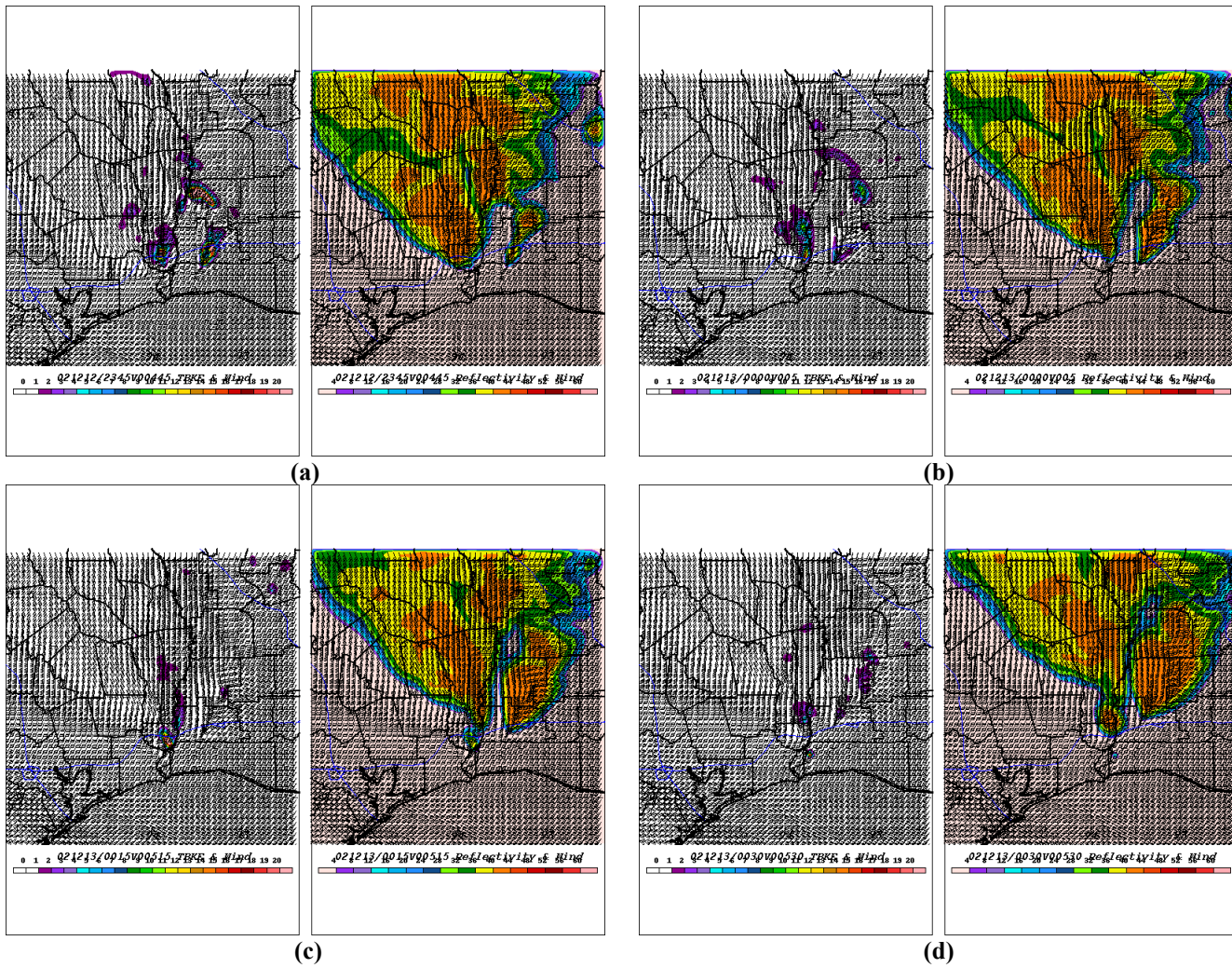


Figure 23: As with Fig. 21, but valid (a) 2345 UTC; (b) 0000 UTC; (c) 0015 UTC; (d) 0030 UTC 12-13 December 2002.

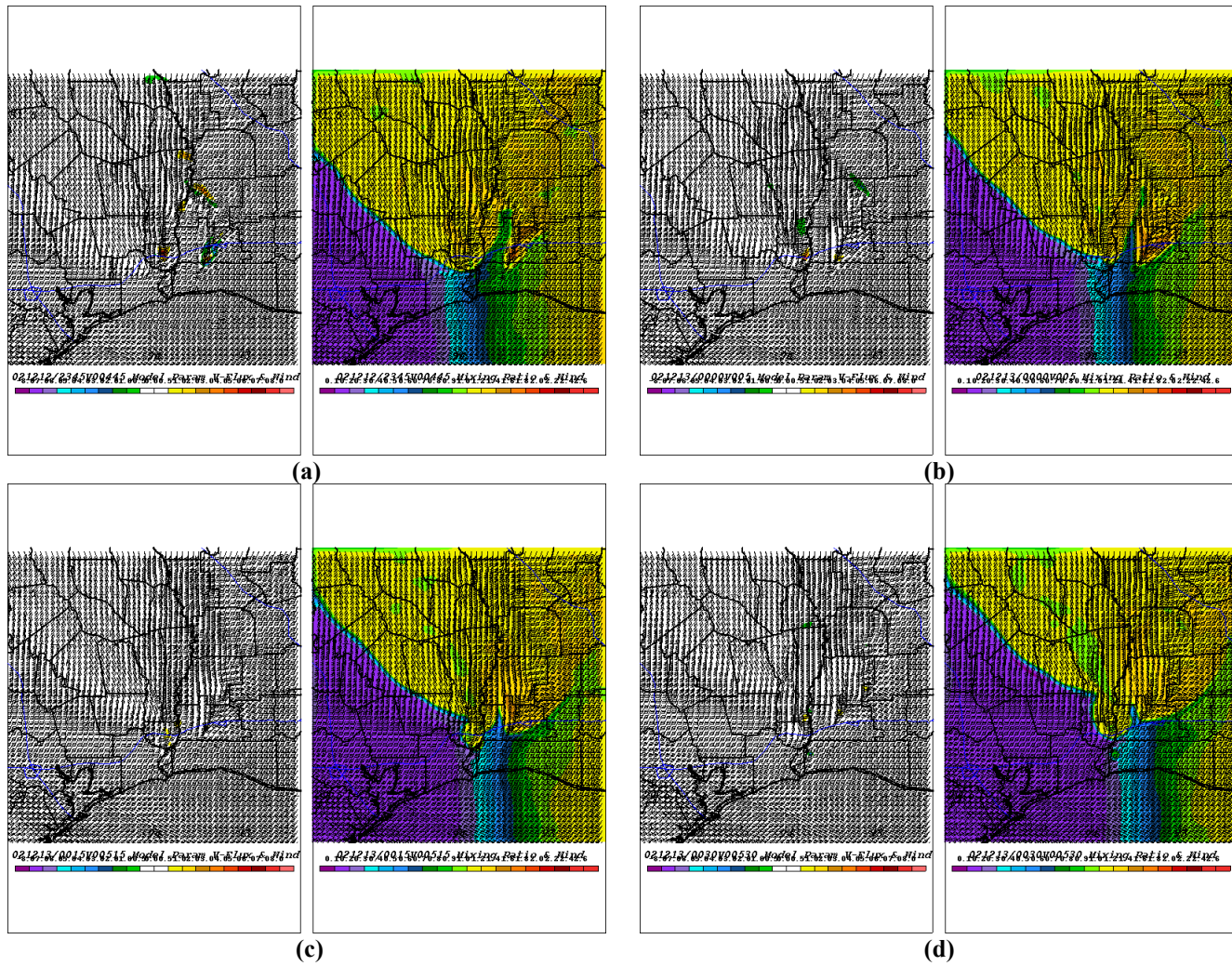


Figure 24: As with Fig. 22, but valid (a) 2345 UTC; (b) 0000 UTC; (c) 0015 UTC; (d) 0030 UTC 12-13 December 2002.

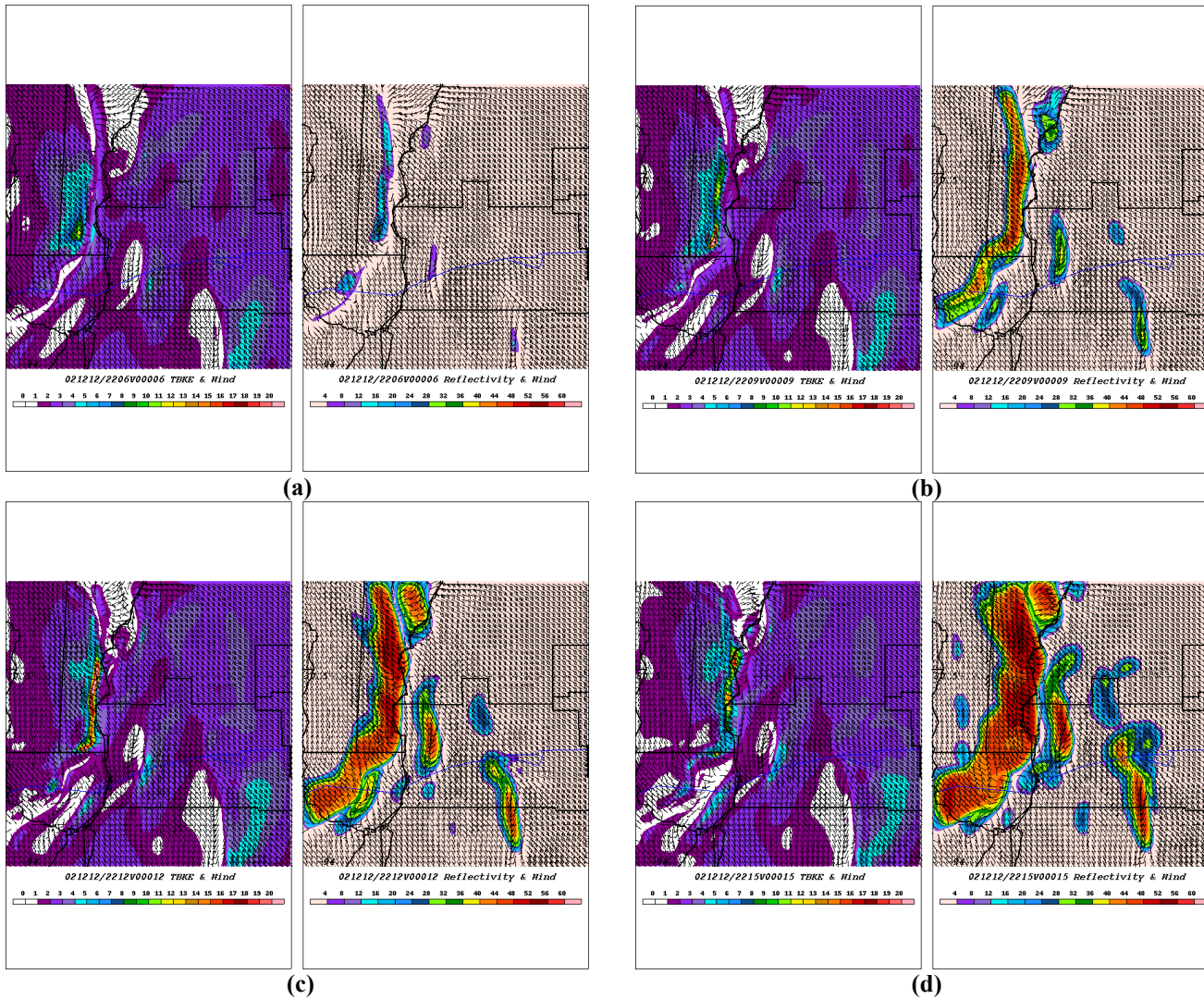


Figure 25: MASS667C composite plots of model-derived TKE (left panel) and model-derived reflectivity (right panel) and wind at 250-m MMSL valid (a) 2206 UTC; (b) 2209 UTC; (c) 2212 UTC; (d) 2215 UTC 12 December 2002.

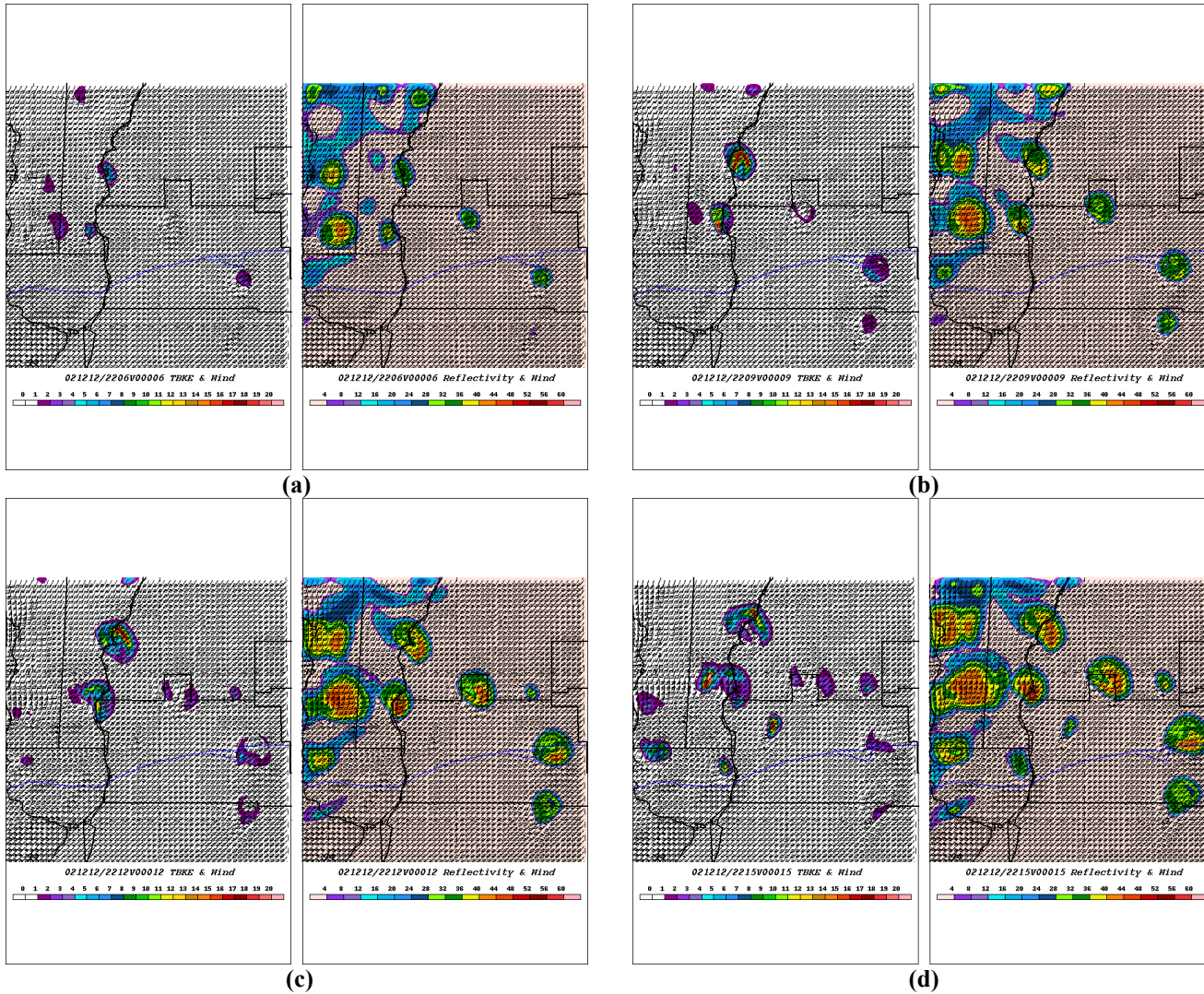


Figure 26: As with Fig. 25, but for 8km MMSL valid (a) 2206 UTC; (b) 2209 UTC; (c) 2212 UTC; (d) 2215 UTC 12 December 2002.

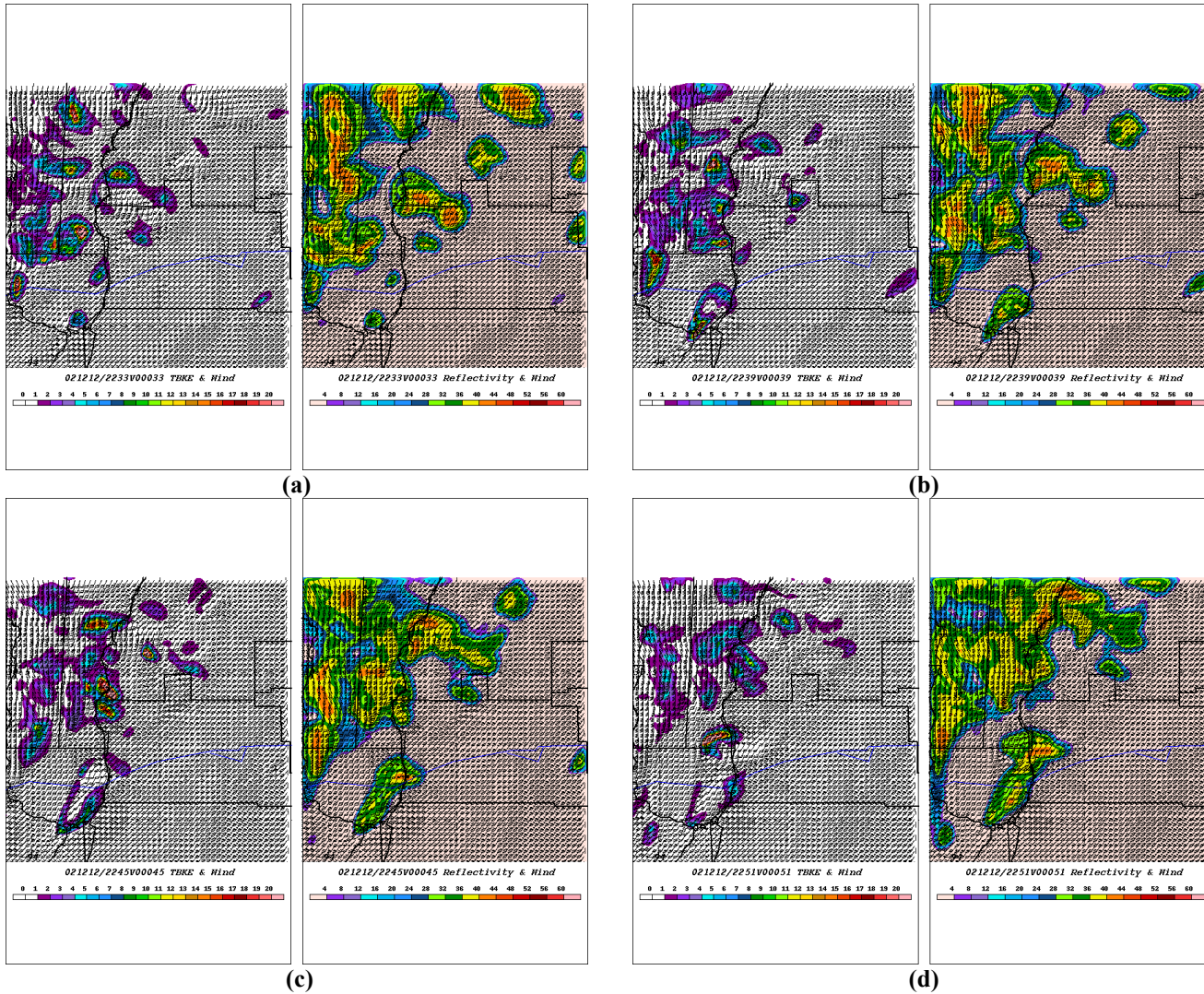


Figure 27: As with Fig. 26, but valid (a) 2233 UTC; (b) 2239 UTC; (c) 2245 UTC; (d) 2251 UTC 12 December 2002.

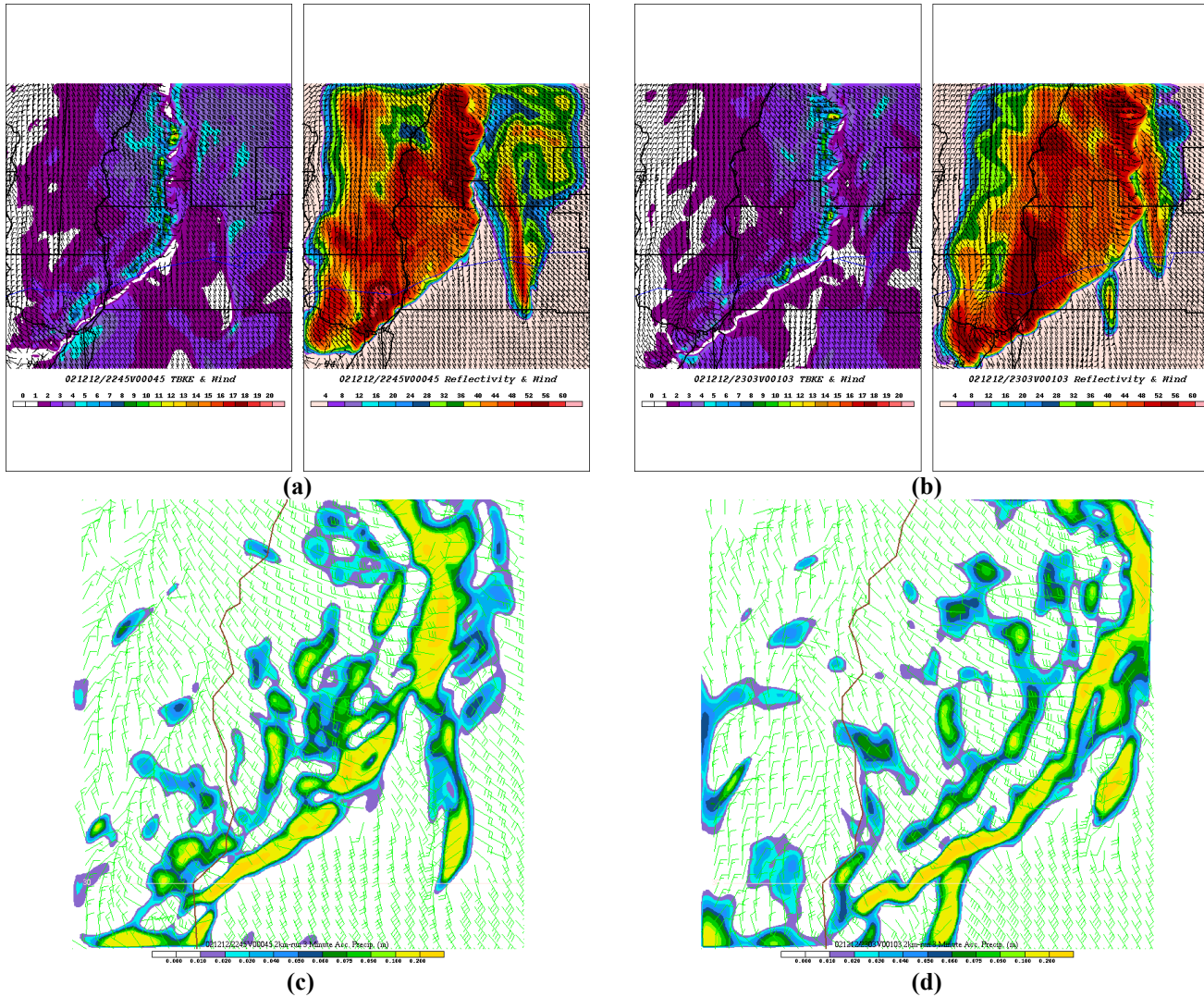


Figure 28: Model TKE and reflectivity at (a) 2245 and (b) 2303 UTC 12 December, and grid accumulated precipitation at (c) 2245 UTC; (d) 2303 UTC 12 December 2002.

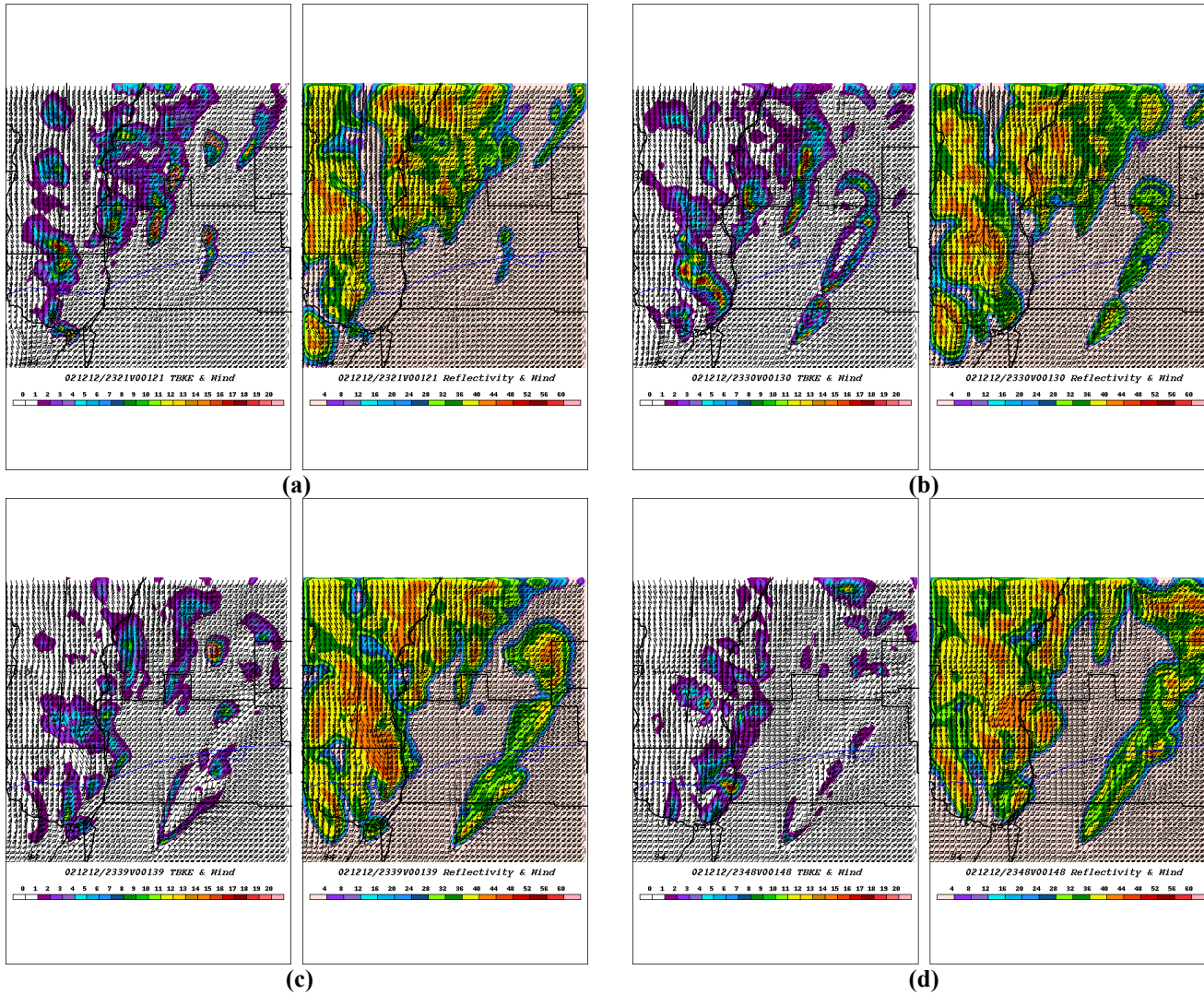


Figure 29: As with Fig. 27, but valid (a) 2321 UTC; (b) 2330 UTC; (c) 2339 UTC; (d) 2348 UTC 12 December 2002.

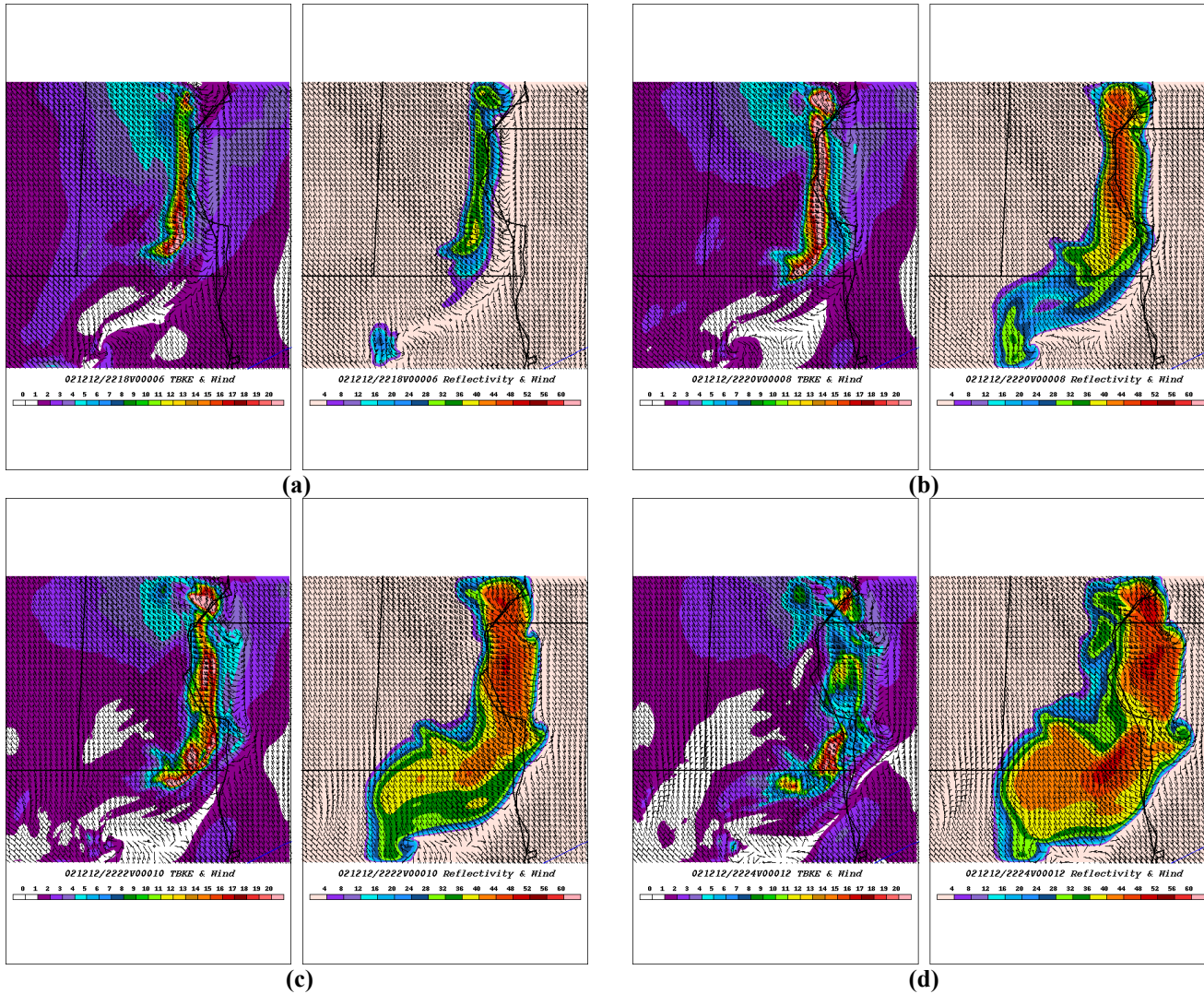


Figure 30: MASS222C composite plots of model-derived TKE (left panel) and model-derived reflectivity (right panel) and wind at 250-m MMSL valid (a) 2218 UTC; (b) 2220 UTC; (c) 2222 UTC; (d) 2224 UTC 12 December 2002.

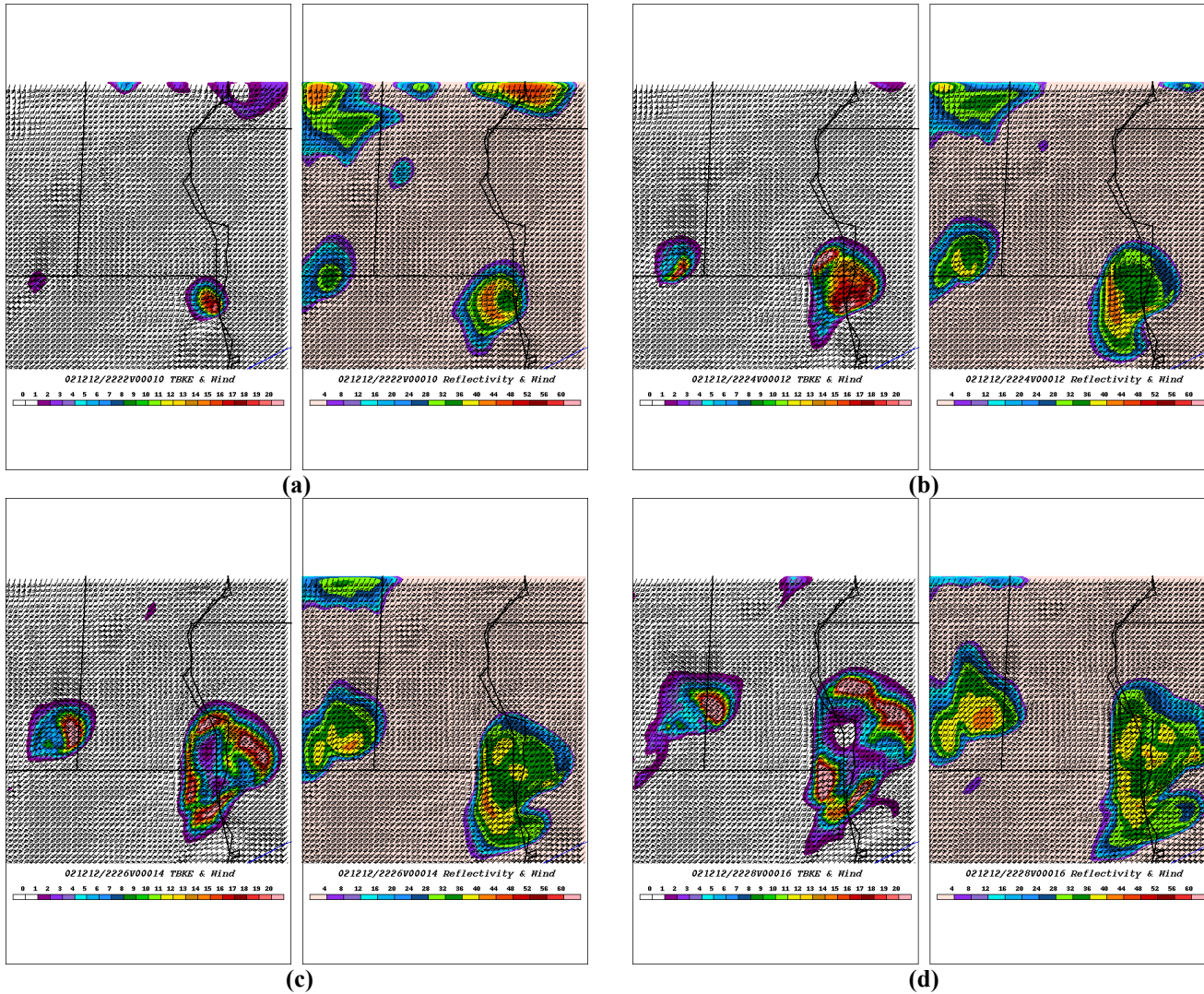


Figure 31: As with Fig. 30, but for 8km MMSL valid (a) 2218 UTC; (b) 2220 UTC; (c) 2222 UTC; (d) 2224 UTC 12 December 2002.

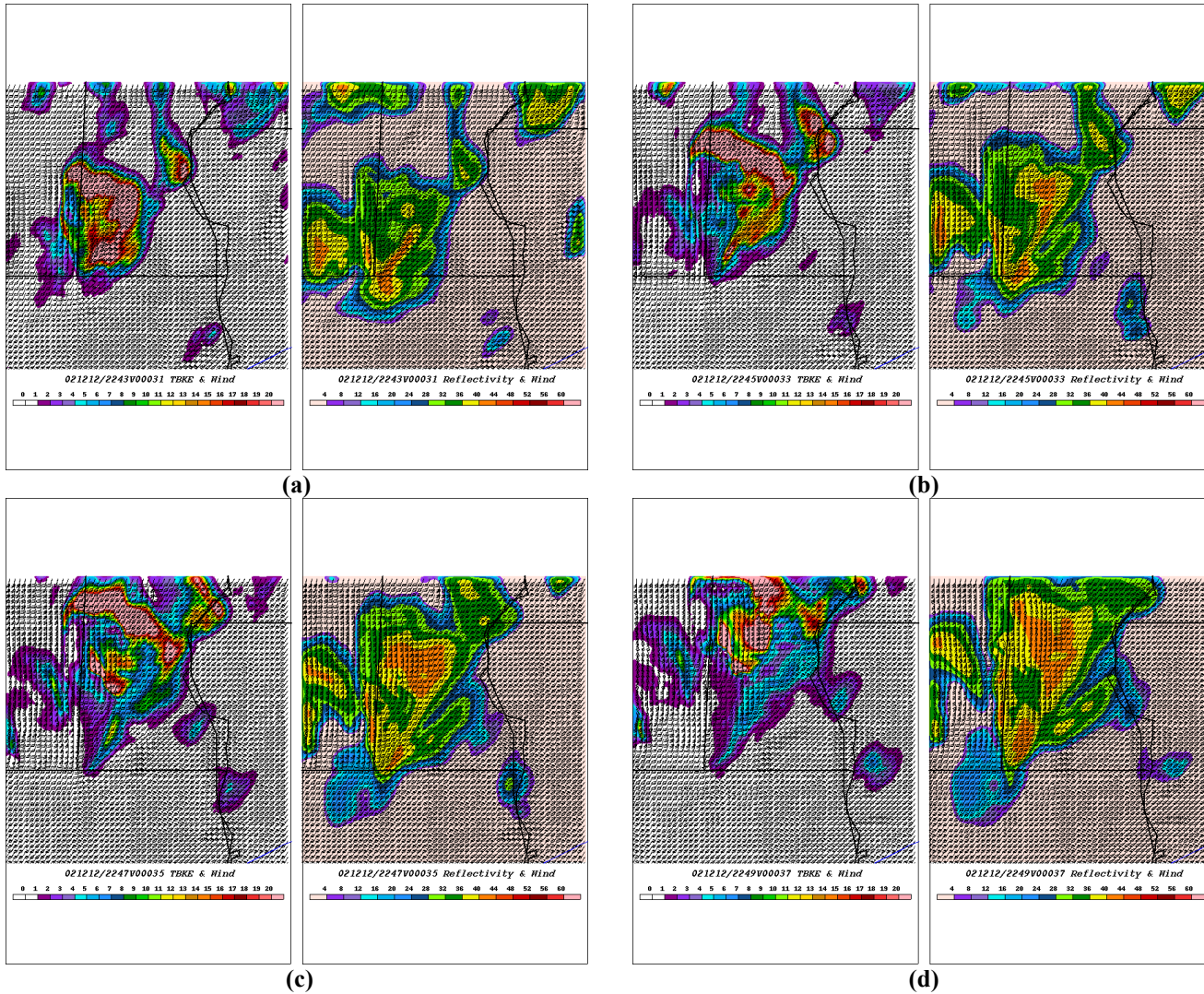


Figure 32: As with Fig. 31, but for 8km MMSL valid (a) 2243 UTC; (b) 2245 UTC; (c) 2247 UTC; (d) 2249 UTC 12 December 2002.

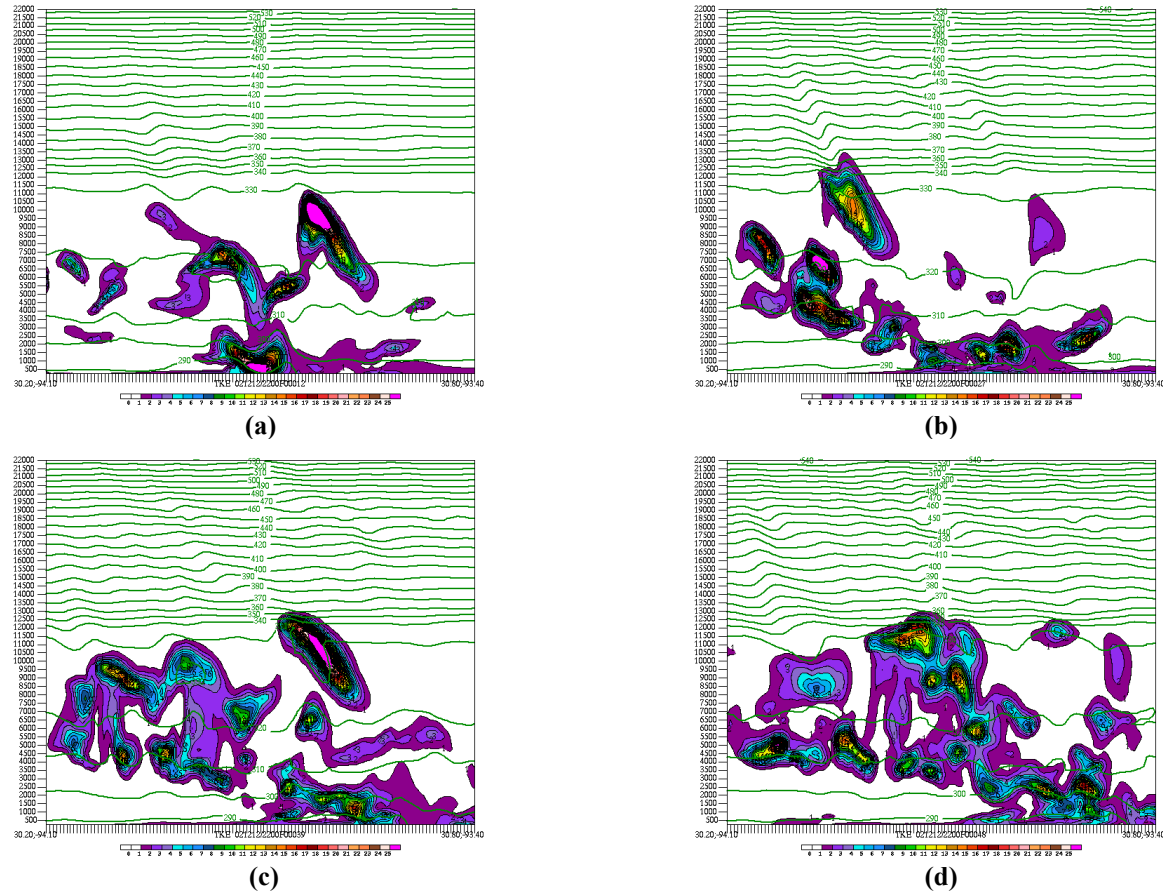


Figure 33: MASS667C MMSL crosssections of model derive TKE (color fill) and virtual potential temperature (green contours) from 250m-20km at (a) 2212 UTC; (b) 2227 UTC; (c) 2239 UTC; (d) 2248 UTC 12 December 2002.

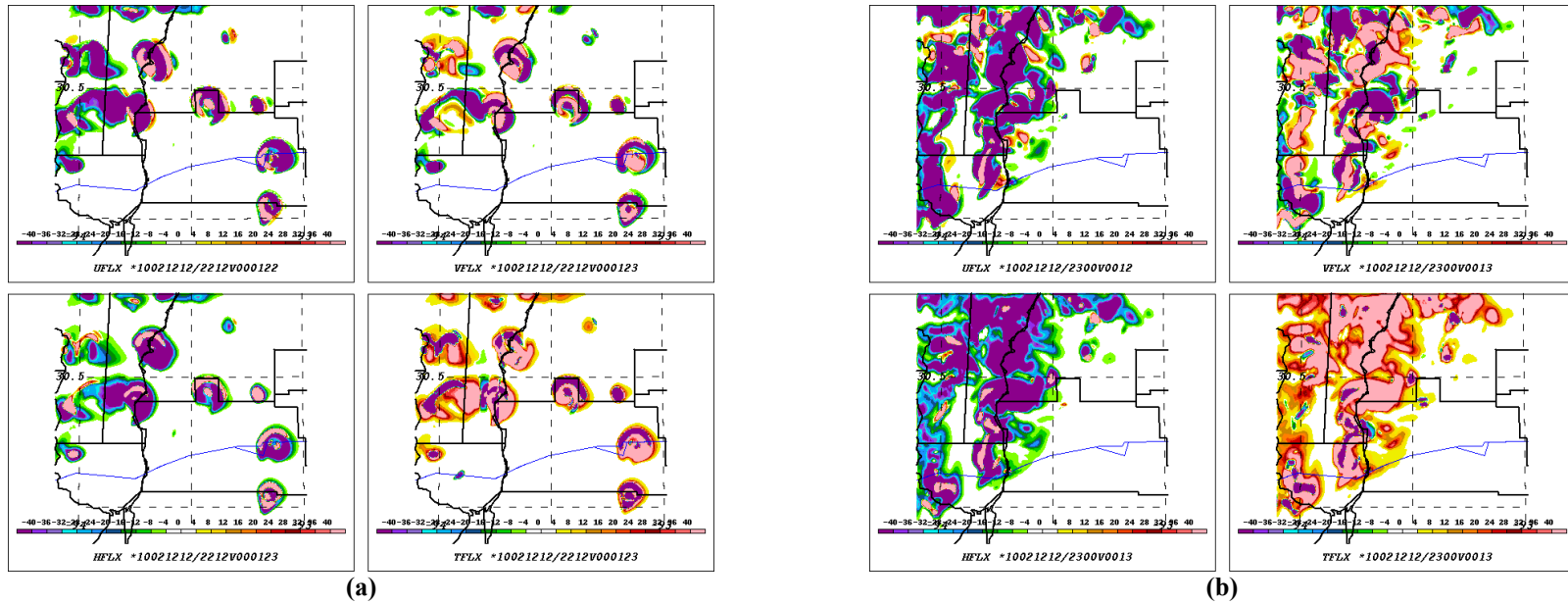


Figure 34: MASS667C four-panel plot (color fill) of scaled model-parameterized u-momentum (top left), v-momentum (top right), heat (bottom left) and TKE (bottom right) flux at 8 km valid (a) 2212 UTC; (b) 2300 UTC 12 December 2002.

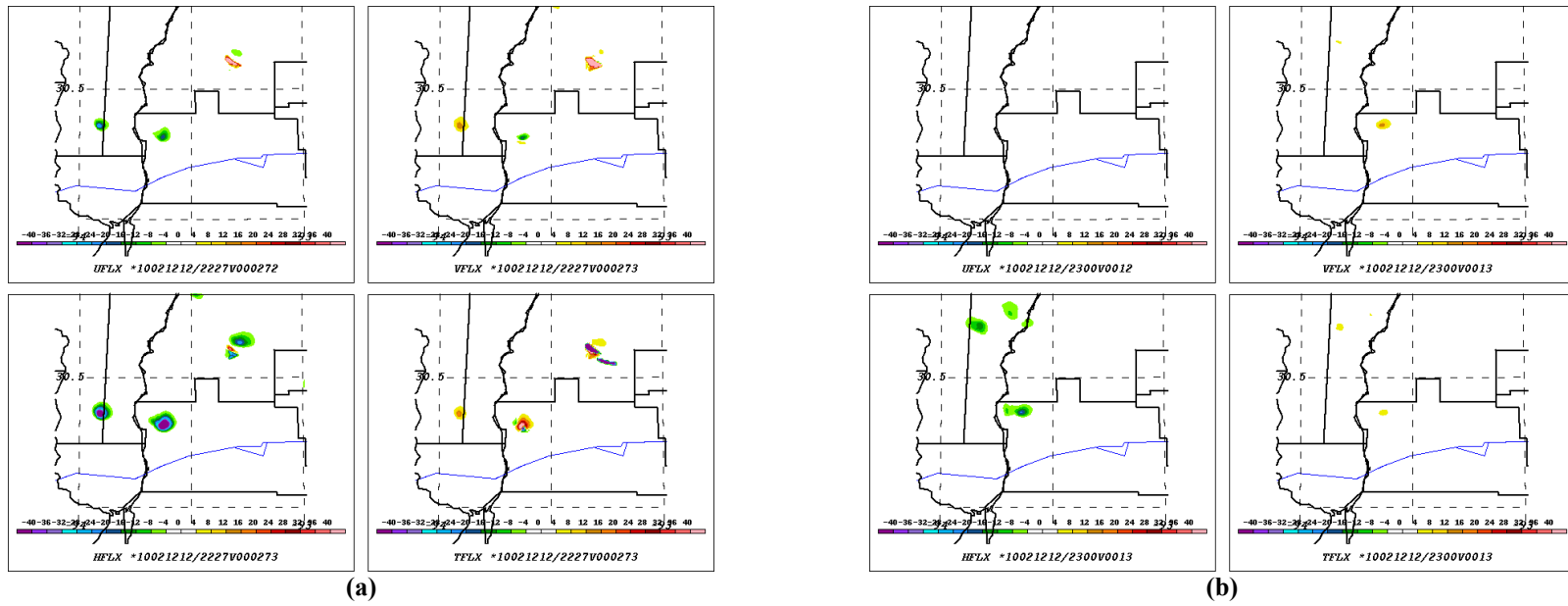


Figure 35: As with Fig. 34, but for 14 kilometers valid (a) 2212 UTC; (b) 2300 UTC 12 December 2002.

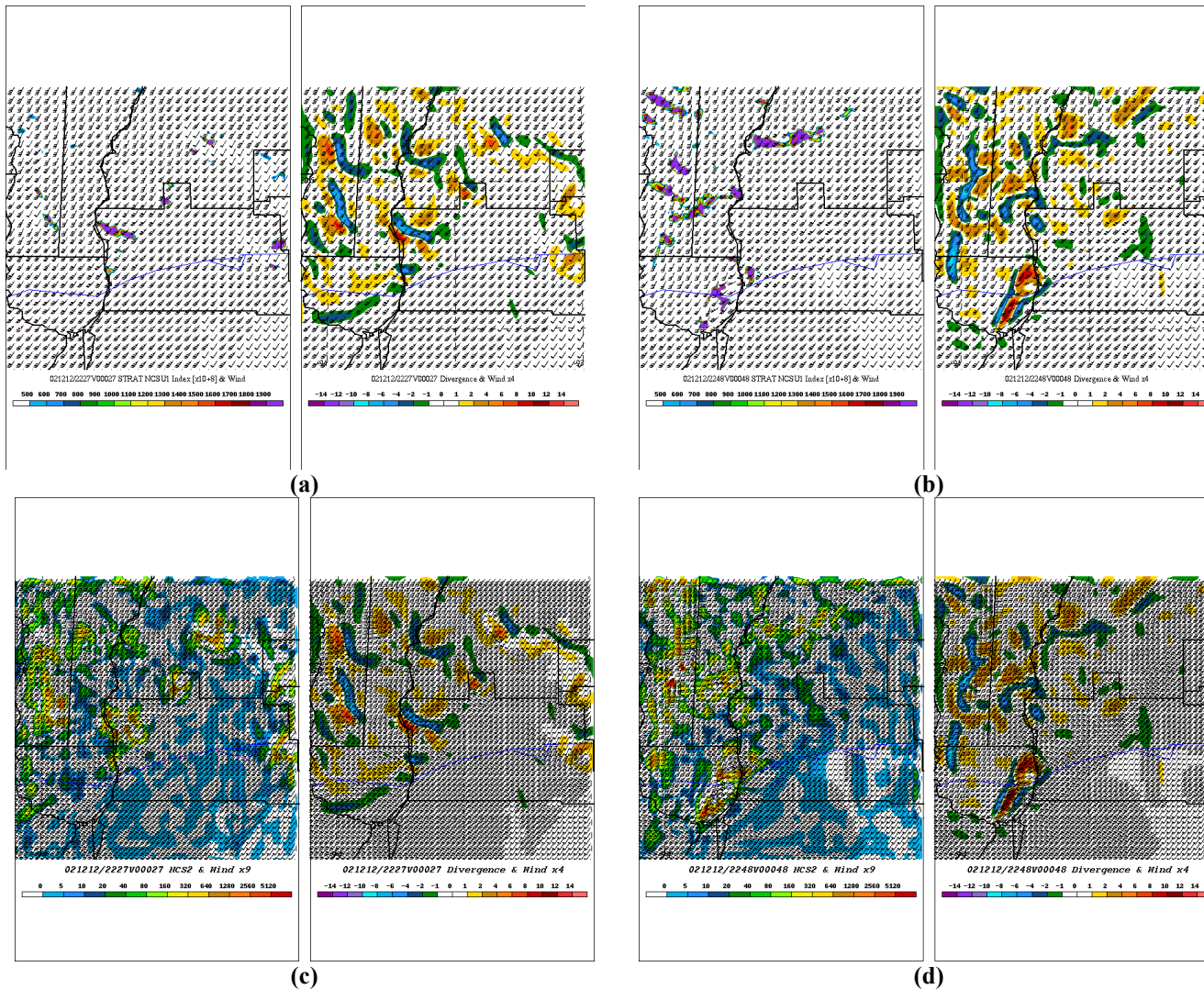


Figure 36: MASS667C NCSU1 turbulence index (left panel ) and divergence (right panel) valid (a) 2212 UTC; (b) 2227 UTC; NCSU2 turbulence index (left panel) and divergence (right panel) valid (c) 2212 UTC; (d) 2239 UTC 12 December 2002.

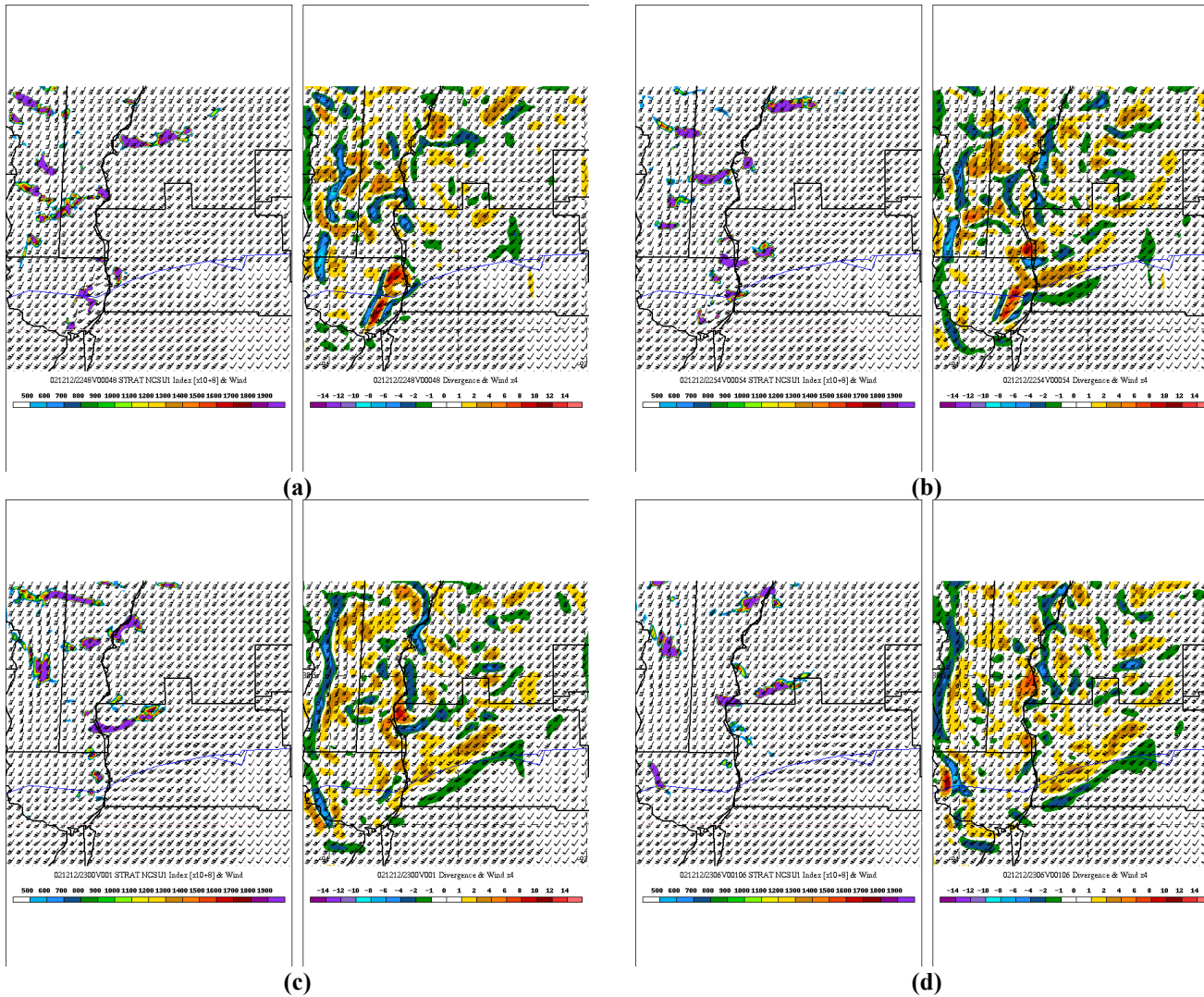
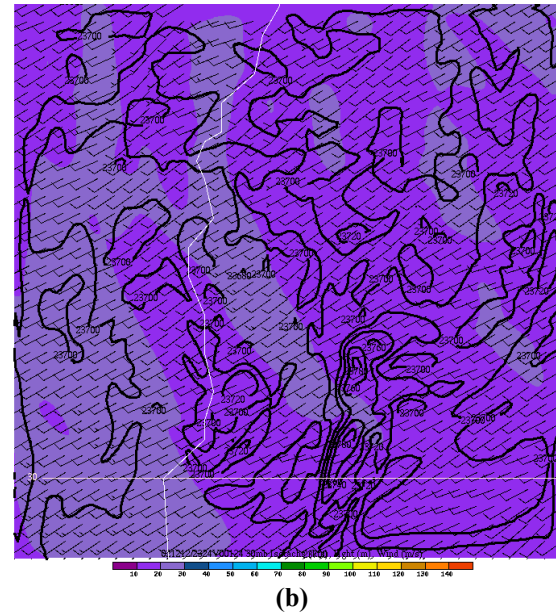
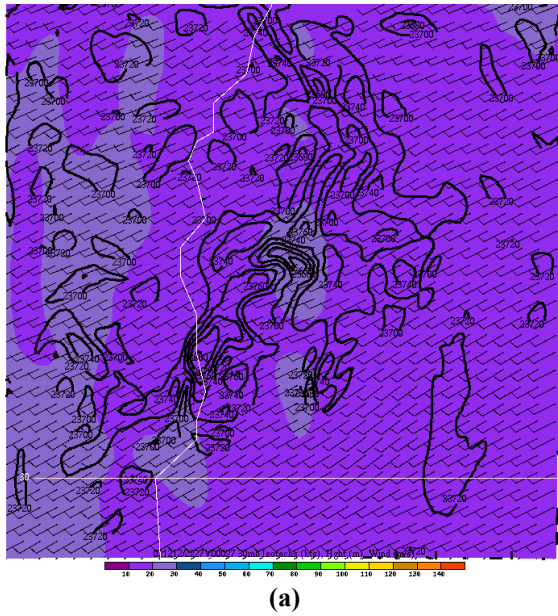


Figure 37: MASS667C NCSUI turbulence index (left panel ) and divergence (right panel) valid (a) 2248 UTC; (b) 2254 UTC; (c) 2300 UTC; (d) 2306 UTC 12 December 2002.



**Figure 38: MASS667C 30-hPa winds (barbs), isotachs (color fill) and heights (black contours) associated with each deep convective burst valid (a) 2230 UTC; (b) 2334 UTC 12 December 2002.**

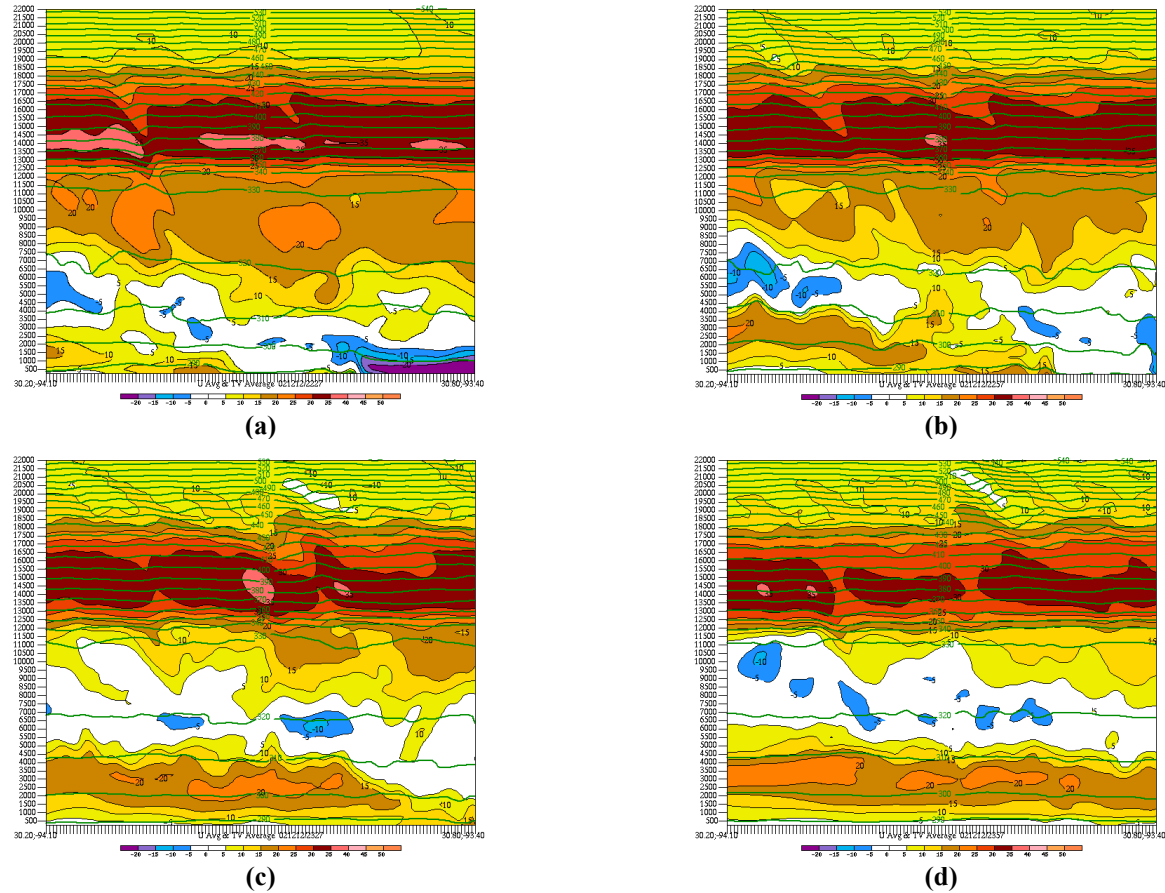


Figure 39: MASS667C temporally-averaged u-wind velocity (color fill), and virtual potential temperature (green contours) from 250n-22 km valid (a) 2227 UTC; (b) 2257 UTC; (c) 2327 UTC; (d) 2357 UTC 12 December 2002.

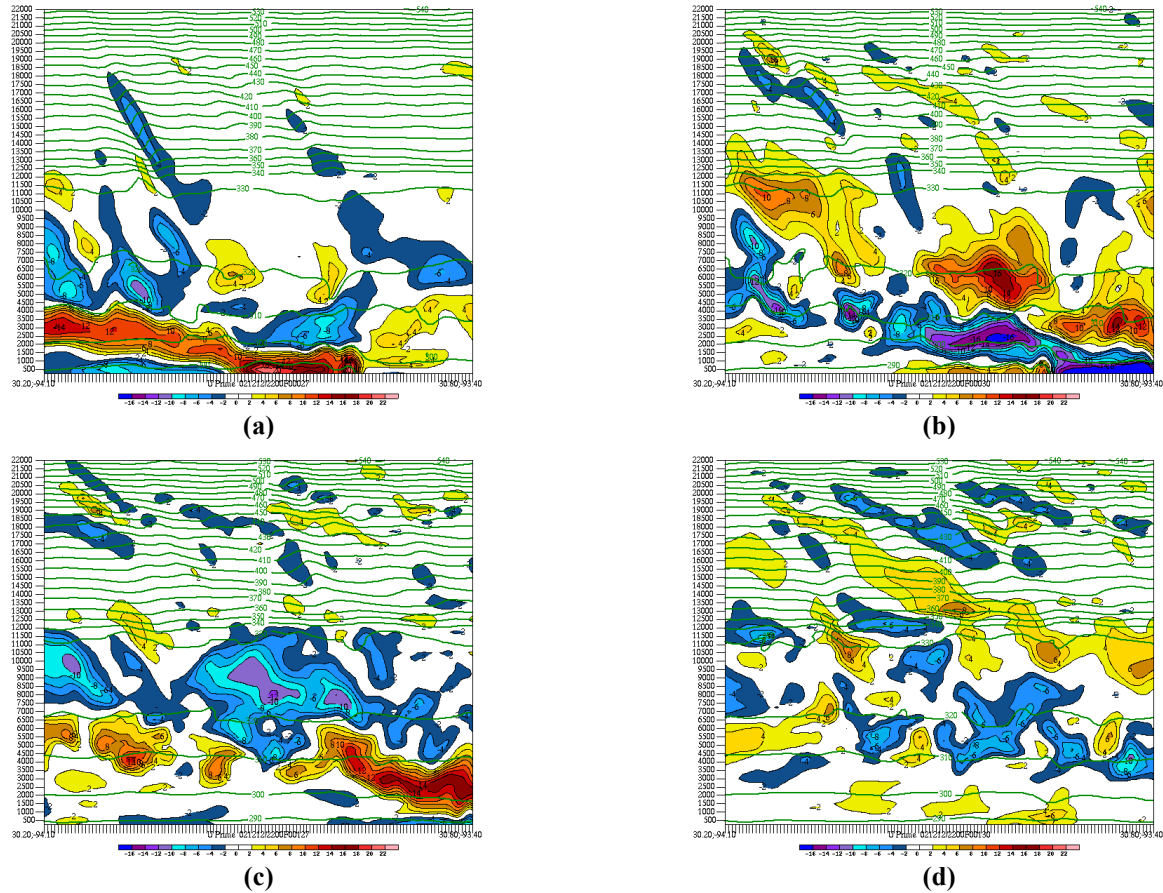


Figure 40: MASS667C temporally-derived u-wind velocity perturbations (color fill), and virtual potential temperature (green contours) from 250n-22 km valid (a) 2227 UTC; (b) 2230 UTC; (c) 2327 UTC; (d) 2330 UTC 12 December 2002. Note the dramatic shift in flux contribution because of a shift in the temporal average.

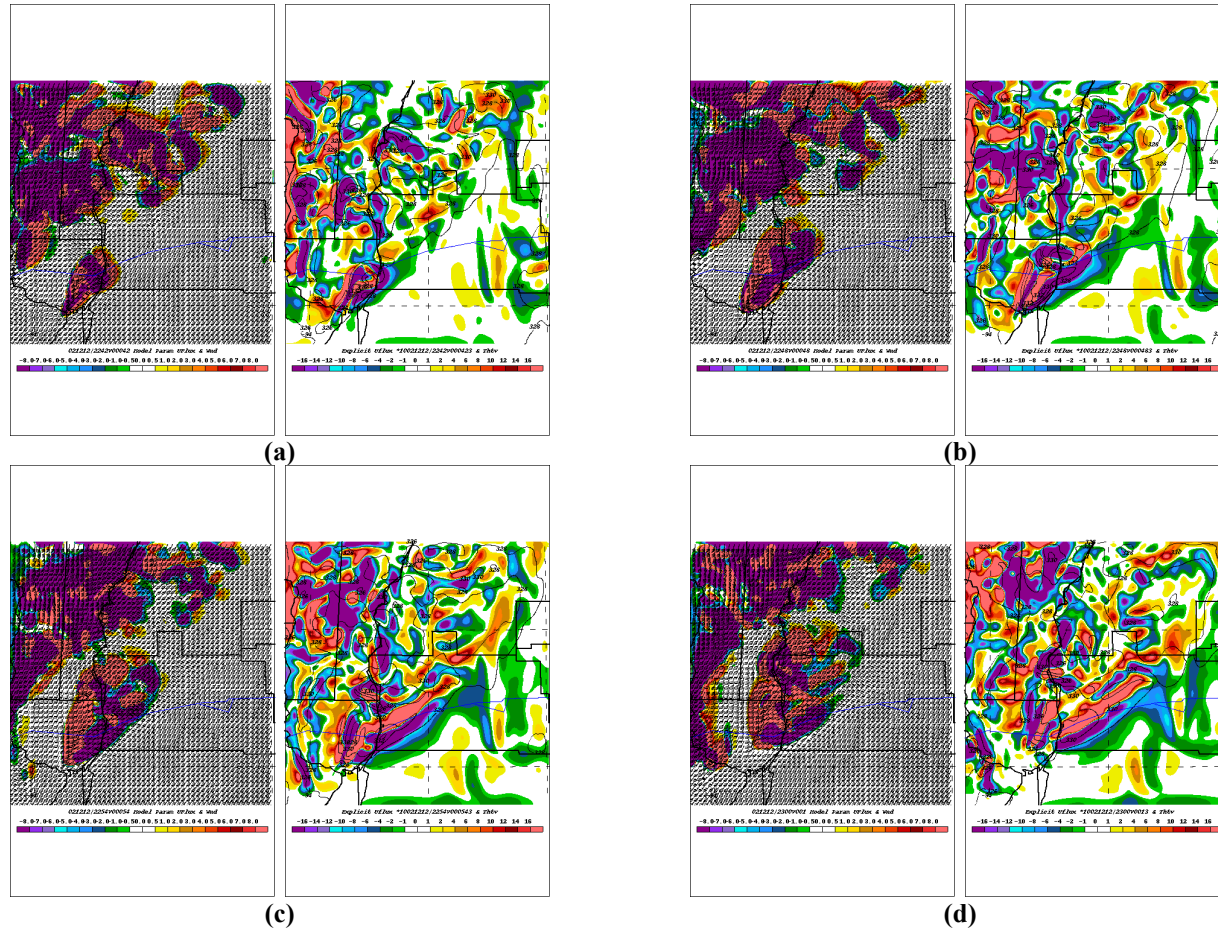


Figure 41: MASS667C two-panel plots of model parameterized u-momentum flux (left panel) and spatially-derived explicit u-momentum flux valid (right panel) valid (a) 2242 UTC; (b) 2248 UTC; (c) 2254 UTC; (d) 2300 UTC 12 December 2002.

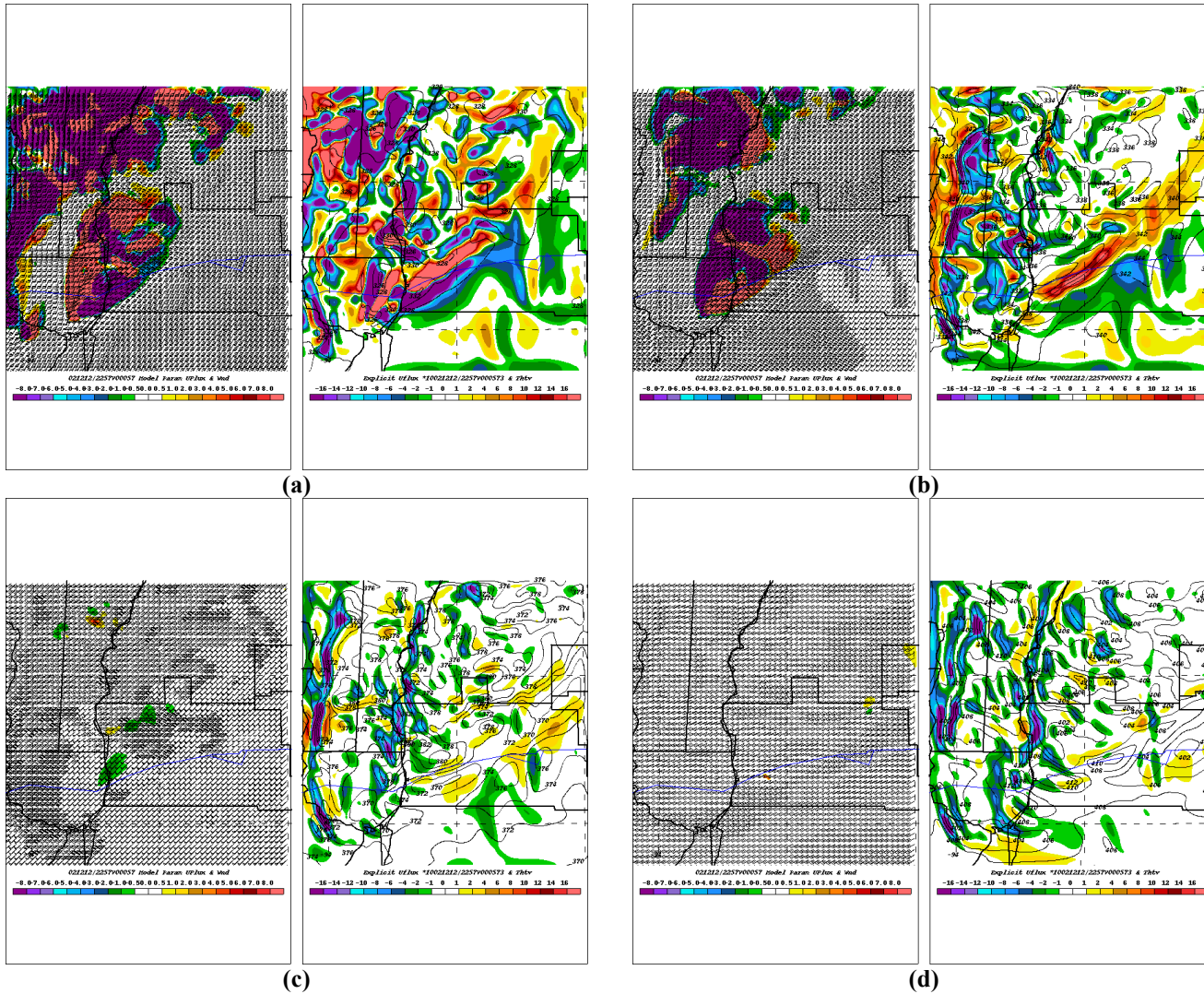


Figure 42: MASS667C two-panel plots of model parameterized u-momentum flux (left panel) and spatially-derived explicit u-momentum flux valid 2257 UTC 12 December 2002 at (a) 10km; (b) 12km; (c) 14km; (d) 16km MMSL.

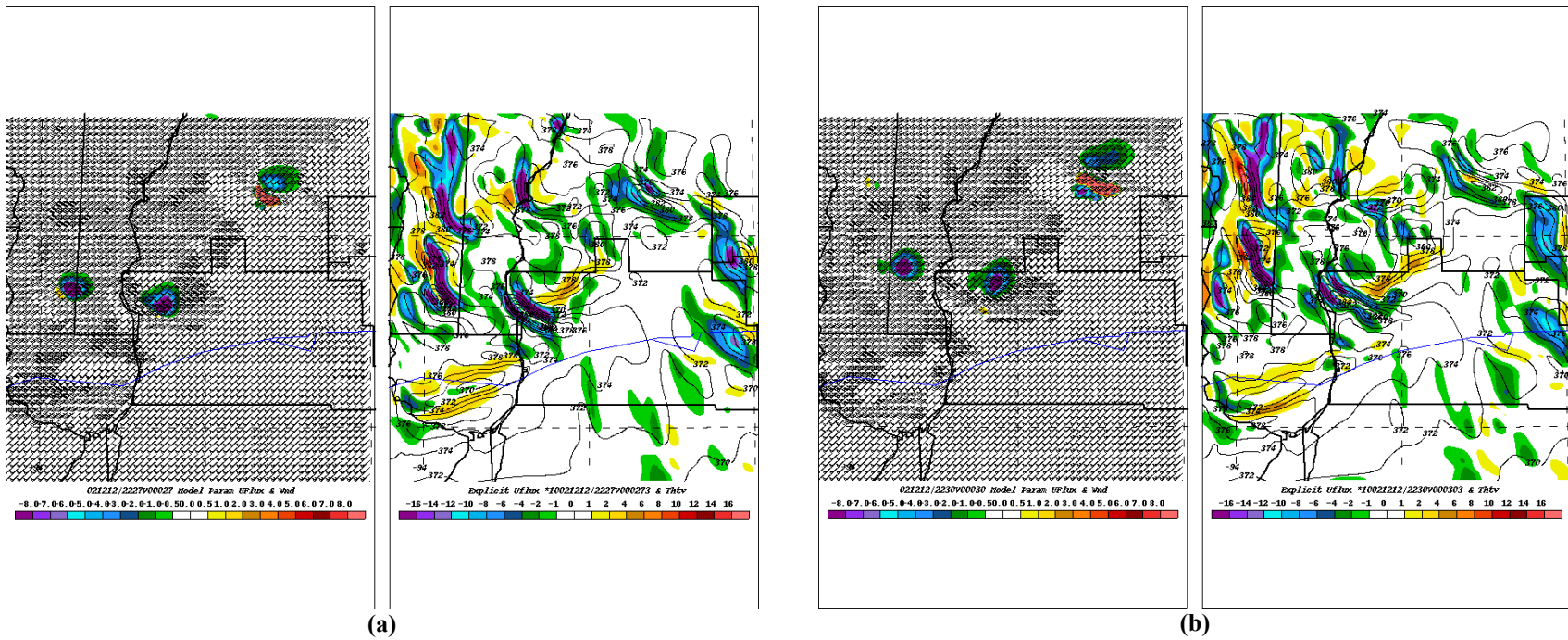


Figure 43: As with Fig. 42, but for 14 km valid (a) 2227 UTC; (b) 2230 UTC 12 December 2002.

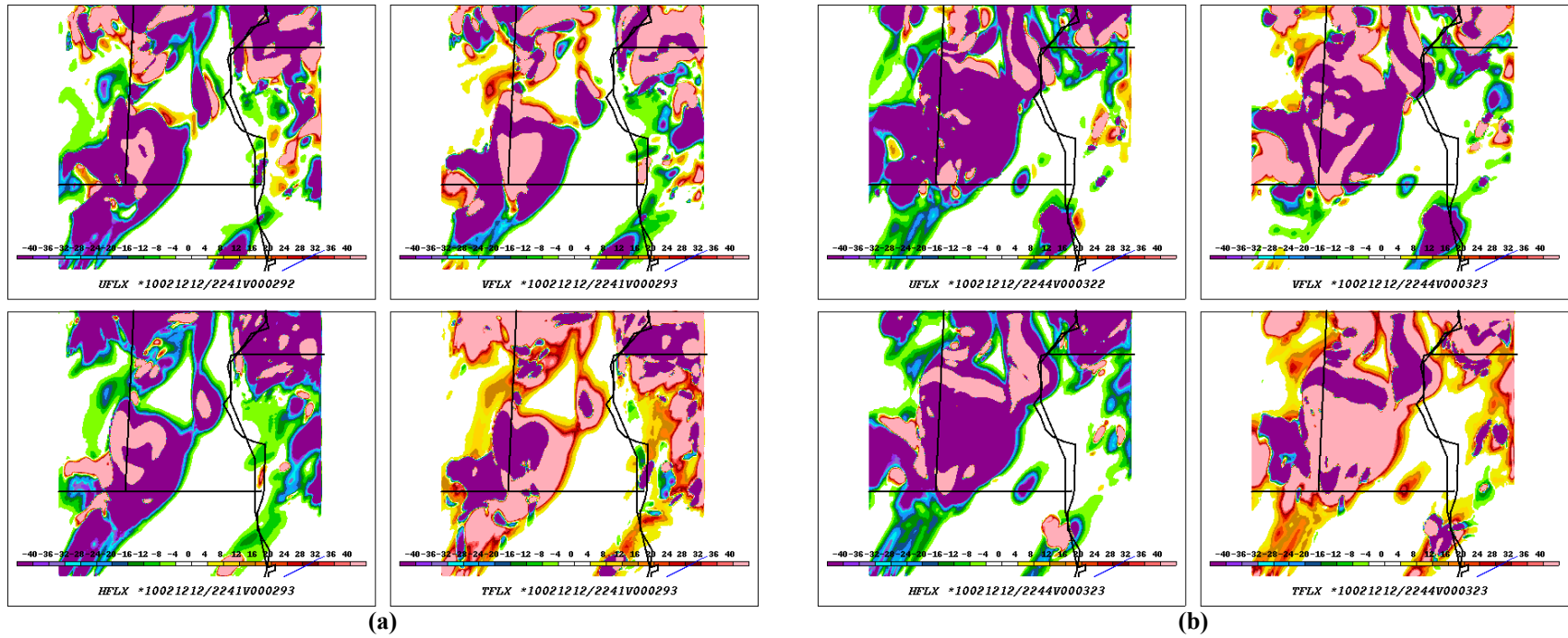


Figure 44: MASS222C four-panel plot (color fill) of scaled model-parameterized u-momentum (top left), v-momentum (top right), heat (bottom left) and TKE (bottom right) flux at 8 km valid (a) 2241 UTC; (b) 2244 UTC 12 December 2002.

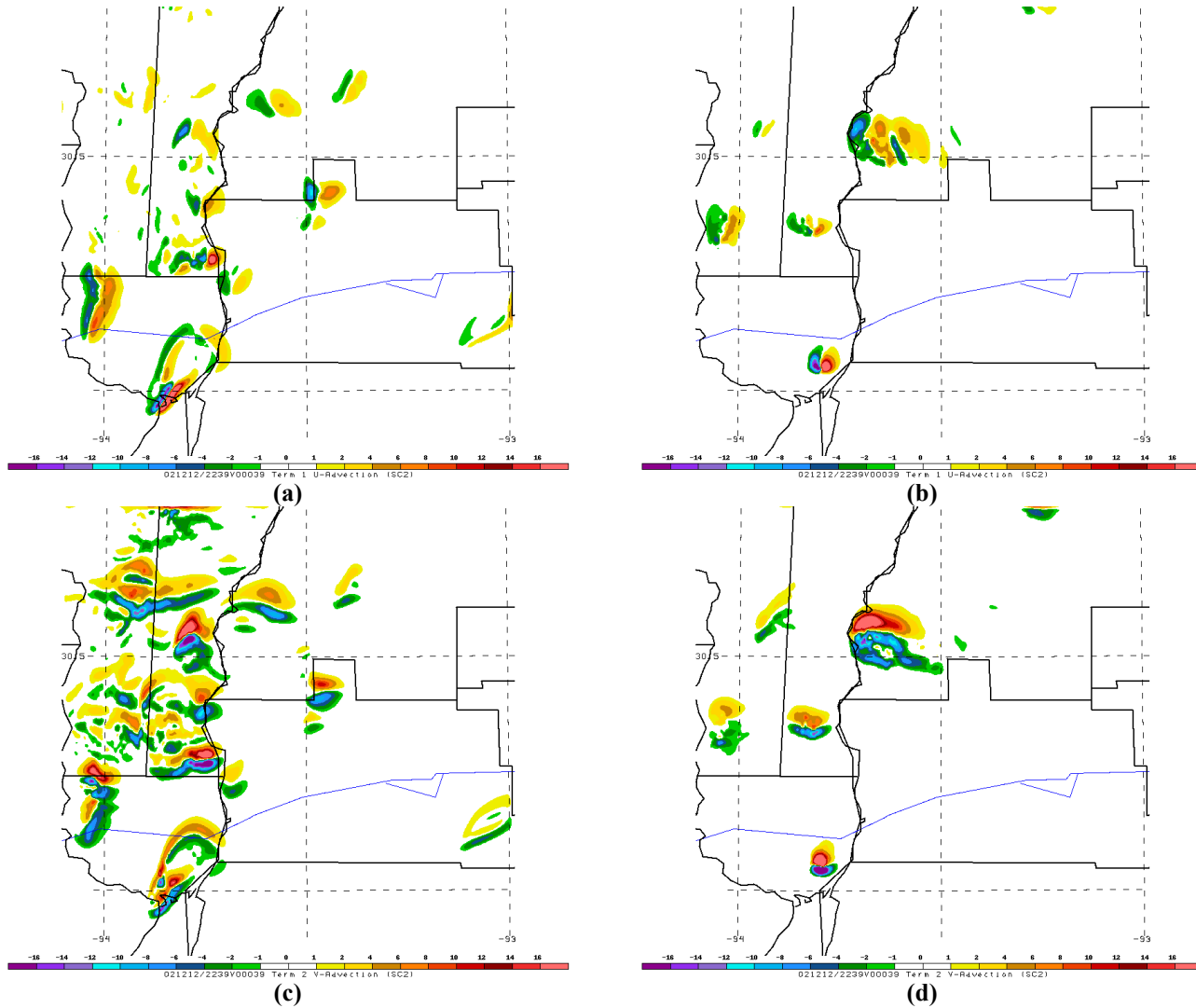
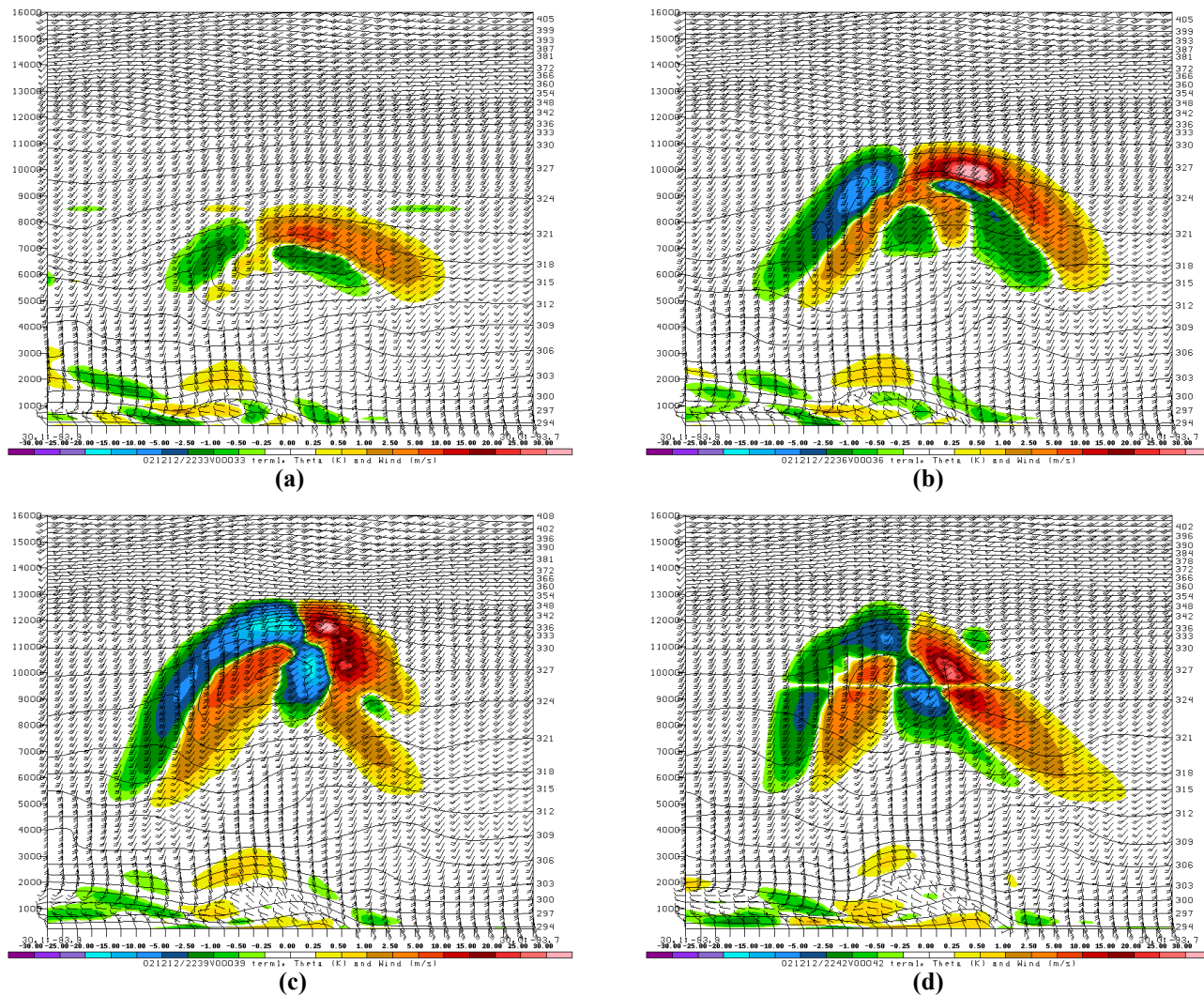
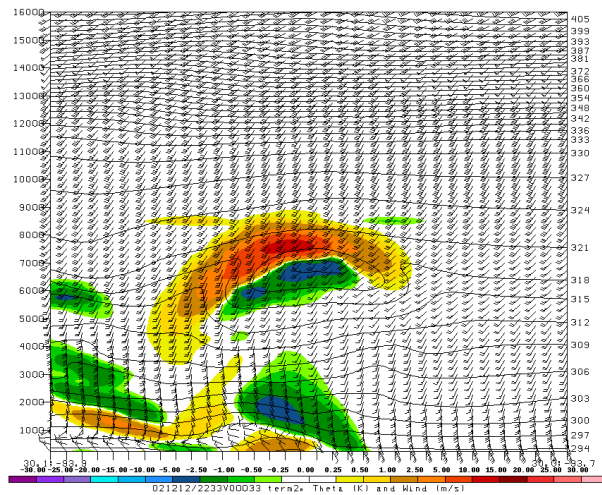


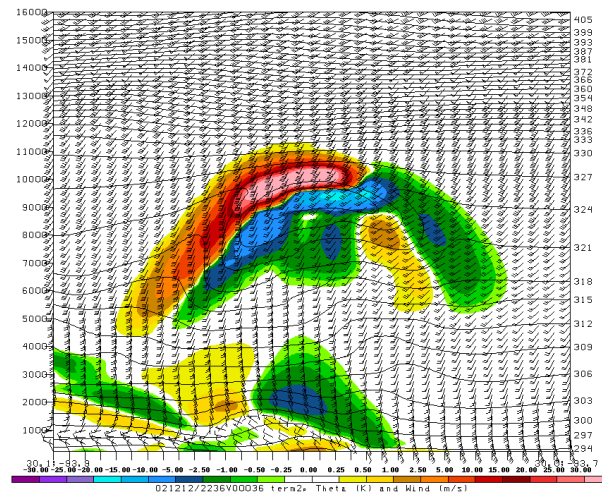
Figure 45: MASS667C explicit grid-based turbulence diagnostics valid 2239 UTC 12 December 2002 for Term 1: U-Advection at (a) 8km; (b) 12km; and for Term 2: V-Advection, for (c) 8km; (d) 12km MMSL.



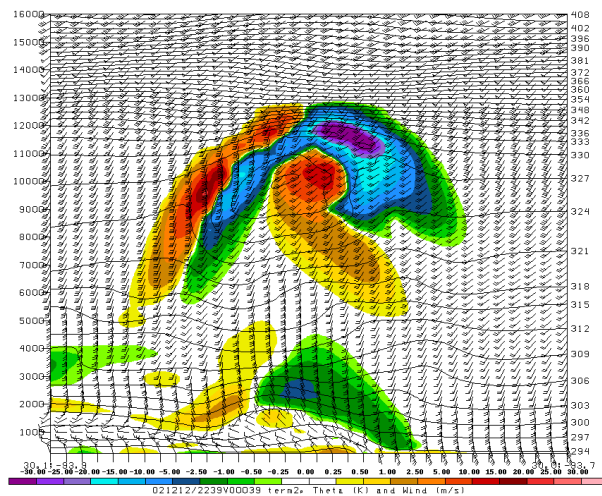
**Figure 46: MASS667C cross-section through Orange County, TX convection of Term 1- U-Mechanical Shear (color fill), wind (barbs) and virtual potential temperature (contoured) valid (a) 2233 UTC; (b) 2236 UTC; (c) 2239 UTC; (d) 2242 UTC 12 December 2002.**



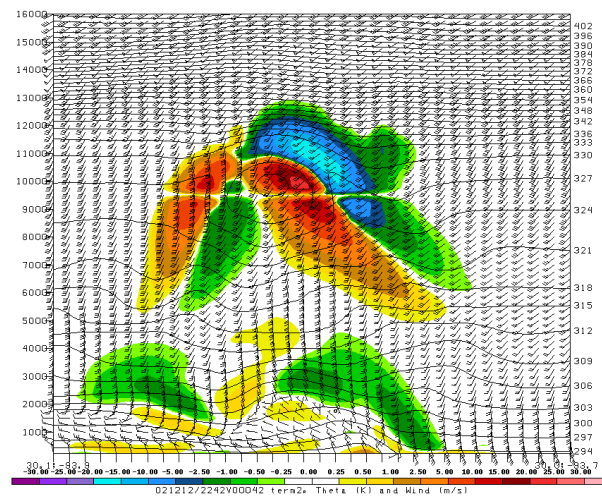
(a)



(b)



(c)



(d)

Figure 47: As with Fig. 46, but for Term 2: V-Advection, valid (a) 2233 UTC; (b) 2236 UTC; (c) 2239 UTC; (d) 2242 UTC 12 December 2002.

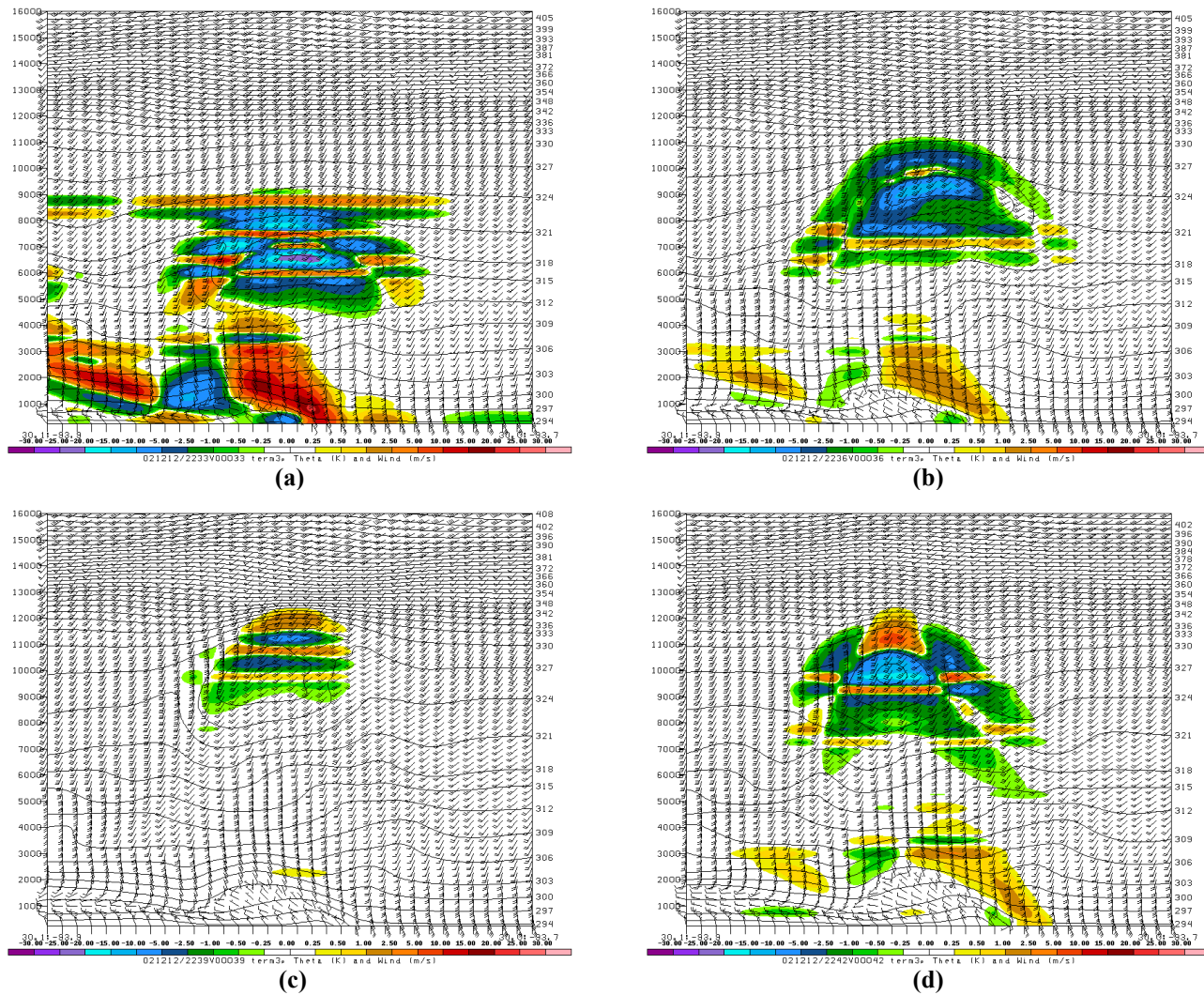


Figure 48: As with Fig. 47, but for Term 3: W-Advection, valid (a) 2233 UTC; (b) 2236 UTC; (c) 2239 UTC; (d) 2242 UTC 12 December 2002.

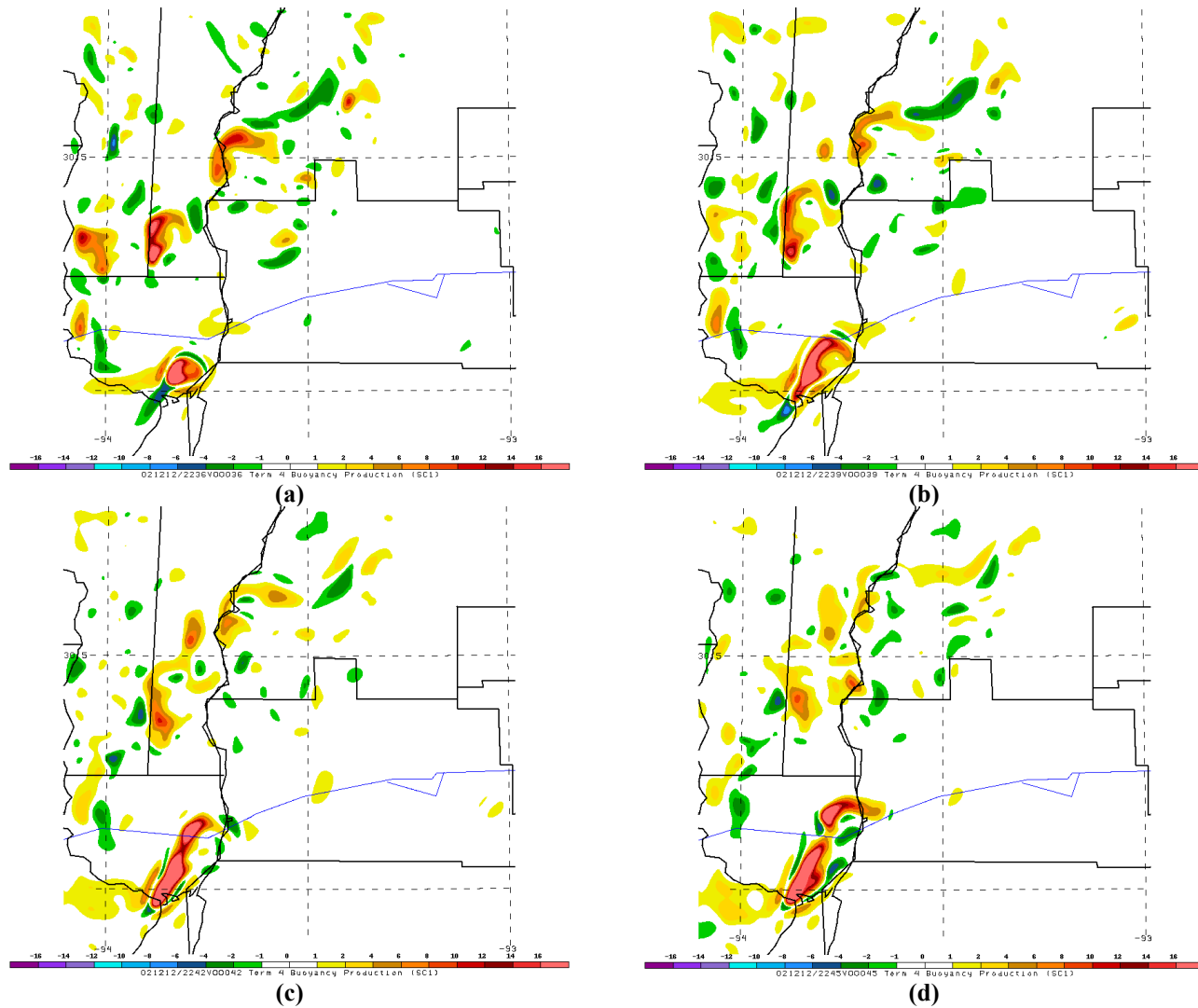


Figure 49: MASS667C explicit grid-based turbulence diagnostics valid 2239 UTC 12 December 2002 for Term 4: Buoyancy Production at 8 km for (a) 2236 UTC; (b) 2239 UTC; (c) 2242 UTC; (d) 2245 UTC 12 December 2002.

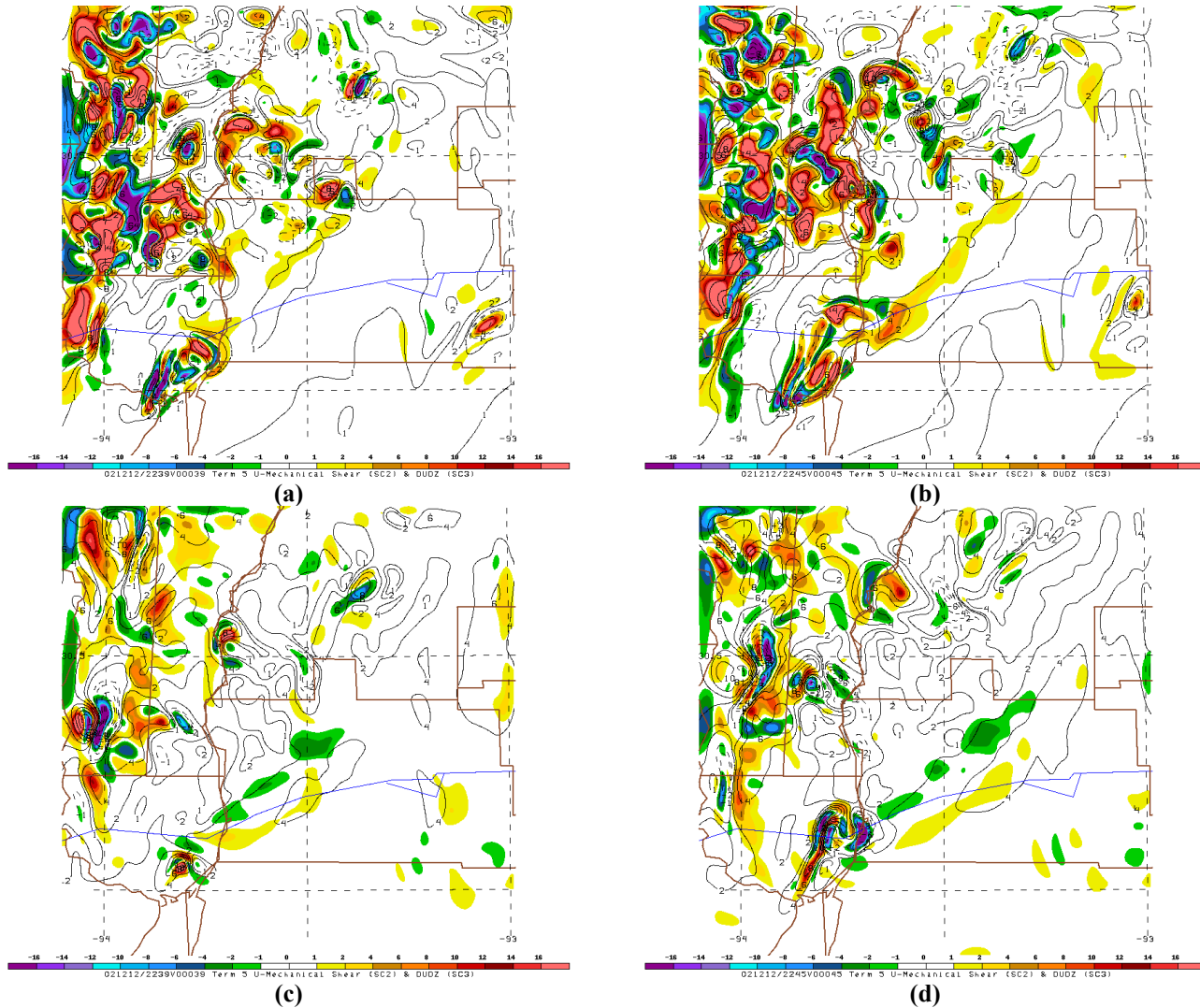


Figure 50: MASS667C explicit grid-based turbulence diagnostics for Term 5: U-Mechanical Shear (color fill) and u-wind shear (solid positive, dash negative contours) for 8 km at (a) 2239; (b) 2245 UTC; and 12 km at (c) 2239 UTC; (d) 2245 UTC 12 December 2002.

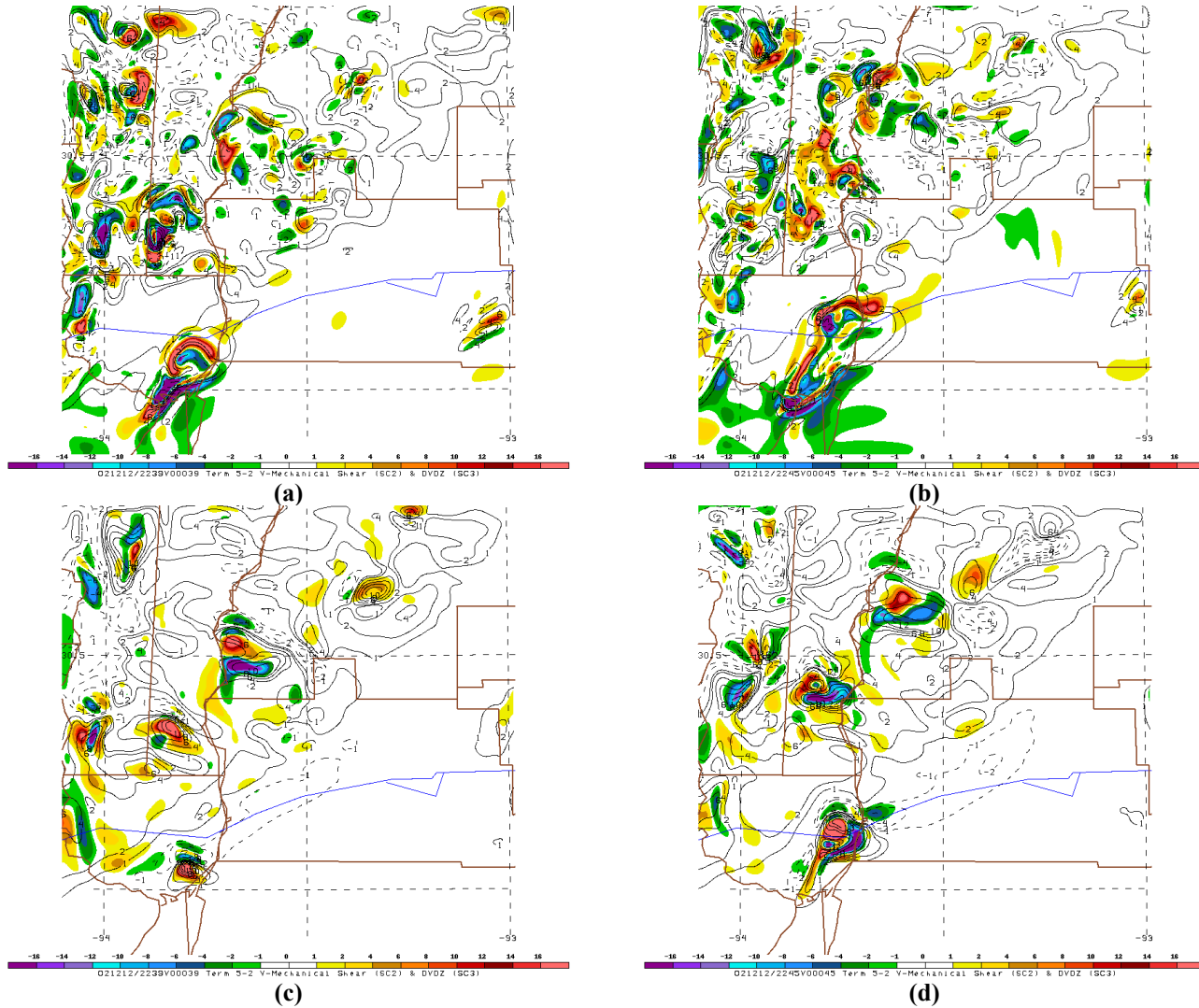
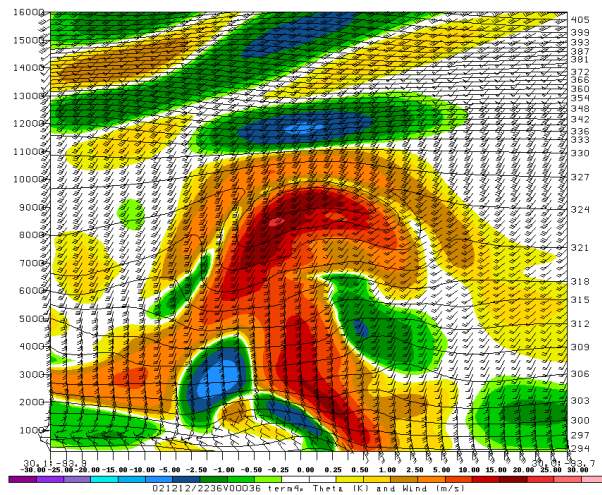
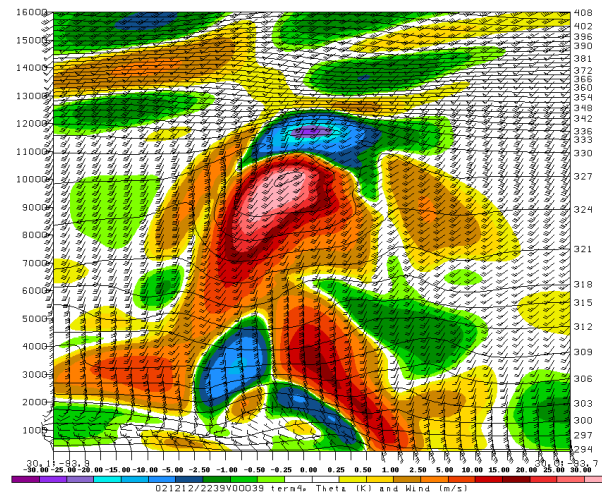


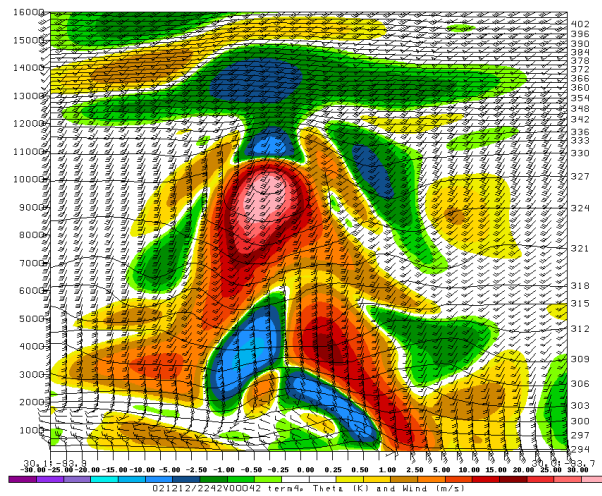
Figure 51: As with Fig. 50, but for Term 5-2: V-Mechanical Shear and v-wind shear for (a) 2239 UTC; (b) 2245 UTC at 8 km and (c) 2239 UTC; (d) 2245 UTC 12 December 2002 at 12 km.



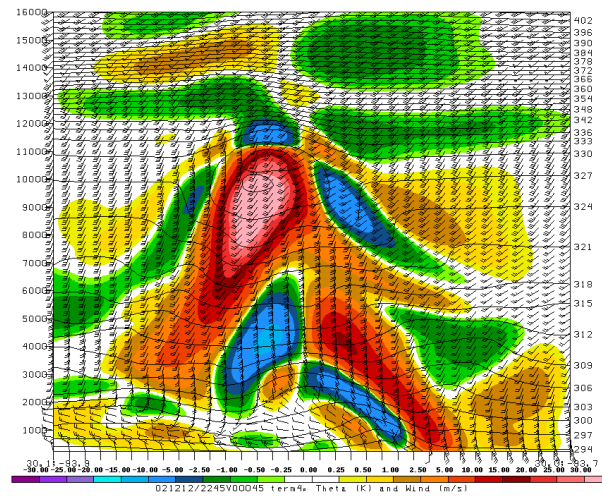
(a)



(b)

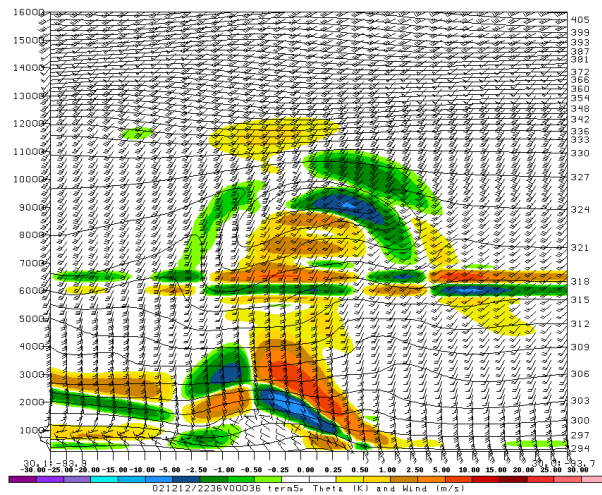


(c)

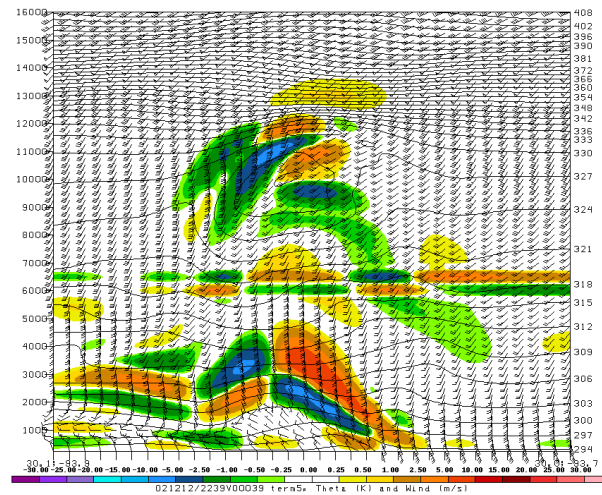


(d)

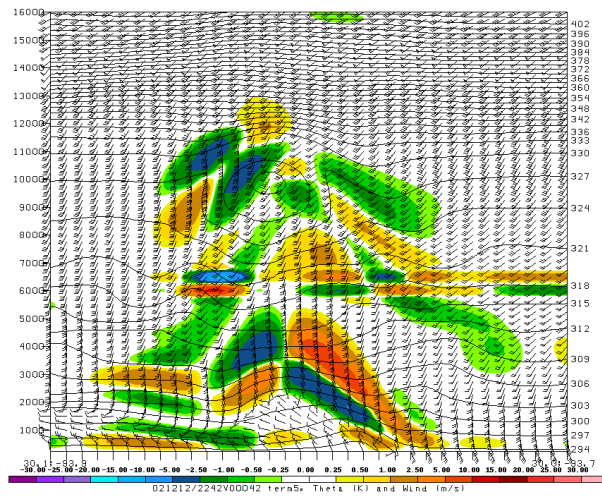
Figure 52: MASS667C cross-section through Orange County, TX convection of Term 4- Buoyancy (color fill), wind (barbs) and virtual potential temperature (contoured) valid (a) 2233 UTC; (b) 2236 UTC; (c) 2239 UTC; (d) 2242 UTC 12 December 2002.



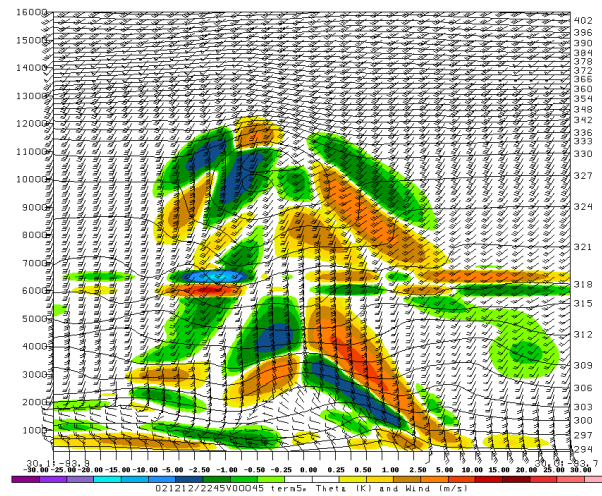
(a)



(b)

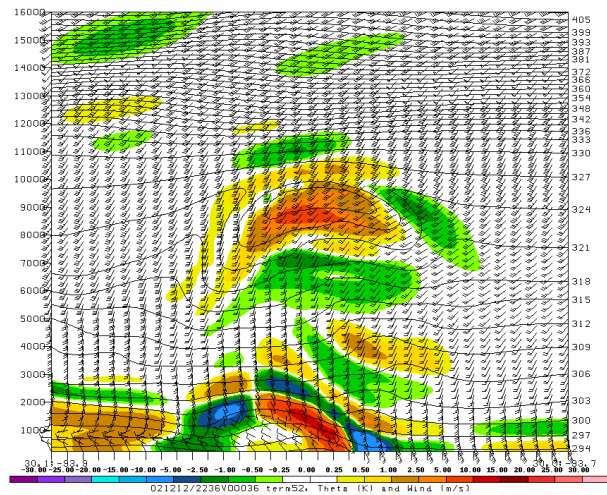


(c)

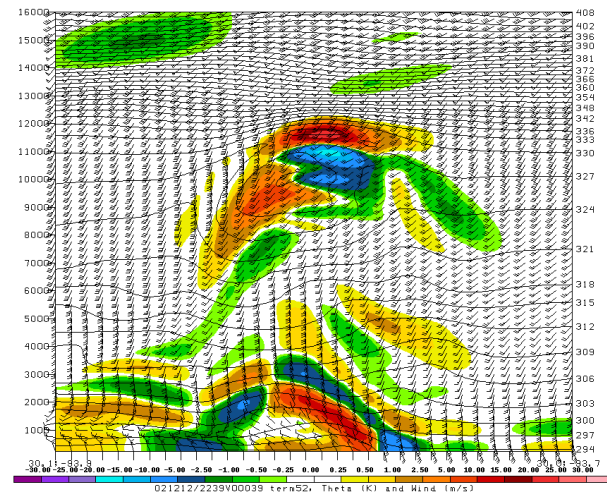


(d)

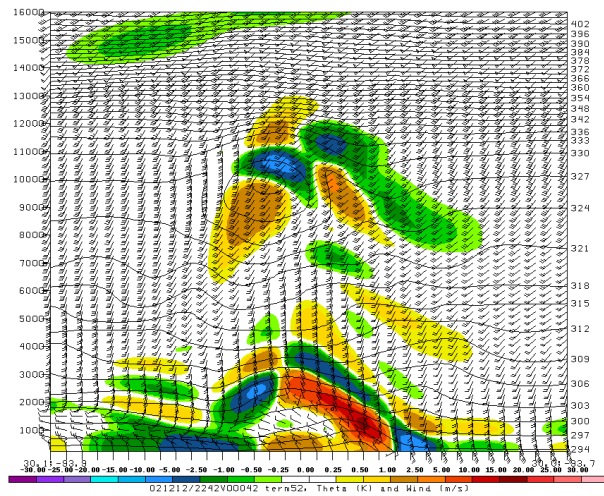
Figure 53: As with Fig. 52, but for Term 5- U-Mechanical Shear, valid (a) 2233 UTC; (b) 2236 UTC; (c) 2239 UTC; (d) 2242 UTC 12 December 2002.



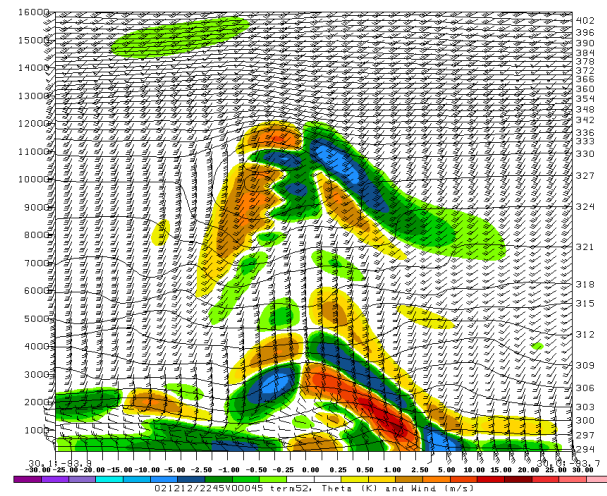
(a)



(b)



(c)



(d)

Figure 54: As with Fig. 53, but for Term 5-2 V-Mechanical Shear, valid (a) 2233 UTC; (b) 2236 UTC; (c) 2239 UTC; (d) 2242 UTC 12 December 2002.

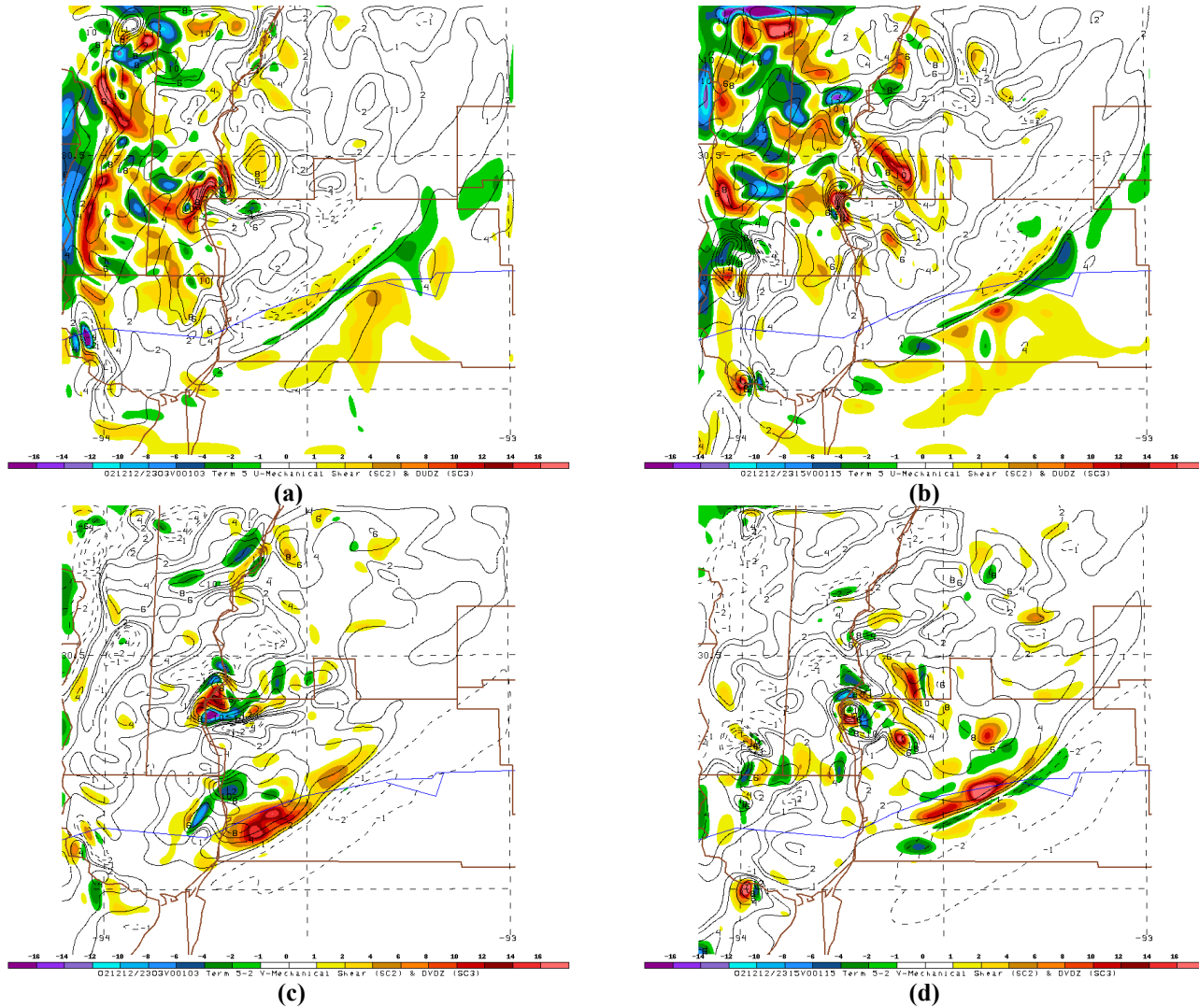


**Figure 55: MASS667C Term 5 U-Mechanical Shear at 12 km valid (a) 2303 UTC; (b) 2315 UTC; and Term 5-2 V-Mechanical at 12km valid (c) 2303 UTC; (d) 2315 UTC 12 December 2002.**

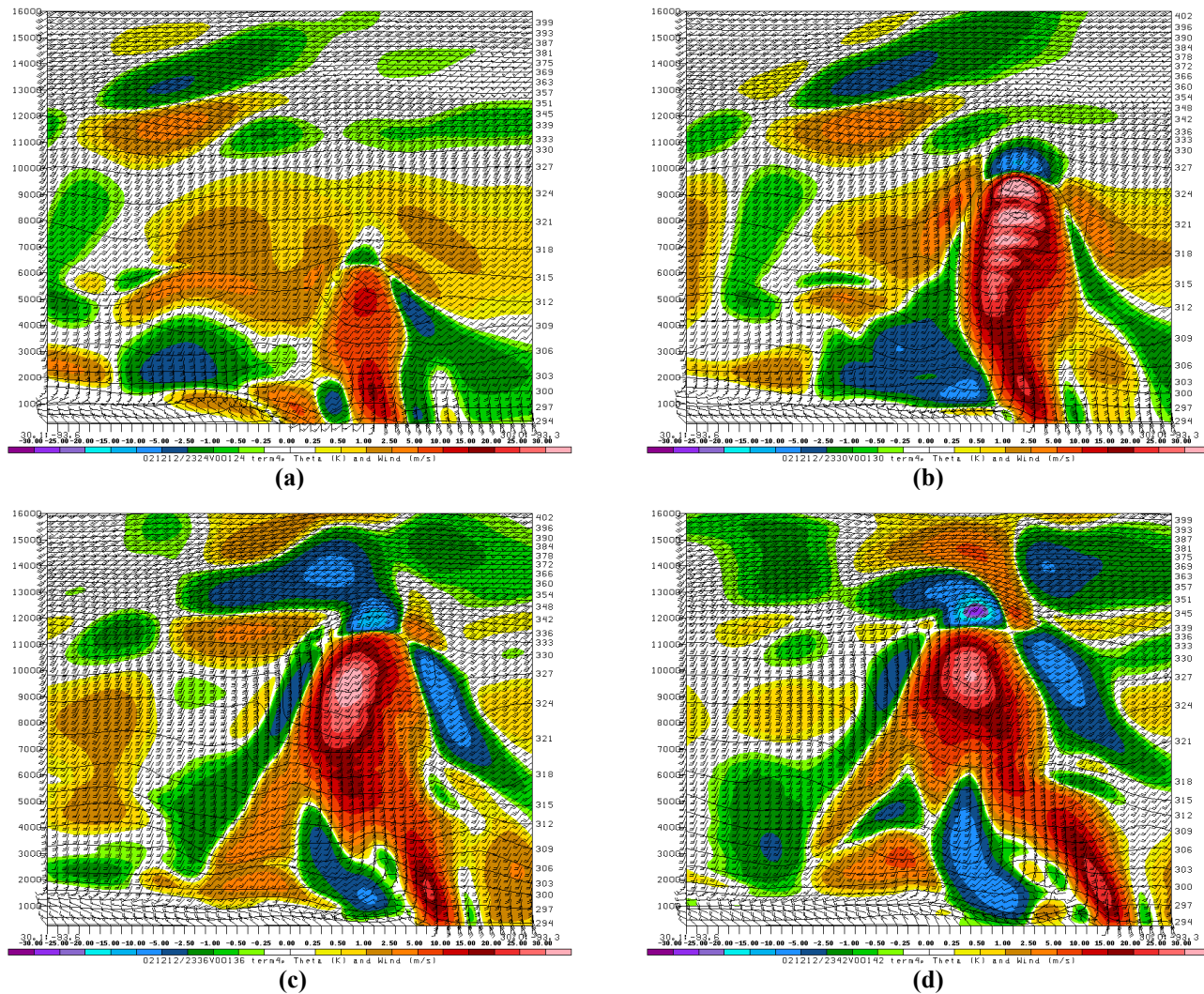


Figure 56: MASS667C cross-section through Beauregard Parish, LA convection of Term 4- Buoyancy (color fill), wind (barbs) and virtual potential temperature (contoured) valid (a) 2324 UTC; (b) 2330 UTC; (c) 2336 UTC; (d) 2342 UTC 12 December 2002.

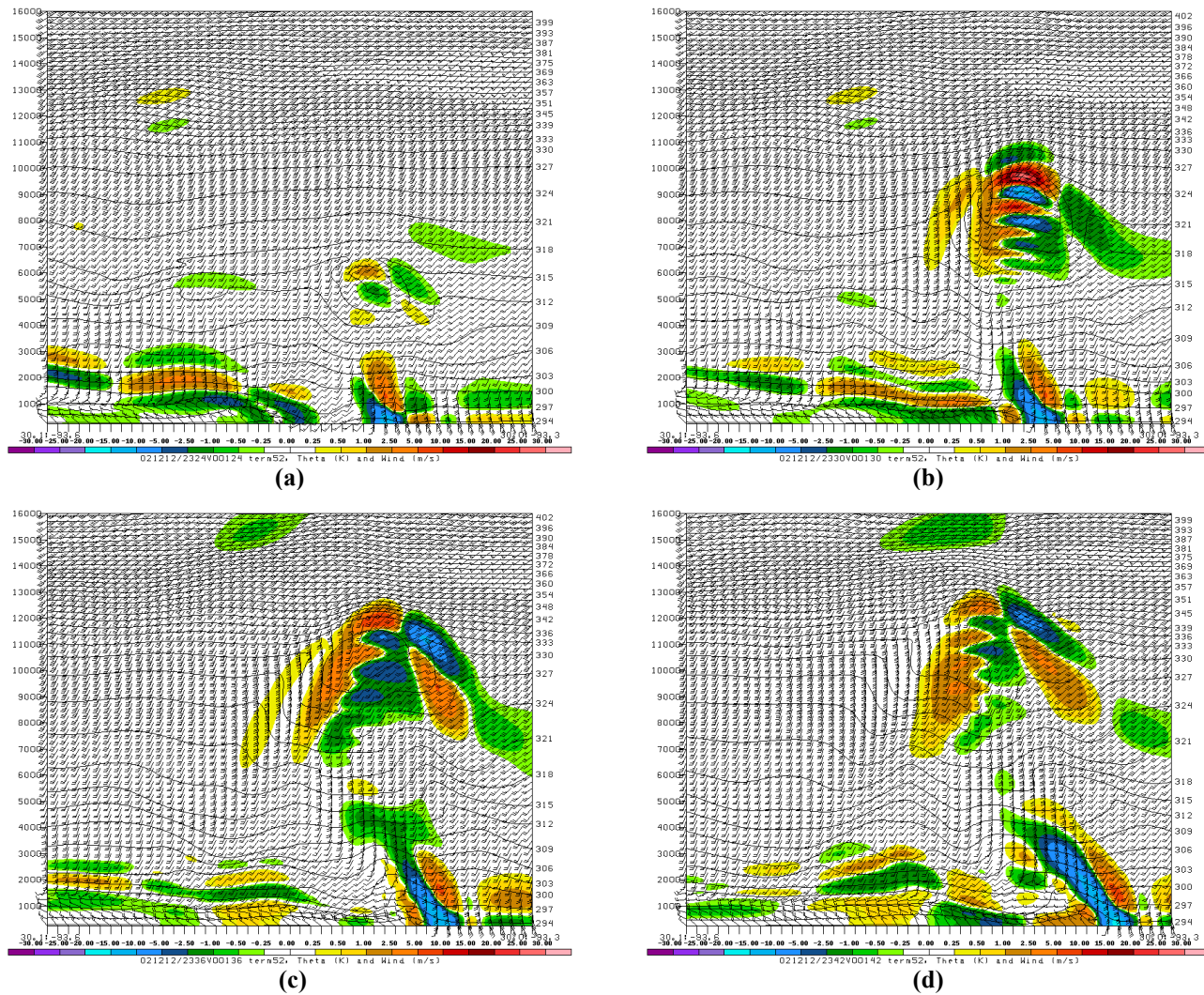
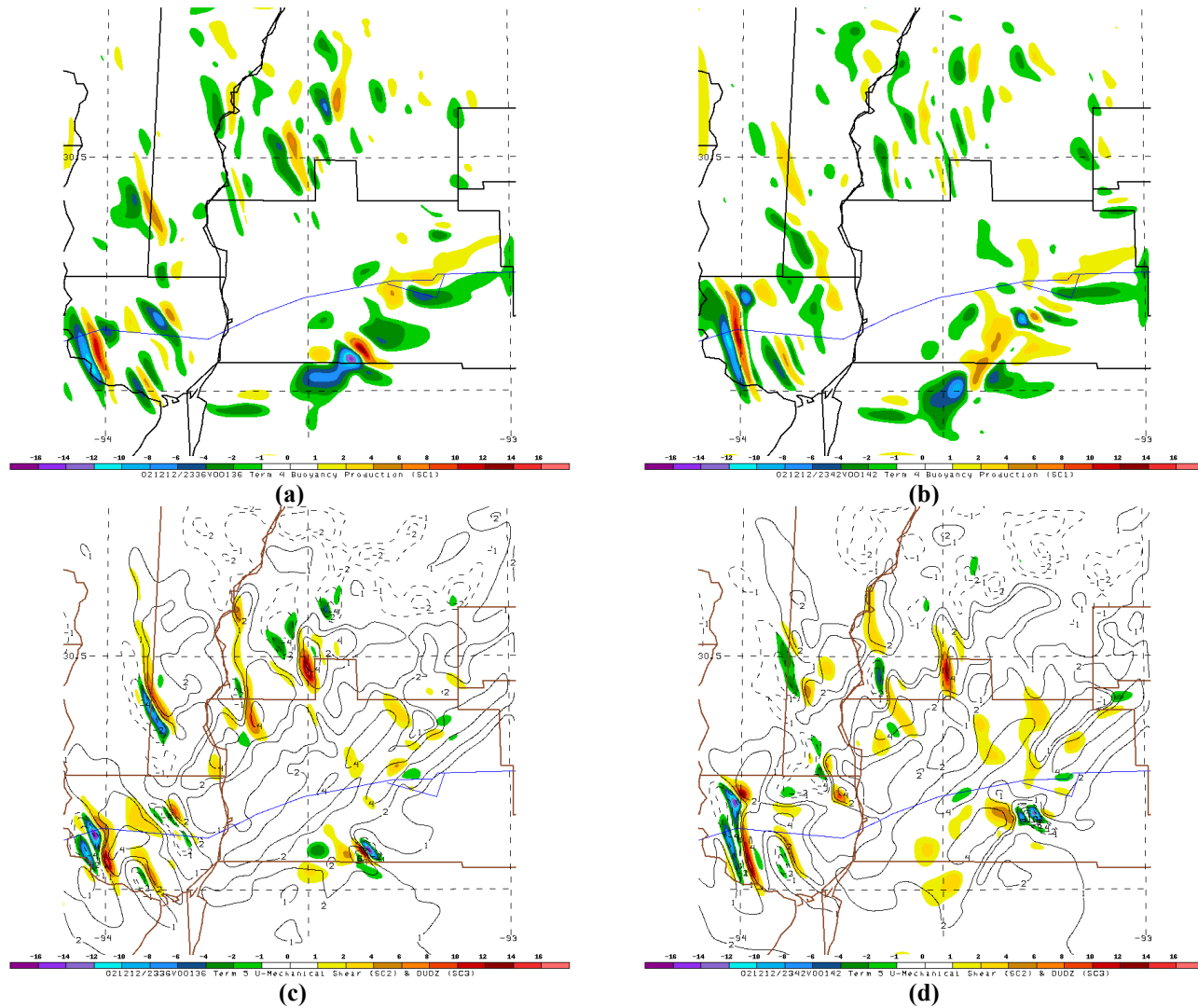


Figure 57: As with Fig. 56, but for V-Mechanical Shear, valid (a) 2324 UTC; (b) 2330 UTC; (c) 2336 UTC; (d) 2342 UTC 12 December 2002.



**Figure 58: MASS667CBuoyancy Production at 14 km valid (a) 2336 UTC; (b) 2342 UTC; and for V-Mechanical Shear Production (contour filled) and v-wind shear (contoured) at 14 km valid (c) 2336 UTC; (d) 2342 UTC 12 December 2002.**

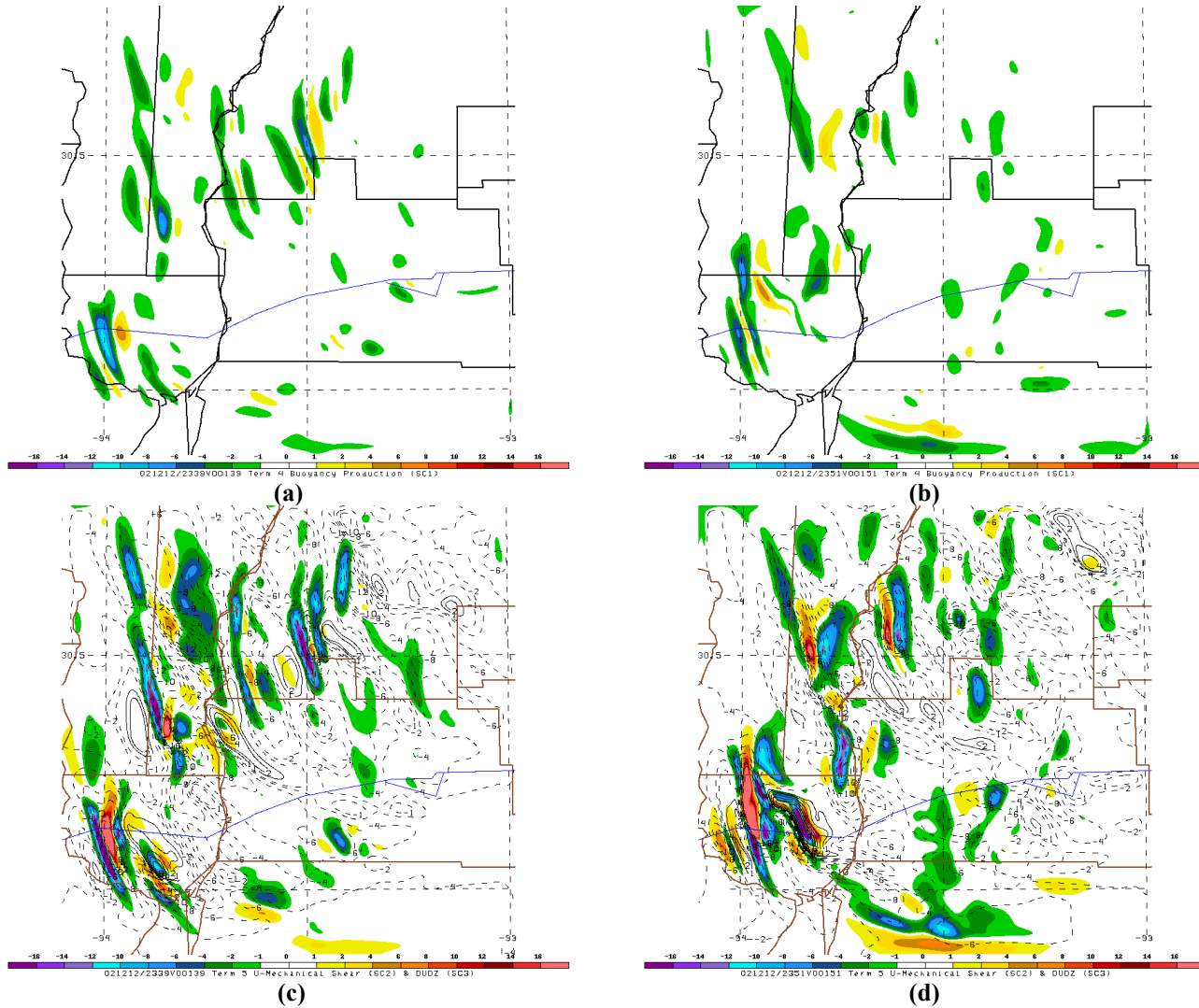


Figure 59: MASS667C Buoyancy Production at 18 km valid (a) 2339 UTC; (b) 2351 UTC; and for U-Mechanical Shear Production (color fill) and wind shear (countoured) at 18 km valid (c) 2339 UTC; (d) 2351 UTC 12 December 2002.

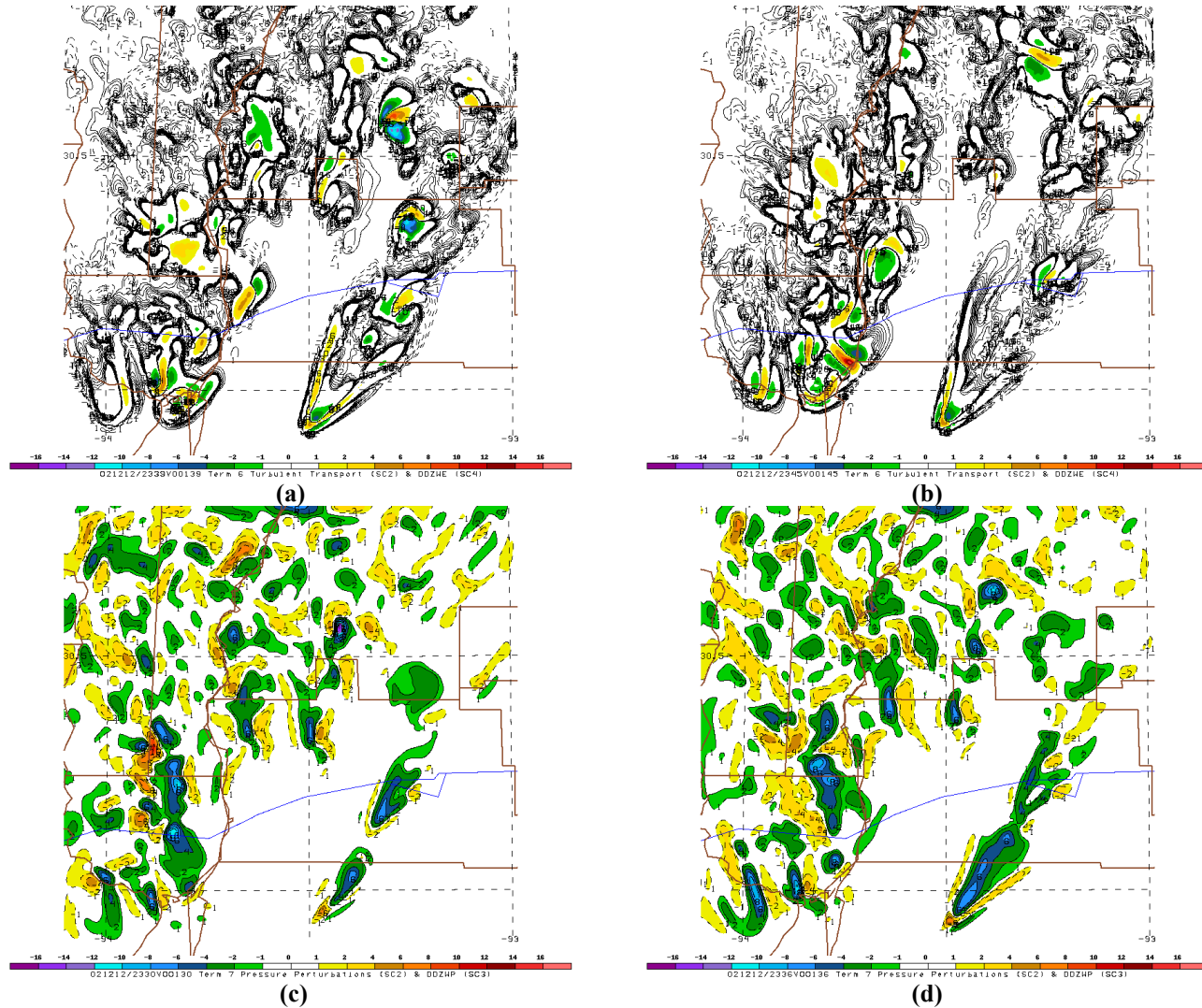


Figure 60: MASS667C Term 6: Turbulent Transport at 8 km valid (a) 2339 UTC; (b) 2351 UTC; and for Term 7: Pressure Perturbations at 8 km valid (c) 2339 UTC; (d) 2351 UTC 12 December 2002.

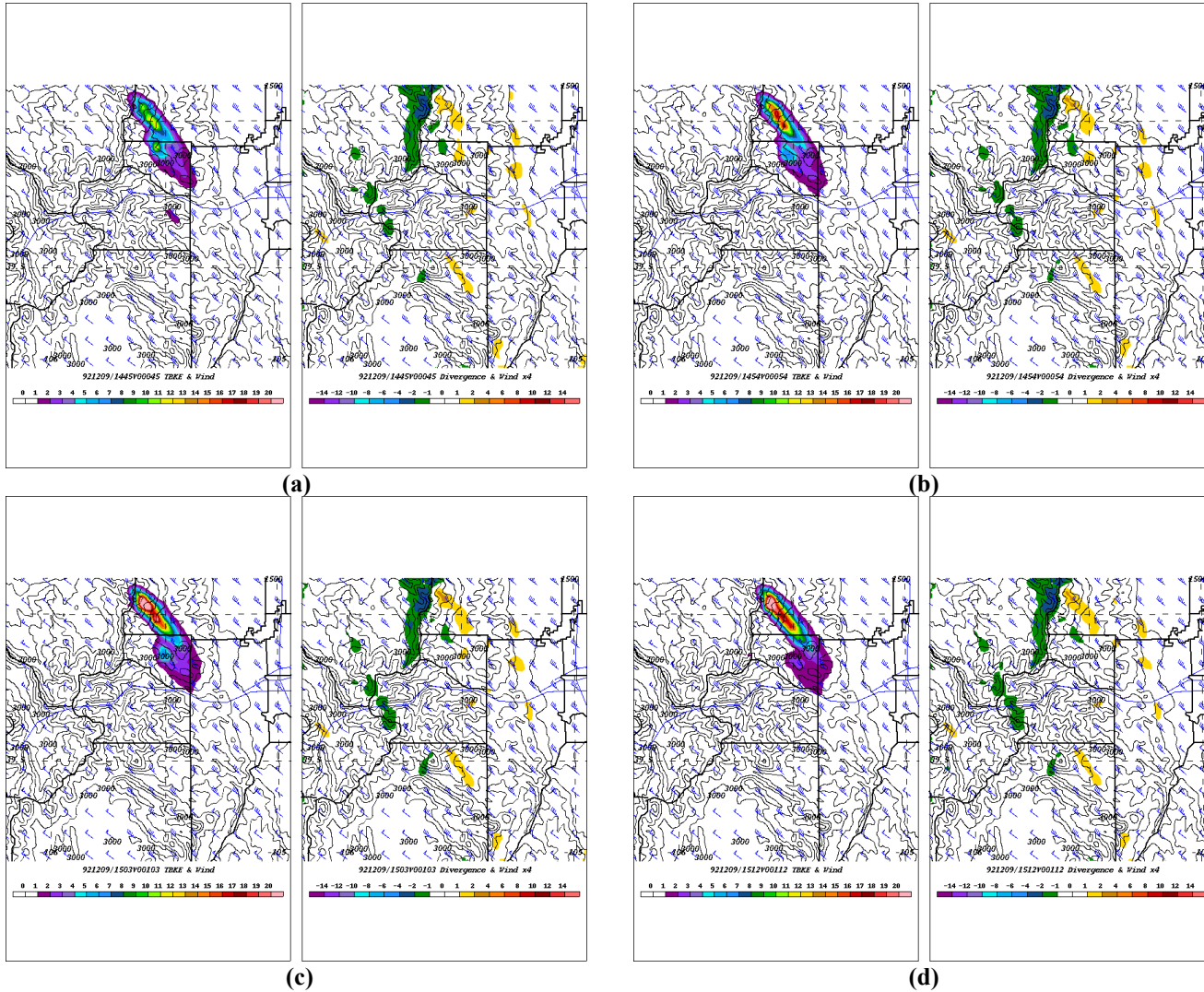


Figure 61: MASS2M 10 km model-derived TKE (left panel) and divergence (right panel) valid (a) 1445 UTC; (b) 1454 UTC; (c) 1503 UTC; (d) 1512 UTC 9 December 1992.

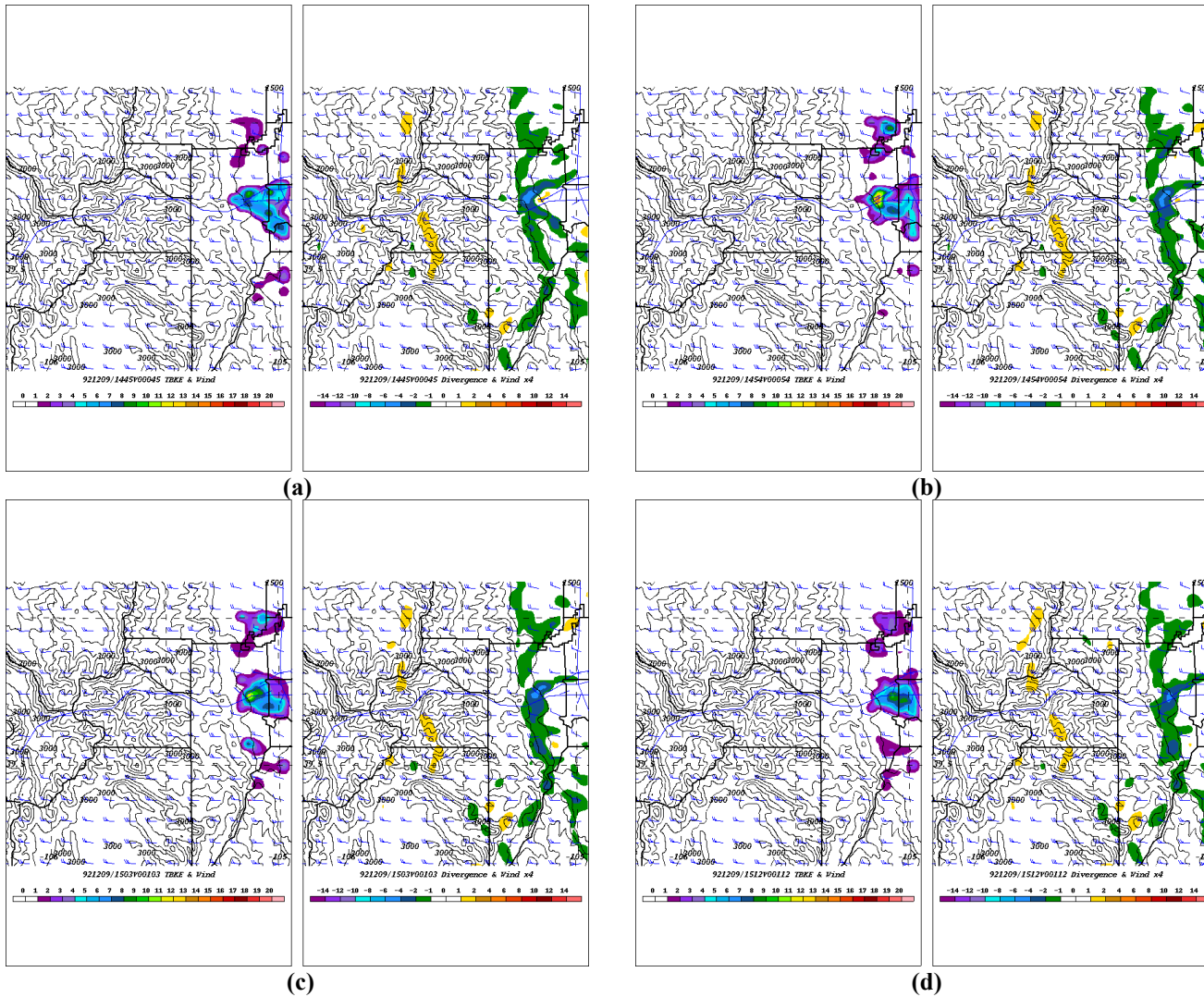


Figure 62: As with Fig. 61, but for 14 km valid (a) 1445 UTC; (b) 1454 UTC; (c) 1503 UTC; (d) 1512 UTC 9 December 1992.

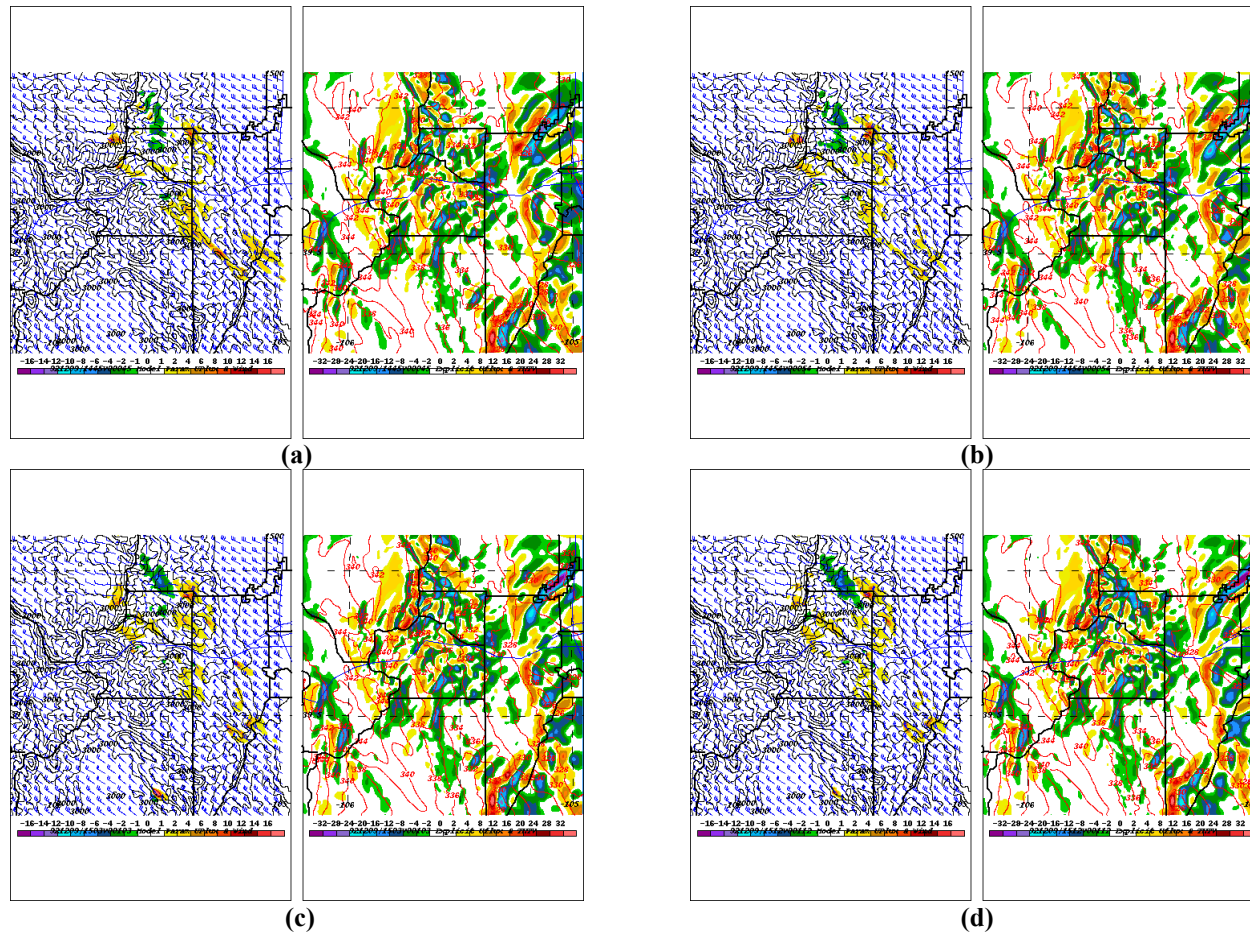


Figure 63: MASS667M model-parameterized u-momentum flux (left panel) versus explicit u-momentum flux (right panel) at 11.5 km valid (a) 1445 UTC; (b) 1454 UTC; (c) 1503 UTC; (d) 1512 UTC 9 December 1992.

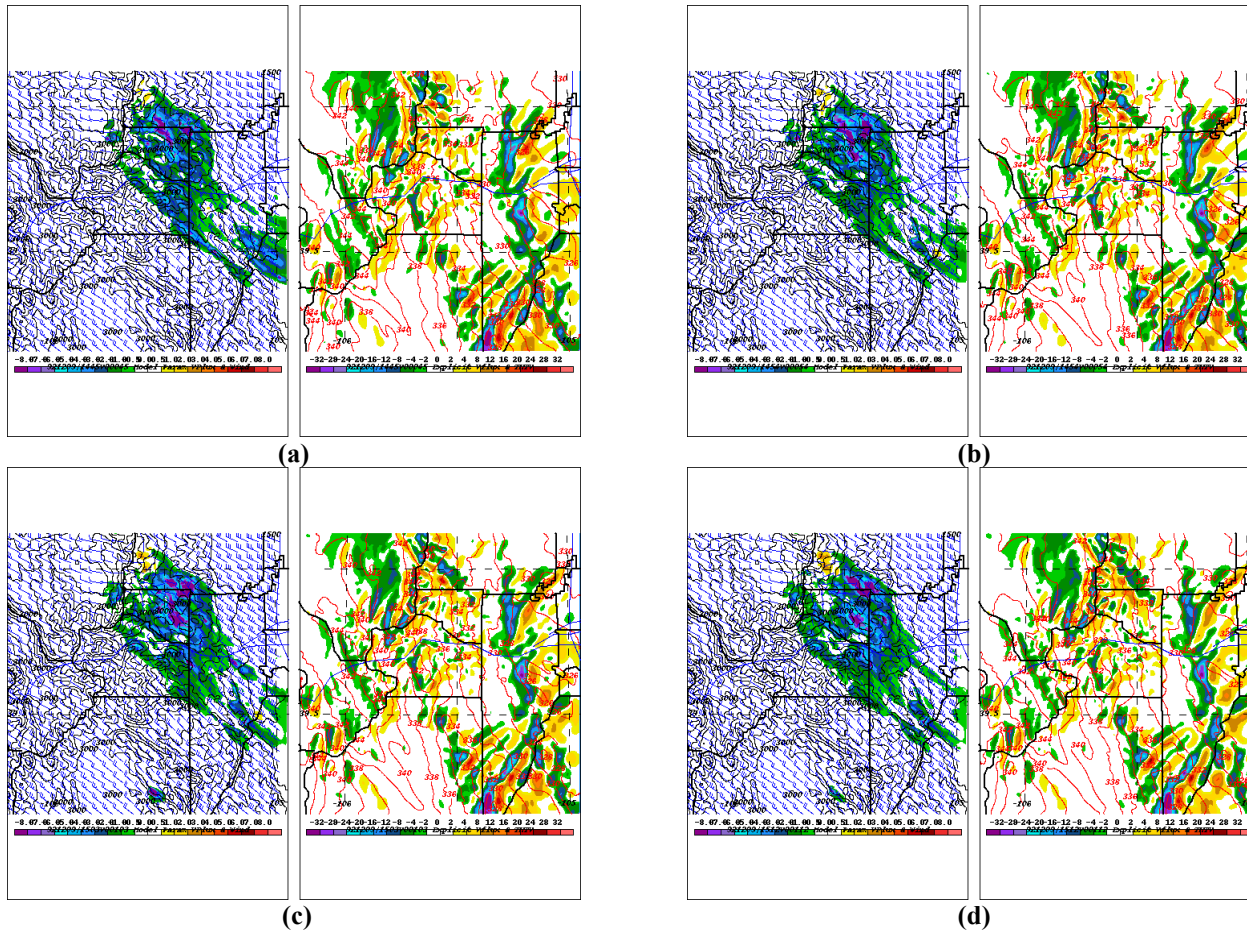


Figure 64: As with Fig. 63, but for v-momentum flux at 11.5 km valid (a) 1445 UTC; (b) 1454 UTC; (c) 1503 UTC; (d) 1512 UTC 9 December 1992.

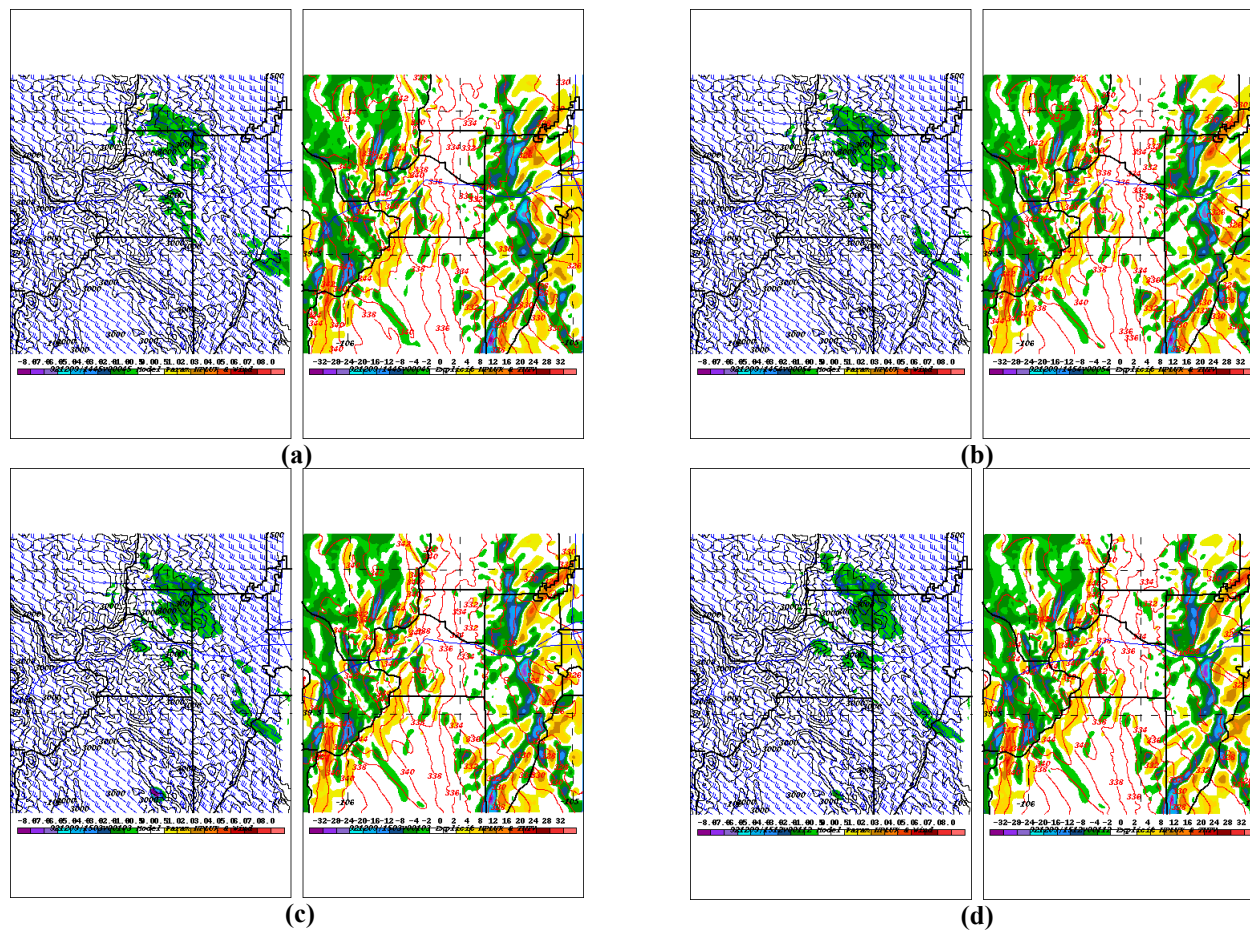
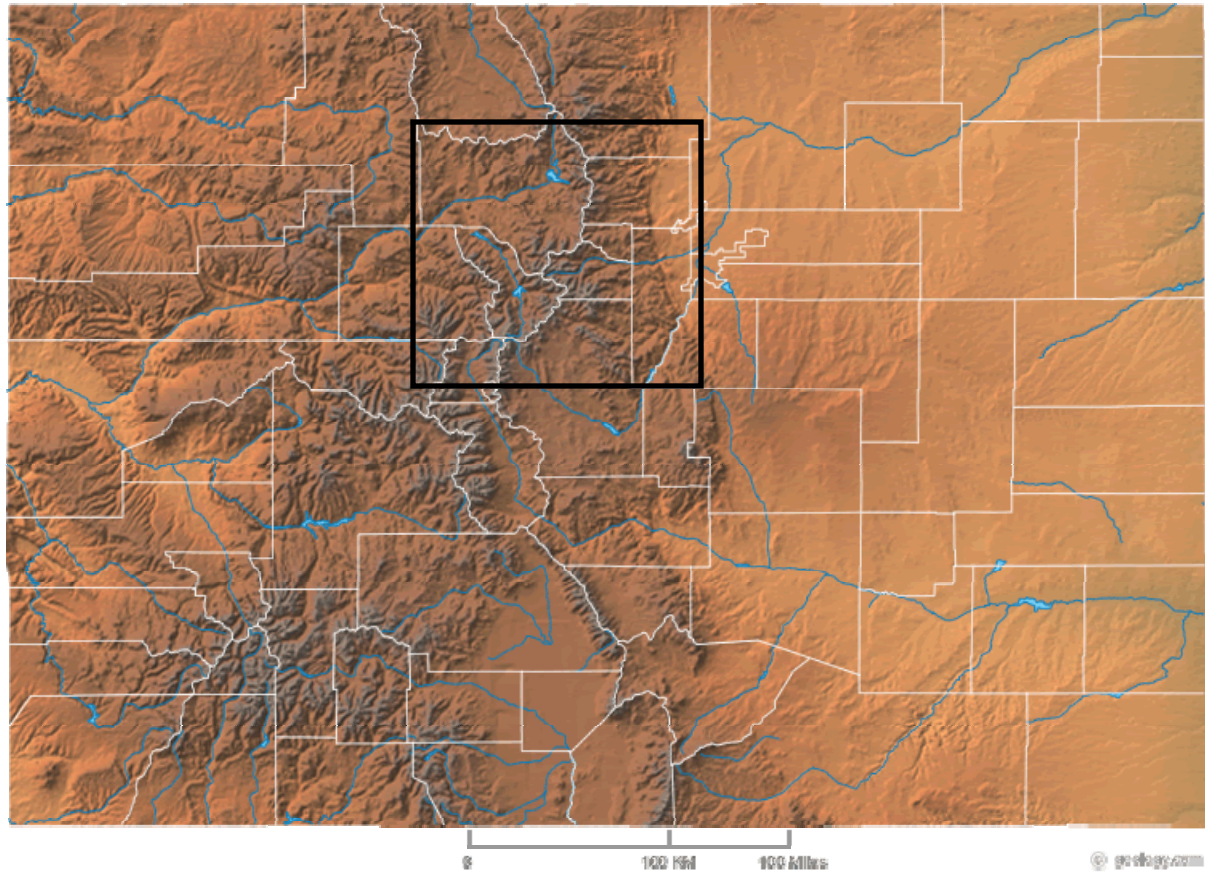


Figure 65: As with Fig. 63, but for v-momentum flux at 11.5 km valid (a) 1445 UTC; (b) 1454 UTC; (c) 1503 UTC; (d) 1512 UTC 9 December 1992.



**Figure 66: Physical map of the state of Colorado with county boundaries, highlighting the region of interest in the 9 December 1992 mountain wave study. Image courtesy geology.com.**

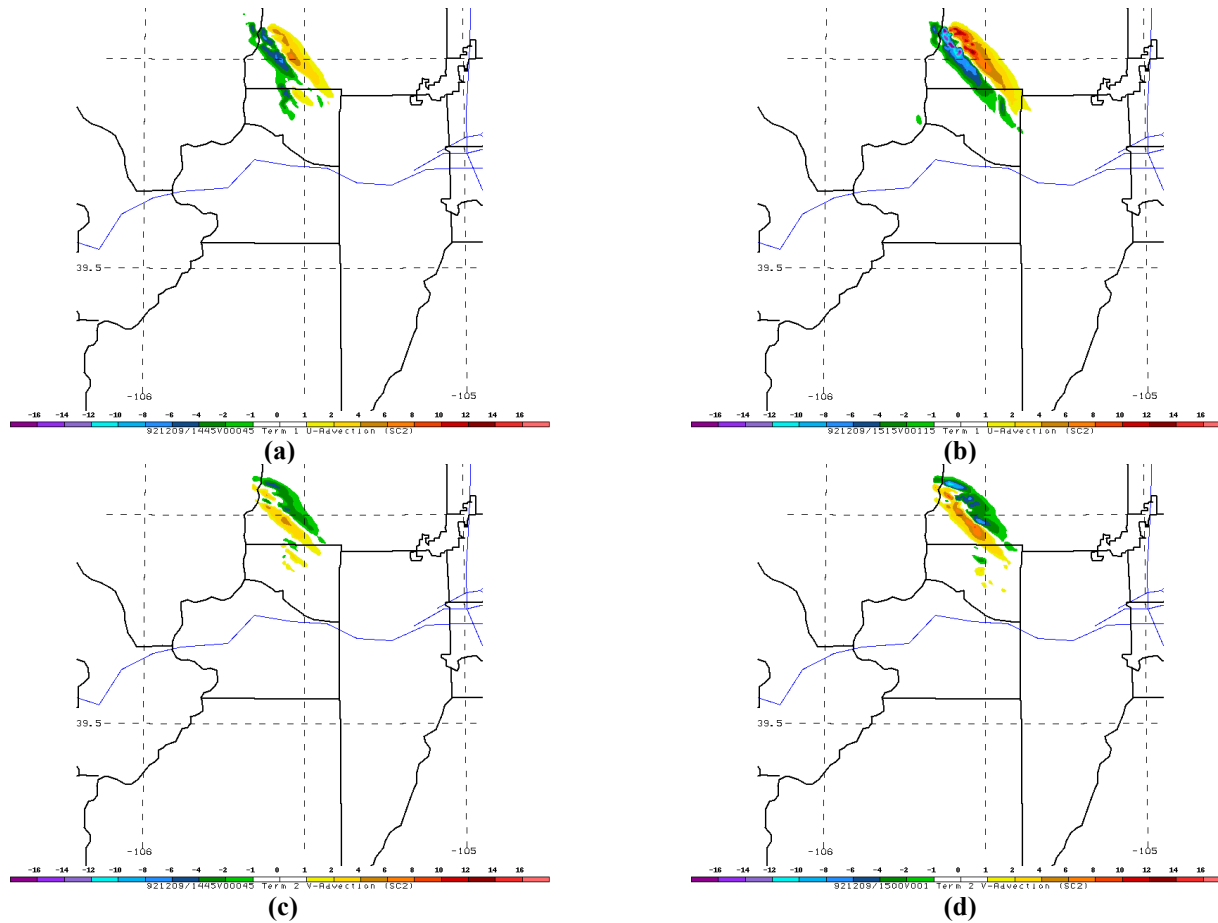


Figure 67: MASS667M explicit grid based turbulence diagnostics for Term 1: U-Advection at 9.75 km valid (a) 1445 UTC; (b) 1515 UTC; and for Term 2: V-Advection at 9.75 km valid (c) 1445 UTC; (d) 1515 UTC 9 December 1992.

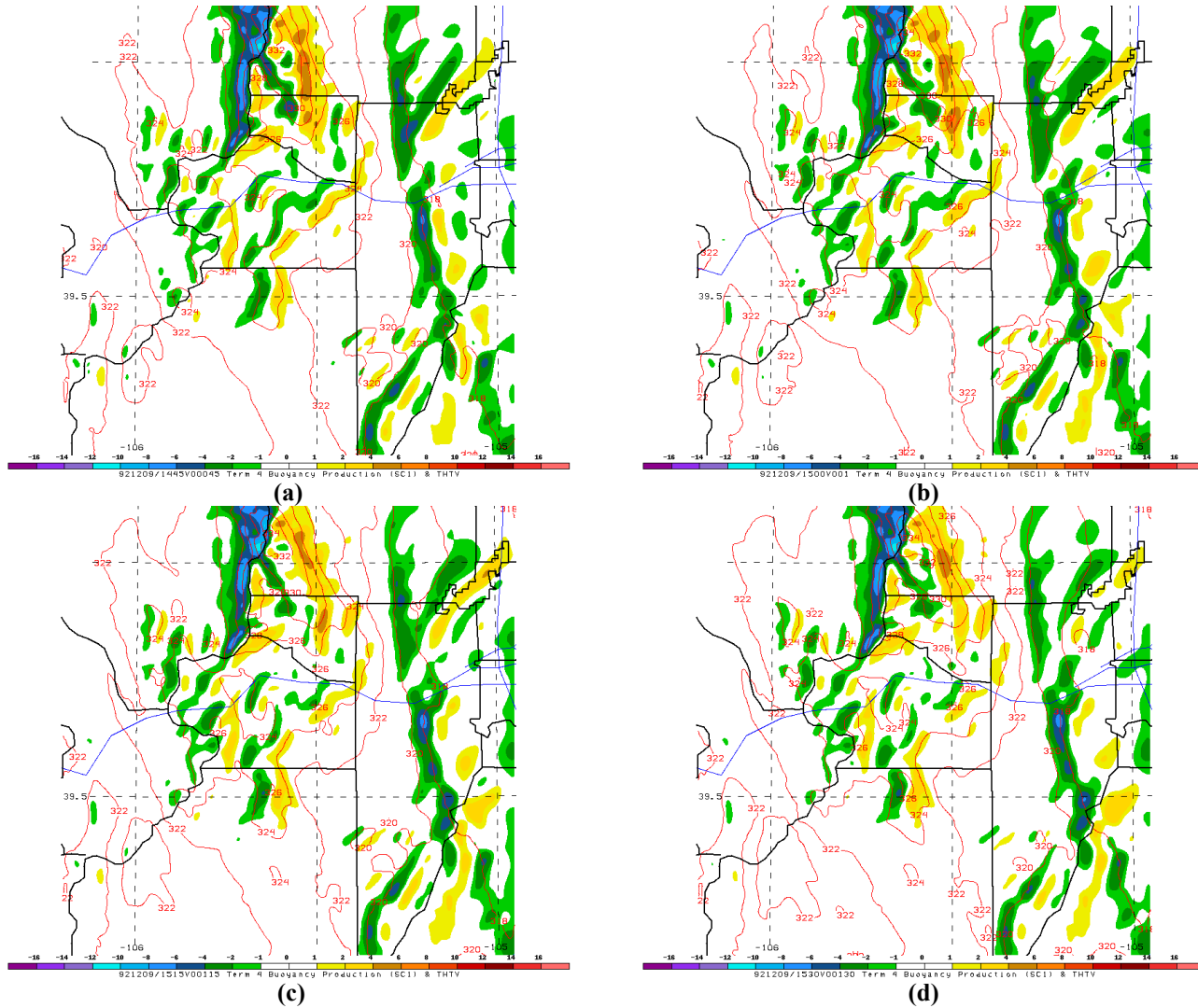
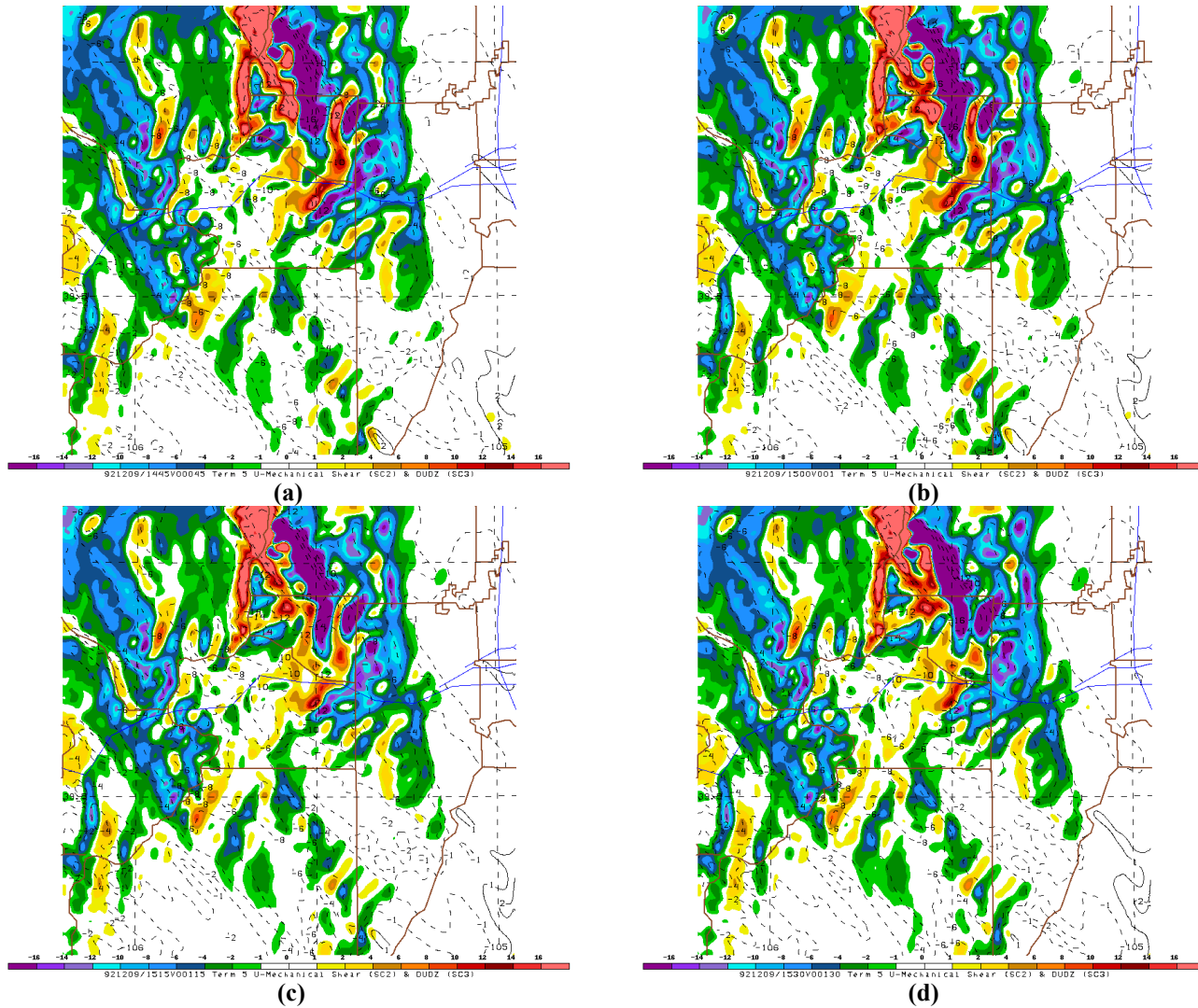
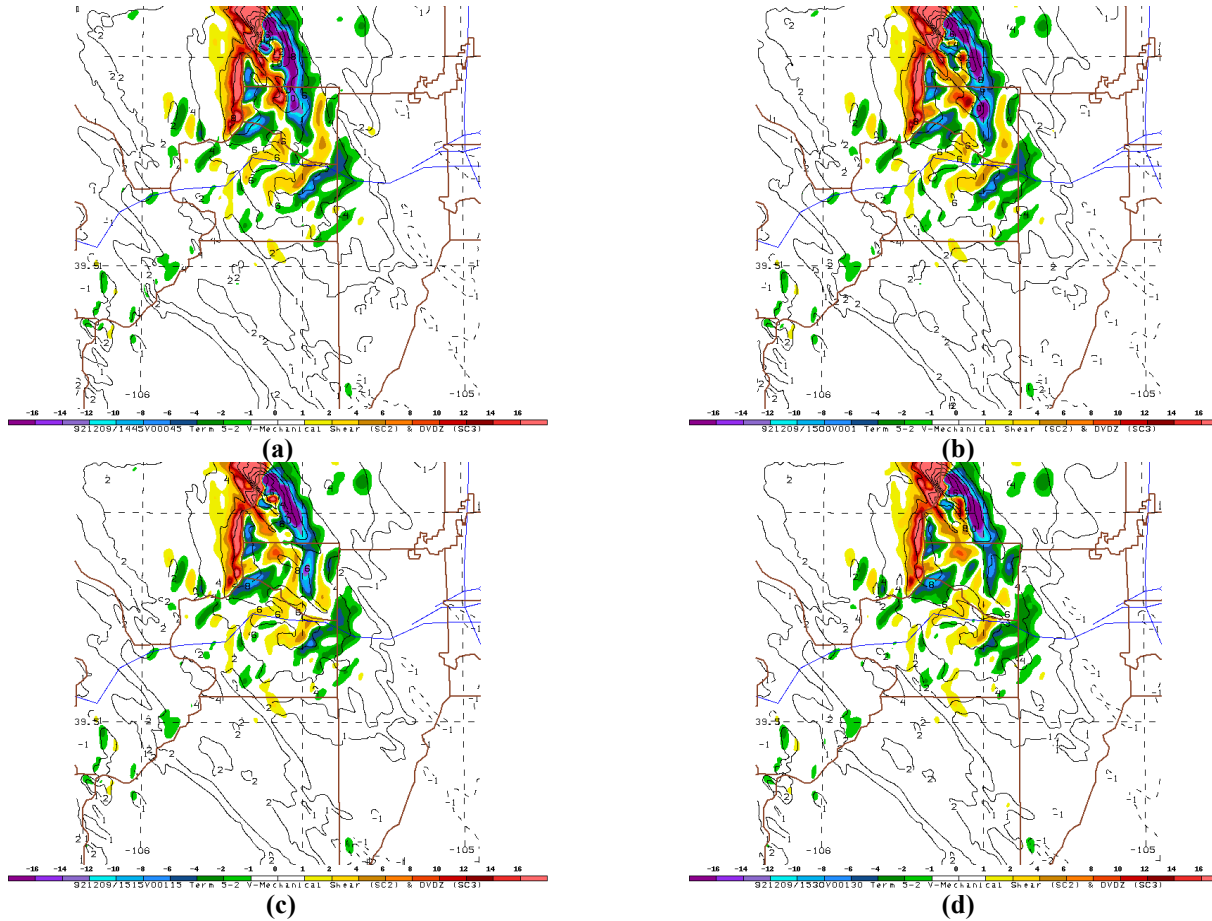


Figure 68: MASS667M explicit grid based turbulence diagnostics for Term 4: Buoyancy Production at 9.75 km valid (a) 1445 UTC; (b) 1500 UTC; (c) 1515 UTC; (d) 1530 UTC 9 December 1992.



**Figure 69:** As with Fig. 68, but for Term 5: U-Mechanical Shear Production at 9.75 km valid (a) 1445 UTC; (b) 1500 UTC; (c) 1515 UTC; (d) 1530 UTC 9 December 1992.



**Figure 70: As with Fig. 69, but for Term 5-2: V-Mechanical Shear Production at 9.75 km valid (a) 1445 UTC; (b) 1500 UTC; (c) 1515 UTC; (d) 1530 UTC 9 December 1992.**

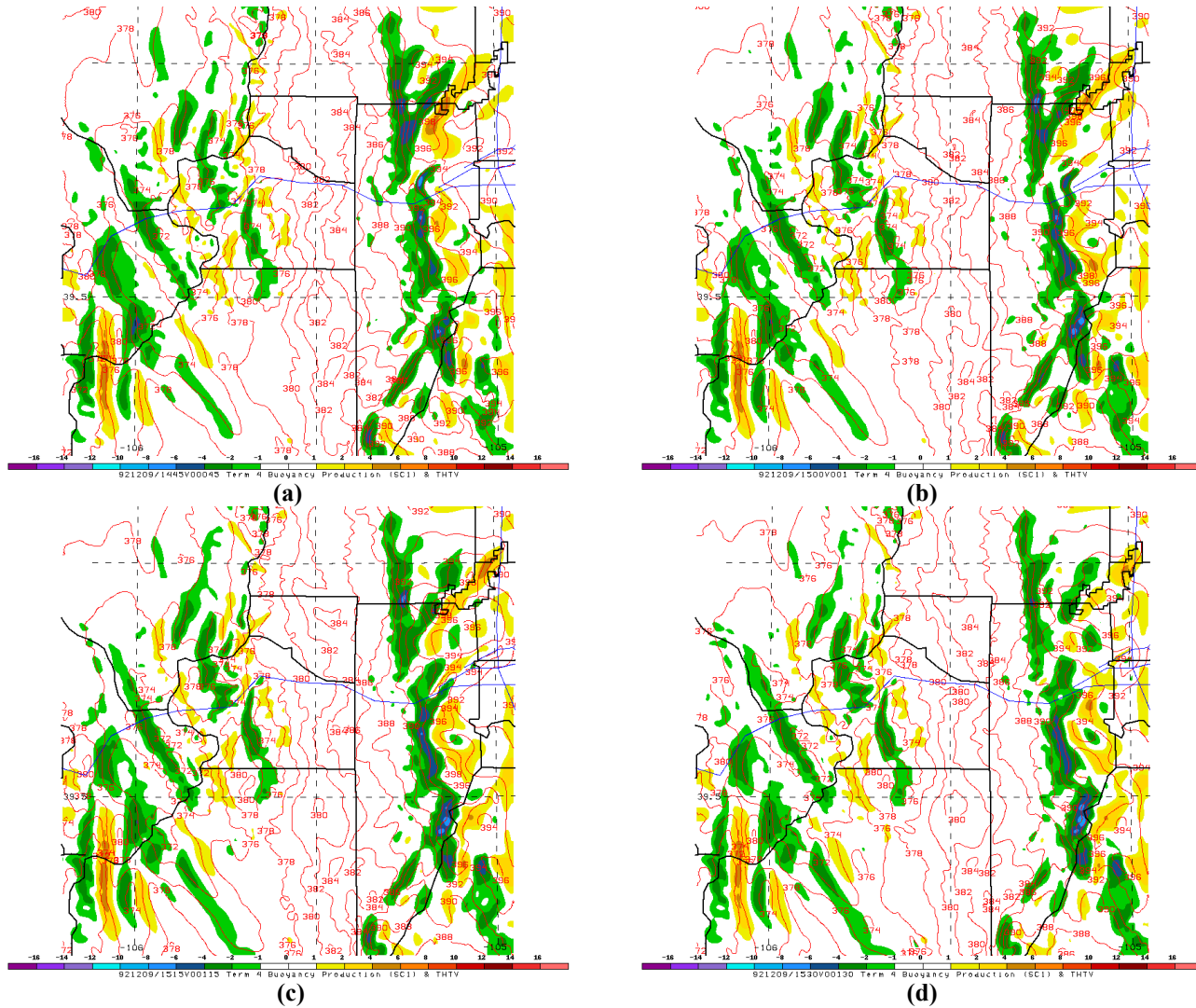


Figure 71: As with Fig. 70, but for Term 4: Buoyancy Production at 14 km valid (a) 1445 UTC; (b) 1500 UTC; (c) 1515 UTC; (d) 1530 UTC 9 December 1992.

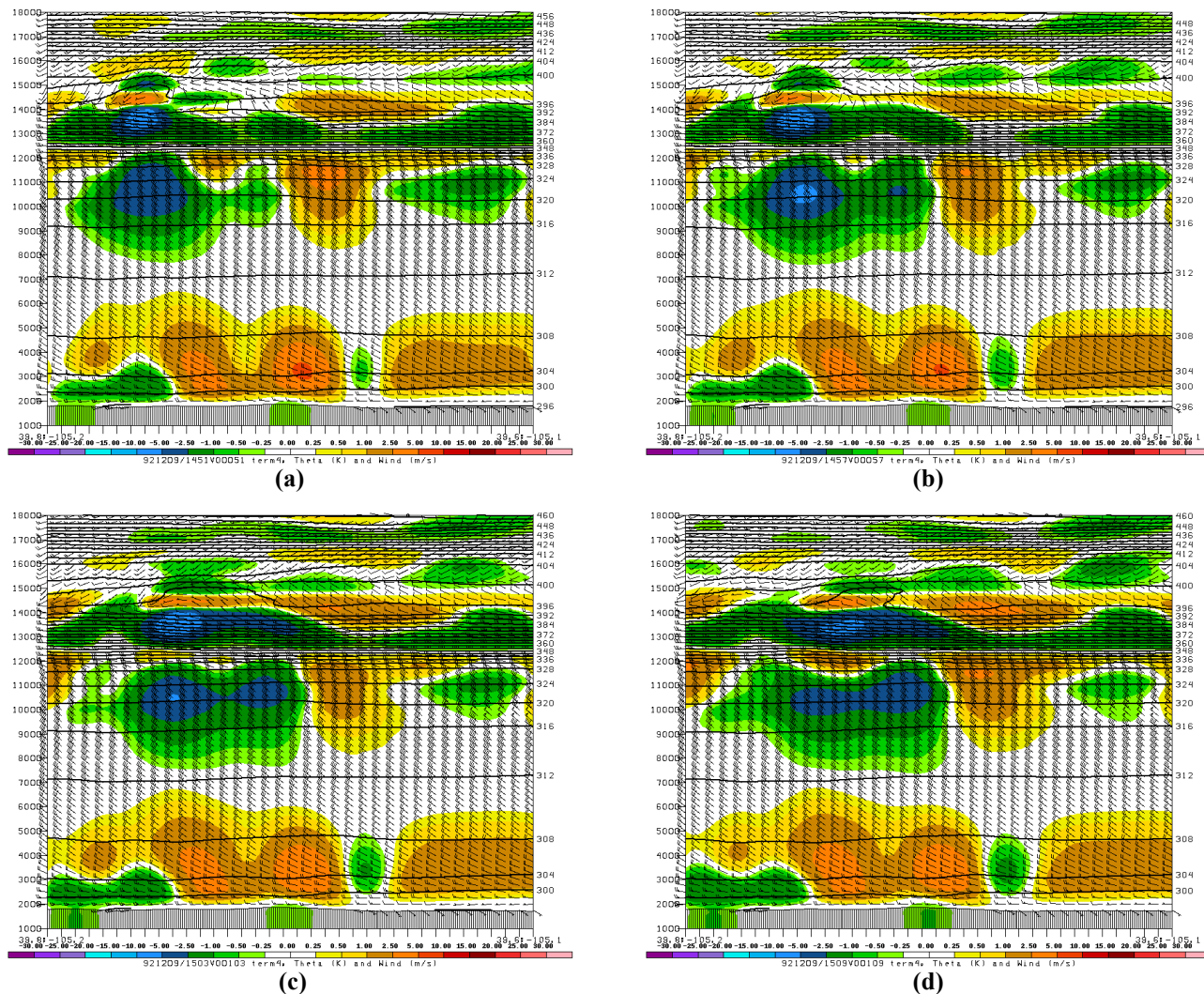


Figure 72: MASS667M cross-section through transient features in the Palmer Divide of Term 4: Buoyancy Production valid (a) 1451 UTC; (b) 1457 UTC; (c) 1503 UTC; (d) 1509 UTC 9 December 1992. Note the wave propagating through the unstable layer between 13.5-15.5 km.

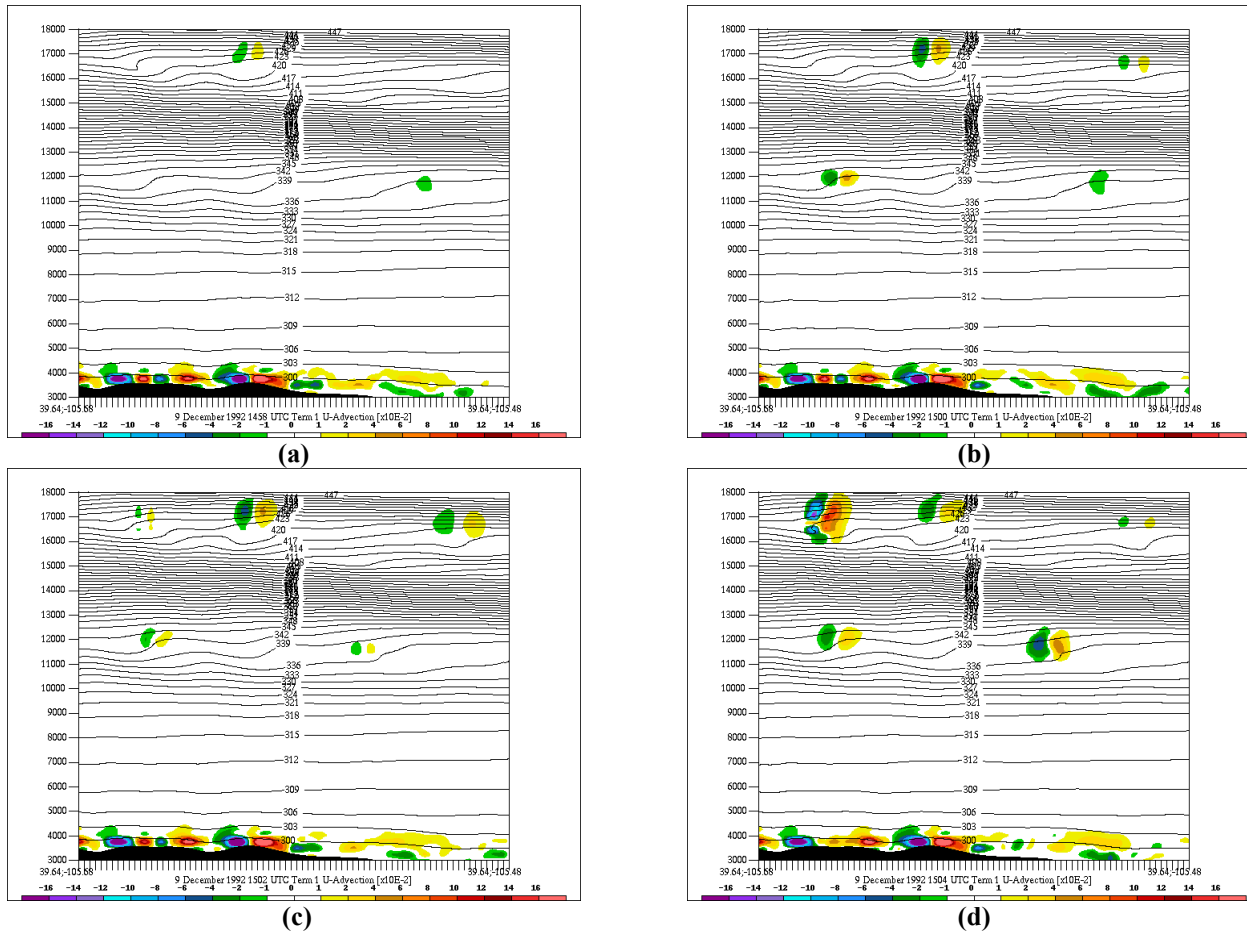


Figure 73: MASS222M Cross-Section through the accident location of Term 1: U-Advection (color fill) and virtual potential temperature (contoured) valid (a) 1458 UTC; (b) 1500 UTC; (c) 1502 UTC; (d) 1504 UTC 9 December 1992.

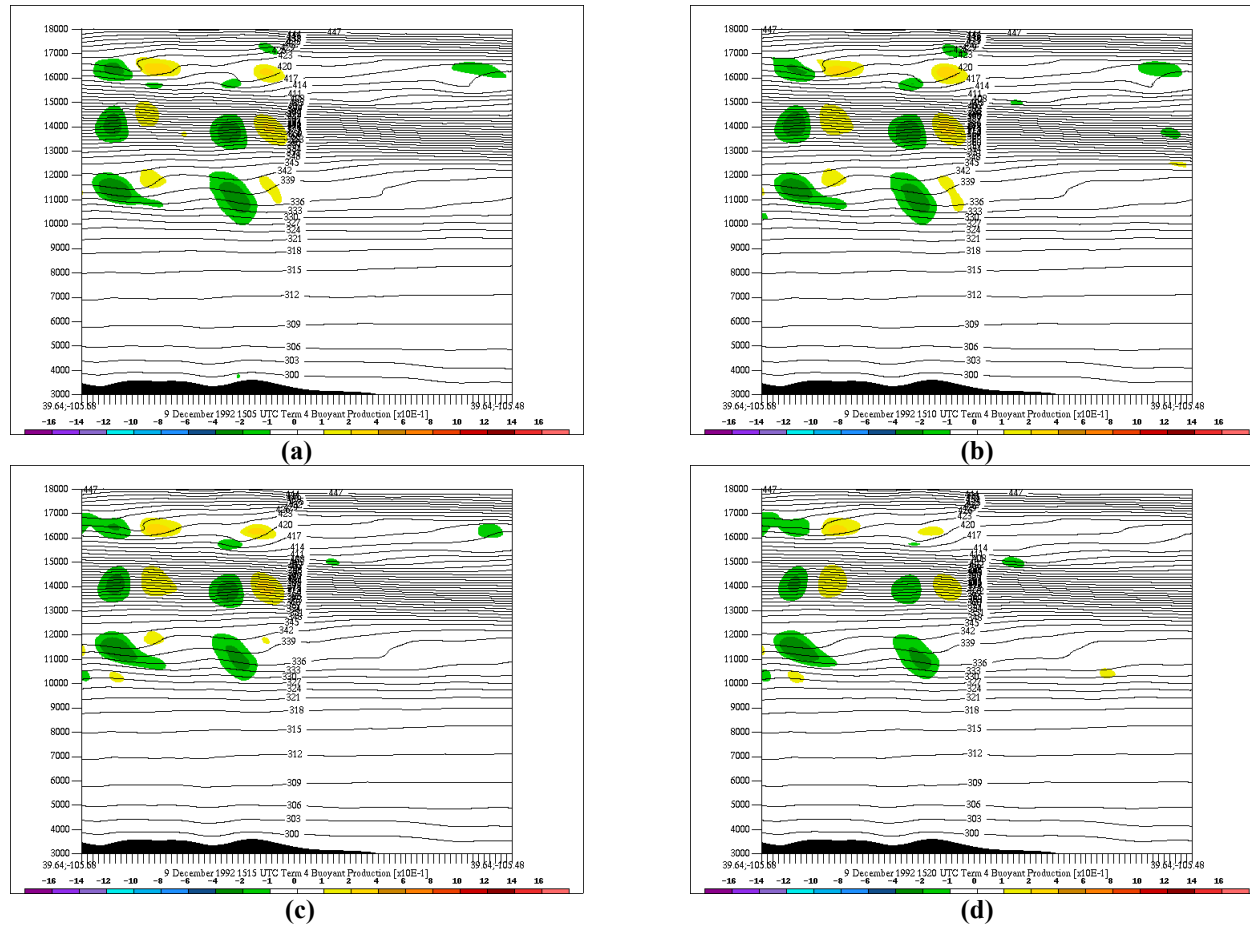


Figure 74: As with Fig. 73, but for Term 4: Buoyancy production valid (a) 1505 UTC; (b) 1510 UTC; (c) 1515 UTC; (d) 1520 UTC 9 December 1992.

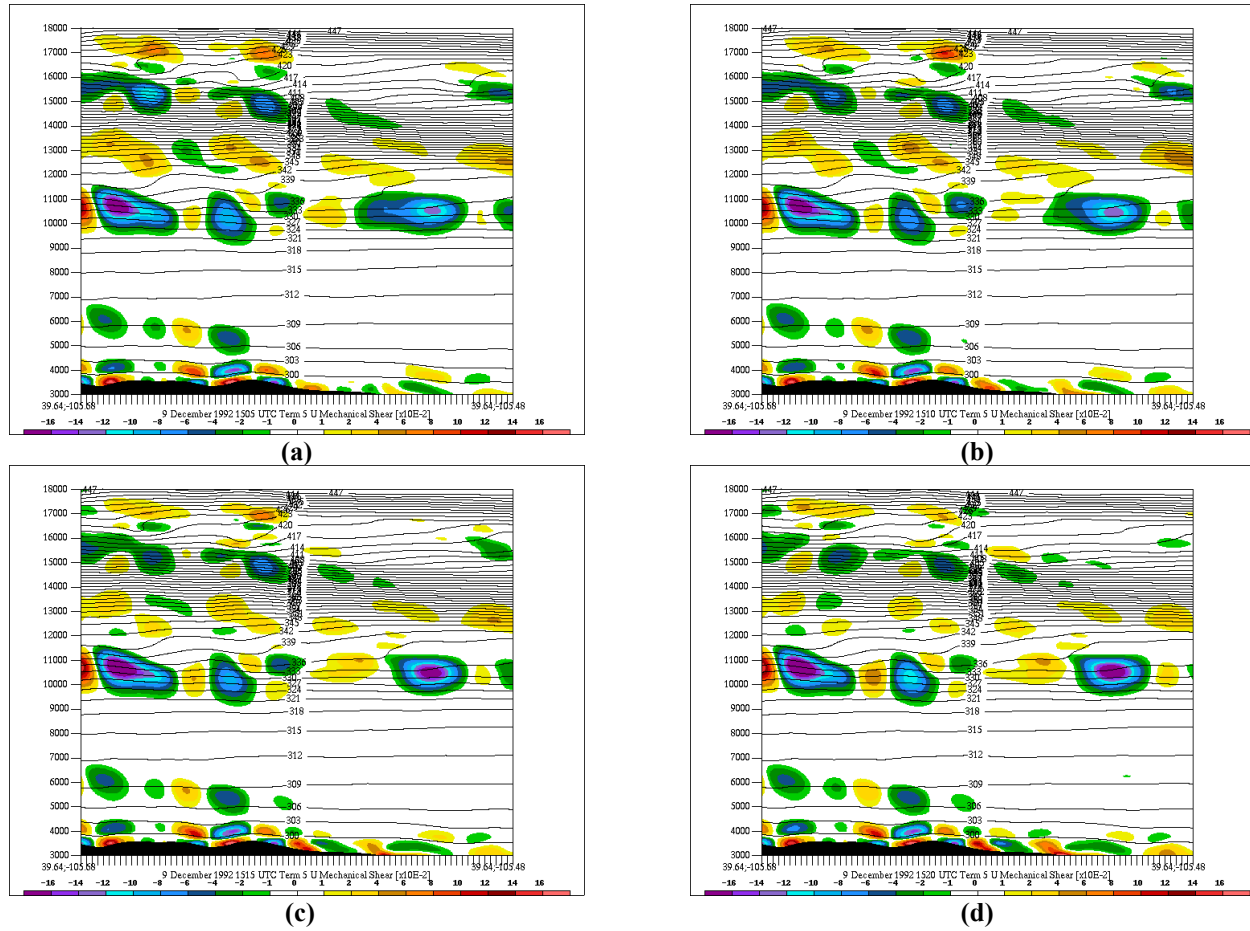


Figure 75: As with Fig. 74, but for Term 5: U-Mechanical shear production valid (a) 1505 UTC; (b) 1510 UTC; (c) 1515 UTC; (d) 1520 UTC 9 December 1992.

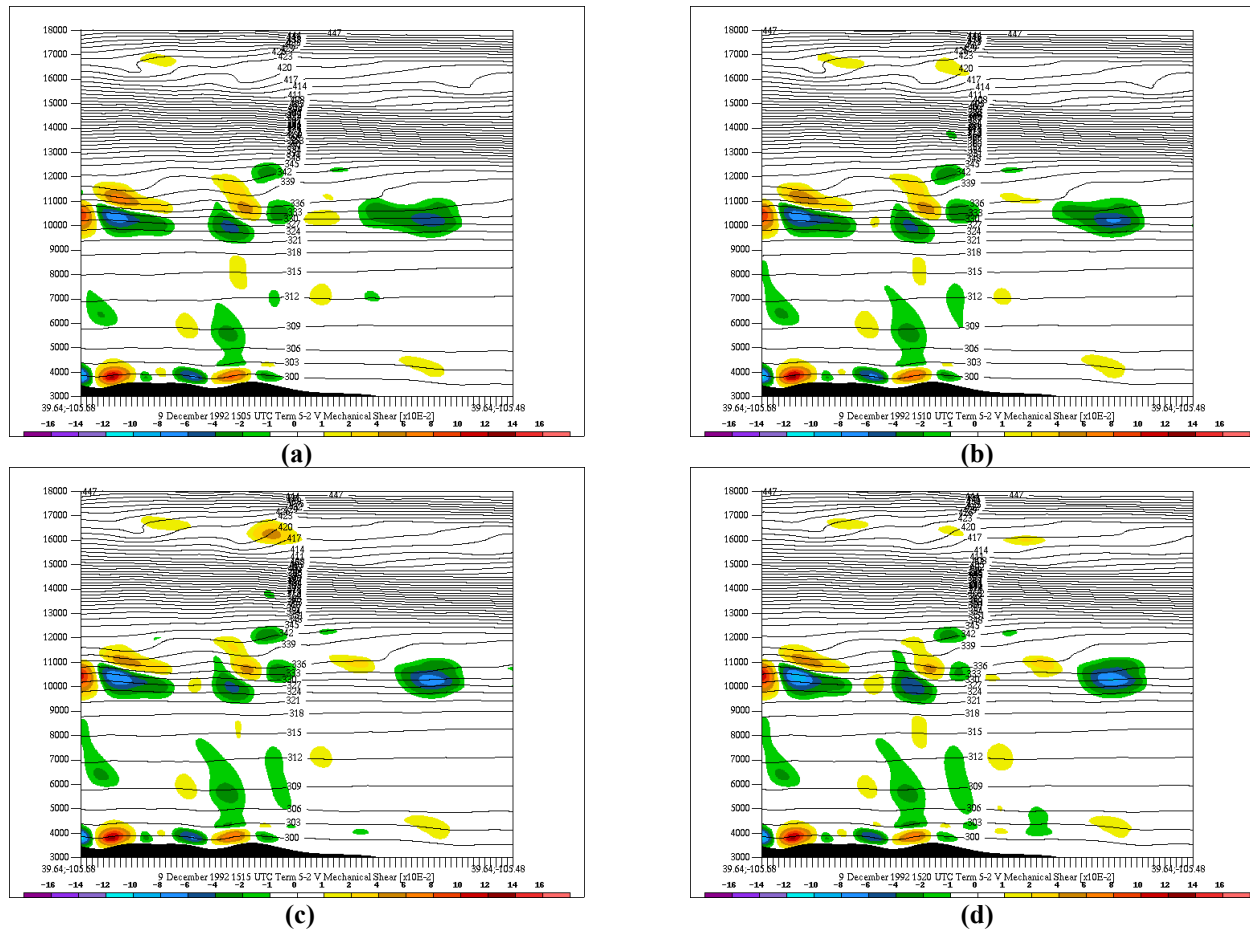


Figure 76: As with Fig. 75, but for Term 5-2: V-Mechanical shear production valid (a) 1505 UTC; (b) 1510 UTC; (c) 1515 UTC; (d) 1520 UTC 9 December 1992.

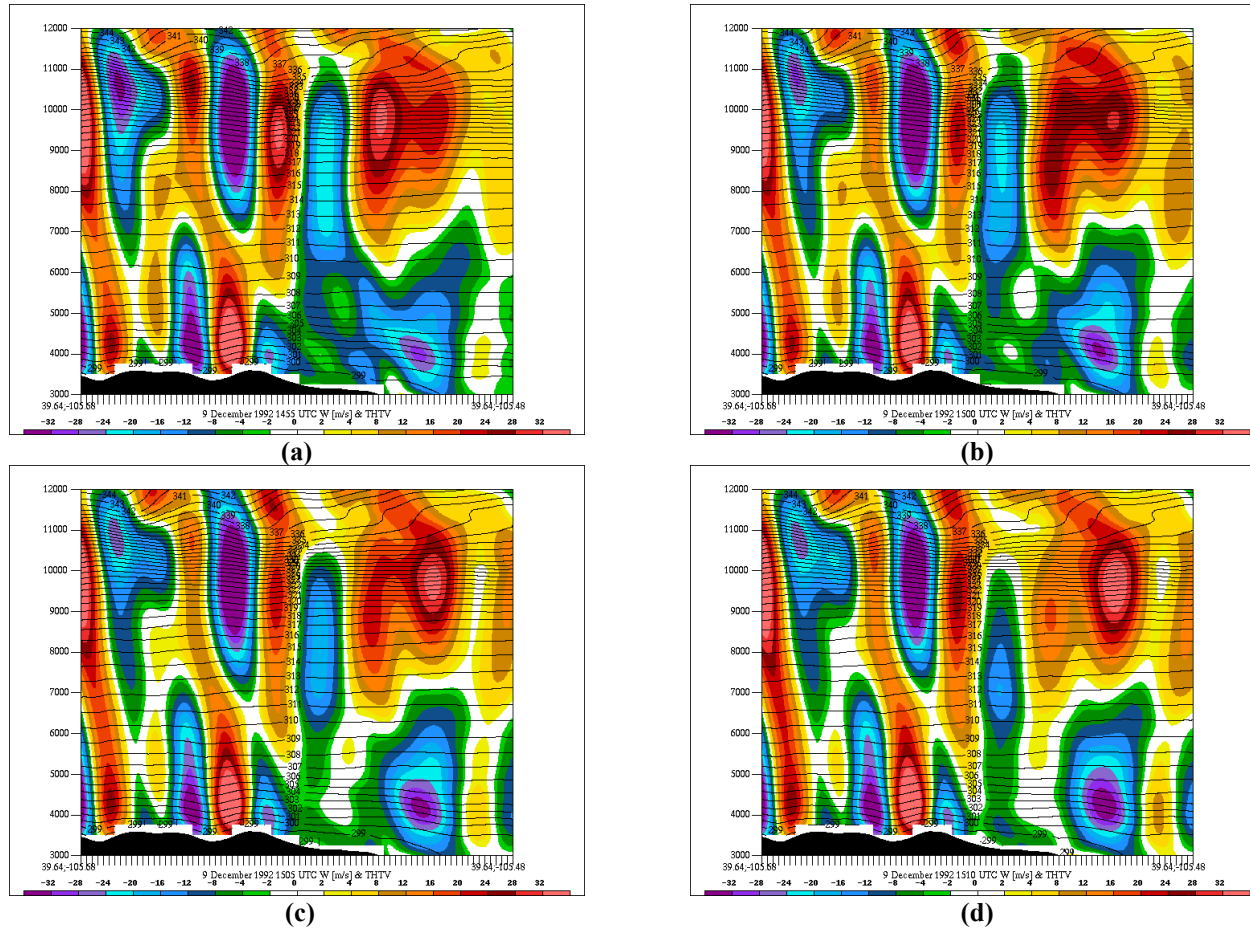
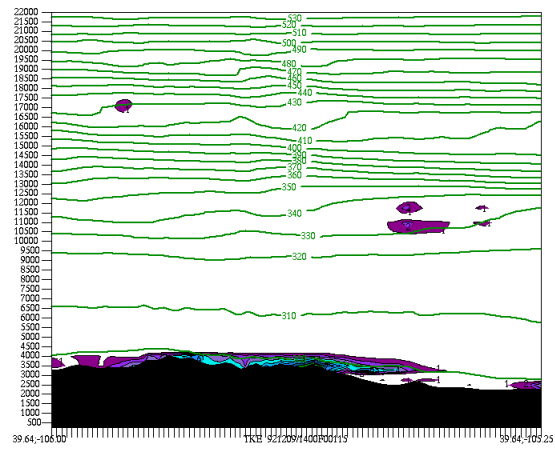
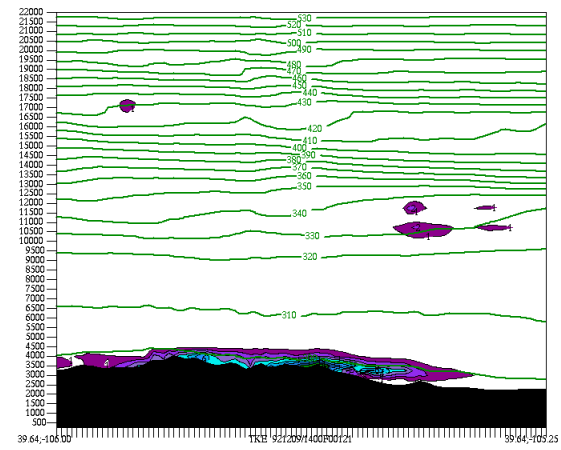


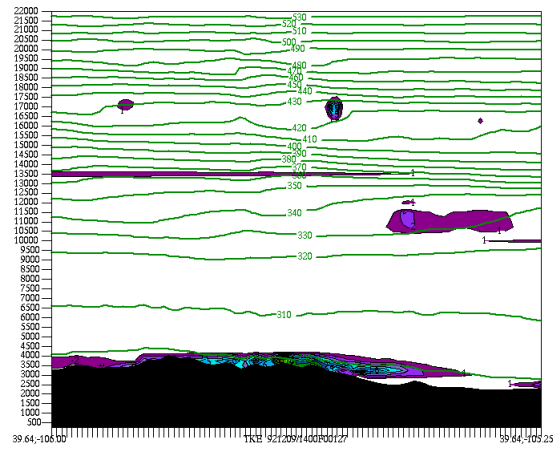
Figure 77: MASS222M cross-section of vertical velocity ( $W$ , color fill) with positive (negative) in warm (cool) colors and isentropes (contoured) valid (a) 1455 UTC; (b) 1500 UTC; (c) 1505 UTC; (d) 1510 UTC 9 December 1992.



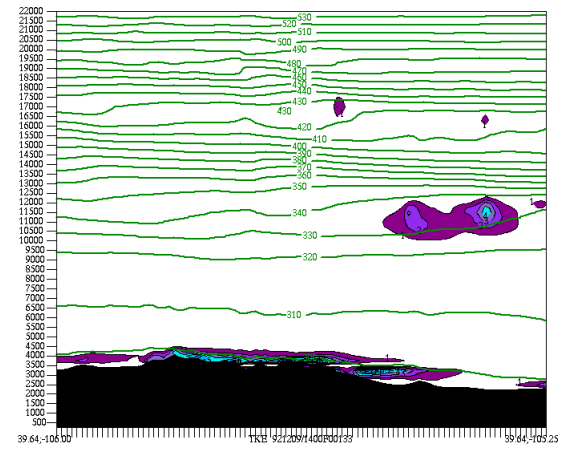
(a)



(b)



(c)



(d)

Figure 78: MASS667M cross-section of TKE (color fill) and isentropes (contoured) valid (a) 1455 UTC; (b) 1500 UTC; (c) 1505 UTC; (d) 1510 UTC 9 December 1992.